

Enhancing the Mechanical Properties of Engineered Cementitious Composites through 3D-Printed Auxetic and Non-Auxetic Reinforcement

A numerical and experimental research

Tahira Lee-On



Enhancing the Mechanical Properties of Engineered Cementitious Composites through 3D printed Auxetic and Non-Auxetic Reinforcement

A numerical and experimental research

by

Tahira Lee-On

to obtain the degree of Master of Science
at the Delft University of Technology,
to be defended publicly on Friday August 25th, 2023 at 1:00 PM.

Student number: 4555031
Project duration: September, 2022 – August, 2023
Thesis committee: Dr. B. Šavija, TU Delft, Chair & supervisor
Dr. Y. Xu, TU Delft, Co-supervisor
Dr. Ir. M. Luković, TU Delft, Independent member

"The road to success is always under construction" - Lily Tomlin

Preface

This thesis marks the completion of my Master's degree in Structural Engineering, representing my final project in this academic pursuit. The journey of working on my MSc thesis has been both fulfilling and enlightening, providing me with valuable skills and knowledge that I will carry forward in my future endeavors. While a part of me feels sad that this project is coming to an end, I am very happy and proud of the work I have produced.

I would like to express my appreciation to my supervisors, Dr. Branko Šavija, Dr. Yading Xu and Dr. Ir. M. Luković for their guidance and collaborative support throughout the past year. I am grateful to Dr. Branko Šavija and Dr. Yading Xu for providing me with the research topic and the opportunity to work under their supervision, building upon the foundation established during my bachelor thesis. Their knowledge, ideas, and helpful feedback have been helpful in shaping the direction and quality of this research. Working with such distinguished professionals in the field has been a privilege, and I am grateful for their mentorship and the knowledge gained through their guidance.

I want to thank my superior, Dr. Branko Šavija, for his critical thinking, extensive knowledge, and contributions during our meetings. His insightful ideas and expertise have significantly expanded my understanding and broadened my horizons. I sincerely appreciate his advice, which was significant in expanding my understanding and improving the quality of this research.

I would also like to acknowledge the exceptional support provided by my daily supervisor, Dr. Yading Xu. His prompt and dependable assistance has been indispensable in the progression of this research. From the initial stages until completion, he has consistently been available to address both minor and major inquiries, as well as assist during testing sessions. I am particularly grateful for his dedication in the lab, where he went above and beyond. Collaborating with Dr. Yading Xu has been an enriching experience, and I am grateful for the knowledge and skills I have acquired through our collaborative work. It has been an absolute pleasure to work with him, and I am grateful for his time and flexibility, even extending into late hours.

Additionally, I would like to extend my gratitude to the technician Maiko van Leeuwen. Maiko provided me with a thorough safety tour of the laboratory facilities, ensuring a secure working environment. I appreciate his assistance during the laboratory tests. I gratefully thank him for his contributions to this study.

Furthermore, I want to thank Rowin Bol and Zhaozheng Meng for their contributions during the progress meetings. Their advice and suggestions have helped to improve the quality and progress of this research.

Lastly, I would like to conclude by expressing my heartfelt appreciation to my family and friends. Their support and presence in my life have been invaluable, particularly during my most difficult and challenging days. I am incredibly grateful for their continuous willingness to help me in any way possible and their constant belief in my decisions and goals. Their love and support have provided me with strength and encouragement, and I am deeply thankful for their support.

*Tahira Lee-On
Delft, August 2023*

Abstract

Currently concrete is one of the most used building materials in the world. Despite its ability to withstand compressive loads, concrete has a low tensile strength, making it prone to cracking when pulled apart. Therefore, reinforcement is required to withstand the tensile stresses. This is generally achieved by applying steel rebars into the tension zone of the concrete structure. In recent years, there has been a growing trend of incorporating fibers into concrete mixtures to develop cement-based materials with properties resembling steel, such as Engineered Cementitious Composites (ECC).

This thesis explores innovative approaches to improve the mechanical properties of ECC by employing 3D-printed auxetic and non-auxetic reinforcements. Auxetic materials display a distinctive characteristic where, upon vertical stretching, they exhibit lateral expansion, and upon vertical compression, they undergo lateral contraction. In other words, when subjected to tensile loading, auxetic materials expand horizontally, and when subjected to compressive loading, they contract horizontally. The main research question revolves around the possibility of enhancing the deformation capacity of ECC through these innovative reinforcements. To address this question, numerical simulations, experimental tests, and comprehensive analyses were conducted.

The study begins with the creation of ECC samples reinforced with 3D printed polymeric meshes, exploring different angles, volumes, and sizes of reinforcements using two distinct 3D printing materials, namely Acrylonitrile Butadiene Styrene (ABS) and Thermoplastic Polyurethane (TPU). The mechanical characteristics of the composite materials were assessed by uniaxial tensile testing, and their response to stress was thoroughly examined.

The results conclusively demonstrate that the incorporation of 3D printed auxetic and non-auxetic reinforcements significantly increases the deformation capacity of ECC. The auxetic designs have improved deformation and flexibility, which makes them perfect for applications that value ductility and strain capacity. In contrast, non-auxetic designs, in particular honeycomb structures, exhibit higher stiffness and load-bearing capacities, making them appropriate for situations that demand structural rigidity and resistance to deformation.

Moreover, the study highlights the crucial role played by the choice of 3D printing material in influencing the strength and strain capacity of the reinforcement. ABS exhibits superior load-bearing capacity due to its high stiffness, while TPU showcases exceptional strain capacity, owing to its elastic and flexible properties. The investigation of many factors, including angles, volumes, and sizes, highlights their substantial influence on the mechanical characteristics of the ECC reinforcement. These characteristics can be changed to allow for alternatives between stiffness, load-bearing capacity, and strain capacity, which can be used to optimize the design of reinforcement for a variety of applications.

In conclusion, this thesis makes a contribution to the developing topic of "designer construction materials," where the properties of cementitious composites can be tailored and optimized through innovative reinforcement strategies. Future constructions that are durable, flexible, and sustainable will be made possible by the combination of 3D printing technology with ECC. This thesis encourages researchers to go further, where imagination and creativity meet concrete, creating a world where materials work with us to create a physical environment that is more resilient.

Nomenclature

Abbreviations

ABS	Acrylonitrile Butadiene Styrene
AM	Additive Manufacturing
AOI	Area of Interest
CAD	Computer-Aided Design
DIC	Digital Image Correlation
ECC	Engineered Cementitious Composites
FDM	Fused Deposition Modeling
FEM	Finite Element Modeling
FRC	Fiber Reinforced Concrete
HPFRC	High-Performance Fiber Reinforced Concrete
LVDT	Linear Variable Displacement Transducer
OPC	Ordinary Portland Cement
PE	Polyethylene
PLA	Polylactic Acid
RP	Reference Point
SCC	Self-Compacting Concrete
SHCC	Strain Hardening Cementitious Composite
SP	Superplasticizer
TPU	Thermoplastic Polyurethane
VMA	Viscosity Modifying Agent

Symbols

ΔL	Change in length	mm
ν	Poisson's ratio	-
σ	Stress	MPa
ε	Strain	-
A	Cross-sectional area	mm ²

B	Bulk modulus	N/m^2
F	Force	N
G	Shear modulus	N/m^2
L_0	Original length	mm
u	Displacement	mm

Contents

Abstract	v
Nomenclature	viii
List of Figures	xvi
List of Tables	xviii
1 Introduction	1
1.1 Motivation	2
1.2 Goal and research questions	2
1.3 Research approach and methods	3
1.4 Thesis outline	4
2 Literature Review	5
2.1 Introduction	6
2.2 Fiber-reinforced concrete	6
2.2.1 Engineered cementitious composites	7
2.2.2 Types of fibers	8
2.3 Mechanical properties	8
2.3.1 Fracture	9
2.4 Poisson's ratio	10
2.4.1 Auxetic material: re-entrant structure	12
2.4.2 Non-auxetic material: rectangular and honeycomb structure	12
2.5 Additive manufacturing	12
2.5.1 AM process	14
2.5.2 Fused deposition modeling	14
2.5.3 Build orientation	16
2.6 Material filament	16
2.6.1 ABS	16
2.6.2 TPU	17
2.7 Digital image correlation	17
2.7.1 Theory	18
2.8 Summary Literature Review	18
3 Numerical Study: Method and Setup	21
3.1 Geometric modeling	22
3.1.1 Phase 1	23
3.1.2 Phase 2	24
3.1.3 Phase 3	25
3.2 Finite element modeling	26
3.2.1 Parts	27
3.2.2 Material properties	27
3.2.3 Assembly	29
3.2.4 Analysis steps	29

3.2.5	Interactions and constraints	30
3.2.6	Load and boundary conditions	30
3.2.7	Mesh	30
3.3	Analyses	30
3.3.1	Poisson's ratio calculation	31
4	Numerical Study: Results and Discussion	33
4.1	Overview Numerical Study	34
4.2	Results phase 1 ABS	35
4.2.1	ABS design A	37
4.2.2	ABS design B	38
4.2.3	ABS design C	39
4.2.4	ABS design D	40
4.3	Results phase 1 TPU	41
4.3.1	TPU design A	43
4.3.2	TPU design B	44
4.3.3	TPU design C	45
4.3.4	TPU design D	46
4.4	Analyzing results and discussion phase 1	47
4.5	Results phase 2 ABS	50
4.5.1	ABS design C_{adj}	51
4.5.2	ABS design D_{adj}	52
4.6	Results phase 2 TPU	53
4.6.1	TPU design C_{adj}	54
4.6.2	TPU design D_{adj}	55
4.7	Analyzing results and discussion phase 2	56
4.8	Results phase 3 ABS	58
4.8.1	ABS design C_{mod}	59
4.9	Results phase 3 TPU	60
4.9.1	TPU design C_{mod}	61
4.10	Analyzing results and discussion phase 3	62
4.10.1	Comparison phase 2 and 3	62
4.11	Summary of numerical study	63
5	Experimental Study: Method and Setup	65
5.1	Material properties reinforcement	66
5.1.1	Reinforcement designs: Phase 1	67
5.1.2	Reinforcement designs: Phase 2	69
5.1.3	Reinforcement designs: Phase 3	71
5.2	Material properties cementitious matrix material	72
5.3	Casting and curing	72
5.4	Sample preparation	74
5.5	Uniaxial tensile test	74
5.6	ABS and TPU bars results	78
5.7	Summary samples	79
6	Experimental Study: Results and Discussion	81
6.1	Overview Experimental study	82
6.2	Results Reference	82
6.3	Results Phase 1 ABS	85
6.3.1	Design A	85

6.3.2	Design C	88
6.3.3	Design D	91
6.4	Results Phase 1 TPU	94
6.4.1	Design A	94
6.4.2	Design C	97
6.4.3	Design D	100
6.5	Analysis and discussing phase 1	103
6.6	Results Phase 2 ABS	106
6.6.1	Design C _{adj}	106
6.6.2	Design D _{adj}	109
6.7	Results Phase 2 TPU	112
6.7.1	Design C _{adj}	112
6.7.2	Design D _{adj}	115
6.8	Analysis and discussing phase 2	118
6.8.1	Comparison phase 1 and 2	120
6.9	Results Phase 3 ABS	122
6.9.1	Design C _{mod}	122
6.10	Results Phase 3 TPU	125
6.10.1	Design C _{mod}	125
6.11	Analysis and discussing phase 3	128
6.11.1	Comparison phase 2 and 3	130
6.12	Summary results and discussion samples	131
7	Conclusions and Recommendations	135
7.1	Conclusions	136
7.2	Recommendations	138
	Bibliography	146
A	Tables	147
B	Numerical Study	151
C	Experimental Study	155

List of Figures

2.1	Difference between how (a) conventional concrete and (b) ECC reacts to being put under severe stress, adapted from [11].	7
2.2	Stress-strain curves: (left), typical stress-strain curve, exhibiting both elastic and plastic regions, along with hysteresis (dashed line), and (right) stress-strain curves for various materials are depicted, adapted from [16].	9
2.3	Milton map of bulk modulus (B , y-axis) versus shear modulus (G , x-axis), showing the regimes of ν , and the differences in material characteristics, adapted from [20].	11
2.4	Comparison between (a) re-entrant honeycomb and (b) honeycomb structure, adapted from [19].	11
2.5	Comparison of the honeycomb (non-auxetic) and re-entrant (auxetic) design, adapted from [42].	13
2.6	Factors affecting mechanical properties, adapted from [49].	14
2.7	Schematic representation of the additive manufacturing technique: Fused deposition modeling, adapted from [51].	15
2.8	Different build orientations, adapted from [52].	16
2.9	Digital image correlation (a) Subset and area of interest in a reference image; (b) Graphic demonstration of correlation between reference image and deformed image, adapted from [61].	18
3.1	Auxetic unit cell: re-entrant honeycomb structure.	22
3.2	Auxetic and non-auxetic designs with labels.	22
3.3	Reinforcing designs phase 1 with measurements presented in mm.	23
3.4	Unit cells of the different designs phase 1 with measurements presented in mm.	23
3.5	Reinforcing designs phase 2 with measurements presented in mm.	24
3.6	Unit cells of the different designs phase 2 with measurements presented in mm.	25
3.7	Unit cell design phase 3 with measurements presented in mm.	26
3.8	Reinforcing designs phase 3 with measurements presented in mm.	26
3.9	FEM step by step method.	28
3.10	Assembly of the parts.	29
3.11	Top plate with displacement.	31
3.12	Length and width of the designs with the locations of the nodes.	32
4.1	Load-displacement curves Phase 1 ABS.	35
4.2	Load-displacement curves and Poisson's ratio-displacement curves for the different designs with ABS reinforcement (axes differ).	36
4.3	Boundary conditions and contour plots of deformed shapes.	37
4.4	Boundary conditions and contour plots of deformed shapes.	38
4.5	Boundary conditions and contour plots of deformed shapes.	39
4.6	Boundary conditions and contour plots of deformed shapes.	40
4.7	Load-displacement curves Phase 1 TPU.	41
4.8	Load-displacement curves and Poisson's ratio-displacement curves for the different designs with TPU reinforcement (axes differ).	42

4.9	Boundary conditions and contour plots of deformed shapes.	43
4.10	Boundary conditions and contour plots of deformed shapes.	44
4.11	Boundary conditions and contour plots of deformed shapes.	45
4.12	Boundary conditions and contour plots of deformed shapes.	46
4.13	Stiffness phase 1 for both materials (axes differ)	47
4.14	Load-displacement curves Phase 2 ABS.	50
4.15	Load-displacement and Poisson's ratio-displacement curves for design C_{adj} and design D_{adj} with ABS reinforcement (axes differ).	50
4.16	Boundary conditions and contour plots of deformed shapes.	51
4.17	Boundary conditions and contour plots of deformed shapes.	52
4.18	Load-displacement curves Phase 2 TPU	53
4.19	Load-displacement and Poisson's ratio-displacement curves for design C_{adj} and design D_{adj} with TPU reinforcement (axes differ).	53
4.20	Boundary conditions and contour plots of deformed shapes.	54
4.21	Boundary conditions and contour plots of deformed shapes.	55
4.22	Load-displacement curves Phase 2 (values on the y-axis differ).	56
4.23	Stiffness phase 2 for both materials (axes differ).	57
4.24	Load-displacement curve and Poisson's ratio-displacement curve design C_{mod} with ABS reinforcement.	58
4.25	Boundary conditions and contour plots of deformed shapes.	59
4.26	Load-displacement curve and Poisson's ratio-displacement curve design C_{mod} with TPU reinforcement.	60
4.27	Boundary conditions and contour plots of deformed shapes.	61
4.28	Load-displacement curves Phase 2 vs 3 (values on the y-axis differ).	63
5.1	Printing setup in the Ultimaker 2+.	66
5.2	Measurements of a unit cell in mm. From left to right: Design A, C and D.	67
5.3	Centerline for design A, C and D respectively.	67
5.4	Different angle designs of 3D printed polymeric reinforcement with their measurements for phase 1. (a) Design A: 63°; (b) Printed reinforcement of design A; (c) Design C: 90°; (d) Printed reinforcement of design C; (e) Design D: 117°; (f) Printed reinforcement of design D.	68
5.5	Printed supports near the ends: (a) Side view supports; (b) Isometric view supports.	69
5.6	Centerline for design C_{adj} (left); design D_{adj} (right).	69
5.7	Design C_{adj} : 90° (a) Length and width of printed reinforcement; (b) 3D printed polymeric reinforcement; (c) Side view supports; (d) Isometric view supports.	70
5.8	Design D_{adj} : 117°. (a) Length and width of printed reinforcement; (b) 3D printed polymeric reinforcement; (c) Side view supports; (d) Isometric view supports.	71
5.9	Centerline for design C_{mod}	72
5.10	Designs of the 3D printed polymeric reinforcement with their measurements for phase 3. (a) Design C_{mod} : 90°; (b) Printed reinforcement of design C_{mod}	72
5.11	Prepared molds.	73
5.12	Visualization of the mold with the reinforcement and cementitious matrix.	74
5.13	Prepared samples for testing.	74
5.14	Visualization of the uniaxial tensile test.	75
5.15	Uniaxial tensile test definitions of tensile strength and strain capacity, adapted from [1].	75
5.16	Camera placement.	76
5.17	Left: Printed TPU bar; Right: untested bar compared to tested bar.	76

5.18	Small TSTM top view.	77
5.19	Small TSTM side view.	77
5.20	Load-displacement curves for the tested ABS and TPU bars (axes are not similar).	78
6.1	Stress-strain curves reference samples.	82
6.2	Stress-strain curve and crack formation pattern for sample R_1	83
6.3	Crack location alongside the crack width curve for sample R_1	84
6.4	Stress-strain curves design A.	85
6.5	Stress-strain curves sample A_1 against reference samples.	86
6.6	Stress-strain curve and crack formation pattern for sample A_1	86
6.7	Crack location alongside the crack width curve for sample A_1	87
6.8	Stress-strain curves design C.	88
6.9	Stress-strain curves sample C_4 against reference samples.	89
6.10	Stress-strain curve and crack formation pattern for sample C_4	89
6.11	Crack location alongside the crack width curve for sample C_4	90
6.12	Stress-strain curves design D.	91
6.13	Stress-strain curves sample D_3 against reference samples.	92
6.14	Stress-strain curve and crack formation pattern for sample D_3	92
6.15	Location of cracks.	93
6.16	Crack width against measured displacement.	93
6.17	Crack width against measured displacement without crack 3.	93
6.18	Crack location alongside the crack width curve for sample D_3	93
6.19	Stress-strain curves design A.	94
6.20	Stress-strain curves sample A_2 against reference samples.	95
6.21	Stress-strain curve and crack formation pattern for sample A_2	95
6.22	Crack location alongside the crack width curve for sample A_2	96
6.23	Stress-strain curves design C.	97
6.24	Stress-strain curves sample C_1 against reference samples.	98
6.25	Stress-strain curve and crack formation pattern for sample C_1	98
6.26	Crack location alongside the crack width curve for sample C_1	99
6.27	Stress-strain curves design D.	100
6.28	Stress-strain curves sample D_4 against reference samples.	101
6.29	Stress-strain curve and crack formation pattern for sample D_4	101
6.30	Crack location alongside the crack width curve for sample D_4	102
6.31	Results phase 1.	104
6.32	Stress-strain curves design C_{adj}	106
6.33	Stress-strain curves sample $C_{3,adj}$ against reference samples.	107
6.34	Stress-strain curve and crack formation pattern for sample $C_{3,adj}$	107
6.35	Crack location alongside the crack width curve for sample $C_{3,adj}$	108
6.36	Stress-strain curves Design D_{adj}	109
6.37	Stress-strain curves sample $D_{4,adj}$ against reference samples.	110
6.38	Stress-strain curve and crack formation pattern for sample $D_{4,adj}$	110
6.39	Crack location alongside the crack width curve for sample $D_{4,adj}$	111
6.40	Stress-strain curves Design C_{adj}	112
6.41	Stress-strain curves sample $C_{3,adj}$ against reference samples.	113
6.42	Stress-strain curve and crack formation pattern for sample $C_{3,adj}$	113
6.43	Crack location alongside the crack width curve for sample $C_{3,adj}$	114
6.44	Stress-strain curves Design D_{adj}	115
6.45	Stress-strain curves sample D against reference samples.	116
6.46	Stress-strain curve and crack formation pattern for sample $D_{3,adj}$	116

6.47 Crack location alongside the crack width curve for sample $D_{3,adj}$.	117
6.48 Results phase 2.	119
6.49 Strength comparison phase 1 and 2	120
6.50 Strain capacity comparison phase 1 and 2	121
6.51 Stress-strain curves Design C_{mod} .	122
6.52 Stress-strain curves sample $C_{2,mod}$ against reference.	123
6.53 Stress-strain curve and crack formation pattern for sample $C_{2,mod}$.	123
6.54 Crack location alongside the crack width curve for sample $C_{2,mod}$.	124
6.55 Stress-strain curves Design C_{mod} .	125
6.56 Stress-strain curves sample $C_{3,mod}$ against reference.	126
6.57 Stress-strain curve and crack formation pattern for sample $C_{3,mod}$.	126
6.58 Crack location alongside the crack width curve for sample $C_{3,mod}$.	127
6.59 Results phase 3.	129
6.60 Stress-strain curves comparison phase 2 and 3 for material ABS.	130
6.61 Stress-strain curves comparison phase 2 and 3 for material TPU.	131
6.62 Comparison of phase 2 and 3 samples	132
B.1 Tie constraint bottom	151
B.2 Tie constraint top	152
B.3 Element type	152
B.4 Mesh controls	153
B.5 Triangular shaped mesh	153
C.1 Sample R_1 backside showing multiple cracks	155
C.2 Sample C_1 -TPU backside showing multiple cracks	156
C.3 Air void in Sample B-ABS	156
C.4 Sample B casting complications	157
C.5 Segregation	157
C.6 Sample surface as a result from bleeding and segregation	157

List of Tables

3.1	Dimensions reinforcement phase 1.	24
3.2	Dimensions reinforcement phase 2.	25
3.3	Dimensions reinforcement phase 3.	25
3.4	Plastic behavior of ABS.	27
3.5	Plastic behavior of TPU.	27
5.1	Printing parameters of the 3D printed reinforcement.	66
5.2	Dimensions reinforcement Phase 1.	67
5.3	Reinforcing volume Phase 2.	70
5.4	Reinforcing volume Phase 3.	71
5.5	Self-compacting ECC mix proportion [g/l], adapted from [9].	72
5.6	Summary of the tested samples.	79
6.1	Test results reference samples	83
6.2	Stress and strain corresponding to the different stages.	83
6.3	Test results for samples with design A.	85
6.4	Stress and strain corresponding to the different stages.	86
6.5	Test results for samples with design C.	88
6.6	Stress and strain corresponding to the different stages.	89
6.7	Test results for samples with design D.	91
6.8	Stress and strain corresponding to the different stages.	92
6.9	Test results for samples with design A.	94
6.10	Stress and strain corresponding to the different stages.	95
6.11	Test results for samples with design C	97
6.12	Stress and strain corresponding to the different stages.	98
6.13	Test results for samples with design D.	100
6.14	Stress and strain corresponding to the different stages.	101
6.15	Test results phase 1.	103
6.16	Test results for samples with design C_{adj}	106
6.17	Stress and strain corresponding to the different stages.	107
6.18	Test results for samples with design D_{adj}	109
6.19	Stress and strain corresponding to the different stages.	110
6.20	Test results for samples with design C_{adj}	112
6.21	Stress and strain corresponding to the different stages.	113
6.22	Test results for samples with design D_{adj}	115
6.23	Stress and strain corresponding to the different stages.	116
6.24	Test results phase 2.	118
6.25	Test results for samples with design C_{mod}	122
6.26	Stress and strain corresponding to the different stages.	123
6.27	Test results for samples with design C_{mod}	125
6.28	Stress and strain corresponding to the different stages.	126
6.29	Test results phase 3.	128

A.1	Desired dimensions of the samples	147
A.2	Actual dimensions of the cut samples	148
A.3	Actual dimensions of the cut samples	149

1

Introduction

This chapter provides an overview of the research topic, focusing on the exploration of 3D printed auxetic and non-auxetic reinforcement in ECC. The primary goal of the study is to investigate the potential of enhancing the deformation capacity of ECC through the incorporation of innovative 3D printed polymeric reinforcement. To achieve this objective, the research questions are formulated, addressing both the feasibility of increasing the deformation capacity and specific aspects related to 3D printed polymeric reinforcement, the influence of different printing materials, and the effects of altering parameters on the mechanical properties of the reinforcement. The research approach and methods utilized in this study are then detailed. Lastly, the thesis outline is presented, consisting of seven chapters, each with a specific focus.

1.1. Motivation

Concrete, the most used building material in the world, bears large compressive loads, but exhibits a low tensile strength when subjected to tension. This limitation has led to innovative advancements, such as Engineered Cementitious Composites (ECC). ECC has emerged as remarkable construction materials, known for their exceptional ductility and strain-hardening behavior. These cement-based composites offer a unique combination of toughness and tensile strain capacity, making them a compelling choice for various engineering applications, particularly in the construction and infrastructure sectors. However, despite their remarkable qualities, there is still an increasing need to further improve the mechanical properties of ECC. The multiple cracking behaviors observed in conventional materials has sparked significant interest in their potential to revolutionize construction practices.

Digitized construction is becoming increasingly popular. Although 3D printing of concrete structures has received the most interest, 3D printing of reinforcement is becoming more popular. In contrast to conventional reinforcement, 3D printed reinforcement offers greater design flexibility to enhance performance, such as enhancing bond strength by printing a rough surface. If reinforcements were printed, they could easily be mass-produced with ideal forms, minimum alterations and faults, thus shortening the building time, using less materials and ultimately saving costs.

The advancement of 3D printing technology has opened doors to creating complex structures with customized reinforcement patterns. Among the various possibilities offered by 3D printing, the incorporation of 3D printed reinforcement in concrete has gained significant attention. Xu and Šavija [1] proposed an innovative approach to develop ECC using additive manufacturing to create polymeric reinforcement meshes. ECC was developed by incorporating the polymeric meshes into conventional concrete, without the incorporation of fibers. Their research demonstrated the feasibility of producing cementitious composites with deflection hardening or strain hardening properties, offering new possibilities for enhancing the mechanical behavior of the material. Moreover, the findings showed that by incorporating proper designs, the manufactured ECC can replicate the multiple cracking behavior observed in conventional ECC.

Building on these findings, this thesis explores the possibility to further enhance the deformation capacity of conventional ECC by introducing 3D printed polymeric reinforcements to the samples. The investigation involved diverse reinforcing designs, utilizing two distinct 3D printing materials, namely Acrylonitrile Butadiene Styrene (ABS) and Thermoplastic Polyurethane (TPU). ABS, known for its high stiffness and strength, is expected to enhance the load-bearing capacity of the reinforced ECC. In contrast, TPU, with its exceptional flexibility and elastomeric properties, is anticipated to improve the deformation capacity of the material. This study delves into the use of both auxetic and non-auxetic reinforcement in ECC. Specifically, auxetic materials were characterized by a negative Poisson's ratio, resulting in lateral expansion under tension, while non-auxetic materials displayed the conventional positive Poisson's ratio behavior. By applying these innovative approaches, this research aims to unlock new horizons in the construction industry and further enhance the mechanical performance of cementitious materials.

1.2. Goal and research questions

This thesis aims to investigate the potential for enhancing the deformation capacity of conventional ECC by incorporating 3D printed reinforcements into the cementitious matrix. Hence, the first hypothesis of this study is as follows:

Hypothesis 1: The incorporation of 3D printed reinforcement in ECC will lead to an increase

in deformation capacity compared to ECC.

Thus the main research question of this thesis is: "Is it possible to increase the deformation capacity of ECC when reinforced with 3D printed auxetic and non-auxetic reinforcement?" This thesis aims to optimize the design of custom 3D printed polymeric reinforcement by thoroughly investigating its effects on the mechanical properties of ECC. To address the primary research question, several essential sub-questions have been formulated:

- *How do the different printing materials (ABS and TPU) influence the strength and strain capacity of the reinforced ECC?* By investigating the mechanical behavior of ECC reinforced with these distinct 3D printed materials, the aim is to understand how their individual characteristics impact the load-bearing capacity and deformation capacity of the composite material.
- *How does altering parameters such as the angle, volume and size affect the mechanical properties of the reinforcement and composite?* Different reinforcement configurations will be explored, including auxetic and non-auxetic designs, characterized by angles ranging from 52° to 117°. Additionally, the influence of the volume and size changes in the reinforcement will be investigated to determine how it impacts the overall performance of the ECC.

Based on the research questions, the following hypotheses have been formulated:

Hypothesis 2: The use of ABS as the 3D printing material for reinforcement in ECC will result in enhanced load-bearing capacity compared to TPU as the 3D printing material, while using TPU will result in increased deformation capacity when compared to ABS.

Hypothesis 3: Altering the angle, volume and size of 3D printed reinforcement designs will significantly influence the mechanical properties of the ECC, with certain configurations leading to increased strain capacity and improved performance.

These hypotheses will serve as the foundation for the numerical and experimental investigations conducted in this study. By systematically testing and analyzing the different 3D printed reinforcement designs and materials, this research aims to provide valuable insights into the development of innovative reinforcement strategies for ECC. This work will help us to better understand how reinforcement designs, material choices, and 3D printing processes interact to produce optimal ECC with improved mechanical performance. Moreover, this research aims to offer valuable contributions to the development of innovative reinforcement strategies for ECC, unlocking new possibilities to elevate its deformation capacity and overall performance as an advanced construction material. Overall, this research seeks to advance the field of construction materials by investigating innovative ways for reinforcing ECC through 3D printed auxetic and non-auxetic patterns. The ultimate objective is to fully realize the potential of ECC, revolutionizing its application in sustainable and robust infrastructure development.

1.3. Research approach and methods

A dual approach that combines numerical simulations and experimental testing has been used to comprehensively address these research questions. Fused deposition modeling will be employed to analyze the mechanical behavior of ECC reinforced with various 3D printed designs. Additionally, uniaxial tension tests will be conducted on the ECC specimens to provide practical insights into the performance of the material. The investigation will focus on two commonly used 3D printing materials to assess their influence on the strength and strain capacity of the

ECC. Furthermore, this thesis will investigate how different angles of reinforcement designs affect the mechanical behavior of ECC. The designs, ranging from traditional bowtie structures to honeycomb configurations, will be analyzed for their load-displacement characteristics and stress distributions.

1.4. Thesis outline

There are seven chapters in this thesis, including the current Introduction chapter. Chapter 2 provides a review of relevant literature and studies relating to the research topic. Relevant literature and studies related to the topic will be critically reviewed to establish a strong foundation for the research.

The third chapter focuses on the numerical study carried out as part of this research. Numerical simulations were conducted to predict the fracture behavior, load-displacement response of the 3D printed reinforcement for both printing materials and to validate the auxetic or non-auxetic nature of the reinforcement. In this chapter the research design and methodology will be described in detail, followed by an explanation of the finite element modeling (FEM) approach used in the study. The simulation setup and parameters will be outlined.

Chapter 4 delves into the results of the numerical study which will be presented and analyzed. The chapter will provide a comprehensive interpretation and analysis of the results. The obtained data including stress-strain curves, Poisson's ratio, elastic modulus, and fracture behavior are among the parameters present in the acquired data.

Chapter 5 provides a comprehensive description of the experimental setup used in the study. The materials and samples used in the experiments will be detailed, along with the test equipment and procedures. This chapter will also cover the sample preparation, as well as the procedures taken.

Chapter 6 presents and discusses the experimental results obtained from the conducted tests. Specifically, the uniaxial tension test results will be analyzed, and the load-displacement curves and behavior of the materials will be examined. This chapter will highlight the strength and deformation characteristics of the materials and provide a comparison of different reinforcement strategies.

The final chapter of the thesis presents the key findings from this study. The contributions of this research to the field will be highlighted, and the limitations of the study will be acknowledged. Additionally, recommendations for future research directions will be provided to guide further investigations in the area.

The thesis will conclude with a list of references and appendices containing detailed numerical simulation data, uniaxial tension test raw data, and supplementary figures and graphs. The outlined structure aims to ensure a logical and cohesive presentation of the research, facilitating a comprehensive understanding of the outcomes of the study.

2

Literature Review

This chapter presents a comprehensive review of the relevant literature and studies related to the research topic. To create a strong foundation for the research, pertinent literature and papers will be critically analyzed.

2.1. Introduction

Concrete, while an excellent construction material with high compressive strength, has relatively low tensile strength and is susceptible to cracking and failure when subjected to tensile forces or bending [2]. To address this limitation, concrete is often reinforced with materials like steel bars to enhance its tensile strength and overall structural performance. This combination of concrete and reinforcement is known as reinforced concrete.

Concrete is a brittle material and reinforcement is used to make concrete structures ductile [3]. Ductility refers to the ability of a material to undergo substantial deformation before failing. Steel, being a ductile material, can absorb energy through plastic deformation, which helps in preventing sudden brittle failures in the concrete [4]. The combination of concrete and reinforcement creates a material that can efficiently carry both compressive and tensile loads, resulting in a structurally stable and durable construction. Reinforcement helps control the width and propagation of cracks that may occur in concrete due to shrinkage, temperature changes, or external loads. By adding reinforcement, the load-bearing capacity of the concrete structure can be significantly increased, allowing for the construction of larger and more complex buildings and infrastructures.

Furthermore, advancements in construction technology have introduced innovative materials like fiber-reinforced concrete (FRC) and ECC, which offer enhanced mechanical properties and unique deformation behavior. This review delves into the characteristics, mechanical properties of these composites. Followed by relevant literature to serve as a solid foundation for this investigation.

2.2. Fiber-reinforced concrete

FRC is a composite material that incorporates short, discrete fibers into the concrete mix to enhance its mechanical properties and overall performance. The fibers used in FRC can be made from various materials, such as steel, glass, synthetic polymers, or natural fibers [5]. Each type of fiber offers specific advantages and is chosen based on the intended application and performance requirements. The addition of fibers in FRC significantly improves the ductility of the concrete, enabling it to absorb energy through mechanisms like fiber bridging and crack deflection [6]. The fibers act as reinforcement when cracks form under external loads, limiting their propagation and preventing sudden failures, thereby enhancing crack control and ensuring the durability and longevity of concrete structures. Moreover, FRC mitigates the risk of spalling during fire exposure by creating pathways for steam escape, reducing internal pressure buildup [7]. This is only the case when FRC is reinforced with polypropylene fibers.

Fiber-reinforced concrete finds applications in a wide range of civil engineering projects, including pavements, bridge decks, tunnel linings, shotcrete applications, and precast elements [5]. Its ability to provide improved flexural strength and resistance to cracking makes it suitable for structures subjected to dynamic and seismic loads. Researchers and engineers continue to explore novel fiber materials and optimized mix designs to further enhance the performance of fiber-reinforced concrete and expand its use in various construction scenarios. FRC can be divided into three categories. Low fiber volume fractions ($\leq 1\%$) used to minimize shrinkage cracking [5], moderate fiber volume fractions (between 1% and 2%) offering enhanced mechanical properties like fracture toughness and impact resistance, and high-performance FRC (HPFRC) with high fiber contents ($> 2\%$) demonstrating visible strain-hardening behavior [8]. Additionally, a brand-new variety of fiber-reinforced cementitious composite, known as ECC, has recently emerged, paving the way for further advancements in the field of FRC.

2.2.1. Engineered cementitious composites

The brittleness of concrete places restrictions on both resilience and durability of concrete structures, even on those that include steel reinforcement. To address this issue, ECC, also known as strain hardening cementitious composite (SHCC), was created [9]. ECC is the first cement-based material to produce tensile ductility at comparatively low fiber levels of 1 to 2% by volume and was also created to reduce the amount of reinforcement needed [10]. ECC is a fairly new material recognized for its ability to manage cracks and its ductile behavior, which indicates strain hardening behavior followed by multiple crack formation. Due to their magnificent mechanical properties, ECC is now one of the essential materials to fix damaged structures. In Fig. 2.1, a comparison of a flexural test between conventional concrete and ECC is depicted, showing the differences when trying to bend the concrete.

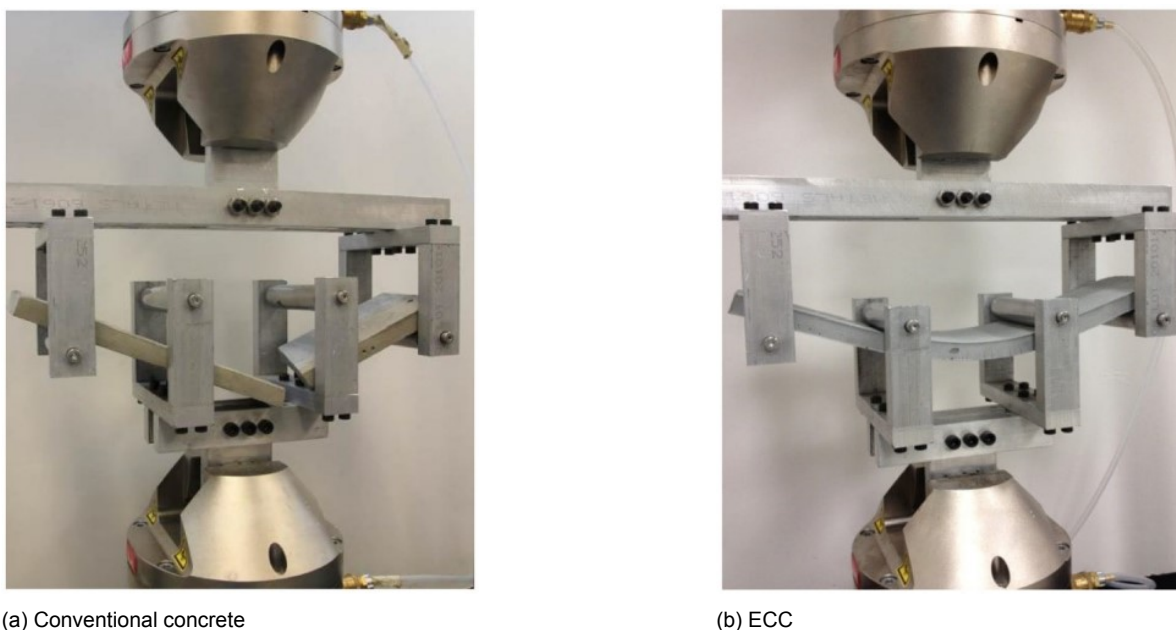


Figure 2.1: Difference between how (a) conventional concrete and (b) ECC reacts to being put under severe stress, adapted from [11].

ECC is a cementitious material that mostly consists of Ordinary Portland cement (OPC) with supplements and does not include coarse aggregates. Due to the lack of these aggregates, it has a greater binder concentration. ECC is typically composed of OPC, fine sand, water, fibers and chemical admixtures such as superplasticizers which are incorporated into the concrete mix to ensure both optimal workability and strength. These additives effectively enhance the flowability of the concrete without compromising its overall strength. By using superplasticizers, the concrete achieves the desired level of fluidity required for easy flow during placement while retaining its structural integrity and strength properties. The fibers used are usually short and thin, and they are evenly dispersed throughout the matrix.

The moderate fiber content of ECC enables its flexible application in both on-site construction and off-site precast elements [12]. Additionally, specialized versions of ECC with self-compacting behavior have been developed to enhance its usability and performance. This research utilized a self-compacting ECC, a material for which only a few development reports are available [13]. Self-compacting concrete (SCC) is an innovative concrete that can be placed and compacted without the need for vibration. It exhibits the ability to flow under its own weight, effectively filling formwork and achieving complete compaction, even in the presence of densely arranged reinforcement. The resulting hardened concrete is dense, uniform,

and possesses engineering properties and durability similar to traditional vibrated concrete.

To produce SCC, the addition of a viscosity agent is necessary to attain the required level of viscosity in the matrix. SCC offers numerous advantages, including enhanced flowability, workability, pumpability, and bond performance. Therefore, this study applied a self-compacting ECC [14].

2.2.2. Types of fibers

Incorporating fibers into concrete is a well-established method to enhance its tensile response, which is typically weak in conventional concrete. The primary functions of the reinforcing fibers in concrete are to avoid crack localization, enhance fracture toughness and minimize the crack width [10]. ECC commonly utilizes polymer fibers, which offer remarkable tensile and flexural properties. Among the various options, Polyvinyl alcohol (PVA) and Polyethylene (PE) fibers are frequently chosen as the preferred reinforcement materials for ECC. PVA fibers are well-known for their high tensile strength and excellent bonding properties with cementitious matrices. They enhance the toughness and ductility of ECC, making it more resistant to cracking and improving its overall performance [10]. PE fibers are widely used in ECC due to their low density, high strength, and excellent resistance to chemical attack. These fibers effectively disperse and bridge cracks, improving the durability and flexural behavior of ECC [5]. However, the comparatively expensive cost of PE fibers prevents broad application of PE-ECC [12].

2.3. Mechanical properties

When concrete is subjected to external forces, it undergoes stress, which may cause deformation and potentially lead to failure if the stress exceeds the strength of the material. Tensile tests are commonly used to apply external forces to concrete samples. When concrete is subjected to a uniaxial load, the stress can be calculated using the formula:

$$\sigma = \frac{F}{A} \quad (2.1)$$

where:

σ is the stress in the concrete, measured in force per unit area (usually in MPa),
 F is the applied force on the concrete, measured in force units (such as N), and
 A is the cross-sectional area of the concrete specimen experiencing the force, measured in area units (such as mm²).

On the other hand, strain refers to the measure of deformation or elongation experienced by the material due to the applied stress. Strain is a dimensionless quantity that describes the relative change in length or shape of the concrete specimen under stress. It is a crucial parameter in concrete mechanics as it helps engineers understand how the material responds to external forces and how it deforms under various loading conditions. Strain is also essential in determining the behavior of a material, such as whether it will exhibit elastic deformation or undergo permanent plastic deformation or failure. The formula to calculate strain in concrete when subjected to a uniaxial load is given by:

$$\varepsilon = \frac{\Delta L}{L_0} \quad (2.2)$$

where:

ε represents the strain in the concrete, a dimensionless quantity that represents the change in length or shape of the specimen,

ΔL is the change in length of the concrete specimen under the applied stress, and L_0 is the original length of the concrete specimen before the application of stress.

The volume and shape of a solid can be somewhat altered when a material is subject to external stress. There are two categories of material deformation: elastic deformation and plastic deformation [15]. When a solid is subjected to a relatively low stress, the deformation is elastic, meaning that if the stress is removed, the solid will revert to its initial equilibrium state. However, in the case of plastic deformation, removing the external stress does not ensure complete recovery of the solid to its initial state [16]. Elastic deformation and plastic deformation differ primarily in their reversibility, where elastic deformation can be reversed, while plastic deformation is irreversible. The left image displayed in Fig. 2.2 illustrates both elastic and plastic deformation. A material is characterized as brittle when it undergoes minimal strain before failure, as observed in substances like glass. In contrast, a material is considered ductile when it experiences significant strains before failure, as observed in plastics and metals. The right image in Fig. 2.2 serves as an illustration of this.

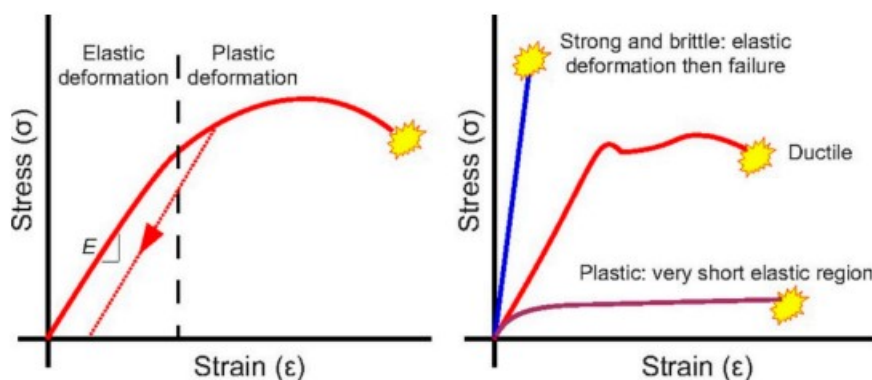


Figure 2.2: Stress-strain curves: (left), typical stress-strain curve, exhibiting both elastic and plastic regions, along with hysteresis (dashed line), and (right) stress-strain curves for various materials are depicted, adapted from [16].

The Young's modulus or elastic modulus represents the ability of a material to resist elastic deformation. Materials with low modulus exhibit significant flexibility and elongation when subjected to tension (or compression). However, high modulus materials display minimal elongation under tension (or compression) and have limited compressibility [17]. The Young's modulus, denoted by E , is determined using Eq. (2.3), and its unit of measurement is force per unit area, typically expressed in MPa.

$$E = \frac{\sigma}{\epsilon} \quad (2.3)$$

2.3.1. Fracture

The ability of a material to resist crack propagation and failure in the presence of cracks or faults is characterized by fracture toughness [18]. It measures how resistant a material is to catastrophic breakdown under applied pressures and is an important factor to take into account when constructing secure and dependable constructions. The area under the stress-strain curve, which represents the inelastic strain capacity before failure, is frequently used to calculate the toughness.

Higher fracture toughness values signify that a material has better crack resistance and is

more resistant to brittle fracture [18]. Such materials are highly desirable for structural applications where safety is of utmost importance, as they can withstand the presence of defects or flaws without leading to catastrophic failure. In situations like earthquakes, materials with high fracture toughness are preferred because they exhibit greater ductility. The presence of cracks allows these materials to dissipate energy effectively, enhancing their ability to withstand incidental loads and external impacts.

When bonds between atoms in a material are broken, energy is released, leading to crack formation and energy dissipation [18]. The total work conducted during the deformation of a material can be determined by calculating the area under the force-displacement curve, providing valuable insights into the response of the material to external forces.

In conclusion, the performance of a material in different engineering applications is largely dependent on its fracture toughness. It affects how well the material can absorb energy, sustain applied stresses, and prevent cracks from spreading. To ensure structural integrity and dependability, it is crucial to design materials with high fracture toughness, especially in situations with dynamic loads or potential faults.

2.4. Poisson's ratio

Another material property is the Poisson's ratio, ν , which is defined as the negative ratio of transverse strain to axial strain, as presented in Eq. 2.4. The numerical research conducted in this project focuses on understanding the Poisson's ratio of materials, which is a fundamental property associated with their mechanical behavior. Poisson's ratio is a metric used to compare the performance of different materials when subjected to elastic deformation, specifically measuring their resistance to distortion under mechanical load while maintaining volume [19]. It quantifies the Poisson effect, which refers to the deformation (expansion or contraction) of a material in directions perpendicular to the specific direction of loading [20].

$$\nu = -\frac{\epsilon_{\text{trans}}}{\epsilon_{\text{axial}}} \quad (2.4)$$

Materials possessing various Poisson's ratios display unique mechanical behaviors. This range of properties spans from "rubbery" to "dilatational," encompassing materials such as "stiff" metals and minerals, "compliant" polymers, and "spongy" foams occupying the intermediate range (Fig. 2.3). From an engineering standpoint, understanding how a material will deform is crucial for optimizing performance in applications with low tolerances. Moreover, Poisson's ratio provides insights into other material properties, such as the relationship between the Bulk Modulus and Shear Modulus. Higher Poisson's ratios are often associated with materials exhibiting a high Bulk modulus [20], which is the measure of resistance of how resistant a material is under compression [21]. The resistance of a material to shear deformation is measured by its shear modulus. Eq. 2.5 defines the relationship of the shear modulus G , bulk modulus B , and Poisson's ratio ν in isotropic materials

$$G = \frac{3B(1 - 2\nu)}{2(1 + \nu)} \quad (2.5)$$

It is important to note that the diagram (Fig. 2.3) illustrating the relationship between Poisson's ratio and material behavior stops at the maximum isotropic limit of $\nu = 0.5$. The allowable range for Poisson's ratio is between 0.5 and -1, encompassing all stable isotropic materials, those whose properties remain unchanged regardless of the direction in which they are tested [22]. This restriction arises from the requirement for Young's modulus, shear modulus, and bulk modulus to have positive values in stable, isotropic, linear elastic materials [20].

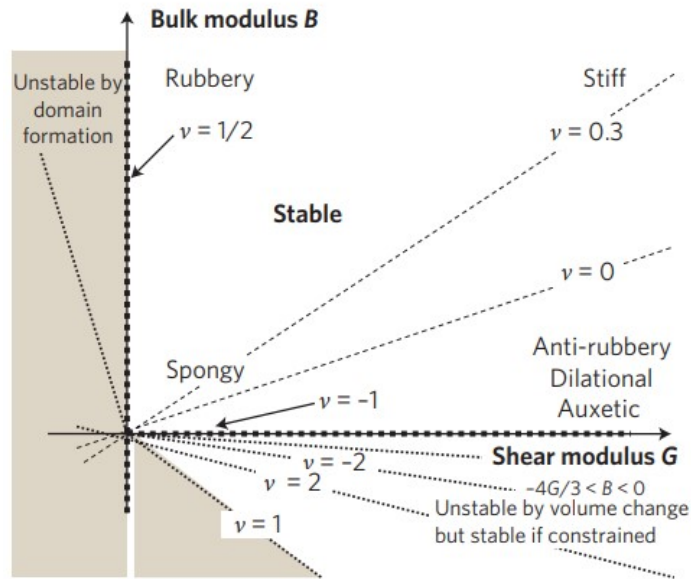


Figure 2.3: Milton map of bulk modulus (B , y-axis) versus shear modulus (G , x-axis), showing the regimes of ν , and the differences in material characteristics, adapted from [20].

While most materials have positive Poisson's ratios, some exhibit negative values, making them "auxetic" [23]. This implies that when a material is stretched or compressed vertically it will expand or contract horizontally, respectively [24]. This is a consequence of their unique internal structure and how it deforms under uniaxial loading. This counter-intuitive behavior has attracted significant attention due to its potential for various applications, including impact absorption, mechanical damping, and protective systems [25]. Auxetic materials are characterized by a value of $B/G \ll 1$, indicating extreme compressibility, unlike rubber, which has an extremely incompressible behavior with $B/G \gg 1$ and $\nu = 0.5$, as seen in Fig. 2.3. The toughness of a material can be increased by a negative Poisson's ratio [20].

Currently, there are several types of auxetic materials available, such as perforated plate structures [26], rotating polygon structures [27], concave structures [28], and chiral structures [29], among others. One of the prominent examples of auxetic materials is the re-entrant structure, which includes models like the re-entrant honeycomb model [30], double arrow model [31], and star model [32]. Among these auxetic structures, the re-entrant structure garners significant attention due to its desirable auxetic performance and ease of manufacturing [33].



(a) Re-entrant honeycomb with $\nu \approx -1$

(b) Conventional honeycomb structure with $\nu = 1$

Figure 2.4: Comparison between (a) re-entrant honeycomb and (b) honeycomb structure, adapted from [19].

2.4.1. Auxetic material: re-entrant structure

The concept of auxeticity was initially reported in re-entrant foams [34]. Re-entrant structures are essentially honeycombs with inverted cells. Honeycombs are structured cellular materials characterized by prismatic cells. These honeycomb cells can exhibit diverse cross-sectional shapes, such as hexagonal, kagome, square, triangular, and mixed triangular and square configurations [35]. Fig. 2.4 illustrates a comparison between a re-entrant honeycomb design and a conventional honeycomb design.

Research revealed that auxeticity is a common feature observed in various honeycomb structures and networks, where ν can take both positive and negative values, depending on the angle [19, 36, 37]. When the re-entrant cell is stretched, it initially exhibits the auxetic property with a negative Poisson's ratio. However, as the deformation progresses, the cell behavior transitions to that of a conventional hexagonal cell with a positive Poisson's ratio. This shift indicates a change in Poisson's ratio from negative to positive during the tensile process. The transition can be identified by a critical point, termed as the transitional point, where the initially inclined cell walls become horizontal [28, 38]. This leads to two distinct regions: one with auxetic features (negative Poisson's ratio) and the other with conventional behavior (positive Poisson's ratio).

Auxetic materials possess remarkable qualities such as high transverse shear modulus, excellent dynamic characteristics, good fracture toughness, and high indentation resistance. However, the limitation of auxetics lies in their lack of rigidity, which restricts their practical application in structural contexts [39]. As a result, auxetics cannot be employed in civil engineering applications that require a high stiffness.

According to a study conducted by Zhang et al. [28], it was demonstrated that the re-entrant structure, when subjected to increasing displacement, gradually transformed into a rectangular shape and eventually approached the characteristics of conventional honeycombs. The initial inclined cell walls in the re-entrant structure undergo a rotation towards a horizontal orientation, and the vertical walls subsequently expand laterally. This unique behavior results in a significant auxetic property of the re-entrant cell. However, as the rotation of the inclined cell walls continues progressively, they eventually become horizontal. At this point, the re-entrant cell transitions into a conventional hexagonal honeycomb, and the auxetic property disappears.

2.4.2. Non-auxetic material: rectangular and honeycomb structure

In contrast, non-auxetic materials behave in the conventional way and contract laterally when stretched longitudinally, displaying a positive Poisson's ratio. This typical response to stress is governed by the elastic properties of the material, which tend to resist deformation and maintain structural integrity. Non-auxetic materials are commonly found in various engineering applications, such as in conventional concrete, metals, and polymers, where their predictable and stable mechanical behavior makes them suitable for many practical purposes [40].

A rectangular and honeycomb structure are some examples of non-auxetic designs. The stiffness of honeycomb structures surpasses that of rectangular configurations [41]. In Fig. 2.5, a comparison between the honeycomb design and the re-entrant design is presented. The honeycomb design exhibits lateral contraction when subjected to stretching, whereas the re-entrant design displays lateral expansion during the same loading conditions.

2.5. Additive manufacturing

Additive manufacturing (AM), previously known as Rapid Prototyping and commonly called 3D Printing, creates objects from 3D model data by joining materials layer-by-layer [43]. AM is highly relevant to this study as it is the core technique used to fabricate the 3D printed

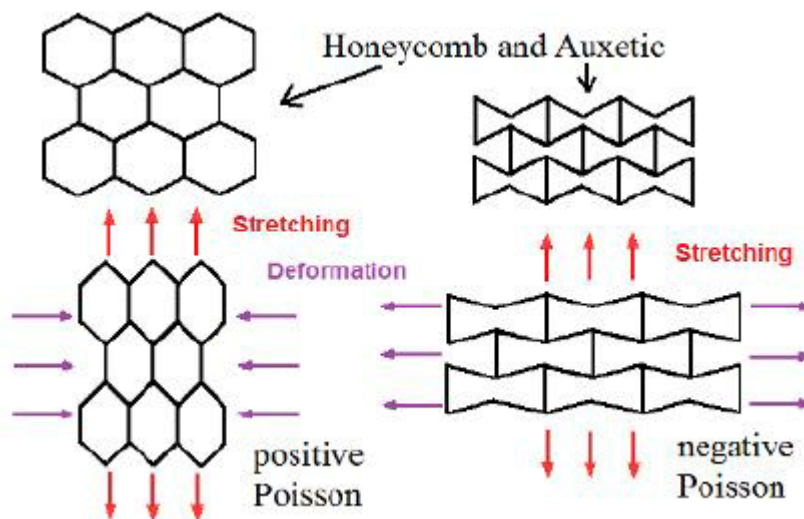


Figure 2.5: Comparison of the honeycomb (non-auxetic) and re-entrant (auxetic) design, adapted from [42].

polymeric meshes. The fundamental concept of this technology is that a 3D CAD (Computer-Aided Design) model can be directly manufactured without the need for process planning. All currently available commercial AM machines employ a layer-based method, with the main differences being the materials that can be used, how the layers are made, and how the layers are connected to one another. These variations will affect things like the precision of the final product, material qualities, and mechanical properties.

The advantages of AM include a faster product development process due to the seamless transfer from 3D CAD to AM, reduction in process steps and resources required, and the ability to make simple design changes without significantly increasing the time required for fabrication [44]. AM also simplifies the manufacturing process by eliminating the need for multiple construction methods and enabling the creation of parts with different characteristics through the addition of supporting technologies. As a result, AM can lead to cleaner, more streamlined, and versatile workshops.

AM has gained significant attention in recent years due to its potential to revolutionize various industries. However, it is essential to consider the limitations associated with this technology to ensure its successful implementation. One notable limitation of AM is the size constraints imposed by the available build volume of the machines. The maximum size of objects that can be produced may be restricted, hindering the fabrication of larger-scale components. Moreover, certain materials may not be compatible with AM processes, limiting the range of available materials for fabrication. Challenges could arise from materials with high melting points or particular qualities that are hard to obtain using AM [44].

Surface quality and resolution are important considerations in AM. The layer-by-layer deposition can result in surface roughness and lower resolution compared to traditional manufacturing methods, which may affect both aesthetics and functional properties of the final product [45]. Post-processing steps such as polishing, support removal, or heat treatment are often necessary to achieve the desired quality and properties, increasing production time and cost. Cost considerations also play a crucial role in AM adoption. The technology can be expensive, including equipment, materials, and maintenance costs. To guarantee the financial feasibility of AM deployment, these elements need to be carefully assessed.

Design limitations are another aspect to be aware of. Complex geometries or intricate designs may be challenging to achieve using AM methods. Additional support structures or

design modifications may be required to ensure successful fabrication [44]. In conclusion, while AM holds immense promise, it is crucial to understand its limitations for effective utilization. By addressing these limitations through ongoing research and development efforts, AM can further advance and find wider applications in various industries.

2.5.1. AM process

To transform a virtual CAD model into a physical part, several processes are required in AM [44]. The first step involves creating a 3D model using professional CAD solid modeling software, followed by converting the model to an STL file. These files store as repositories for important geometric data relating to the shape and surface geometry of an object. It is crucial to understand that these files do not contain information on the color, texture, or other model-related visual properties. The STL file is then transferred to the AM machine and the machine is set up for the build process. The build process itself is largely automated and can run unattended, with the machine monitored for potential errors such as running out of supplies, power failures, or software issues. Once the machine has completed the build, the components can be removed and may require additional cleaning before being put to use. Ultimately, the resulting parts are ready for use.

2.5.2. Fused deposition modeling

Fused deposition modeling (FDM) is a widely used additive manufacturing technology that enables layer-by-layer construction of 3D objects using a thermoplastic filament. It is melted and then extruded through a nozzle that moves along the x, y, and z-axes to construct the desired shape [46]. A schematic representation of the additive manufacturing technique is illustrated in Fig. 2.7. FDM has gained popularity in prototyping and small-scale production due to its low cost, rapid speed and ease of use. Recently, the construction industry has also embraced this technology [46]. However, the mechanical properties of printed objects are affected by several processing variables, such as layer thickness, width, filament orientation, and air gap [47]. Inter-layer distortion has been identified as the primary cause of mechanical weakness in FDM-printed objects [48].

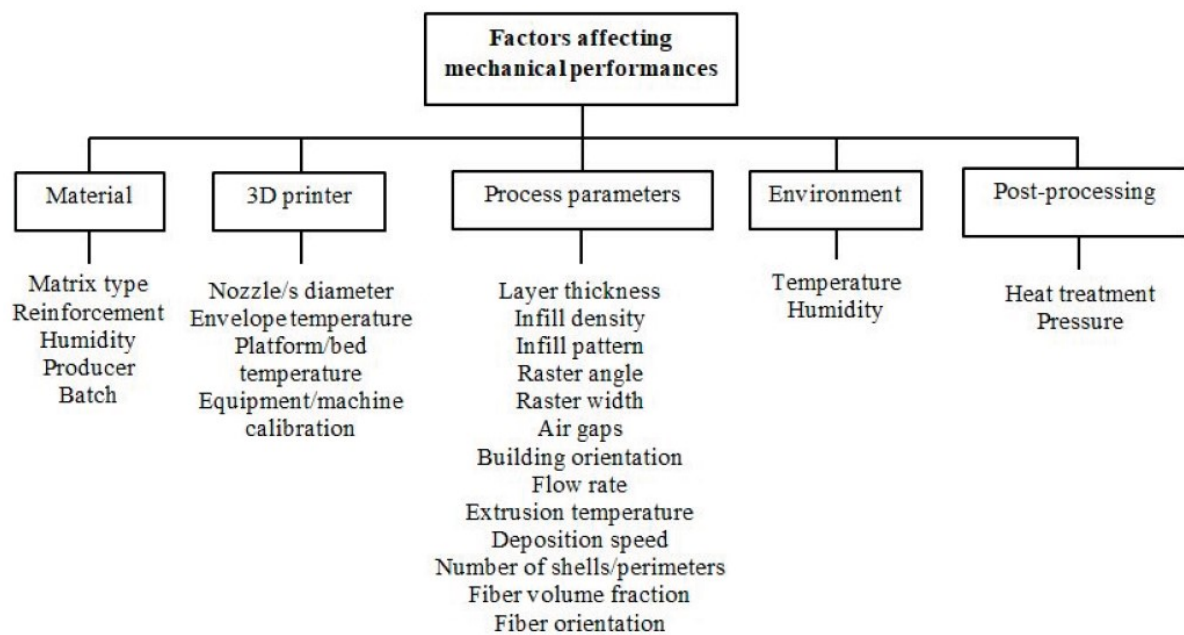


Figure 2.6: Factors affecting mechanical properties, adapted from [49].

In a recent experimental investigation conducted by Srinivasan et al. [50], the mechanical properties of FDM printed parts using ABS material were examined. The study focused on varying three crucial process parameters: infill density, infill pattern, and layer thickness. Tensile strength and hardness were used as response parameters to evaluate the performance of the printed parts. The findings indicate that infill density and layer thickness are the most influential factors affecting the mechanical properties of the printed parts. An overview of factors that influence the mechanical performances of 3D printed specimen are presented in Fig. 2.6.

In addition to the listed challenges, FDM has some limitations that should be considered. Firstly, due to the round nozzle used in the extrusion process, FDM-printed objects may not have sharp corners and precise geometrical features. This can limit the ability to achieve intricate designs and detailed structures. Secondly, the inherent layer-by-layer construction of FDM can result in anisotropic mechanical properties, making the printed objects weaker in the z direction compared to the x and y directions. This anisotropy can affect the overall strength and performance of the printed parts. Furthermore, FDM-printed objects typically have lower material density compared to their counterparts manufactured using traditional methods. The layer-by-layer nature of FDM introduces voids and gaps between the printed filaments, reducing the overall density and potentially impacting the mechanical integrity of the objects. Additionally, FDM-printed objects may exhibit a visible layering appearance on the surface, which can affect the aesthetics and smoothness of the final product. Lastly, the availability of thermoplastic materials for FDM may be limited compared to other additive manufacturing technologies. While a variety of thermoplastics are compatible with FDM, the range of materials may not be as extensive as in other processes, limiting the options for specific applications and material properties [44]. Despite these limitations, FDM remains a popular and cost-effective option for prototyping and small-scale production. Ongoing research and advancements in FDM technology are focused on addressing these limitations and improving the mechanical capabilities, surface quality, and material options for FDM-printed objects.

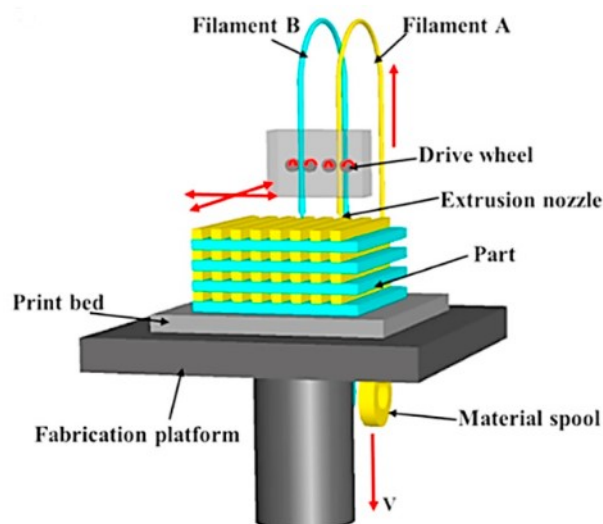


Figure 2.7: Schematic representation of the additive manufacturing technique: Fused deposition modeling, adapted from [51].

2.5.3. Build orientation

The orientation in which a printed part is positioned on the build plate is referred to as build orientation. The mechanical properties of additively manufactured parts are significantly influenced by the build orientation. The choice of orientation can impact factors such as strength, stiffness, and deformation behavior, making it an essential consideration in the additive manufacturing process. Selecting the optimal build orientation is crucial to ensure that the printed parts meet the desired mechanical requirements and performance criteria. Three distinct build orientations are available for use, namely upright, on-edge, and flat, as depicted in Fig. 2.8. Based on the findings presented in [52], it is evident that the flat and on-edge orientations exhibit superior tensile strength and deformability compared to the prints in the upright orientation. Considering the ease of the flat position, it was chosen as the preferred orientation for the prints in this study.

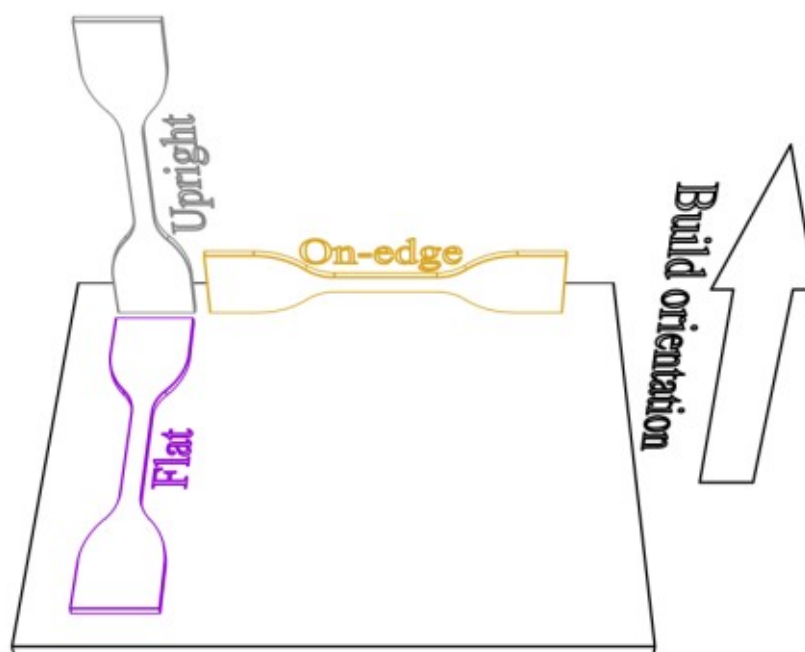


Figure 2.8: Different build orientations, adapted from [52].

2.6. Material filament

Metals, polymers, ceramics, and concrete are just a few of the many materials that can currently be used in 3D printing. The two primary polymers utilized in the 3D printing of composites are polylactic acid (PLA) and acrylonitrile butadiene styrene (ABS) [46]. The polymeric reinforcements used for the experiments are made from commercial plastics, which matches nicely with concrete. The materials ABS and thermoplastic polyurethane (TPU) were used as filament for the 3D printed reinforcement in this study. This master thesis aims to explore the mechanical behavior and potential applications of ABS and TPU in enhancing the deformation capacity of ECC, contributing to the development of innovative and sustainable construction materials.

2.6.1. ABS

ABS is a thermoplastic polymer that is commonly used in various industries due to its high strength, flexibility, and machinability. The material was first developed in the 1940s and has

since become one of the most widely used engineering thermoplastics [53]. ABS is a copolymer that is composed of three monomers: acrylonitrile, butadiene, and styrene. The percentage of each monomer in the copolymer can vary, depending on the desired properties of the final product. In general, ABS contains 20-30% acrylonitrile, 5-30% butadiene, and 40-60% styrene.

ABS is known for its excellent mechanical properties, including high tensile strength, impact resistance, and toughness [53]. The tensile strength of ABS ranges from 40-70 MPa, depending on the composition of the copolymer. ABS also has good elongation at break, with values ranging from 20-50%. ABS has a relatively low melting point of around 230°C, which makes it easy to process using various manufacturing techniques, including injection molding and extrusion. ABS also has some limitations, including its fume emission during processing and its relatively low resistance to UV radiation.

2.6.2. TPU

During the 1950s, the material TPU was developed, bridging the gap between plastic and rubber. TPUs exhibit mechanical performance characteristics similar to rubber but possess the advantage of being processable as thermoplastics [54]. They are known for their excellent flexibility, high elongation and damage resistance [55]. To ensure that the TPU filament has melted and can go through the nozzle smoothly, the extruding temperature must be higher than the melting point of TPU, which is around 220°C. If the extruding temperature is not high enough, the TPU may be highly viscous, which makes it challenging to extrude filament [56].

2.7. Digital image correlation

Recently, several emerging experimental techniques have significantly advanced the precision and accuracy in understanding the mechanical behavior of materials. Among these, digital image correlation (DIC) has emerged as a powerful tool for estimating the mechanical behavior of materials [57]. In this study, DIC was employed to analyze the samples subjected to tensile testing, enabling the collection of crucial information on displacement, crack widths, and strain. The utilization of DIC in this research has provided valuable insights into the mechanical performance of the samples, enhancing our understanding of their behavior under applied tensile forces. The theoretical principles and steps involved in the DIC method are reviewed to get a better understanding.

DIC is an optical technique that enables the measurement of 2D or 3D coordinates for assessing deformation, including displacements and strain, without the need for physical contact [58]. The measurement of these parameters is crucial in engineering and construction projects. DIC has been widely applied in the analysis of concrete reinforced parts and composites. The evolution of DIC techniques and algorithms has led to significant improvements in the efficiency and precision of measurements. As a result, DIC is becoming increasingly popular for evaluating the mechanical behavior of materials and structures.

The Digital Image Correlation method operates by comparing a sequence of digital images of a surface of a test object, taken before, during, and after deformation, to a reference image [59]. This method calculates surface displacement by monitoring pixel blocks, generating 2D and 3D deformation vector fields, and producing full-field strain maps. To operate effectively, DIC requires special and random pixel blocks with varying intensity and contrast rates. However, no specialized lighting is necessary, and in most cases, the natural surface texture of the structure is sufficient for DIC to operate without any additional surface preparation [60].

To apply the 2D DIC method, four steps need to be followed. Firstly, the surface of the sample is covered with a stochastic white and black pattern to measure the in-plane deformation. Next, an area of interest (AOI) is selected, which is a sub-image of the sample surface

used for a specific function, such as strain measurement. Image acquisition of the AOI is done before, during, and after the sample is loaded, and the obtained images are processed using computer software. DIC compares a specific pixel or point within the same AOI between two images before and after deformation, based on which DIC theory is explained in the next paragraph. The selection of AOI is crucial in the DIC method as DIC only provides data within the AOI.

2.7.1. Theory

The surface of interest is manually specified and divided into a virtual grid with equal spacing, as depicted in Fig. 2.9(a). This grid is used to make DIC analysis simpler. DIC enables the determination of full-field deformations by calculating displacements at each point within the virtual grids [61]. In Fig. 2.9(b), the red square represents a subset of pixels that monitors the movement of its center point $P(x, y)$ from the reference image to the deformed images represented by the center point $P'(x', y')$. The reference image is acquired when the load is zero, corresponding to the initial state before deformation.

The following equations can be used to describe the deformation between the two points P and P' :

$$x' = x + u(x, y) \quad (2.6)$$

$$y' = y + v(x, y) \quad (2.7)$$

where the displacements in the x and y directions, respectively, are denoted by u and v .

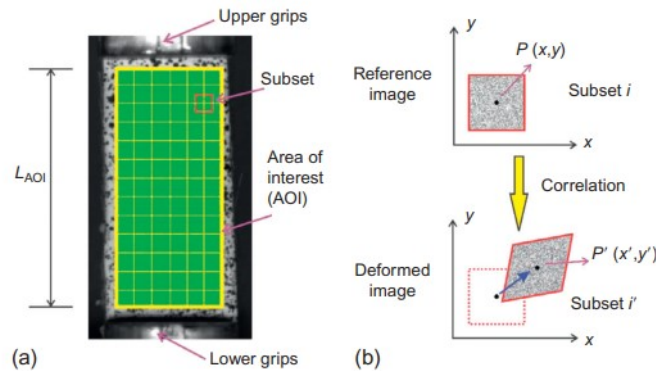


Figure 2.9: Digital image correlation (a) Subset and area of interest in a reference image; (b) Graphic demonstration of correlation between reference image and deformed image, adapted from [61].

2.8. Summary Literature Review

In conclusion, the literature study has provided valuable insights into the use of 3D printed reinforcements in enhancing the mechanical properties of ECC. The investigation into different materials, reinforcement designs, and printing techniques has revealed the potential for significant improvements of strength, strain capacity, and energy absorption capabilities of ECC. The findings from various studies have highlighted the importance of carefully selecting appropriate materials and reinforcement configurations to achieve specific performance objectives in ECC. In this study field, 3D printing has emerged as a key technology that makes it possible to fabricate complex, personalized reinforcement patterns with improved mechanical

properties. The literature study has paved the way for the numerical and experimental study, where the performance of ECC reinforced with 3D printed polymeric meshes, using ABS and TPU, will be assessed through uniaxial tensile tests. This study intends to develop building materials and creative methods in structural design and construction by thoroughly examining the body of existing literature and conducting an experimental examination.

3

Numerical Study: Method and Setup

Numerical simulations were conducted to predict the fracture behavior and load-displacement response of the 3D printed reinforcement for both printing materials. This chapter provides a comprehensive description of the step-by-step process used to create the numerical models. The investigation was divided into three distinct phases, where modifications were made to examine the effects. The cracking pattern of the reinforcement was analyzed during tensile testing simulations, and the numerical study also served to validate the auxetic or non-auxetic nature of the reinforcement.

3.1. Geometric modeling

In this study, the re-entrant honeycomb design was used as shown in Fig. 3.1, characterized by three parameters: thickness t , angle α , and length l . The re-entrant angle is the angle between the two adjacent walls of the unit cell. The thickness of the unit cell was kept constant along the walls. The study was divided into three phases. In the first phase, the re-entrant angle was modified while keeping the thickness and length constant. In the second phase, the volumes of the designs were equalized, resulting in changes in both the thickness and length. Finally, in the third phase, the design was enlarged to allow for easy embedment of the fiber-reinforced mortar into the unit cell.

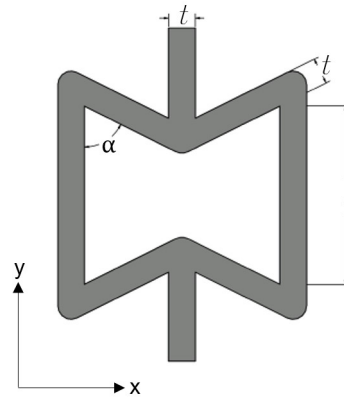


Figure 3.1: Auxetic unit cell: re-entrant honeycomb structure.

The research focused on investigating four angles: 52° , 63° , 90° , and 117° , and their classification as either auxetic or non-auxetic designs. The angles of 52° and 63° were identified as auxetic designs, while the angles of 90° and 117° were categorized as non-auxetic designs. The designs characterized by angles of 52° and 63° are commonly known as bowtie designs, whereas the design featuring an angle of 117° is referred to as a conventional honeycomb design. Additionally, the design with a 90° angle is denoted as a rectangular design. Throughout the study, the four angles were labeled A, B, C, and D, corresponding to 63° , 52° , 90° , and 117° , respectively (Fig. 3.2).

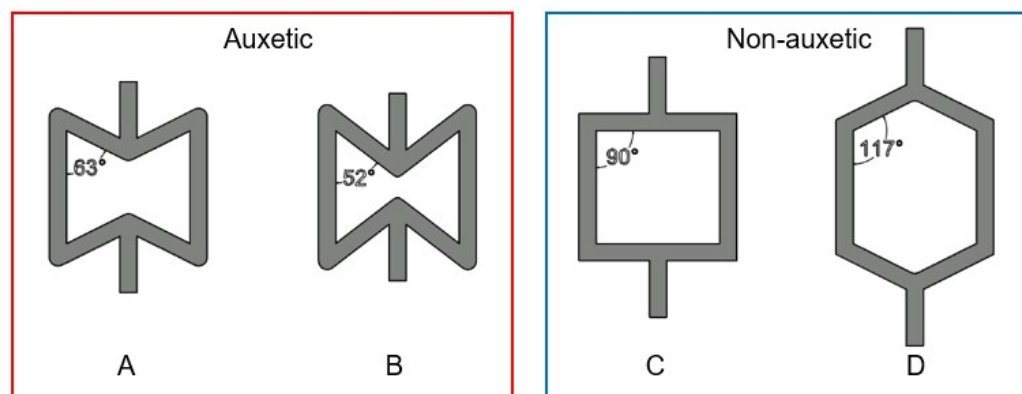


Figure 3.2: Auxetic and non-auxetic designs with labels.

The various reinforcement designs were designed and created using AutoCAD software. After the designs were created, they were sliced into their desired length for analysis. A cross-

sectional view of the 3D designs was created since the simulations were performed in a two-dimensional plane. These cross sections were exported to Abaqus for further analysis.

3.1.1. Phase 1

In this phase, the length of the unit cell and the thickness were kept constant, while the angle was the only parameter altered. To ensure that the designs had a comparable overall length, each unit cell was replicated four times along the x-axis and a varying number of times along the y-axis, with design A replicated seven times, design B replicated eight times, design C replicated six times, and design D replicated five times, as shown in Fig. 3.3. This Figure displays the models that were used in both the numerical and experimental studies. The dimensions of the unit cells for the different angles are illustrated in Fig. 3.4, and a summary of these dimensions is listed in Table 3.1.

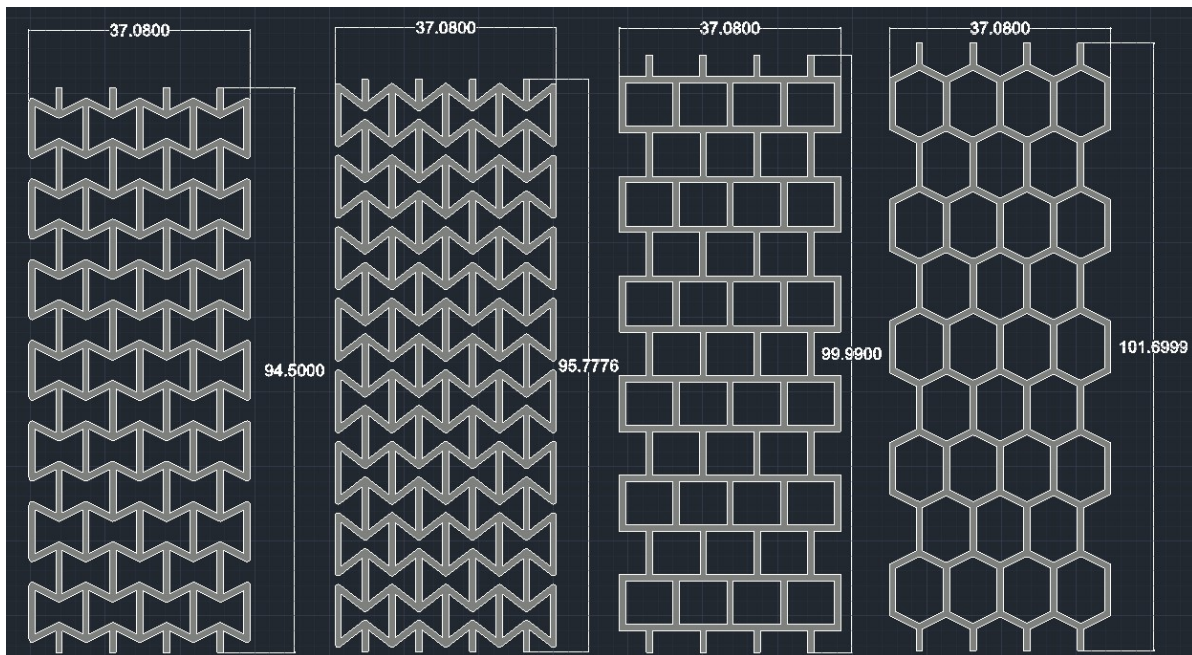


Figure 3.3: Reinforcing designs phase 1 with measurements presented in mm.

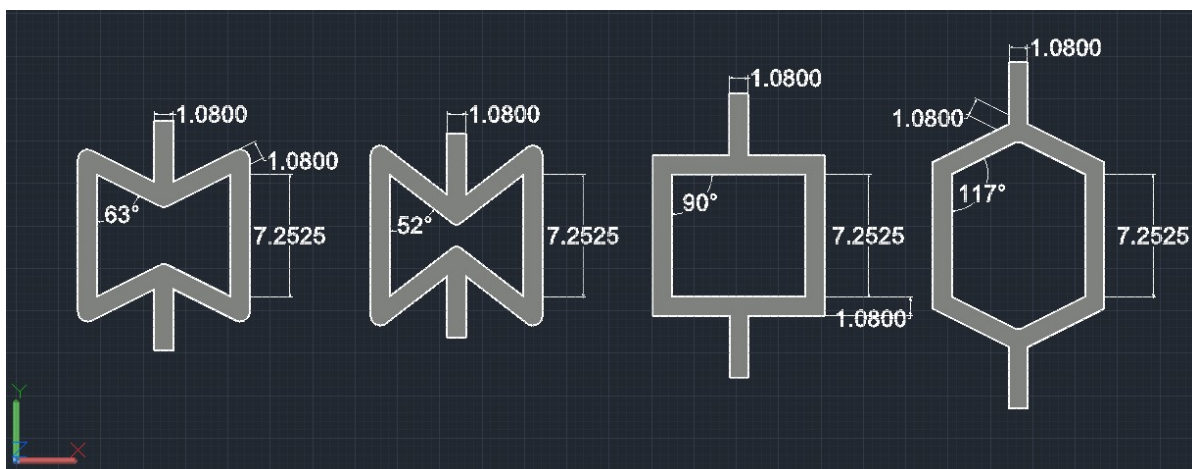


Figure 3.4: Unit cells of the different designs phase 1 with measurements presented in mm.

	Design A	Design B	Design C	Design D
Angle [°]	63	52	90	117
Thickness [mm]	1.08	1.08	1.08	1.08
Length unit cell [mm]	7.2525	7.2525	7.2525	7.2525
Width [mm]	37.08	37.08	37.08	37.08
Total length [mm]	94.5	95.7776	99.99	101.6999
Volume [mm ³]	5683.98	7008.56	4517.61	3924.54

Table 3.1: Dimensions reinforcement phase 1.

3.1.2. Phase 2

In phase 1 of the study, an increase in the angle resulted in a decrease in volume for the designs, as indicated in Table 3.1. To address this volume change, the reinforcing volume of the various designs was made equal during this phase. As a result, the width decreased, and the thickness increased. Design B was excluded from this phase, as the fibers were unable to pass through the reinforcement during the experimental study of phase 1. The models that were utilized in both the numerical and experimental studies are presented in Fig. 3.5. In the provided Figure, it is evident that the total length remained consistent with the initial phase, and the cells also underwent replication along the y-axis across the various designs. The dimensions of the unit cells for the different angles can be found in Fig. 3.6, and a summary of these dimensions is listed in Table 3.2.

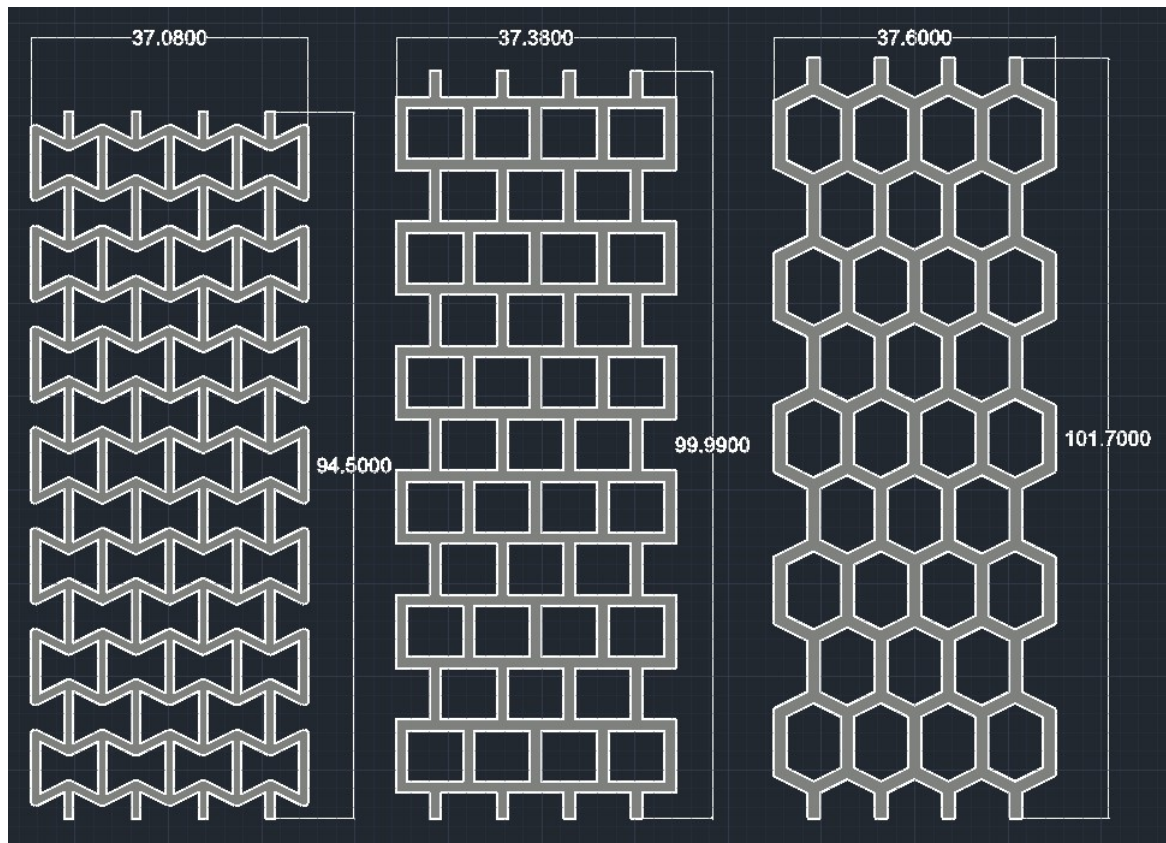


Figure 3.5: Reinforcing designs phase 2 with measurements presented in mm.

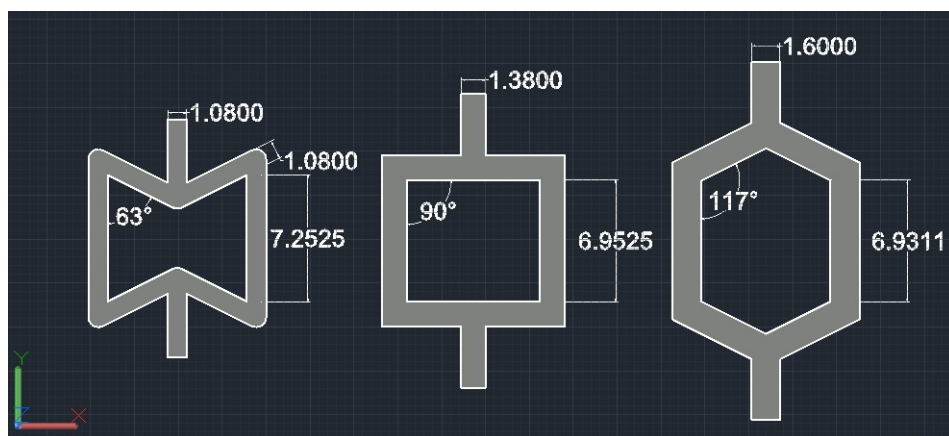


Figure 3.6: Unit cells of the different designs phase 2 with measurements presented in mm.

	Design A	Design C _{adj}	Design D _{adj}
Angle [°]	63	90	117
Thickness [mm]	1.08	1.38	1.60
Length unit cell [mm]	7.2525	6.9525	6.9311
Width [mm]	37.08	37.38	37.60
Total length [mm]	94.5	99.99	101.7
Volume [mm ³]	5683.98	5685.57	5682.26

Table 3.2: Dimensions reinforcement phase 2.

3.1.3. Phase 3

During the casting, it is supposed that fiber in the fiber-reinforced mortar may have difficulties. Thus in this phase, the design was enlarged for design C, so that the fibers could go through more easily. Each unit cell was replicated two times along the x-axis and three times along the y-axis, as shown in Fig. 3.8. The model used in both the numerical and experimental studies is depicted in the Figure. The dimensions of the unit cells corresponding to different angles are illustrated in Fig. 3.7, and a summary of these dimensions is provided in Table 3.3.

	Design C _{mod}
Angle [°]	90
Thickness [mm]	2.45
Length unit cell [mm]	15.55
Width [mm]	38.45
Total length [mm]	108
Volume [mm ³]	5683.3875

Table 3.3: Dimensions reinforcement phase 3.

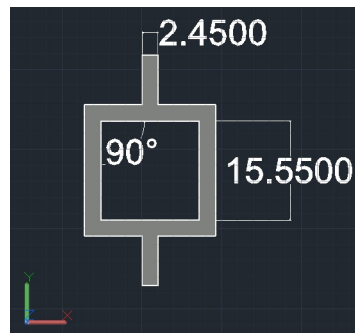


Figure 3.7: Unit cell design phase 3 with measurements presented in mm.

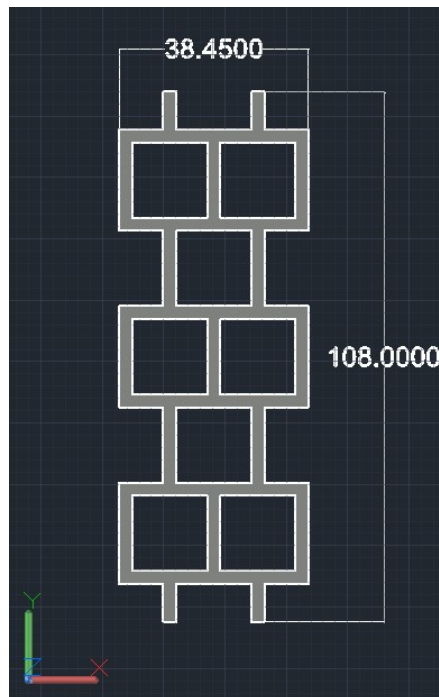


Figure 3.8: Reinforcing designs phase 3 with measurements presented in mm.

3.2. Finite element modeling

This study utilized the software Abaqus/Explicit, a finite element system consisting of multiple programs [62] of which Abaqus/CAE was used to develop and modify finite element models, run analyses, monitor and diagnose jobs, and evaluate results. The software provides an array of tools such as geometry design, material property assignment, mesh generation, boundary condition application, and load creation. Simulation results can be monitored and visualized using the outputs obtained from the simulations.

Abaqus/CAE was used for the creation and analysis of models, using different modules provided by the software. The software has 11 modules and these are: Part, Property, Assembly, Step, Interaction, Load, Mesh, Optimization, Job, Visualization and Sketch. First, the model was constructed by creating parts using the Part module, with the Property module utilized to define material properties and assign sections to the parts. Next, instances of the parts were assembled together in the Assembly module to create the final assembly. In the Step module, analysis steps were defined, and the history output requests were created. The Interaction module was utilized to simulate contact interactions between the different parts.

Then loads and boundary conditions were applied using the Load module, and meshes were generated in the Mesh module. The Job module was used to create jobs and run the simulations. The Optimization and Sketch modules were not utilized in this study. Finally, the Visualization module was used to obtain load-displacement results, calculate the Poisson's ratio for each design, and to generate illustrations of the deformed shapes of the models. A summary of these steps is presented in Fig. 3.9.

3.2.1. Parts

To begin the numerical simulations, the reinforcing designs were imported as parts into the software. To replicate the experimental setup, two plates were created in the simulations. It was necessary to define the modeling space when creating a part. For this particular study, a two-dimensional planar modeling approach was used.

Two 2D planar discrete rigid rectangular plates measuring 100 by 5 mm were created, with a reference point (RP) at the bottom-middle of each plate. A discrete rigid part can have any arbitrary shape and is assumed to remain rigid even when subjected to any kind of load [63]. The various reinforcing designs that were created in AutoCAD were exported to a SAT file and subsequently imported as parts into Abaqus using the "Standard/Explicit" model type. Afterwards, a solid homogeneous section was created, and the reinforcing design was assigned a section assignment.

3.2.2. Material properties

The simulations used the materials ABS and TPU of which the density, elastic, and plastic properties were registered. The parameters utilized for ABS were a density of $1.07\text{E-}09$ ton/mm³, a Young's modulus of 1590 MPa, and a Poisson's ratio of 0.2. Meanwhile, the parameters for TPU were a density of $1.07\text{E-}09$ ton/mm³, a Young's modulus of 60 MPa, and a Poisson's ratio of 0.2. Details on the plastic behavior of both materials are presented in Tables 3.4 and 3.5. In order to get the input parameters for the plastic behavior, experimental tests were performed on small ABS and TPU bars. The procedure for conducting the experimental tests is detailed in section 5.5, and the methods of obtaining the results are explained in section 5.6.

Yield stress [MPa]	Plastic strain [-]
38	0
40	0.6
32	0.7
15	1
1	1.2

Table 3.4: Plastic behavior of ABS.

Yield stress [MPa]	Plastic strain [-]
3	0
5	0.02
6.3	0.04
7.65	0.08

Table 3.5: Plastic behavior of TPU.

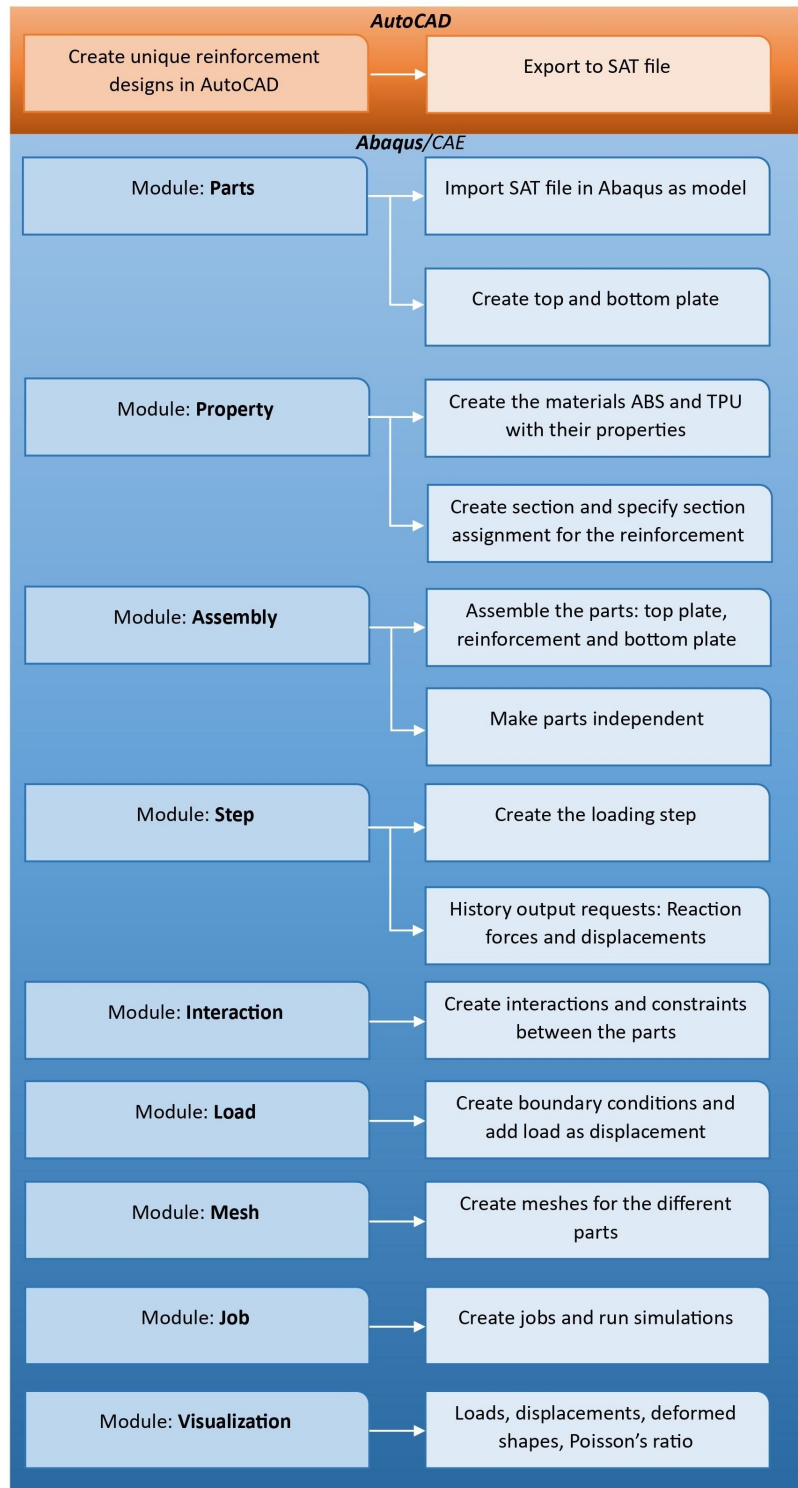


Figure 3.9: FEM step by step method.

3.2.3. Assembly

In the modeling process, each part is initially created in its own coordinate system, and is not connected to the other parts in the model. Therefore, the components must be assembled to form a complete model that can be analyzed. In order to assemble the two rectangular plates and the reinforcing design, various tools were used to position and orientate them relative to each other. The first plate was positioned on top, while the second plate was positioned on the bottom, representing the experimental study where only the top plate moves upwards. In Fig. 3.10, the assembly of the parts are displayed.

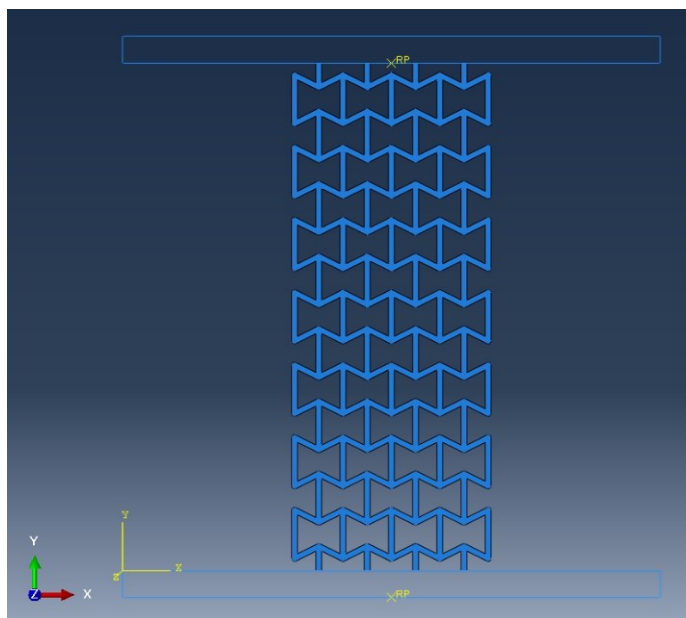


Figure 3.10: Assembly of the parts.

3.2.4. Analysis steps

A model consists of a series of analysis steps, which can contain one or more steps. The step sequence offers a simple way to record any changes made to the model, such as modifications to loading and boundary conditions, changes in the way components interact with each other, removal or addition of components, and any other modifications that may occur during the analysis [64]. Furthermore, these steps allow for the adjustment of the analysis procedure, the data output, and various controls.

A pre-existing initial step was incorporated in the model to allow for the definition of boundary conditions, predefined fields, and interactions at the start of the analysis. Following the initial step, an analysis step, specifically the loading step, was created. Each analysis step in the model is associated with a specific procedure, which determines the type of analysis to be performed during the step. For the loading step, an explicit dynamic analysis was chosen to simulate a structure subjected to a high-speed, rapidly applied load or displacement. The Step Manager tool was used to create, edit, and manipulate the analysis steps in the model.

Abaqus automatically generates default field and history output requests based on the chosen analysis procedure when a step is created. During the simulation, a history output request was used to specify the type of data that needed to be analyzed. Typically, this data is displayed as time history curves that demonstrate the variation of various parameters over time. Once a history output request has been created, the relevant data will be written to the output database during the simulation. In this study, history output requests were created for

the reaction force and displacement of the bottom and top plates, respectively. These requests tracked and recorded the reaction force and displacement in the vertical direction.

3.2.5. Interactions and constraints

To ensure that the parts were properly aligned and connected, constraints and interactions needed to be defined between them. These can include various types of constraints such as fixed or pinned connections, as well as interactions such as contact or tie constraints. The contact constraints can model various types of contact. For these parts, both tangential and normal contact behavior were defined. A friction coefficient of 0.1 was assigned to the tangential behavior. As for the normal behavior, it can be modeled using different types, such as hard contact or soft contact. In this case, hard contact was selected as the most rigid option, as it provides no compression.

In addition to the contact constraints, the model was also subjected to tie constraints. Tie constraints allow to connect two surfaces without transmitting any shear force or moment, even if the created meshes are dissimilar [65]. This allows the surfaces to share the same displacement and rotation, while preventing any relative displacement or rotation between them. To implement the tie constraints, the first step involved defining and creating various surfaces. Next, the two surfaces that needed to be connected were selected and a set of tie nodes was defined on each surface. These nodes were then used to create a tie constraint element that connected the two surfaces. The two tie constraints are illustrated in Figures B.1 and B.2.

3.2.6. Load and boundary conditions

The Load module in Abaqus provides various types of loads and boundary conditions. For the loading step of the model, boundary conditions were assigned in the form of displacement constraints. These restrict the degree of freedom of a node in a particular direction. The bottom plate was constrained with zero displacement in both the x and y directions, while the top plate was constrained with zero displacement in the x direction and varied displacement in the y direction, depending on the design. A visualization of the boundary conditions is displayed in Fig. 3.11. The definition of the amplitude curve was given as a table of values at useful intervals along the time scale. The boundary conditions for the top plate were adjusted during the analysis as needed.

3.2.7. Mesh

To conduct simulations, the creation of a mesh was necessary. However, before meshing could be performed, it was required to make the instances mentioned in Section 3.2.3 independent. This was done to enable a range of operations that are not feasible for dependent parts. Element type, instance seed, and mesh controls were used as tools for making the meshes. Figures B.3 and B.4 show the element type and mesh controls used, respectively. The meshes for all designs were triangular in shape, as shown in Fig. B.5.

3.3. Analyses

Numerical simulations were performed to analyze the load-displacement response and fracture processes of the 3D printed reinforcement during the tensile tests. Also to validate the auxetic or non-auxetic nature of the reinforcement. Using the Job module, jobs were created for each model and the simulations were conducted. The Visualization module was utilized to obtain load-displacement curves and illustrate the deformed shapes for each model.

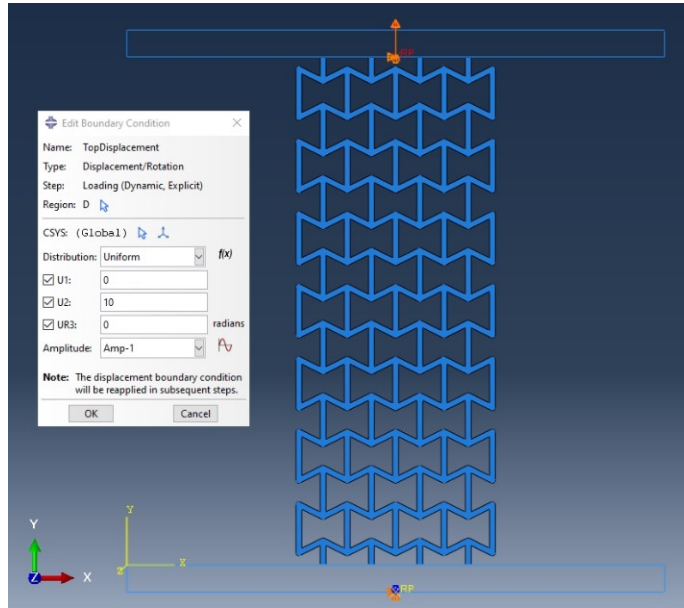


Figure 3.11: Top plate with displacement.

3.3.1. Poisson's ratio calculation

The finite element models were used to calculate the strains caused by the applied displacement. Based on the calculated strains, the Poisson's ratio was determined for each model according to [66]. The extraction of coordinate sets for individual nodes can be easily performed using the nodal probe tool available in Abaqus. By utilizing the data, it became feasible to ascertain the precise positions of the edge nodes within the model. The distance between the top and bottom nodes represented the length of the design, with the original length (L) corresponding to the displacement set to zero. Similarly, the width (W) of the reinforcement was determined by measuring the distance between the left and right nodes located in the middle of the design, as seen in Fig. 3.12.

After running the simulations, both the top plate and the top node moved upward, resulting in an increase in the length of the reinforcement. This increased length is referred to as the deformed length. The difference between the deformed length and the original length is quantified as the change in length (ΔL). Likewise, the distance between the deformed width and the original width is referred to as the change in width (ΔW). Using the change in length and width, the axial strain and transverse strain were calculated as follows:

$$\varepsilon_{\text{axial}} = \frac{\Delta L}{L} \quad (3.1)$$

$$\varepsilon_{\text{trans}} = \frac{\Delta W}{W} \quad (3.2)$$

The equation of the Poisson's ratio is presented in Eq. 3.3. The Poisson's ratio was computed for each the increment of applied load and plotted against the corresponding displacements. It was observed that the auxetic materials exhibited a negative Poisson's ratio, while the non-auxetic materials displayed a positive Poisson's ratio.

$$\nu = -\frac{\varepsilon_{\text{trans}}}{\varepsilon_{\text{axial}}} \quad (3.3)$$

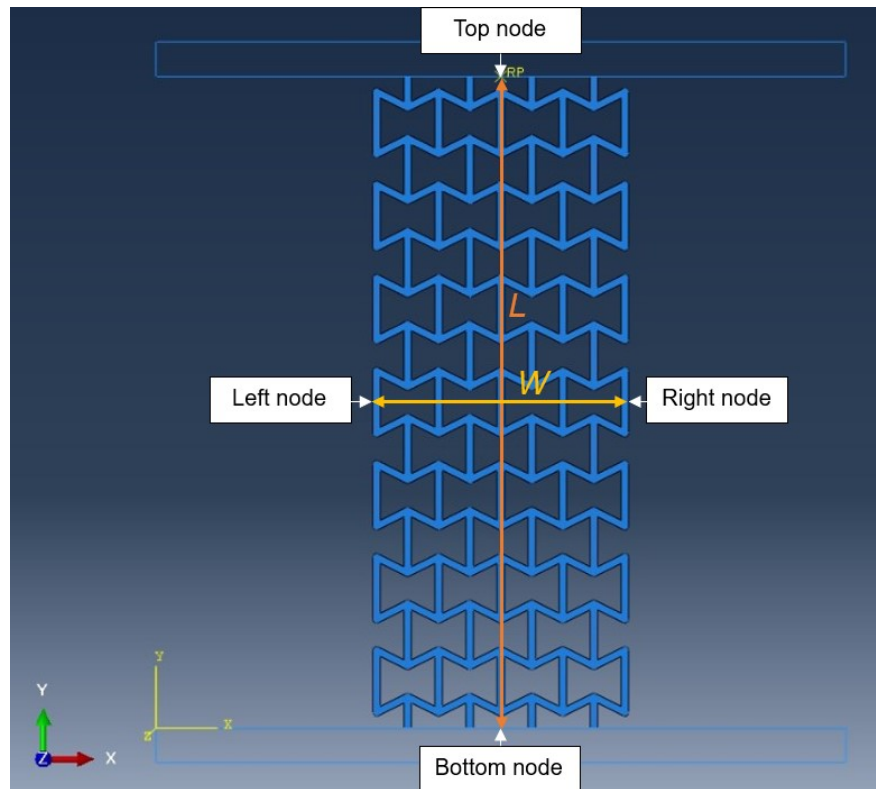


Figure 3.12: Length and width of the designs with the locations of the nodes.

4

Numerical Study: Results and Discussion

The results of the numerical study are presented in this chapter. These results have been obtained and are subject to thorough analysis and in-depth discussions to extract valuable insights and draw meaningful conclusions. The obtained data includes essential parameters such as stress-strain curves, Poisson's ratio, and deformation patterns, among others.

4.1. Overview Numerical Study

Numerical simulations conducted in Abaqus serve as a powerful tool for researchers to comprehensively evaluate and understand complex mechanical processes, optimize designs, and derive informed engineering conclusions. In the context of this study, the numerical investigation aimed to achieve several objectives. Firstly, the simulations focused on reproducing and analyzing the load-displacement response of the 3D printed reinforcement. This enabled a thorough understanding of the mechanical behavior of the reinforcement under different loading conditions. Furthermore, the study aimed to compare the strengths of the various design configurations and the two different materials, ABS and TPU. By examining the load-displacement curves and fracture behavior obtained from the simulations, valuable insights were gained regarding the performance and effectiveness of different design configurations.

Additionally, the numerical investigation aimed to predict the fracture behavior of the reinforcement. By simulating the mechanical response, the study provided crucial information regarding the structural integrity and failure mechanisms of the reinforced materials, facilitating the assessment of their overall performance. Moreover, the calculation of Poisson's ratio was employed as a means to validate the auxetic or non-auxetic nature of the reinforcing design. By analyzing the relationship between Poisson's ratio and displacement, the study offered evidence regarding the distinctive mechanical properties and behavior of the reinforced materials. Overall, the numerical study successfully addressed these objectives, providing valuable insights into the load-displacement response, strength characteristics, fracture behavior, and auxetic properties of the 3D printed reinforcement.

In the case of the ABS material, the designs underwent simulations with varied displacement values since the point of failure differed for each reinforcement. This approach was necessary to capture the specific behavior and response of each design under different loading conditions. On the contrary, the TPU material, known for its high elasticity, exhibited different characteristics. Due to its flexible nature, reaching the point of failure required applying a substantial displacement. Therefore, to simplify the analysis and facilitate comparison, identical displacements were assigned to the TPU designs. This ensured a consistent testing framework and allowed for a comprehensive evaluation of the material its performance under similar loading conditions.

The results for each material and phase are presented in section 4.2 through section 4.9. Initially, a comprehensive presentation of load-displacement curves for all designs within a specific phase and material were provided in a single graph. Further analysis was conducted for each design, providing detailed insights into their behavior. A load-displacement curve was shown alongside a corresponding Poisson's ratio-displacement curve. The combined presentation of load-displacement and Poisson's ratio curves provides valuable insights into the mechanical behavior of the different designs, shedding light on their auxetic or non-auxetic nature and the occurrence of stress localization within the material structure. In this graph, gray dashed lines were incorporated to indicate the locations of kinks. Subsequently, the boundary conditions and the applied displacement for each design were presented.

Finally, contour plots illustrating the deformed shape were presented, starting with a displacement of 0.5 mm, followed by a specific displacement indicated with a gray dashed line, and finally the displacement at the end of the simulation. The plot contours depict the maximum in-plane principal stresses for the design, with a zoomed-in image provided on the right. Understanding stress distribution and concentration patterns is crucial for optimizing the design of structures and components, as it can help identify critical regions prone to failure and aid in devising appropriate reinforcement strategies to improve overall performance.

4.2. Results phase 1 ABS

In this phase with this particular material, specific displacements were assigned to each design: 10 mm for design A, 10 mm for design B, 30 mm for design C, and 15 mm for design D. This distribution was based on the various stages of fracture that each design experienced. The load-displacement curves for all designs are illustrated in Fig. 4.1. Furthermore, Figures 4.2a, 4.2b, 4.2c, and 4.2d present the load-displacement curves accompanied by the corresponding Poisson's ratio-displacement curves for designs A, B, C, and D, respectively.

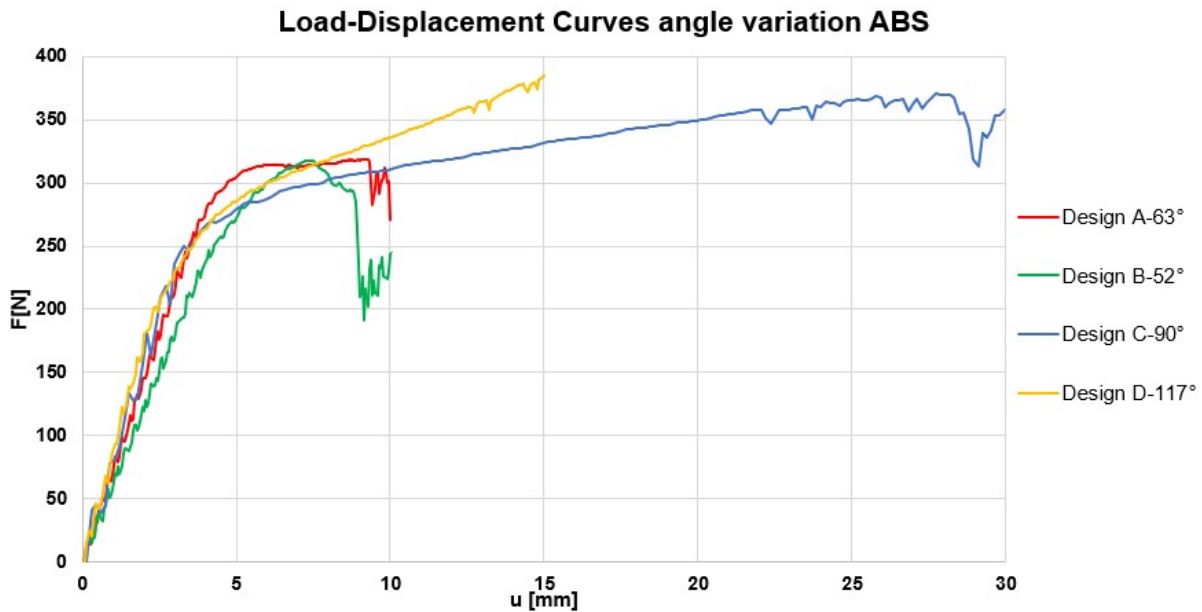


Figure 4.1: Load-displacement curves Phase 1 ABS.

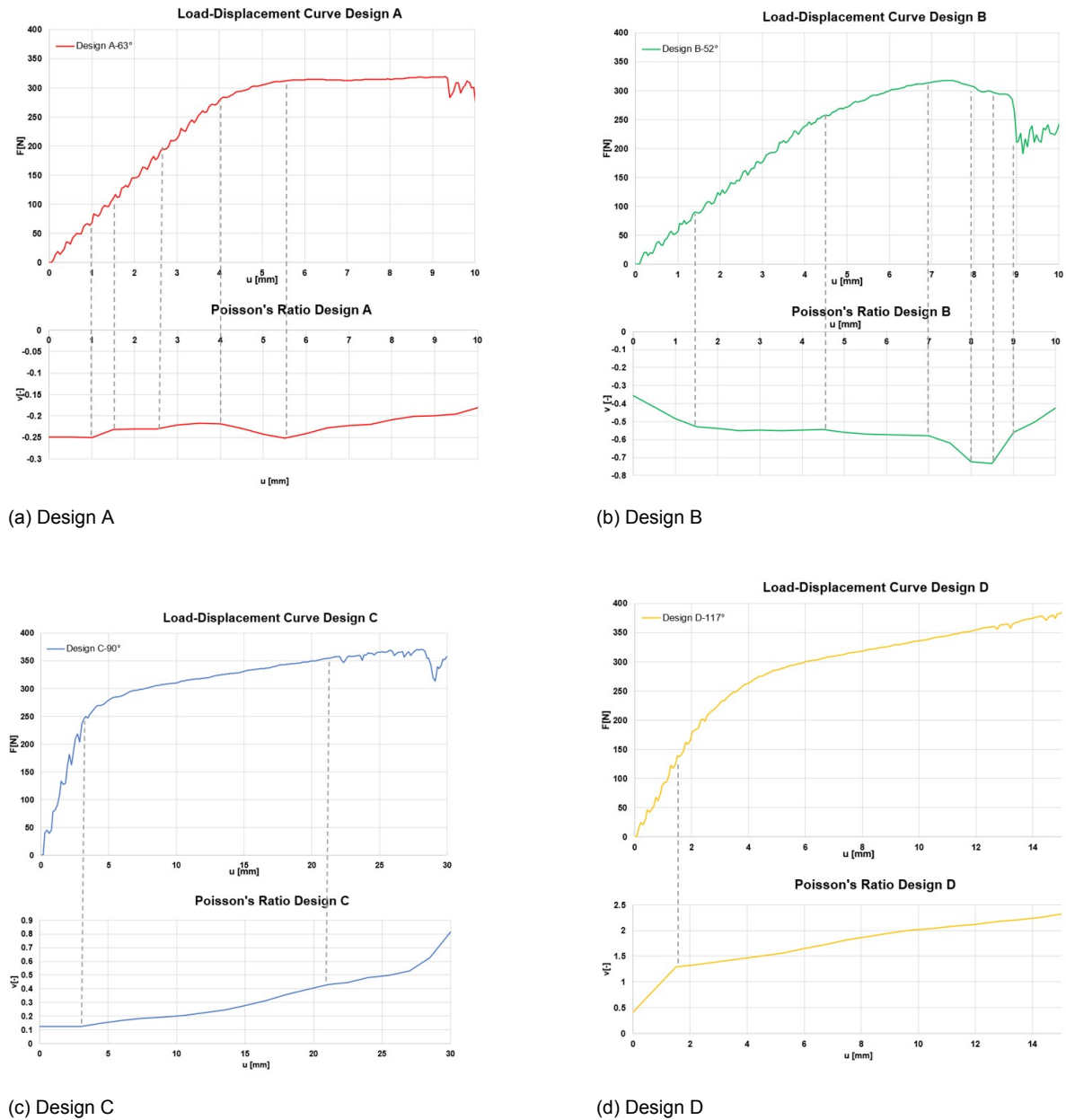


Figure 4.2: Load-displacement curves and Poisson's ratio-displacement curves for the different designs with ABS reinforcement (axes differ).

In Fig. 4.2, it is evident that design A and B exhibit a negative Poisson's ratio, indicating their auxetic nature, whereas design C and D show a positive Poisson's ratio, indicating their non-auxetic nature. It is important to observe that the y-axes of the Poisson's ratio curves vary across the four different designs. The subsequent chapters present the contour plots for these four distinct designs at specific displacements.

4.2.1. ABS design A

Below are the contour plots illustrating different displacements for design A. A total displacement of 10 mm was applied. This design exhibits a negative Poisson’s ratio, which implies that when it is stretched vertically, the reinforcement expands laterally. The final simulated fracture behavior is depicted in Fig. 4.3d. It was evident that the fracture occurred diagonally. The Figure demonstrates that the highest stresses (emphasized in red) were distributed throughout the reinforcement, primarily concentrated near specific joints.

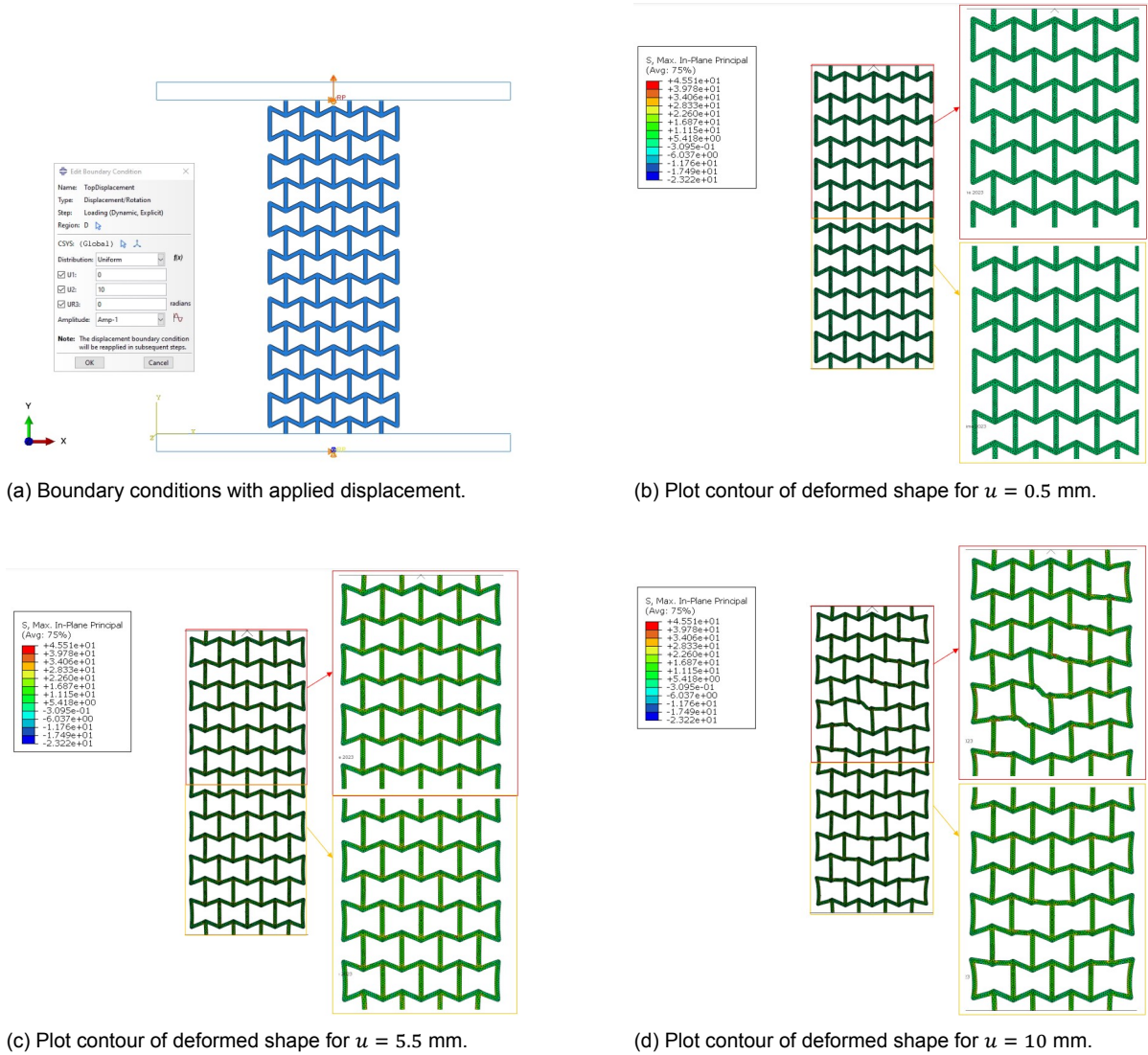


Figure 4.3: Boundary conditions and contour plots of deformed shapes.

4.2.2. ABS design B

Presented below are the contour plots depicting various displacements for design B, with a total applied displacement of 10 mm. This design also possesses a negative Poisson's ratio. The lateral expansion of the reinforcement is clearly evident in the plots presented below. The ultimate simulated fracture behavior is portrayed in Fig. 4.4d. It was apparent that fracture took place diagonally, similar to the previous bowtie design.

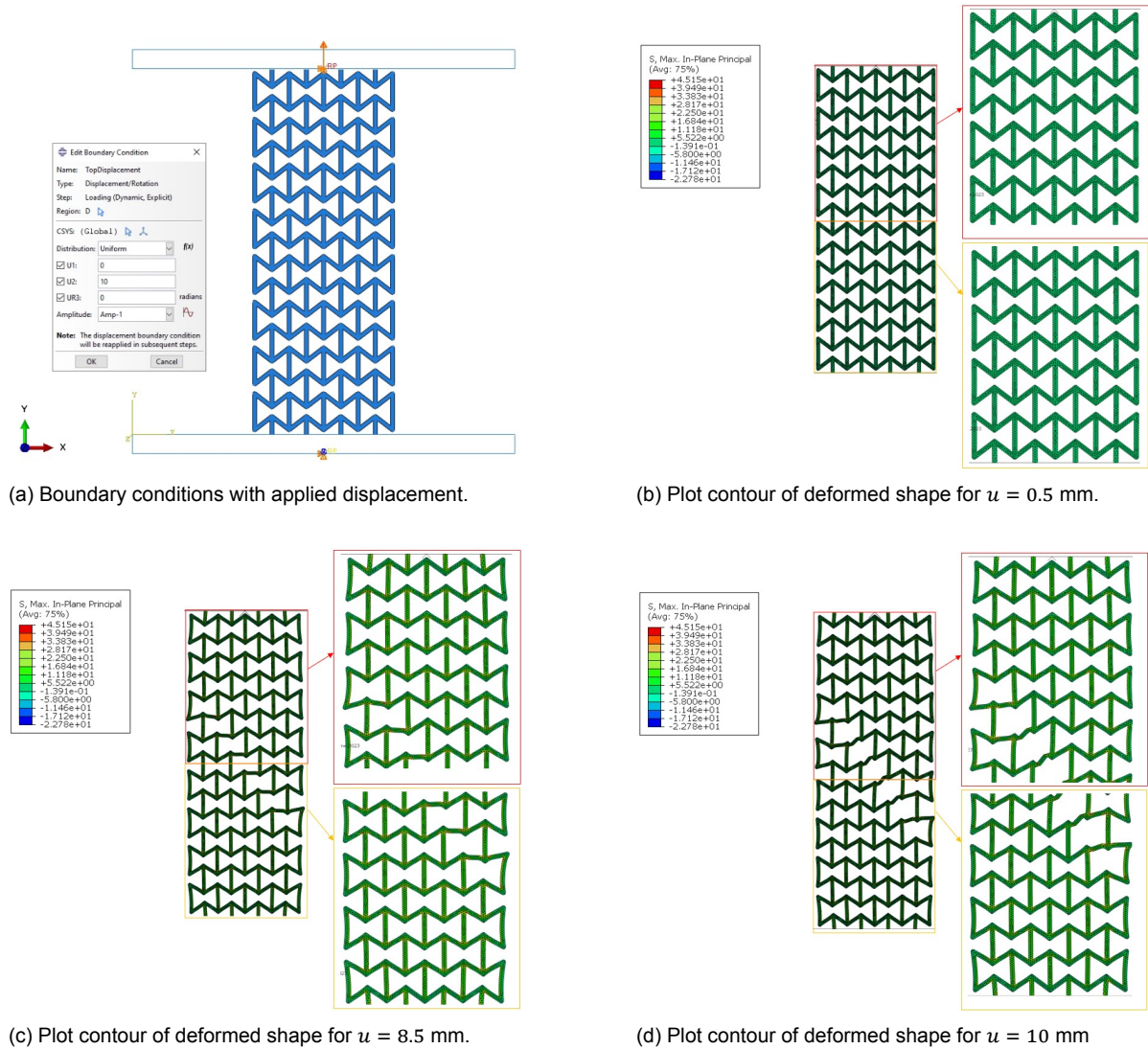


Figure 4.4: Boundary conditions and contour plots of deformed shapes.

4.2.3. ABS design C

Fig. 4.5 presents the contour plots of various displacements for design C, with a total displacement of 30 mm applied. This design displays a positive Poisson’s ratio, signifying that vertical stretching leads to lateral contraction in the reinforcement. This characteristic is distinctly visible in the plots provided. Notably, the rectangular design undergoes a transformation into the honeycomb pattern during vertical stretching. The ultimate simulated fracture behavior is presented in Fig. 4.5d. This Figure clearly illustrates that the most significant stress concentrations were spread across the reinforcement, primarily centered around specific joints, highlighted in red.

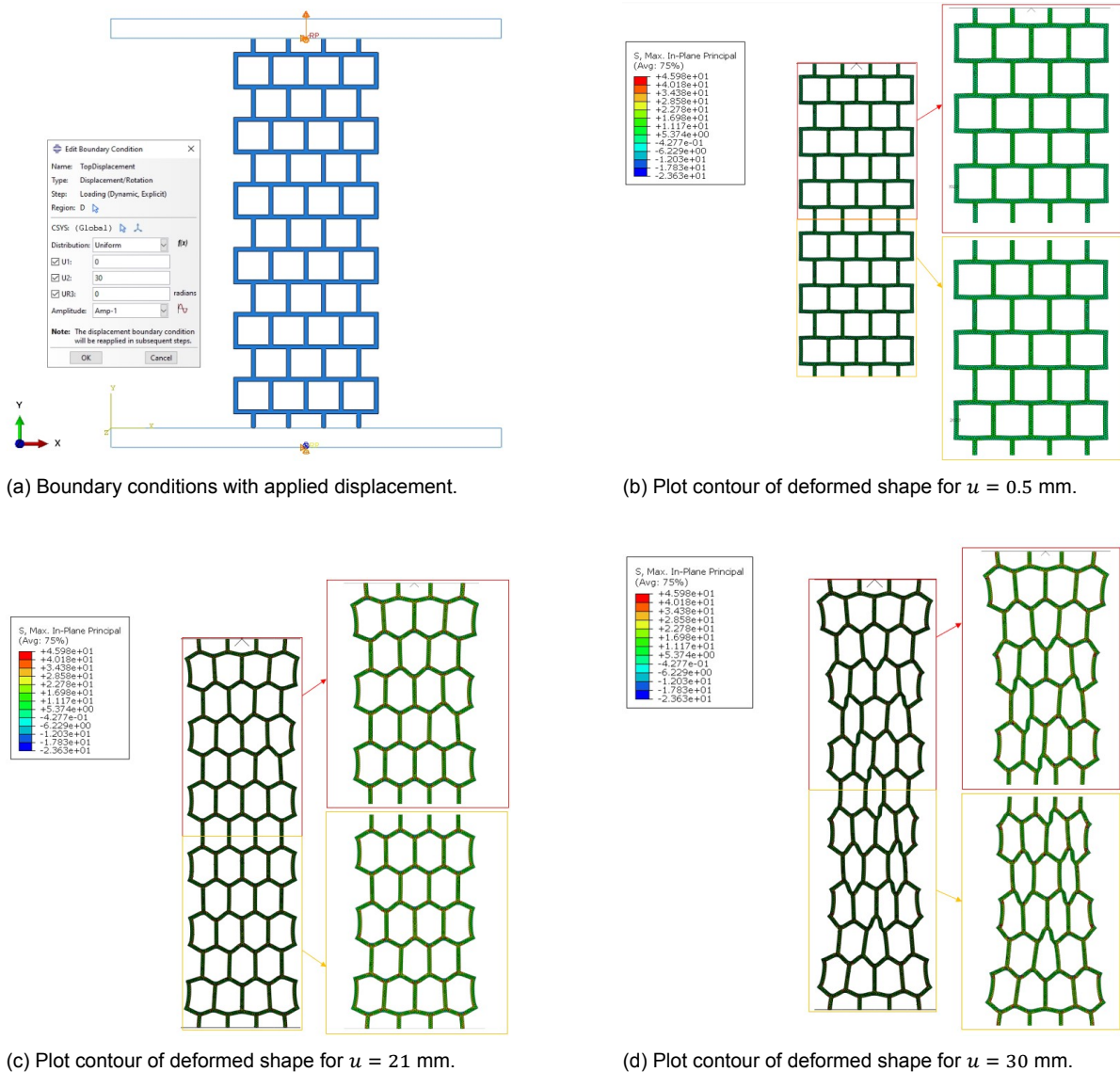


Figure 4.5: Boundary conditions and contour plots of deformed shapes.

4.2.4. ABS design D

Displayed here are the contour plots illustrating different displacements for design D, with a final displacement of 15 mm applied. This material also exhibits a positive Poisson's ratio, and the characteristic lateral contraction is clearly evident in the presented plots. Interestingly, the honeycomb design transforms into a stretched-out honeycomb pattern under vertical stretching. For a comprehensive representation, the ultimate simulated fracture behavior is illustrated in Fig. 4.6d. This Figure showcases that the high stresses were present near every joint. This observation indicates that design D exhibited a more uniform distribution of stress concentrations near each joint.

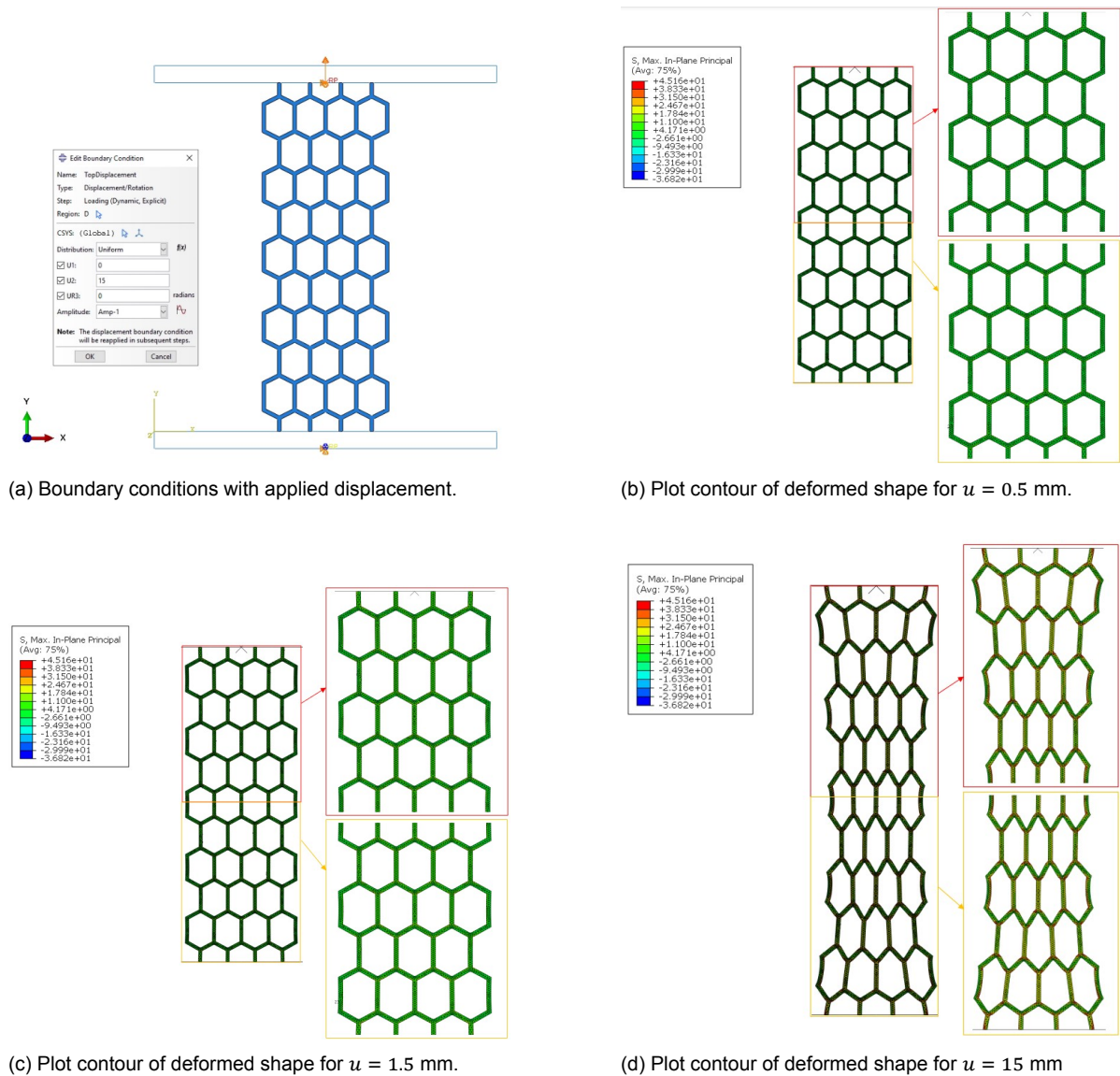


Figure 4.6: Boundary conditions and contour plots of deformed shapes.

4.3. Results phase 1 TPU

In contrast to the ABS material, the TPU material exhibits a highly elastic and flexible nature, requiring a significantly higher applied displacement to reach the point of failure. To simplify the analysis, a uniform displacement of 30 mm was assigned to all designs. The load-displacement curves for each design are depicted in Fig. 4.7. Additionally, Figures 4.8a, 4.8b, 4.8c, and 4.8d showcase the load-displacement curve alongside a corresponding Poisson's ratio-displacement curve for designs A, B, C, and D, respectively.

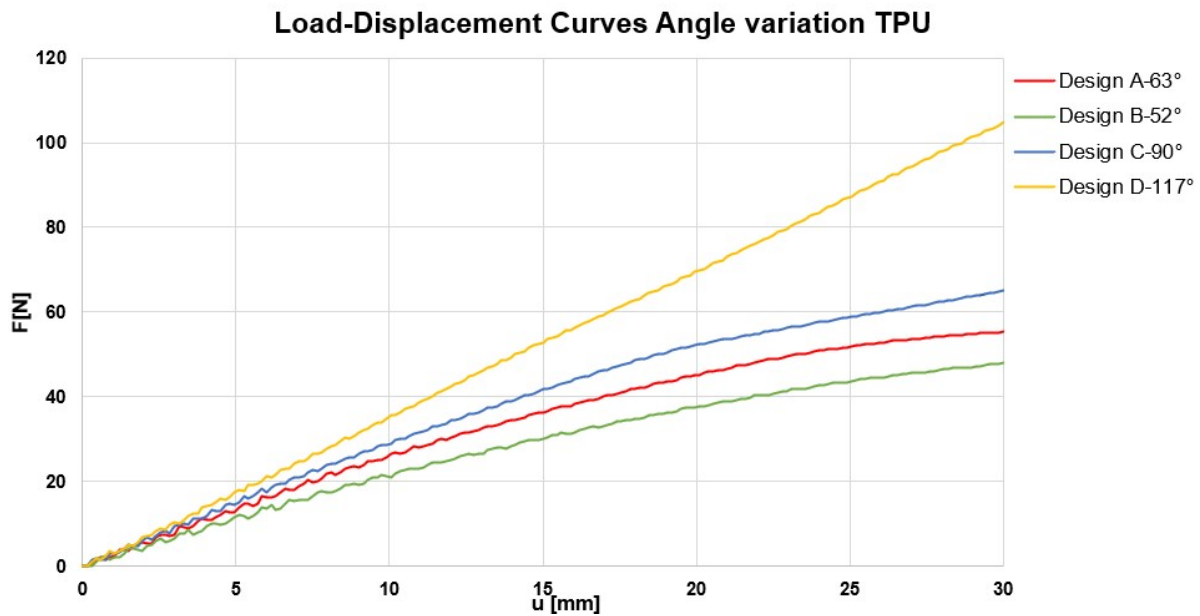


Figure 4.7: Load-displacement curves Phase 1 TPU.

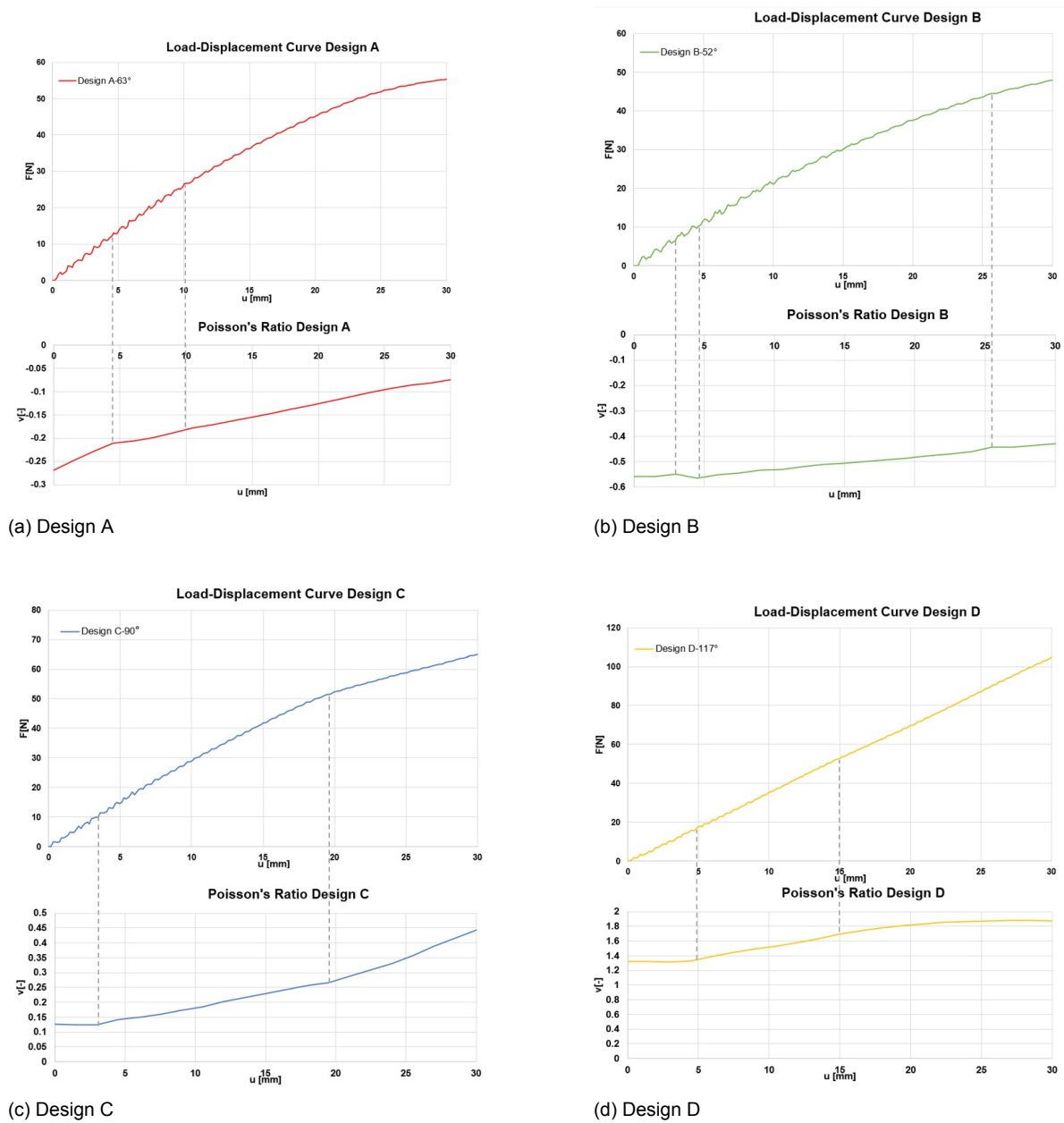


Figure 4.8: Load-displacement curves and Poisson's ratio-displacement curves for the different designs with TPU reinforcement (axes differ).

Fig. 4.8 illustrates the distinct behavior of the different designs. Designs A and B display a negative Poisson's ratio, signifying their auxetic nature, while designs C and D showcase a positive Poisson's ratio, indicating their non-auxetic characteristic. Notably, the y-axes of the Poisson's ratio curves vary among the four designs. In comparison to the ABS material, the Poisson's ratio curves exhibit a more linear response. The upcoming chapters provide detailed contour plots for these four unique designs at specific displacement levels.

4.3.1. TPU design A

Fig. 4.9 displays the contour plots depicting various displacements for design A, with a total displacement of 30 mm imposed. Notably, this design demonstrates a negative Poisson's ratio, evident from the lateral expansion of the reinforcement during vertical stretching. The final simulated fracture behavior is captured in Fig. 4.9d. It is obvious that stretching causes the bowtie design to change into a rectangular shape. The transition point occurs at an approximate displacement of 27 mm. When simulated beyond 30 mm, the rectangular shape transforms into a honeycomb shape.

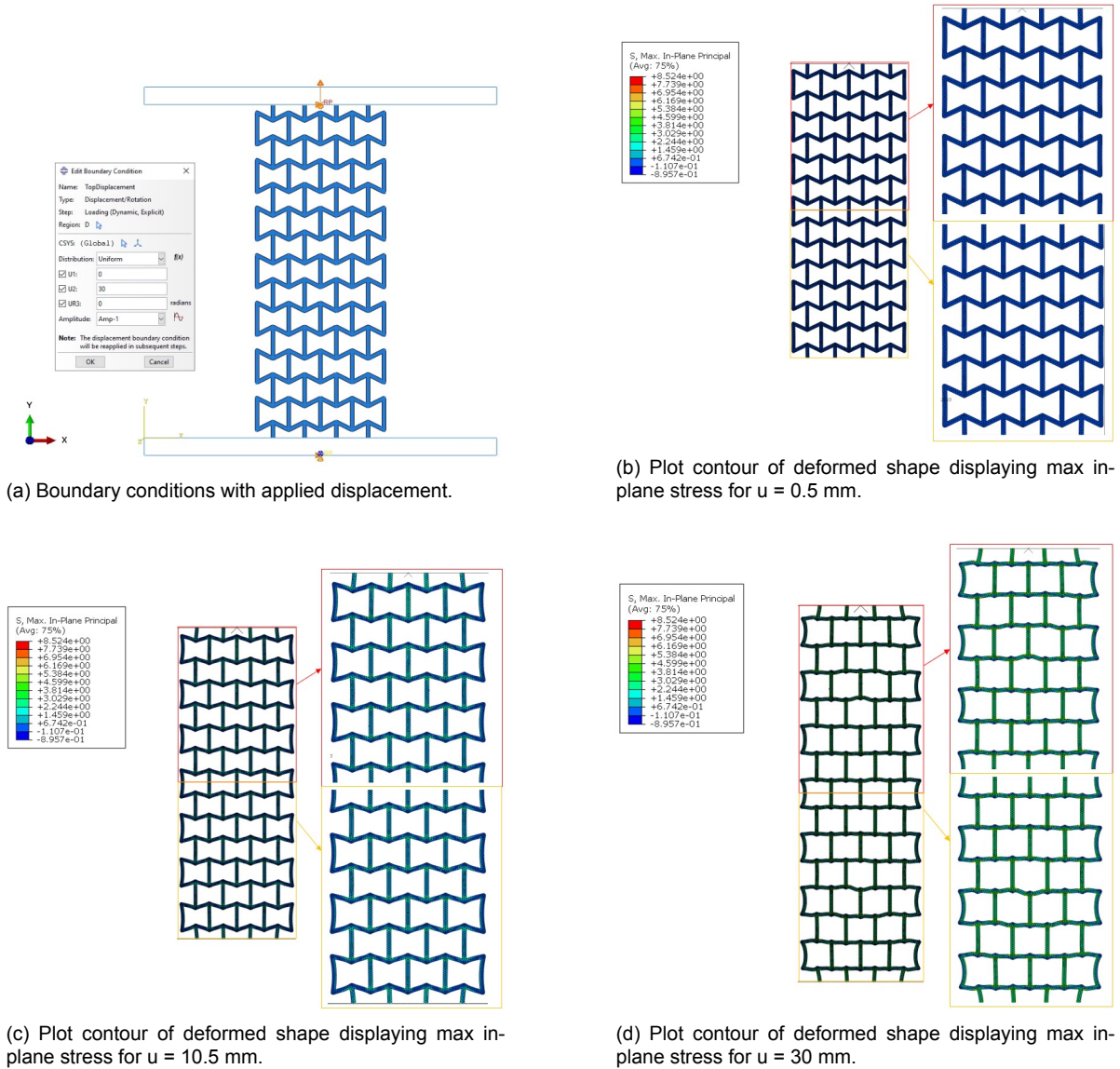


Figure 4.9: Boundary conditions and contour plots of deformed shapes.

4.3.2. TPU design B

Below are the contour plots illustrating different displacements for design B, with a total displacement of 30 mm applied. This design also exhibits a negative Poisson's ratio, indicated by the lateral expansion of the reinforcement during vertical stretching. The final simulated fracture behavior is depicted in Fig. 4.10d. Notably, the stretching process leads the bowtie design to transform into a rectangular shape. It is worth noting that the re-entrant angle of design B is sharper than that of Design A, necessitating a higher displacement to achieve the rectangular configuration. The transition point had not been reached yet.

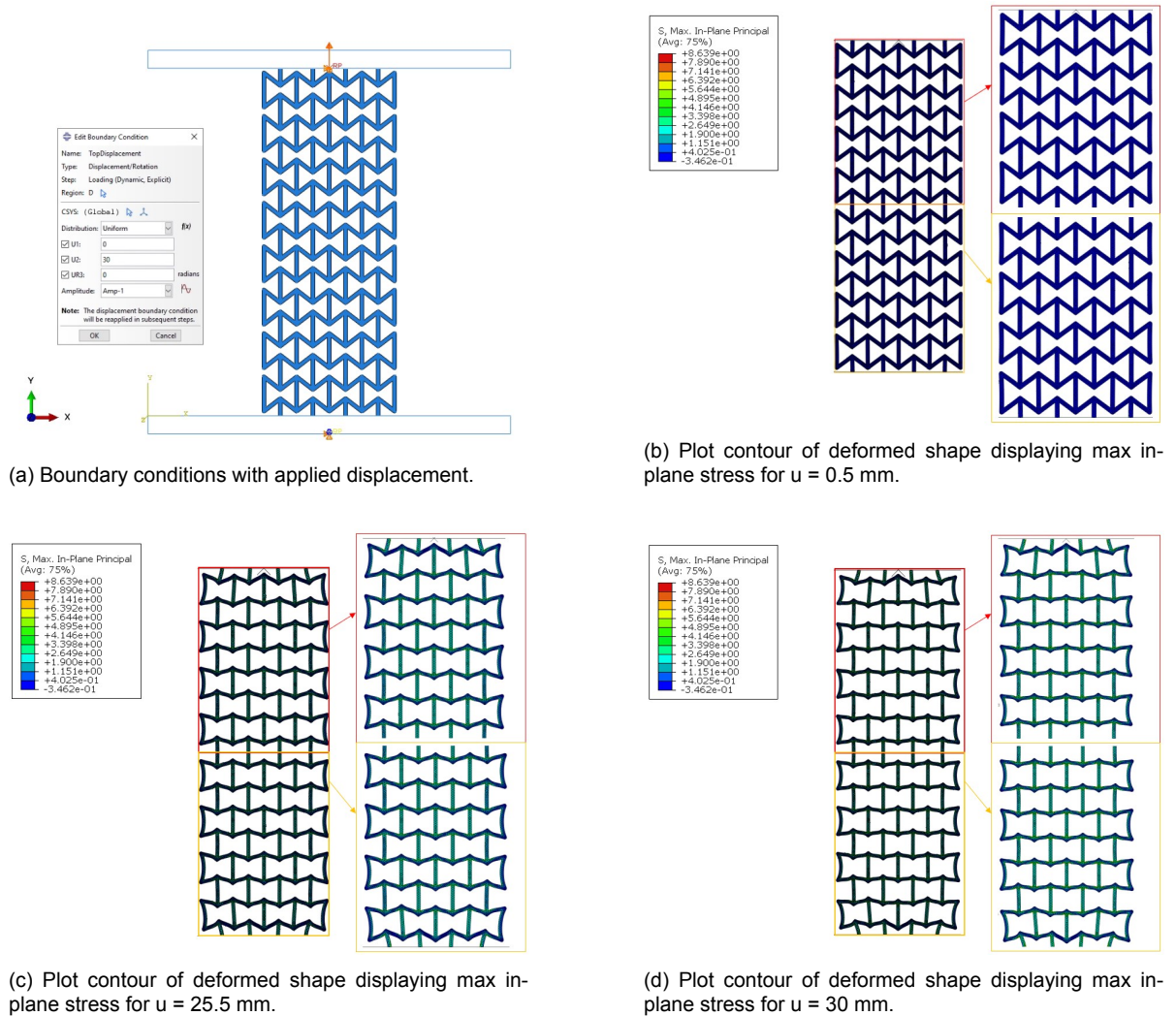


Figure 4.10: Boundary conditions and contour plots of deformed shapes.

4.3.3. TPU design C

Fig. 4.11 displays the contour plots for design C, depicting a total displacement of 30 mm. This design exhibits a positive Poisson’s ratio, which results in pronounced lateral contraction. It is evident that the vertical stretching of the rectangular shape leads to its transformation into a honeycomb configuration. The final simulated shape is illustrated in Fig. 4.11d.

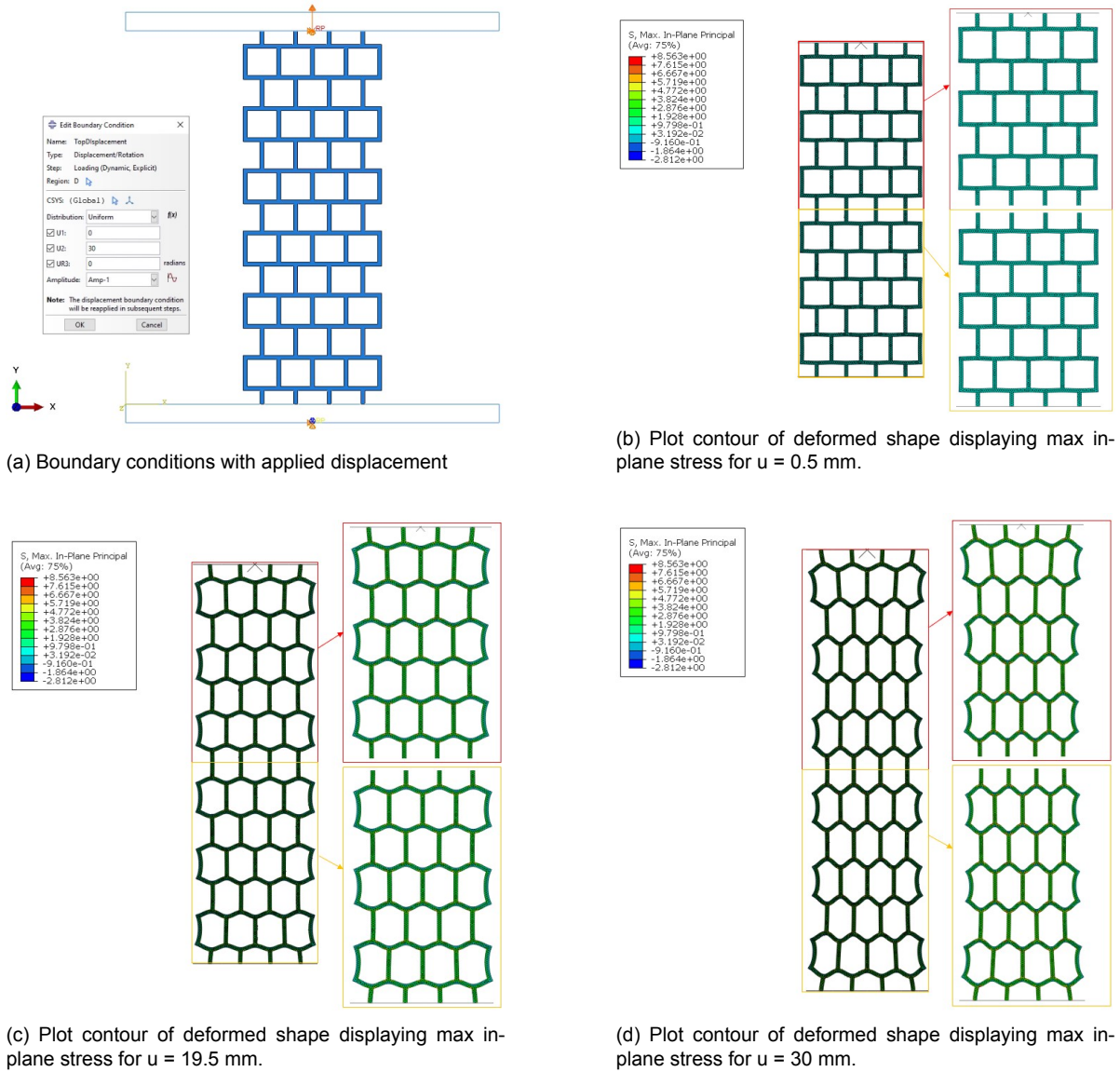
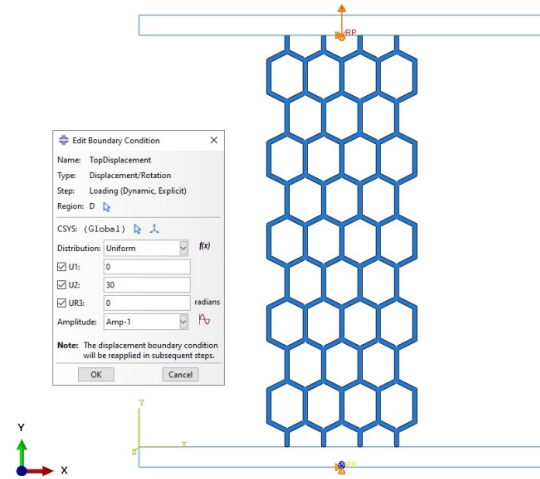


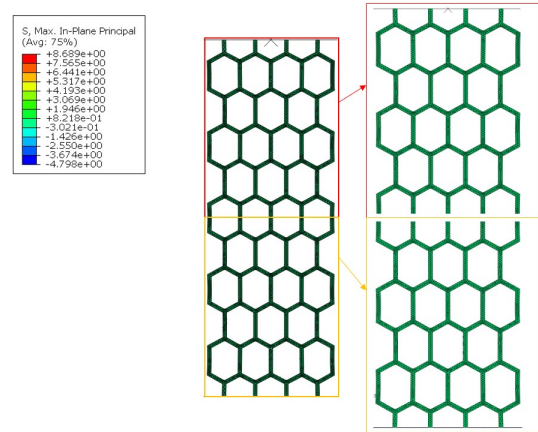
Figure 4.11: Boundary conditions and contour plots of deformed shapes.

4.3.4. TPU design D

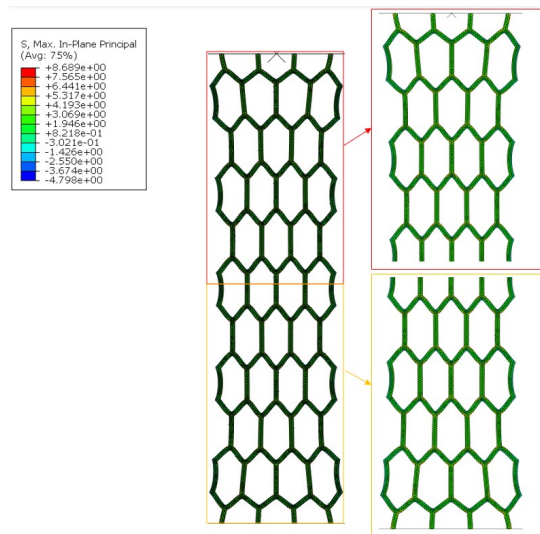
The subsequent section displays the contour plots for design D at different displacement levels. This design also exhibits a positive Poisson's ratio, evident from the observed lateral contraction. As the reinforcement undergoes elongation, the honeycomb structure becomes progressively stretched. The ultimate simulated configuration is depicted in Fig. 4.12d.



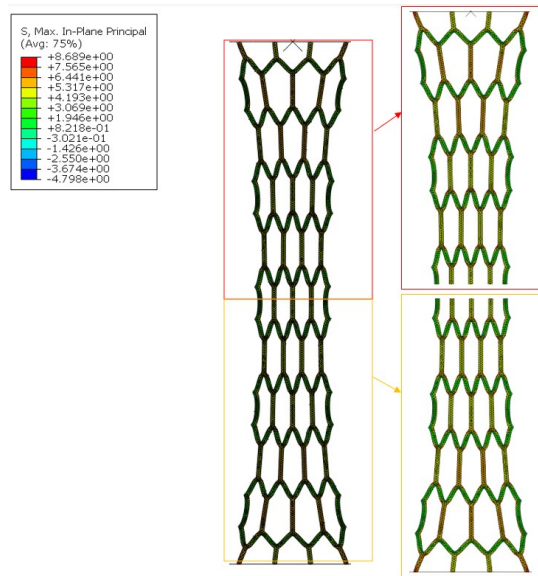
(a) Boundary conditions with applied displacement.



(b) Plot contour of deformed shape displaying max in-plane stress for $u = 0.5$ mm.



(c) Plot contour of deformed shape displaying max in-plane stress for $u = 15$ mm.



(d) Plot contour of deformed shape displaying max in-plane stress for $u = 30$ mm

Figure 4.12: Boundary conditions and contour plots of deformed shapes.

4.4. Analyzing results and discussion phase 1

In the discussion of the load-displacement curves for the ABS reinforcement (Fig. 4.1) across the four different designs, fracture was observed for all the designs. On the other hand, for the TPU reinforcement (Fig. 4.7), fracture was not observed due to its highly elastic nature. This distinction in fracture behavior can be attributed to the different mechanical properties of the materials used. ABS material exhibits a high elastic modulus, indicating its stiffness and resistance to deformation. On the other hand, TPU material possesses a low elastic modulus, signifying its high flexibility and ability to withstand significant deformation without fracture. Upon comparing the load capacities of the two materials, it becomes evident that ABS can withstand a significantly higher force compared to the TPU material. This difference draws attention to the distinctions in the mechanical properties and strength characteristics of ABS and TPU. Examining the behavior of the ABS material (Fig. 4.1), a notable observation is that the auxetic designs exhibited an earlier onset of fracture compared to the non-auxetic designs.

When comparing the stiffness of the four different designs for both ABS and TPU materials, a consistent pattern emerges. For both materials, design D exhibits the highest stiffness among the four designs, followed by design C, then design A, and finally design B, as displayed in Fig. 4.13. However, in the case of the ABS material, the variance in stiffness between design A, C and D was not substantial. The observed order of stiffness for the designs can be attributed to their unique geometric configurations and cell arrangements. From the literature study, the higher stiffness of the honeycomb design in comparison to the rectangular configuration was already established. Design D, being a honeycomb structure, provides a more rigid and robust framework compared to the other designs, resulting in a higher overall stiffness. Design C, with its rectangular arrangement, also offers a considerable level of stiffness, although slightly lower than design D. On the other hand, design A and B, being auxetic bowtie structures, possess lower stiffness due to their characteristic behavior of lateral expansion under tensile loading, which imparts a degree of flexibility to the materials. Overall, the stiffness rankings for the designs suggest that the honeycomb-based structures (design D) tend to exhibit the highest stiffness, while the auxetic bowtie designs (design A and B) demonstrate relatively lower stiffness. This information can be valuable when selecting the appropriate design for specific applications that require specific mechanical properties and stiffness levels.

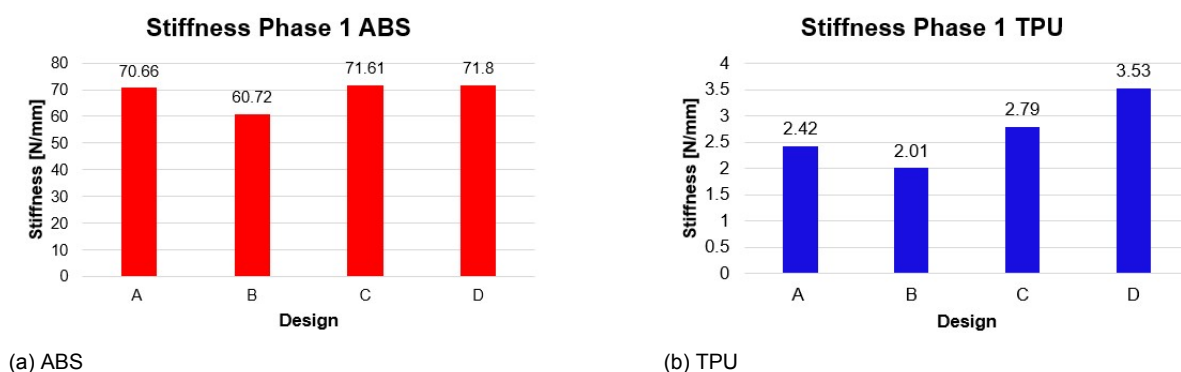


Figure 4.13: Stiffness phase 1 for both materials (axes differ)

In Fig. 4.2 and Fig. 4.8, the load-displacement curves of the four designs are presented alongside the corresponding Poisson's ratio curves for the materials ABS and TPU, respectively. First discussing the ABS material, it is evident that design A and B exhibited a negative Poisson's ratio, indicative of their auxetic behavior, characterized by lateral expansion under tensile loading. On the contrary, design C and D displayed a positive value for Poisson's ratio, signifying their non-auxetic behavior, where lateral contraction occurred during tensile loading as

expected.

Furthermore, the Poisson's ratio curves for designs A, B and C demonstrated non-linearity, suggesting the occurrence of stress localization in the materials. These instances could be identified by the kinks in the Poisson's ratio curve, marked by presence of gray dashed lines. This phenomenon of non-linearity occurred due to the redistribution of stress within the structure, leading to localized regions of high stress concentrations. The non-linearity of the Poisson's ratio curves highlights the complex and nonlinear mechanical response of the materials under load. However, design D showed a distinct linear response for the Poisson's ratio after a displacement of 1.8 mm. As the displacement increased, the Poisson's ratio also increased steadily. Notably, for design A, the Poisson's ratio remained within certain limits. On the other hand, designs C surpassed the limit of $\nu = 0.5$ when fracture started to occur. Remarkably, design D began near the limit of $\nu = 0.5$ and continued increasing up to a value of $\nu = 2.5$.

In the context of the TPU material, the auxetic designs also exhibited a negative Poisson's ratio, while the non-auxetic designs showed a positive value. All designs displayed linearity in their Poisson's ratio curves. The expansion of the auxetic structures can be clearly observed in Figures 4.9 and 4.10, whereas the contraction of the non-auxetic ones is displayed in Figures 4.11 and 4.12. Notably, design A, when subjected to lateral stretching, transformed into design C, and with further simulation, eventually evolved into design D, which aligns with findings from the literature review. Similarly, design C transformed into design D when stretched. However, design D retained its honeycomb shape but with significant stretching. Comparing design A and B, it is evident that design B, with a sharper angle, requires more force to transform it into design C.

Starting with the analysis of design A in the TPU material, the initial Poisson's ratio was approximately -0.27, which progressively decreased as the displacement increased. At a displacement of 30 mm, the observed Poisson's ratio was -0.075, indicating a reduced tendency for lateral expansion during stretching. In contrast, for design B, the initial Poisson's ratio was around -0.55 and approached -0.42 as the displacement increased, indicating a reduction in lateral expansion during stretching compared to its initial state. Overall, these results indicate that the two designs behave differently in response to applied loads. Design C and D exhibited positive Poisson's ratios, indicating their non-auxetic nature, as they began with positive values and became more positive as the displacement increased. For design C, the initial Poisson's ratio was approximately 0.125, and it increased linearly up to 0.45 as the displacement progressed. On the other hand, design D started with a Poisson's ratio near 1.32 and steadily increased until reaching 1.82 with increasing displacement. Essentially, this information suggests that design C and D behaved as non-auxetic materials, with lateral contraction occurring as they were stretched, and the magnitude of this lateral contraction increased with increasing deformation.

Based on the contour plots of the ABS material, the fracture in design A occurred diagonally (Fig. 4.3). This was also the case for design B. In contrast, designs C and D displayed lateral contraction while being vertically stretched, as evidenced in Fig. 4.5 and Fig. 4.6. Notably, the rectangular design transformed into a honeycomb-like structure under high stress, whereas design D maintained its honeycomb shape until fracture, albeit being elongated. Similar to design A, the areas of elevated stress were also localized near the joints for designs C and D. In designs A and C, the highest stresses were observed to be distributed across the reinforcement material, predominantly near specific joints. In design D however, these high stresses occurred near every joint. This observation suggests that design D experienced a more uniform distribution of stress concentrations near each joint, unlike designs A and C, where stress concentrations were localized to specific joint regions. The stress distribution pattern in de-

sign D indicates a more balanced load transfer and potential for enhanced structural integrity compared to designs A and C.

In terms of stress levels, the ABS material displayed substantially higher stresses, approximately five times greater than those observed in the TPU material. This difference in stress levels can be associated with the ability of ABS to withstand more force than TPU. However, the TPU material showcased a higher deformation capacity, allowing it to sustain large deformations without reaching the point of failure. The highest stresses were concentrated near the joints, similar to the ABS material. This indicates that the joints were critical regions where stress concentrations occurred under loading. In addition to high stresses near the joints, there were also high stresses observed in the vertical walls of the cell. This phenomenon was observed because design D underwent significant stretching, resulting in the vertical walls being subjected to extreme deformation and stress. In both materials, the regions near the joints exhibited the highest stress concentrations, making them the most critical areas for stress accumulation.

4.5. Results phase 2 ABS

The load-displacement curves of the adjusted designs, along with the results from phase 1, are depicted in Fig. 4.14. Design C_{adj} was assigned a displacement of 25 mm, while D_{adj} had a displacement of 20 mm, representing the points of failure for these designs. Fig. 4.15a shows the load-displacement curve and the corresponding Poisson's ratio-displacement curve for design C_{adj} , while Fig. 4.15b presents the same curves for design D_{adj} . The y-axes of these two curves are not similar.

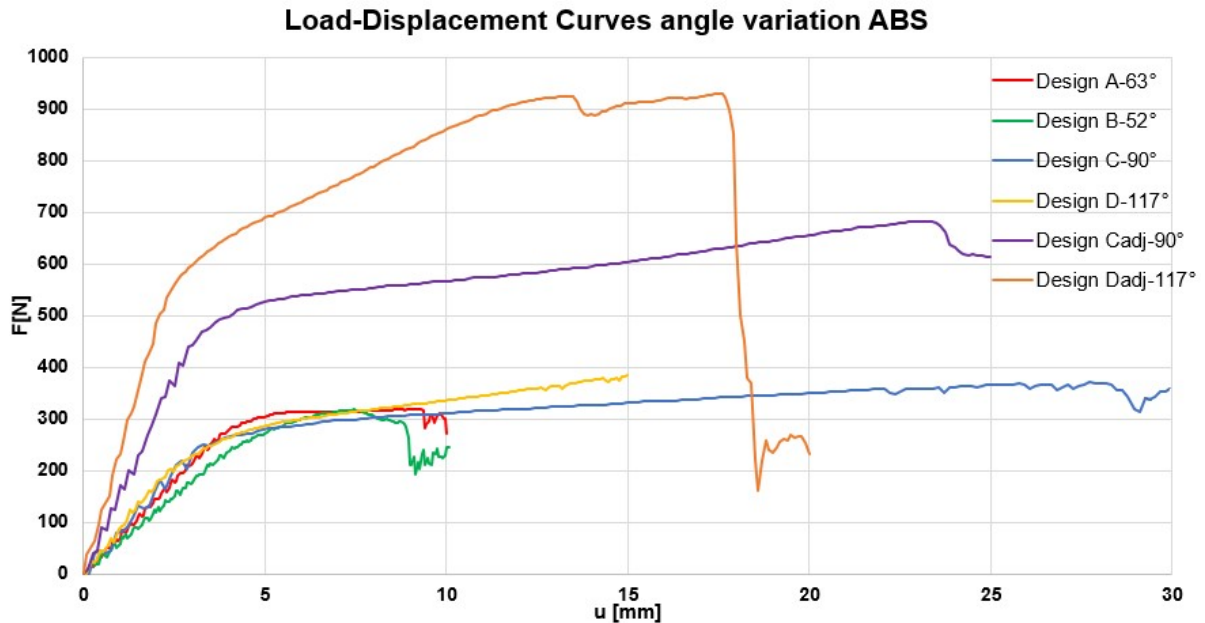
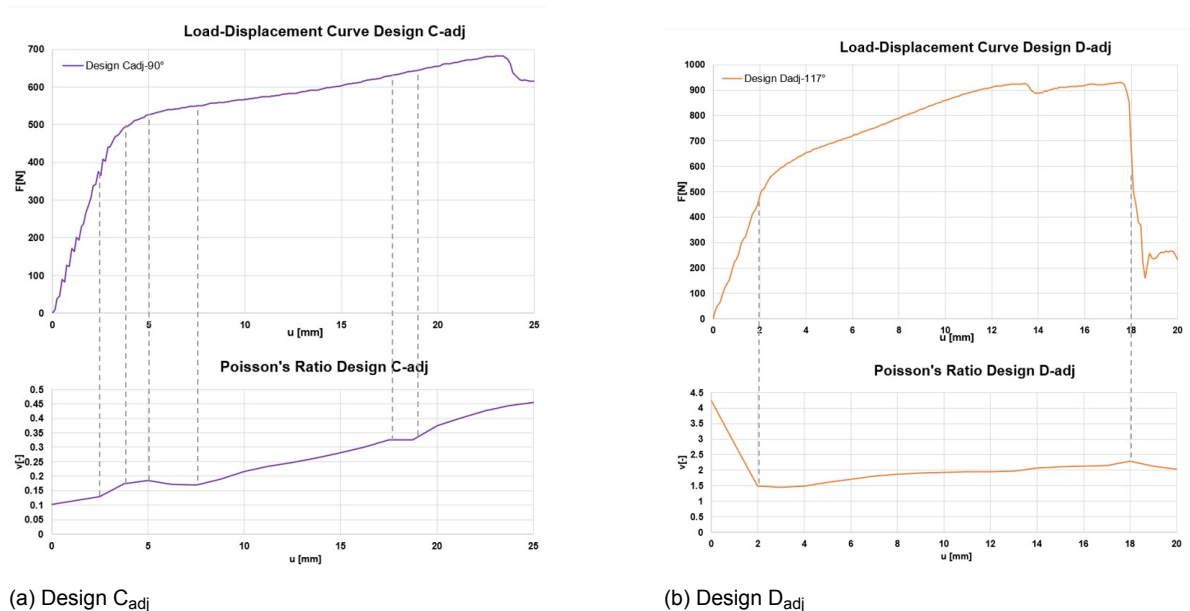


Figure 4.14: Load-displacement curves Phase 2 ABS.



(a) Design C_{adj}

(b) Design D_{adj}

Figure 4.15: Load-displacement and Poisson's ratio-displacement curves for design C_{adj} and design D_{adj} with ABS reinforcement (axes differ).

4.5.1. ABS design C_{adj}

The contour plots of the adjusted design C , denoted as C_{adj} , are presented in Fig. 4.16. In this design, a displacement of 25 mm was applied, which is lower than that of phase 1. Fracture occurred earlier in this phase due to the increased volume. The rectangular design transitions into a honeycomb shape before reaching the point of fracture, similar to the behavior observed in phase 1. The final simulated fracture model is visualized in Fig. 4.16d. The highest stresses were concentrated near the joints.

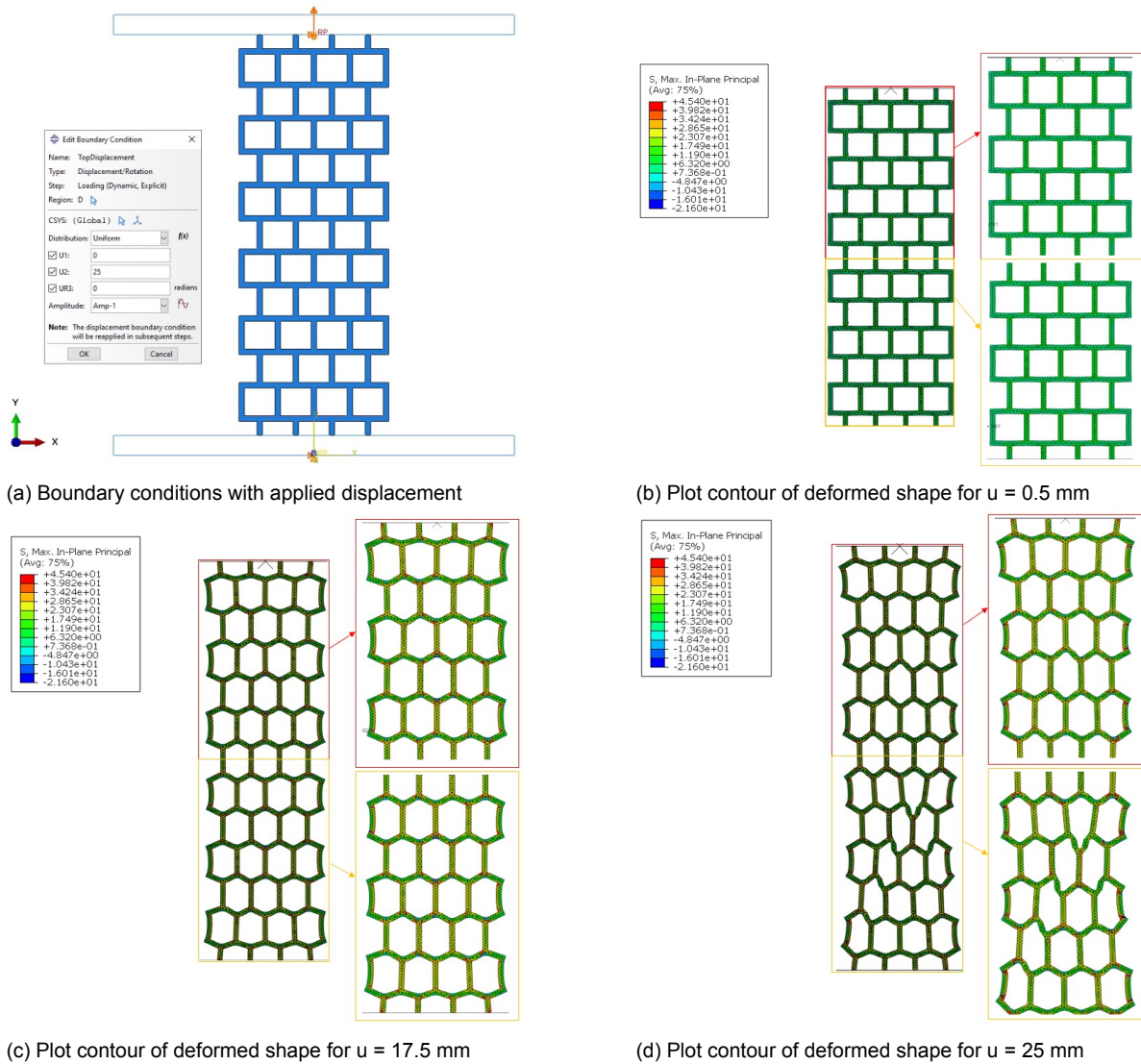


Figure 4.16: Boundary conditions and contour plots of deformed shapes.

4.5.2. ABS design D_{adj}

Displayed below are the contour plots of the adjusted design D_{adj} . In this design, a displacement of 20 mm was applied, which is marginally higher than that used in phase 1. For this particular design, fracture occurred at a later stage in this phase due to the increased volume. The ultimate simulated fracture model is depicted in Fig. 4.17d. The highest stresses were primarily localized at the joints and the vertical walls of the cell.

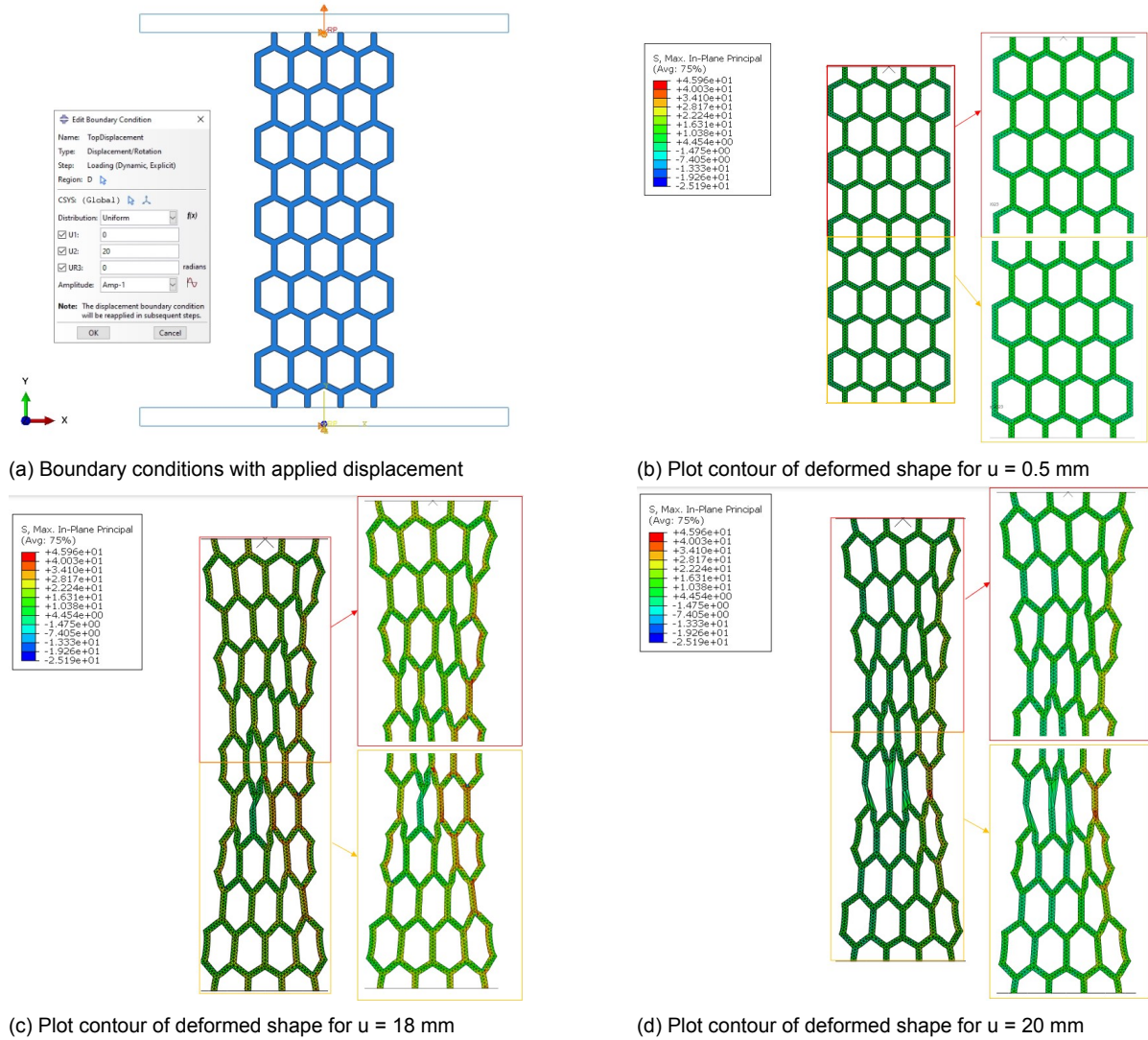


Figure 4.17: Boundary conditions and contour plots of deformed shapes.

4.6. Results phase 2 TPU

Fig. 4.18 displays the load-displacement curves for phase 1 and 2 of the TPU material. Similarly, a displacement of 30 mm was assigned to design C_{adj} and D_{adj} . Fig. 4.19a presents the load-displacement curve and the accompanying Poisson's ratio-displacement curve for design C_{adj} , whereas Fig. 4.19b illustrates the same curves for design D_{adj} . It is important to observe that the y-axes are not the same.

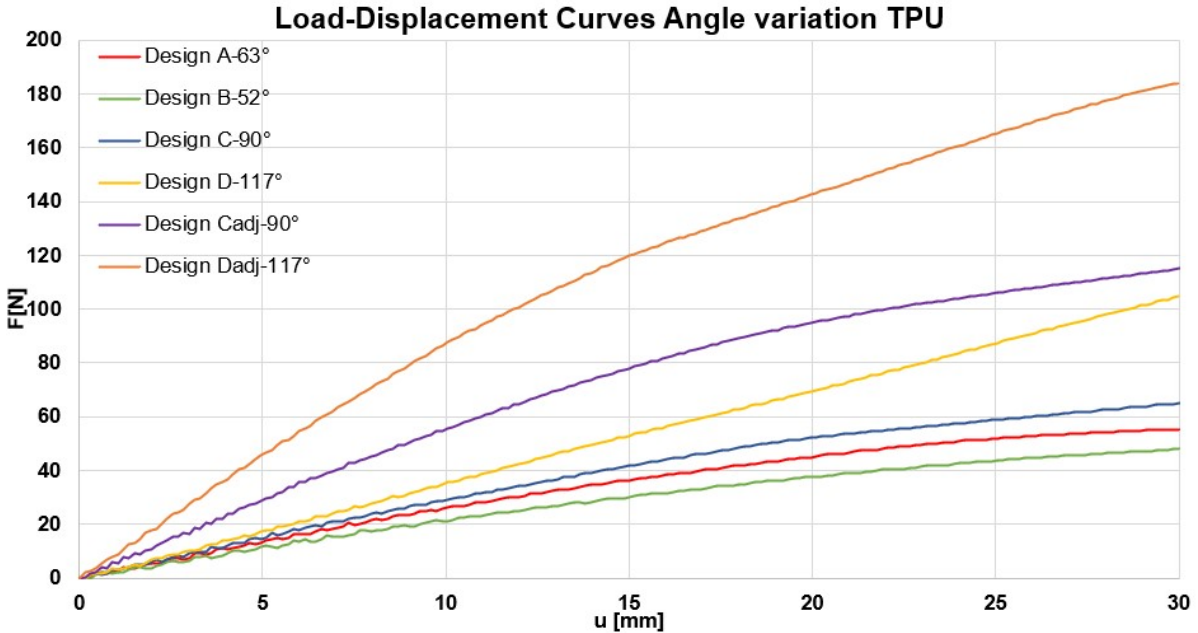
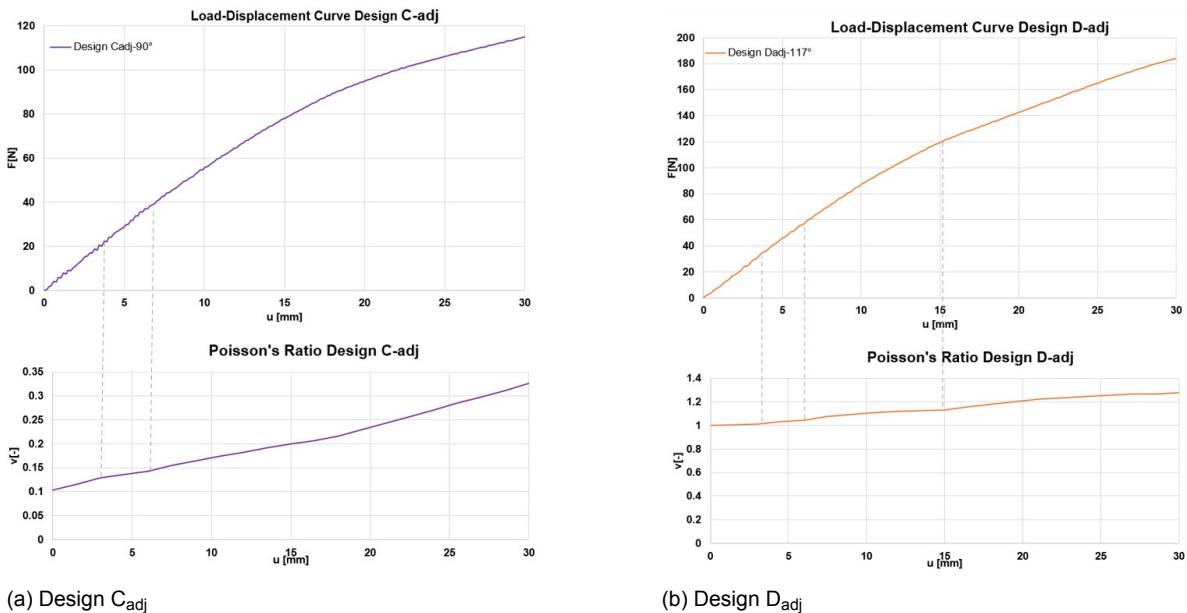


Figure 4.18: Load-displacement curves Phase 2 TPU



(a) Design C_{adj}

(b) Design D_{adj}

Figure 4.19: Load-displacement and Poisson's ratio-displacement curves for design C_{adj} and design D_{adj} with TPU reinforcement (axes differ).

4.6.1. TPU design C_{adj}

Fig.4.20 displays the contour plots for design C_{adj} using the TPU material. Just like in phase 1, the rectangular shape transforms into a honeycomb shape under tension. A displacement of 30 mm was applied for this design, as shown in Fig.4.20d.

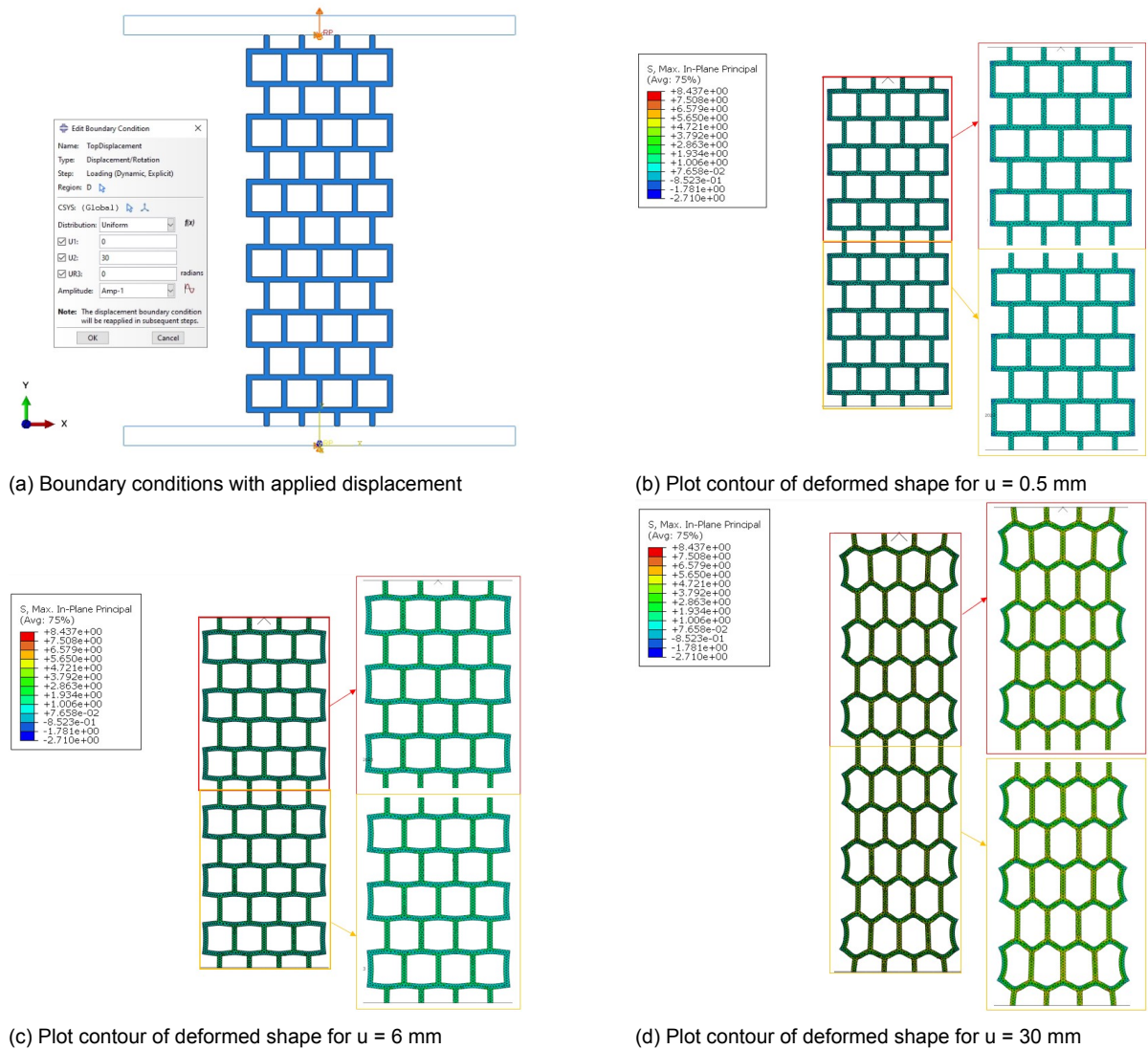


Figure 4.20: Boundary conditions and contour plots of deformed shapes.

4.6.2. TPU design D_{adj}

In the following section, contour plots for design D are presented at various levels of displacement. As the reinforcement undergoes elongation, the honeycomb structure gradually extends. The final simulated configuration is showcased in Fig. 4.21d.

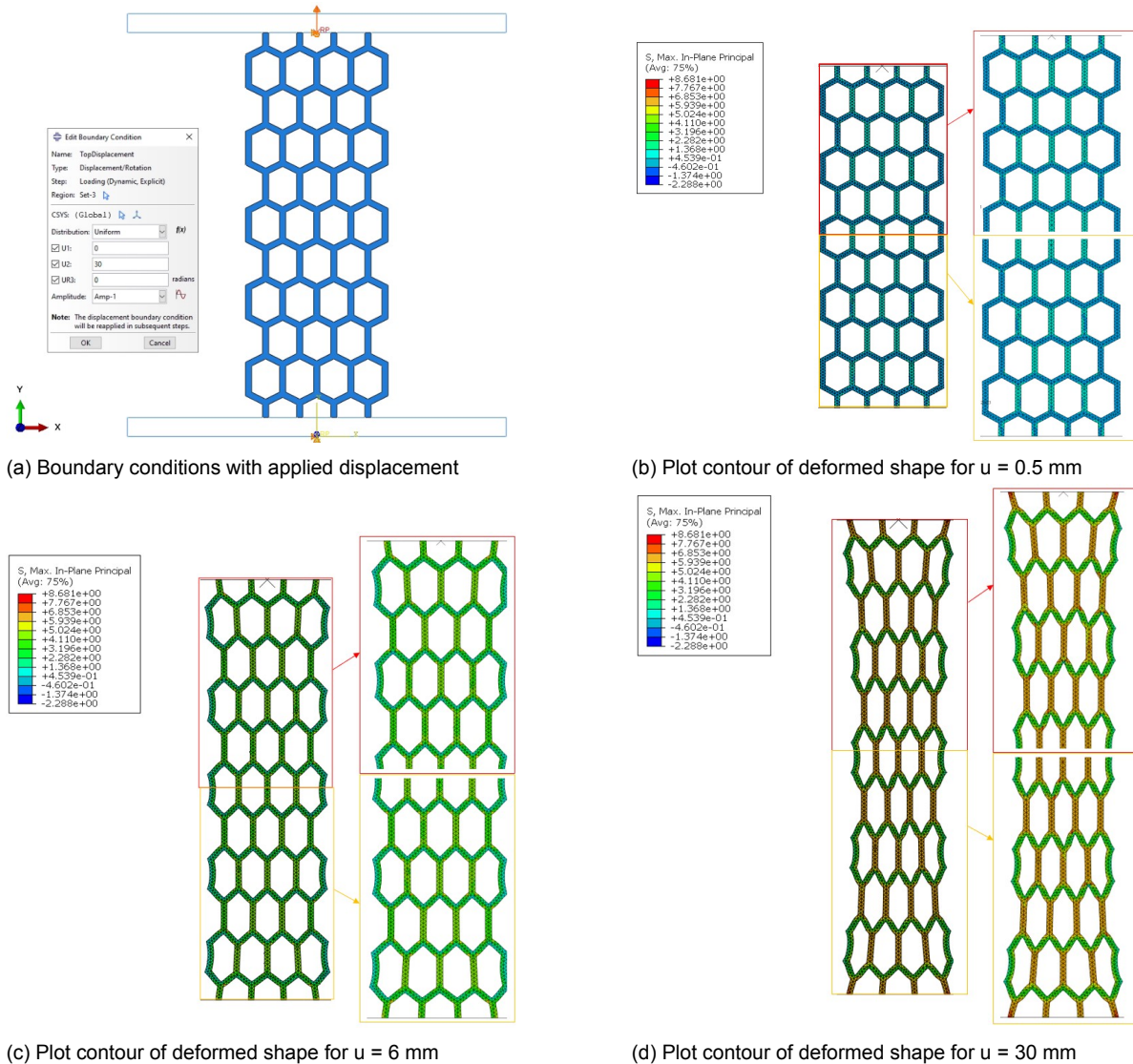


Figure 4.21: Boundary conditions and contour plots of deformed shapes.

4.7. Analyzing results and discussion phase 2

The load-displacement curves depicted in Fig. 4.22 showcase the reinforcing designs with identical volume for both materials. Similar to phase 1, design A reaches fracture first, followed by design D_{adj} , and finally design C_{adj} . Moreover, for both materials, design D_{adj} exhibits the highest stiffness, followed by design C_{adj} , and finally design A, as displayed in Fig. 4.23. For design C_{adj} and D_{adj} , both the adjusted designs displayed higher stiffness compared to the designs in phase 1. For the ABS material, increasing the volume of design C resulted in an increase of approximately two, whereas for design D, the increase was about 2.5 times. Conversely, in the TPU material, the stiffness of design C increased with a factor of 1.8, while design D increased with a factor of 2.25. This observation aligns with the concept that the adjusted designs have a larger volume, leading to increased stiffness due to the more substantial reinforcement present in the structure.

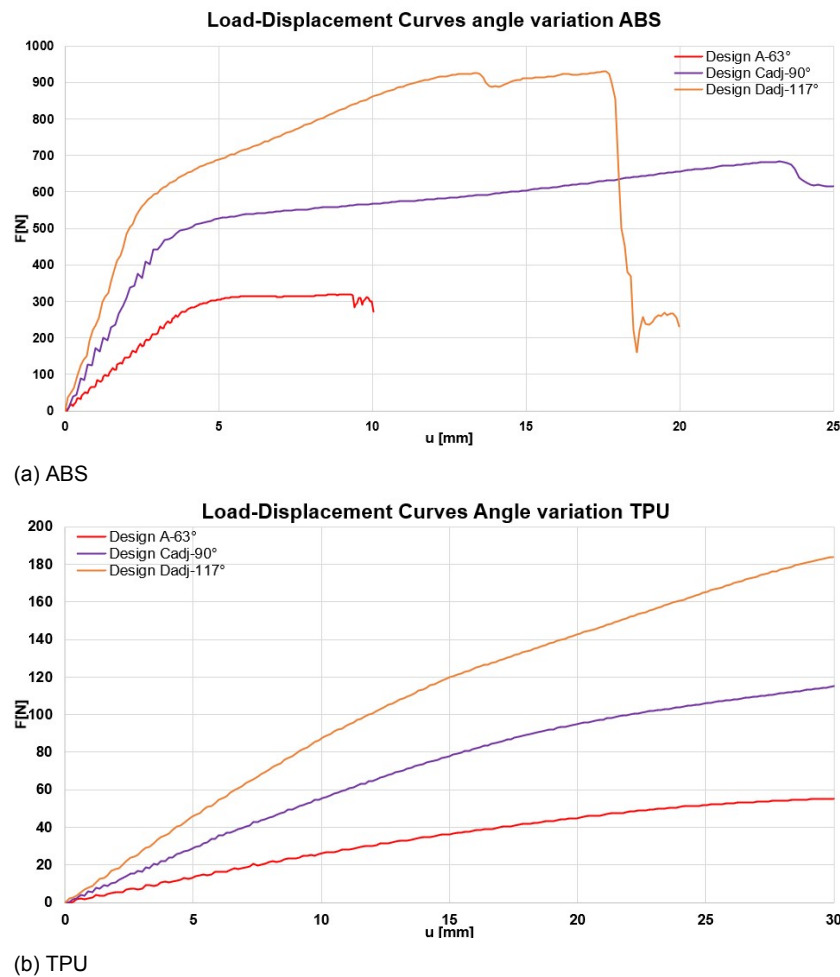


Figure 4.22: Load-displacement curves Phase 2 (values on the y-axis differ).

Upon comparing the Poisson's ratio curves from phase 1 and phase 2 for the material ABS, illustrated in Figures 4.2c and 4.15a for the rectangular design, it is evident that both designs initiated with a ν of 0.1 and reached a value of approximately $\nu = 0.5$ at a displacement of 25 mm. As the displacement increased, the design experienced deformation, leading to changes in its dimensions in both lateral and axial directions. This deformation caused the Poisson's ratio to increase gradually until reaching a value of approximately 0.5. Similar non-linear increases in Poisson's ratio were seen along both curves as the displacement increases. The

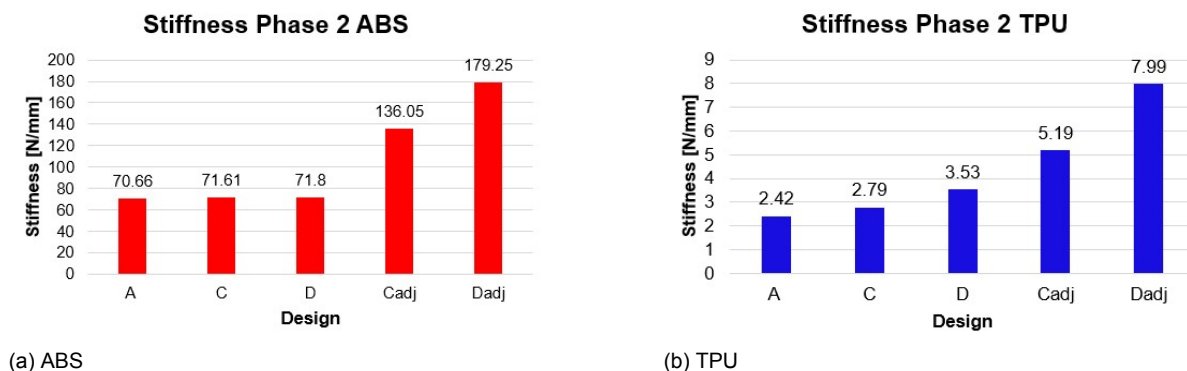


Figure 4.23: Stiffness phase 2 for both materials (axes differ).

non-linear behavior of the Poisson's ratio curve is a consequence due to the response of the material to the applied tensile stress and the subsequent deformation. Similarly, examining the Poisson's ratio curves depicted in Figures 4.2d and 4.15b for the honeycomb design, it is apparent that design D exhibited a linear increase, while design D_{adj} initially demonstrated a linear decrease, followed by an increase as the displacement progressed. This behavior might be attributed to the specific geometrical arrangement and mechanical properties of the honeycomb structure. As the honeycomb design deformed under load, the redistribution of stress within the material might have caused variations in the Poisson's ratio at different stages of deformation.

In Figures 4.8c and 4.19a, the Poisson's ratio curves for phase 1 and phase 2 of the TPU material are presented for the rectangular design. Both curves show a similar behavior, displaying a linear increase in the Poisson's ratio as the displacement increases. This behavior is common in many materials under tensile loading, where they tend to contract laterally while elongating in the axial direction. As the material undergoes deformation, the Poisson's ratio increases linearly until it reaches a certain value. For the designs shown in Figures 4.8d and 4.19b, which represent the honeycomb design for phase 1 and the adjusted honeycomb design for phase 2, respectively, interesting observations can be made. The adjusted design (design D_{adj}) has a lower value for the Poisson's ratio compared to the original design (design D) in phase 1. However, both designs display a linear increase in the Poisson's ratio with increasing displacement. The lower value of the Poisson's ratio for the adjusted honeycomb design may be attributed to the modifications made to the honeycomb structure. These changes could have influenced the distribution of stresses within the material during deformation, resulting in a different Poisson's ratio value compared to the original design. Nevertheless, the fact that both designs exhibit a linear increase in the Poisson's ratio indicates that the material still behaves in a similar anisotropic and nonlinear manner under tensile loading.

In Fig. 4.16, the stress distribution shows that the highest stresses were concentrated near the joints, a pattern consistent with the observations from the first phase. Similarly, for the honeycomb design depicted in Fig. 4.17, the highest stresses were primarily localized at the joints and the vertical walls of the cell. This stress concentration behavior is similar to what was observed in the first phase. For the TPU material illustrated in Figures 4.20 and 4.21, the contour plots displaying the deformed shapes and the associated stress patterns exhibited similarities to those observed in the first phase.

4.8. Results phase 3 ABS

For phase 3, design C_{mod} was subjected to a displacement of 12 mm. This displacement was chosen as the simulated points of failure for the design. Fig. 4.24 depicts the load-displacement curve along with the corresponding Poisson's ratio-displacement curve.

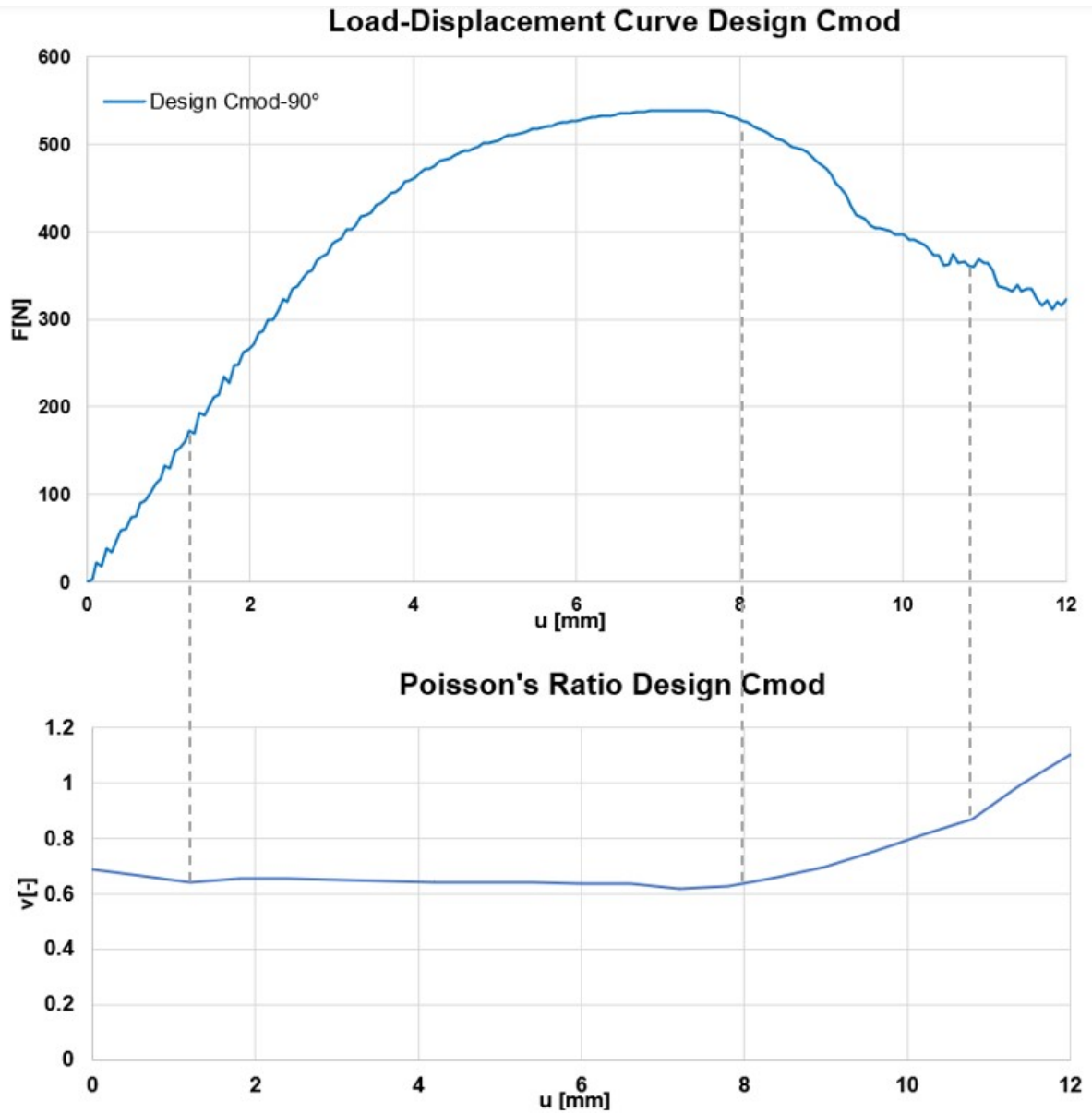


Figure 4.24: Load-displacement curve and Poisson's ratio-displacement curve design C_{mod} with ABS reinforcement.

4.8.1. ABS design C_{mod}

Fig.4.25 showcases the contour plots for design C_{mod} , with a displacement of 12 mm applied. The simulated fracture model is presented in Fig.4.25d. This Figure clearly shows that the highest stresses (highlighted in red) were concentrated on the inner side of the vertical wall of the cell.

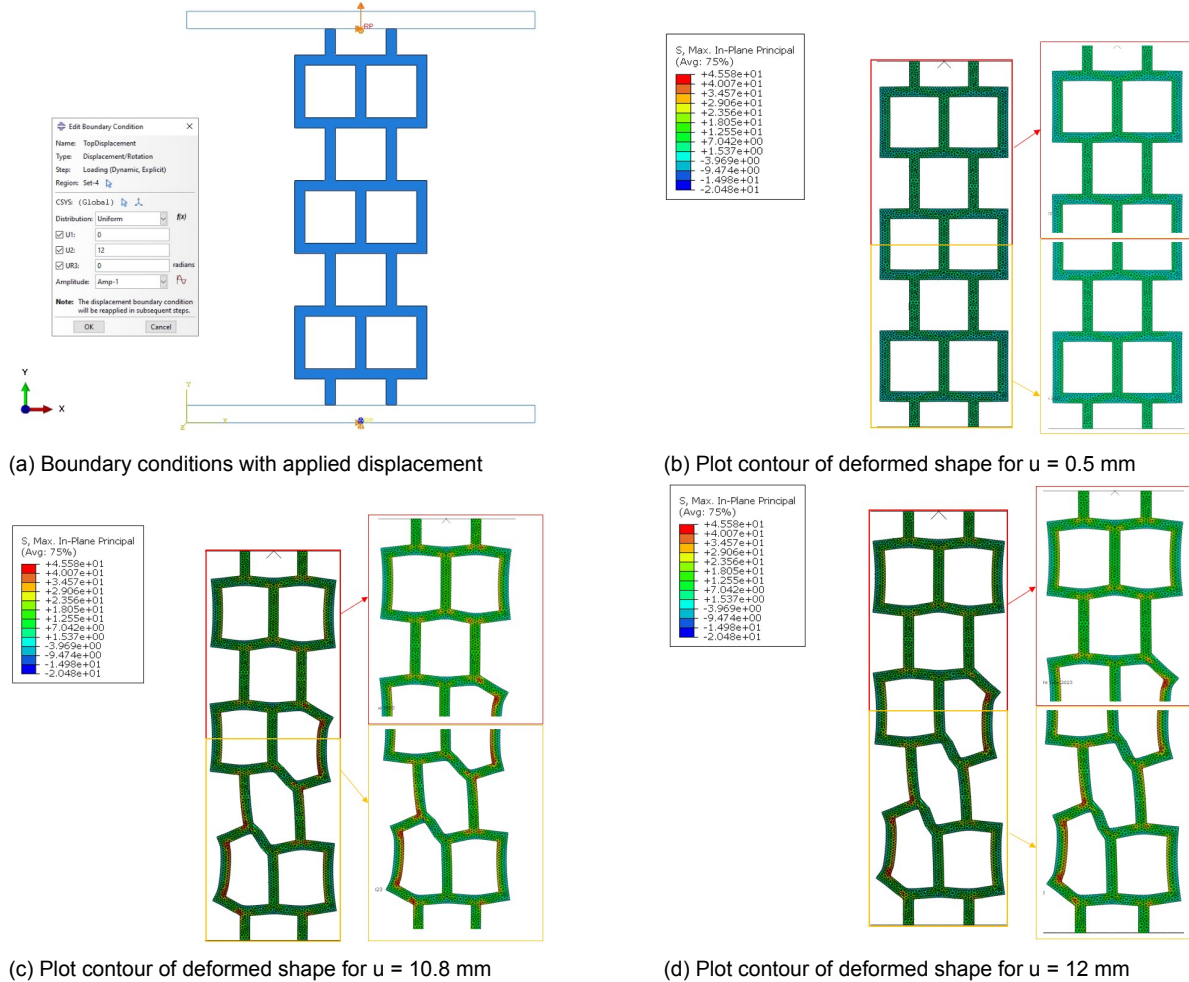


Figure 4.25: Boundary conditions and contour plots of deformed shapes.

4.9. Results phase 3 TPU

Similarly to the previous phases for the TPU material, a uniform displacement of 35 mm was assigned to the modified design in phase 3. Furthermore, Fig. 4.26 illustrates the load-displacement curve along with the corresponding Poisson's ratio-displacement curve.

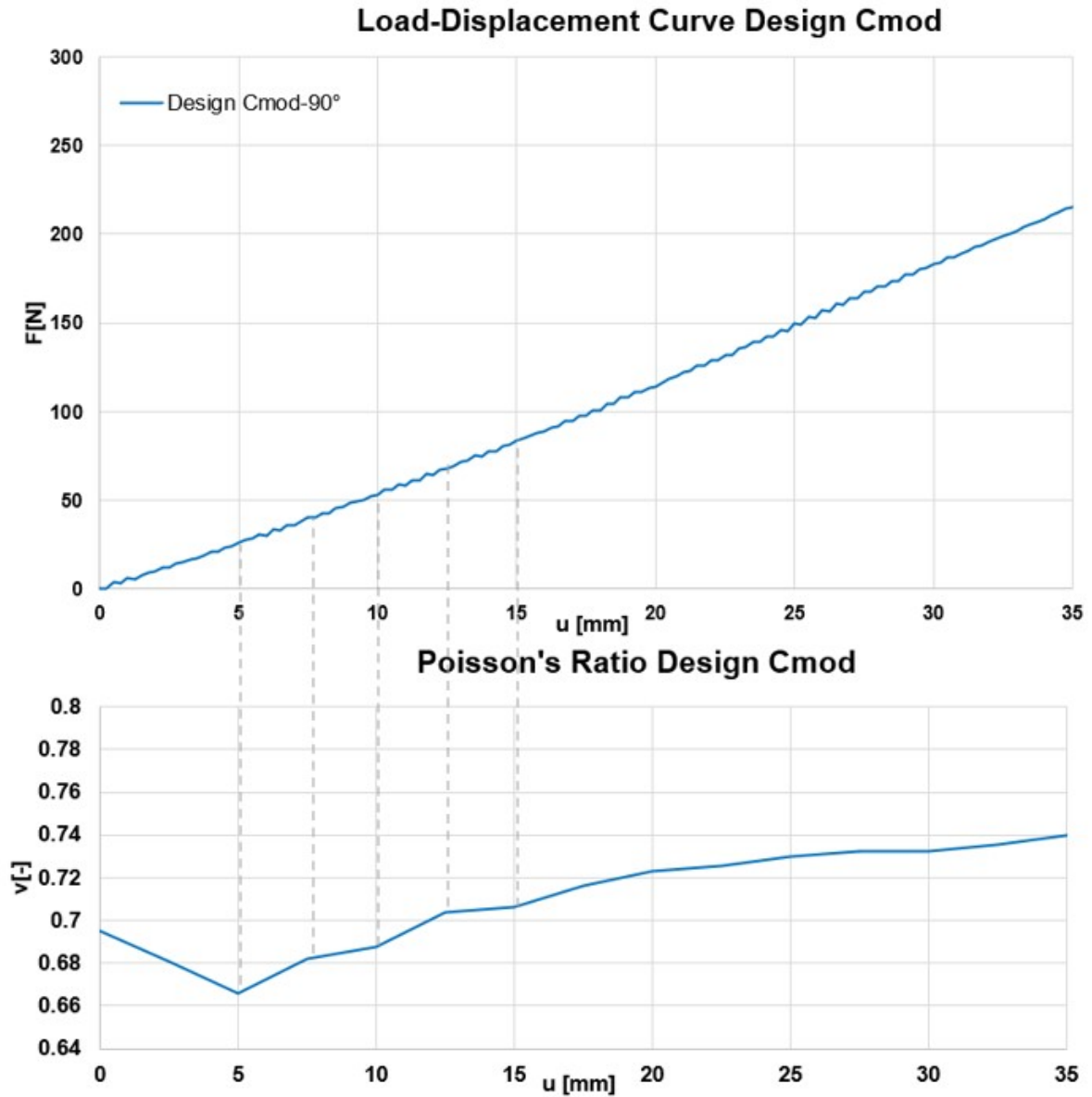


Figure 4.26: Load-displacement curve and Poisson's ratio-displacement curve design C_{mod} with TPU reinforcement.

4.9.1. TPU design C_{mod}

Displayed below are the contour plots for design C_{mod} using the TPU material. As observed in the previous phases, the rectangular shape transforms into a honeycomb configuration. The areas of highest stress were concentrated near the joints, indicated by red in Fig. 4.27d.

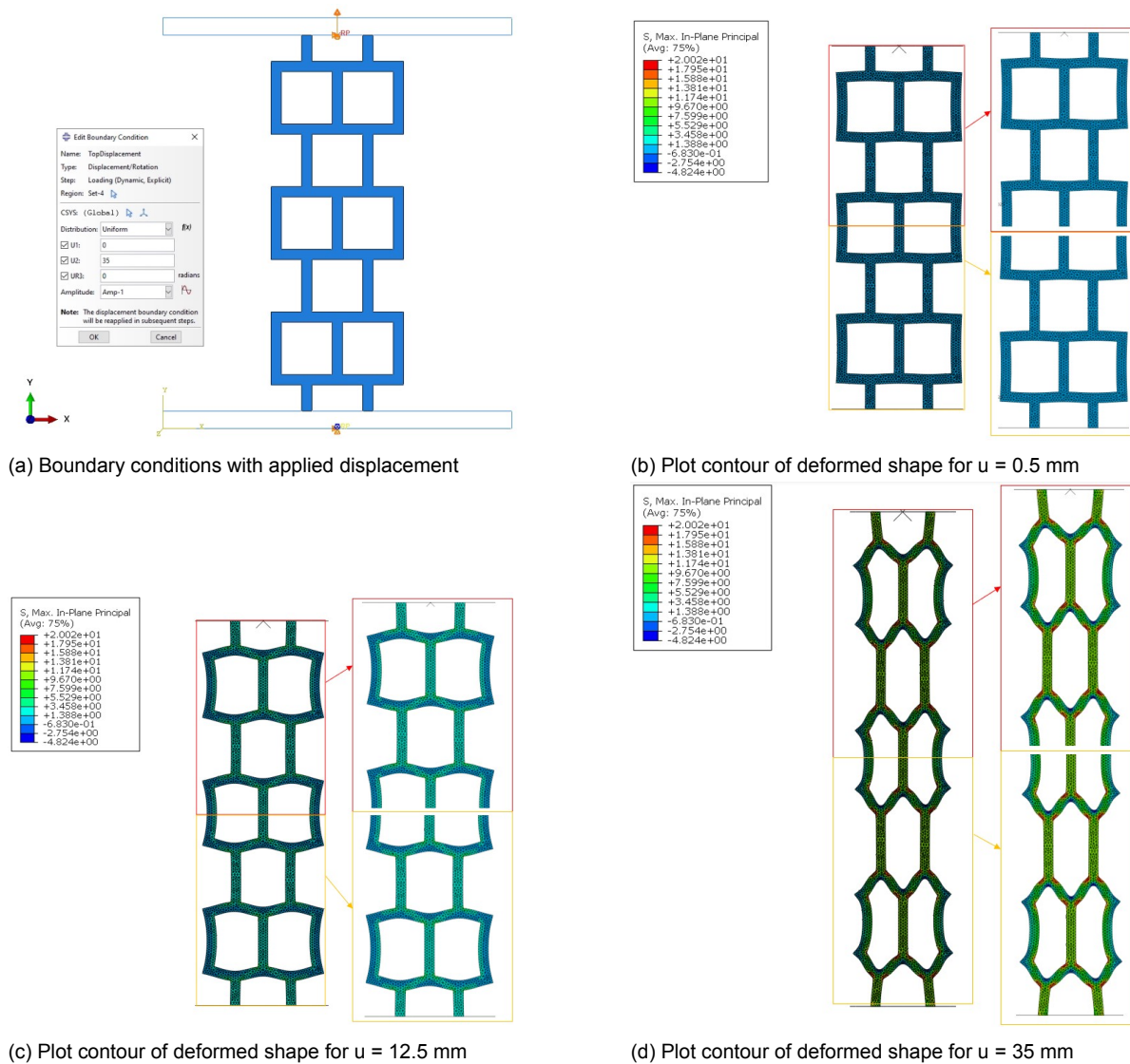


Figure 4.27: Boundary conditions and contour plots of deformed shapes.

4.10. Analyzing results and discussion phase 3

In the discussion of design C_{mod} , it is evident that the ABS material maintains a higher stiffness compared to the TPU material, consistent with the findings from the previous phases. Fracture was not observed for the TPU material during this phase either, further demonstrating its flexibility. The Poisson's ratio for design C_{mod} was positive, indicating its non-auxetic behavior. For the ABS material, the Poisson's ratio curve remained constant until the point of fracture, after which it increased linearly (Fig. 4.24). After reaching the point of fracture, the material underwent more localized deformation and stress concentration, leading to an increase in Poisson's ratio in a linear manner. This behavior is commonly observed in materials that undergo significant deformation and failure, resulting in non-uniform and localized strain distribution. In contrast, the TPU material exhibited a decrease in Poisson's ratio at the beginning of the displacement, followed by a subsequent linear increase (Fig. 4.26). Regarding stress levels, the ABS material exhibited significantly higher stresses, approximately 2.25 times greater than those observed in the TPU material. The highest stresses for the ABS material were observed near the joints and the vertical walls of some cells (Fig. 4.25). In the case of the TPU material, vertical displacement resulted in the transformation of the rectangular design into a stretched-out honeycomb configuration, similar to previous phases. The highest stresses were again located near the joints, as illustrated in Fig. 4.27. These critical areas of stress accumulation need further consideration in the analysis of structural performance.

4.10.1. Comparison phase 2 and 3

The adjusted design had a length of 100 mm, while the modified one had a length of 108 mm. However, despite the difference in length, the volume of the designs remained the same. When comparing design C between phase 2 and phase 3 for the ABS material (Fig. 4.28a), the stiffness values showed relatively minor differences. Even so, there were noticeable differences in the modified and adjusted designs close to fracture. The modified design experienced fracture much earlier than the adjusted design. In the case of the TPU material, as shown in Fig. 4.28b, both the modified and adjusted designs started with similar stiffness values. However, the modified design exhibited linear stiffness increase, whereas the adjusted design started entering the plastic stage, indicating different mechanical behaviors under loading. Upon comparing Poisson's ratio values for phase 2 and phase 3 in ABS and TPU materials, a notable pattern emerged. It became evident that an increase in cell size corresponded to a simultaneous increase in Poisson's ratio. In other words, larger cell sizes exhibited higher Poisson's ratios for both ABS and TPU. This phenomenon points to the significant role that size plays in influencing the mechanical properties of the materials.

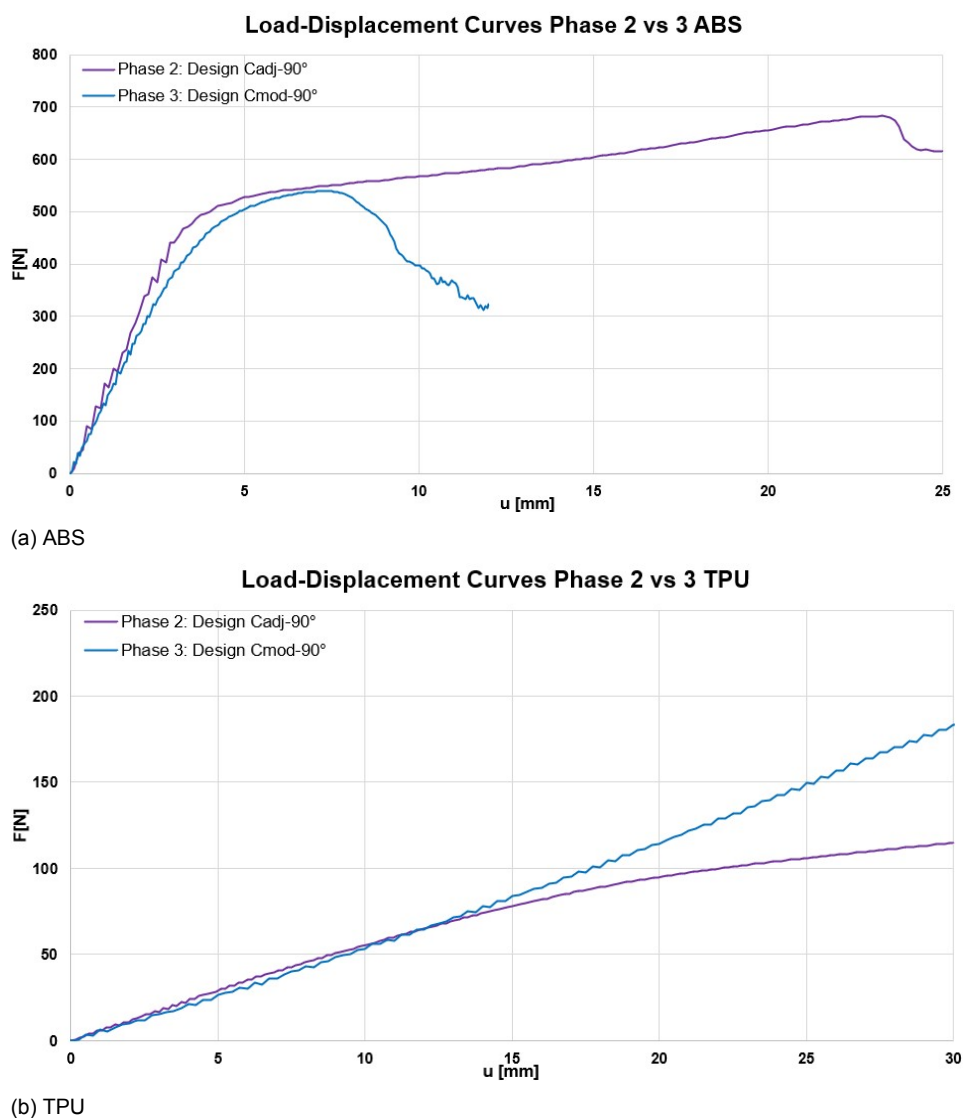


Figure 4.28: Load-displacement curves Phase 2 vs 3 (values on the y-axis differ).

4.11. Summary of numerical study

Design A and B clearly displayed a negative Poisson's ratio, demonstrating their auxetic behavior, which is defined by lateral expansion under tensile loading. In contrast, design C and D showed a positive Poisson's ratio, indicating non-auxetic behavior, with predicted lateral contraction during tensile loading. It was observed that the ABS material reached fracture, while the TPU material did not. ABS demonstrated a notable high load-bearing capacity and resistance to deformation, along with good elongation at break, as supported by the literature. In contrast, TPU demonstrated a relatively low load-bearing capacity but remarkable ductility. These distinct mechanical behaviors highlight the inherent differences between the two materials in terms of strength and deformation characteristics.

As mentioned earlier, the TPU material is highly ductile, allowing it to deform without experiencing fracture. When the re-entrant structure was subjected to lateral stretching, it transformed into a rectangular structure, and with further simulation, eventually evolved into a honeycomb structure, which is consistent with findings from the literature review. This behavior highlights the remarkable adaptability and transformation capabilities of the TPU material un-

der different loading conditions.

Regarding stress levels, the ABS material exhibited significantly higher stresses, approximately five times greater than those observed in the TPU material during the first two phases. In the third phase, this difference reduced to a factor of approximately 2. This difference in stress levels can be associated with the ability of ABS to withstand more force than TPU.

In conclusion, the numerical study provided valuable insights into the mechanical responses of various 3D printed reinforcing designs under different loading conditions. This study predicts that the ABS reinforcement will enhance the strength of the composite, whereas the TPU reinforcement will enhance the ductility of the composite. The findings can guide material selection, design optimization, and reinforcement strategies for different applications, contributing to the advancement of materials engineering and structural design in various fields. The upcoming chapters delve into the experimental study employed in this thesis.

5

Experimental Study: Method and Setup

This chapter outlines the experimental setup utilized for this study, including the material properties of the reinforcement and their designs. The experimental investigation was conducted in three distinct phases. In the first phase, only the angle was varied to understand its impact. The second phase involved equalizing the reinforcing volume. In the third phase, the designs were enlarged to allow the fibers to embed easier within the reinforcing designs, which was identified as a significant challenge during the previous two phases.

In addition to the designs and reinforcements, a detailed description of the cementitious matrix material was provided. Furthermore, the process of casting and curing the cementitious matrix material was explained, outlining the specific steps and conditions involved in ensuring proper formation and hardening. Moreover, detailed information was provided regarding the sample preparation, including the surface treatment techniques used. Lastly, the tensile tests were described, indicating the utilization of an Instron hydraulic testing instrument capable of measuring both the applied force and displacement during the tests.

5.1. Material properties reinforcement

Various reinforcement designs were created using AutoCAD software and subsequently exported to Cura to generate the necessary file for the 3D printer. The reinforcement was fabricated using an Ultimaker 2+ FDM 3D printer. FDM is a rapidly developing prototype technique that makes it possible to quickly produce functional parts with complex geometries. Each reinforcement sample was printed layer-by-layer, starting from the bottom layer to the top layer. ABS and TPU filaments were used as the printing materials. In order to improve adhesion during printing and ease release after cooling, glue was applied to the build plate.

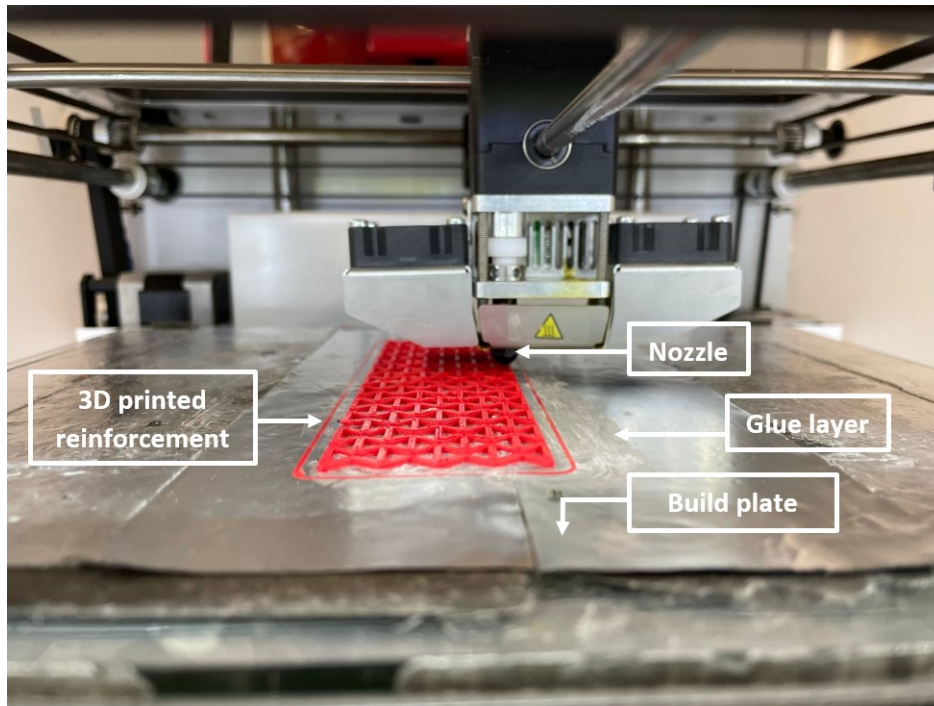


Figure 5.1: Printing setup in the Ultimaker 2+.

The mechanical properties of the printed reinforcement may be subject to variations influenced by printing parameters, as evidenced in the literature. Therefore, it is essential to maintain the constancy of these parameters. Table 5.1 presents the printing parameters used in this study. These parameters were identical for both printing materials.

Printing Parameter	Configuration
ABS temperature [°C]	260
TPU temperature [°C]	235
Top/bottom thickness [mm]	1.2
Nozzle diameter [mm]	0.6
Wall thickness [mm]	1.59
Layer height [mm]	0.15
Print speed [mm/s]	40
Infill speed [mm/s]	55
Infill density [%]	100
Infill pattern	Lines

Table 5.1: Printing parameters of the 3D printed reinforcement.

5.1.1. Reinforcement designs: Phase 1

In this phase, the angle was the only variable modified with the purpose of gaining a better understanding of its impact. Unlike the numerical study, design B with the 52 degree angle was excluded from the experimental study due to the presence of numerous air voids in the composite samples. The sharp angle hindered proper compaction, creating limited space for the fibers to pass through, leading to the formation of excessive air voids. For a visual representation of the air voids, see Appendix C, Fig. C.3. Thus, in this phase of the experimental study, three angles (63, 90, and 117 degrees) were explored. Fig. 5.2 provides the angle, thickness, width, and volume for each design. The centerlines for these designs are depicted in Fig. 5.3.

Fig. 5.4 shows three distinct angle reinforcements that were designed and 3D printed using the Ultimaker 2+. Although both ABS and TPU were used as filament, only ABS (red printing material) is illustrated in the Figure. As depicted in Fig. 5.5, support structures were designed and 3D printed near the ends of the reinforcements to ensure their central positioning within the sample. The height of the concrete samples was 10 mm, and the reinforcements were 5 mm. Therefore, supports of 2.5 mm were designed to position the reinforcement midway.

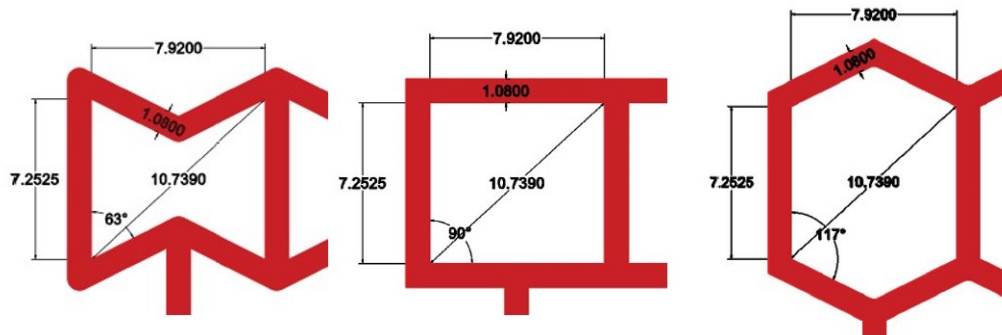


Figure 5.2: Measurements of a unit cell in mm. From left to right: Design A, C and D.

	Design A	Design C	Design D
Angle [°]	63	90	117
Thickness [mm]	1.08	1.08	1.08
Width [mm]	37.08	37.08	37.08
Volume [mm ³]	5683.98	4517.61	3924.54

Table 5.2: Dimensions reinforcement Phase 1.

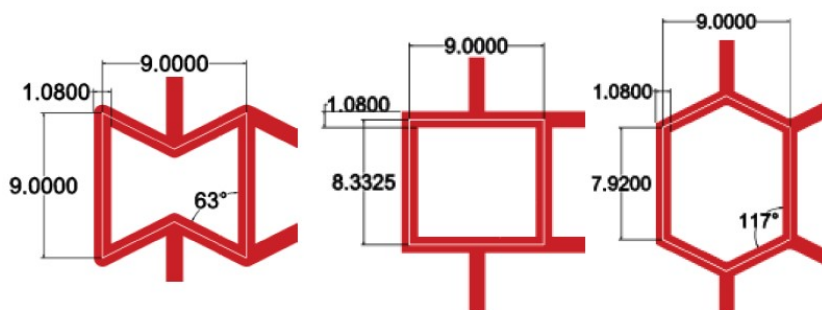


Figure 5.3: Centerline for design A, C and D respectively.

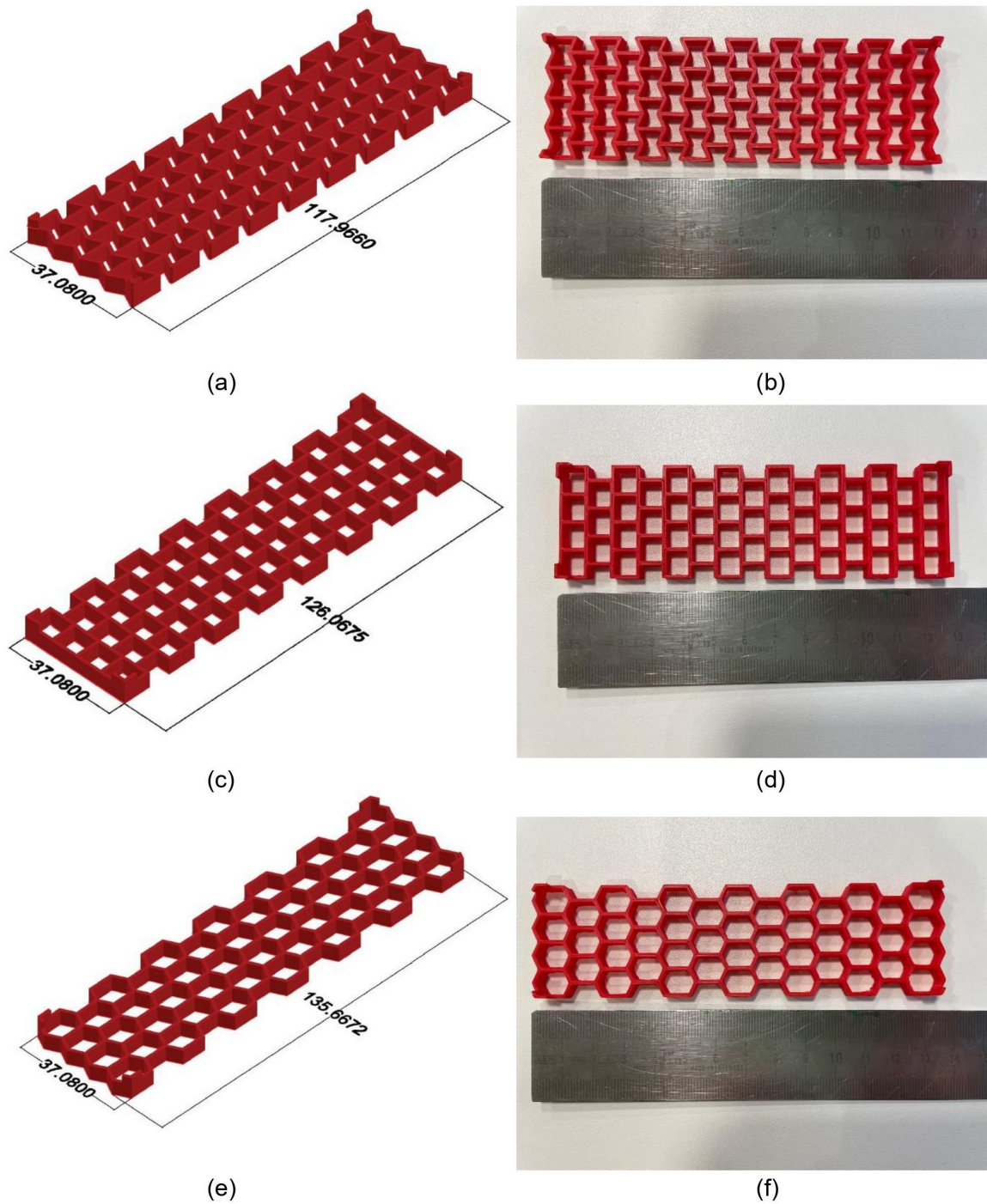


Figure 5.4: Different angle designs of 3D printed polymeric reinforcement with their measurements for phase 1. (a) Design A: 63°; (b) Printed reinforcement of design A; (c) Design C: 90°; (d) Printed reinforcement of design C; (e) Design D: 117°; (f) Printed reinforcement of design D.

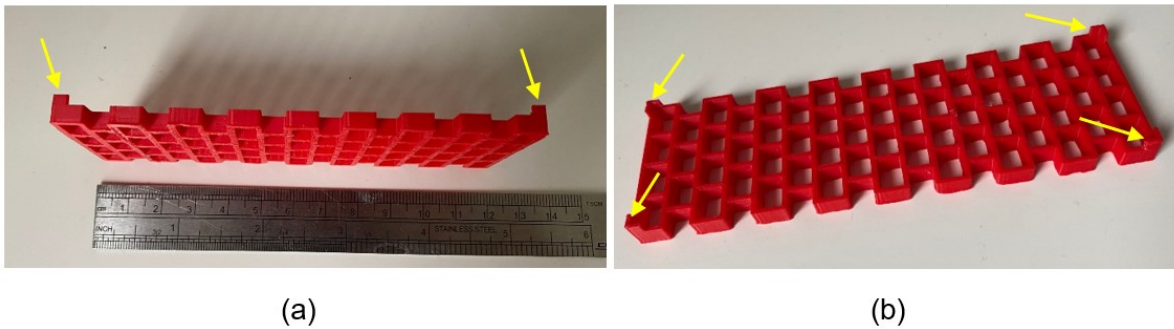


Figure 5.5: Printed supports near the ends: (a) Side view supports; (b) Isometric view supports.

5.1.2. Reinforcement designs: Phase 2

The reinforcing volume of the various designs was equalized during this phase. As displayed in Table 5.2, the largest volume was observed for design A with a value of 5683.98 mm^3 . Consequently, the reinforcing volume for designs C and D were adjusted to match the volume of design A. The adjustment involved increasing the thickness of the samples along the centerline, as illustrated in Fig. 5.3 and Fig. 5.6. This resulted in varying dimensions of the unit cell among the designs, which are presented in Table 5.3. Notably, the volumes of all the designs were nearly equal according to the Table.

Fig. 5.7 and Fig. 5.8 showcase the usage of TPU (blue printing material). Remarkably, it can be observed that supports were designed and printed not only near the ends of the reinforcements, but also in the middle. This was due to the lightweight nature of TPU, which caused bending in the middle section of the reinforcement due to the self-weight of the material. The presence of the additional supports can be identified in the Figures 5.7(c) & 5.7(d) and Figures 5.8(c) & 5.8(d) with yellow arrows. These additional supports were only added for the TPU material in all phases.

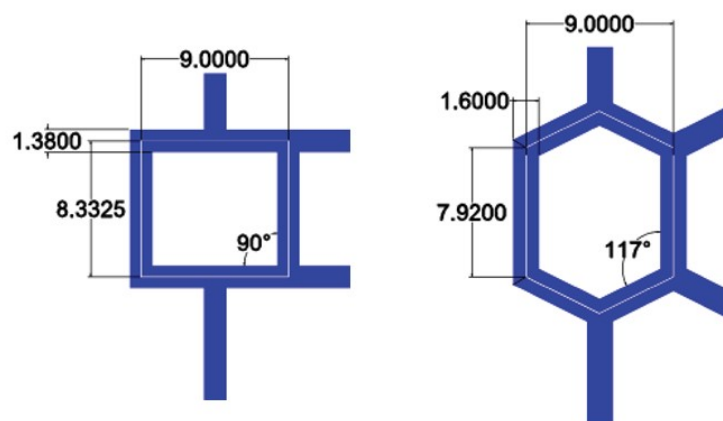


Figure 5.6: Centerline for design C_{adj} (left); design D_{adj} (right).

	Design A	Design C _{adj}	Design D _{adj}
Angle [°]	63	90	117
Thickness [mm]	1.08	1.38	1.60
Width [mm]	37.08	37.38	37.60
Volume [mm ³]	5683.98	5685.57	5682.26

Table 5.3: Reinforcing volume Phase 2.

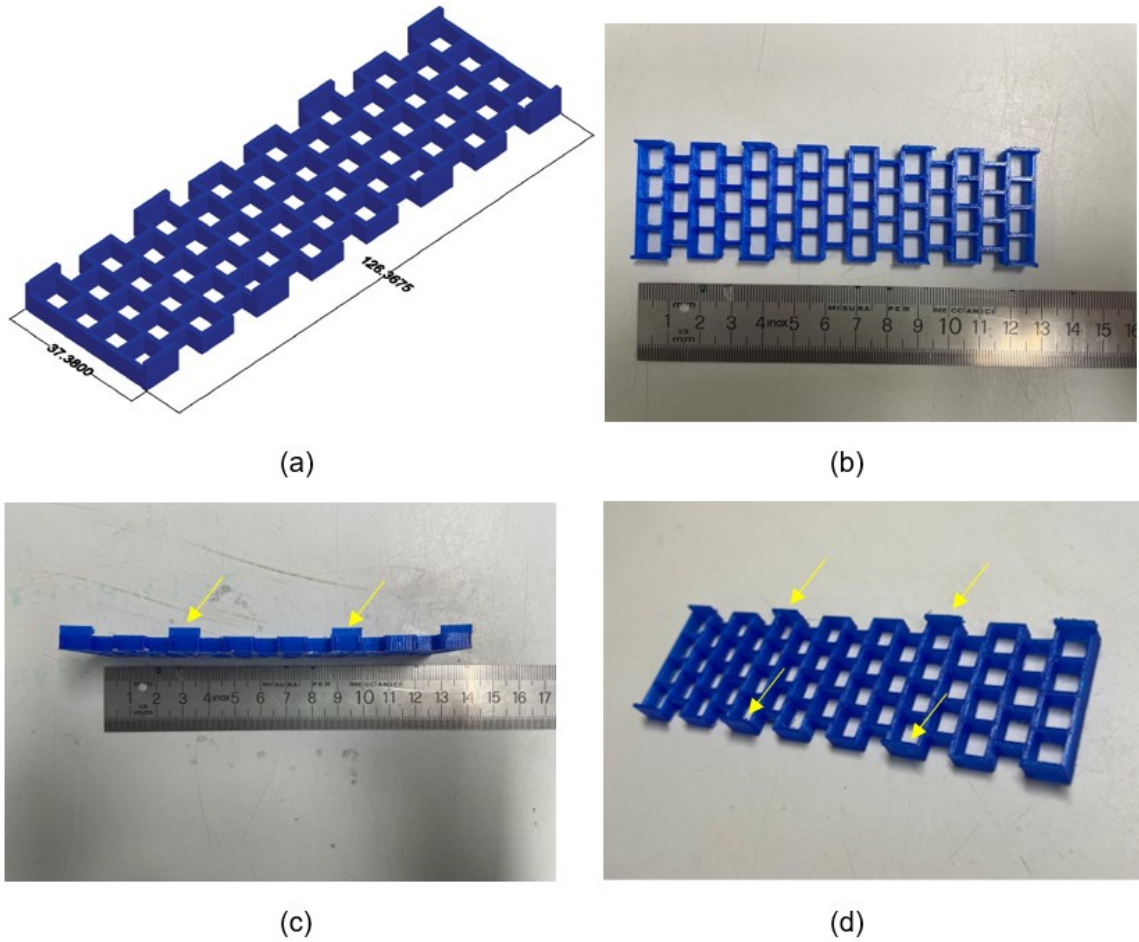


Figure 5.7: Design C_{adj}: 90° (a) Length and width of printed reinforcement; (b) 3D printed polymeric reinforcement; (c) Side view supports; (d) Isometric view supports.

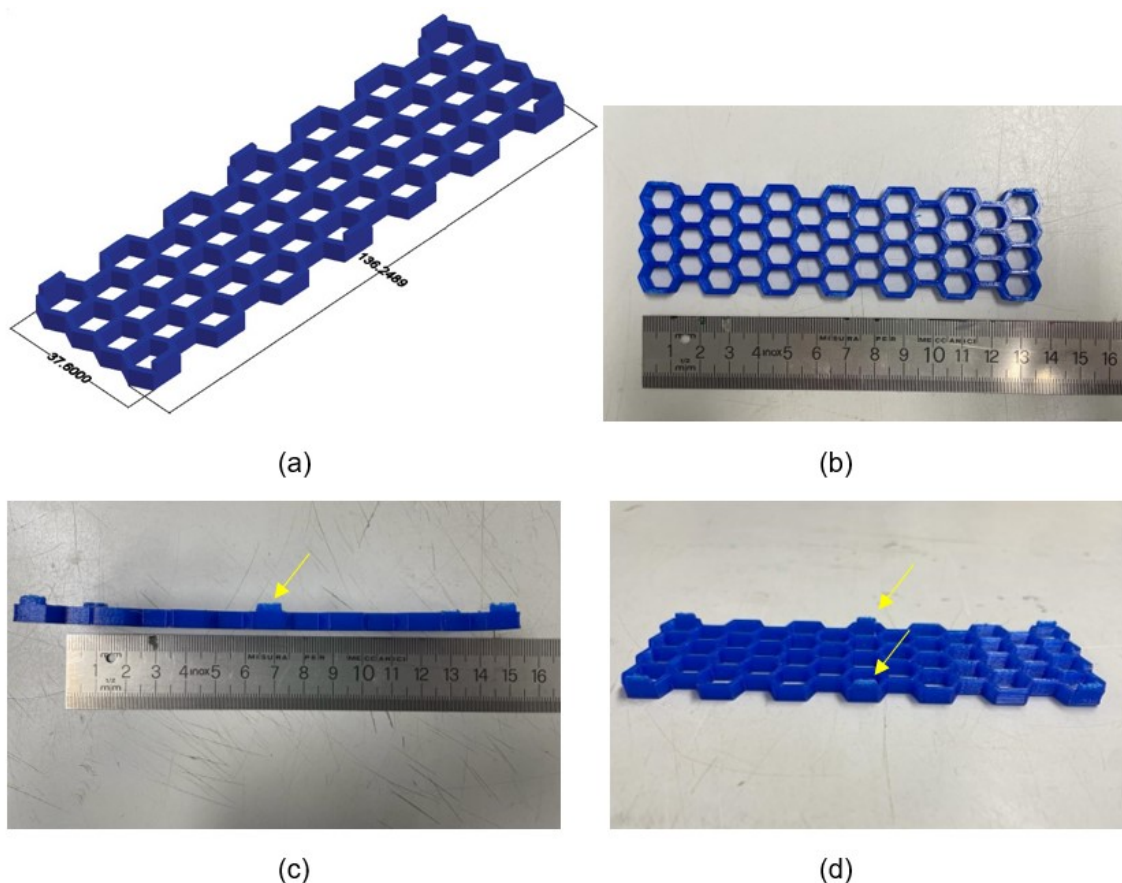


Figure 5.8: Design D_{adj} : 117° . (a) Length and width of printed reinforcement; (b) 3D printed polymeric reinforcement; (c) Side view supports; (d) Isometric view supports.

5.1.3. Reinforcement designs: Phase 3

During this phase of the study, a modification was implemented in the designs to ease the process of embedding fibers. This was accomplished by enlarging design C, thereby creating additional space for the fibers to pass through. Despite this modification, the reinforcing volume remained consistent with phase 2, approximately measuring 5685 mm^3 , as indicated in Table 5.4. The center-line of this design had a length of 18 mm and a width of 18 mm as shown in Fig. 5.9.

Fig. 5.10 showcases the modified reinforcement that was designed and subsequently 3D printed. In this Figure, only the material TPU was illustrated. By implementing these modifications and closely examining the resulting designs, the study aimed to enhance the fiber embedding process and assess the impact of design variations on the overall reinforcement structure.

	Design C_{mod}
Angle [$^\circ$]	90
Thickness [mm]	2.45
Width [mm]	38.45
Volume [mm^3]	5683.3875

Table 5.4: Reinforcing volume Phase 3.

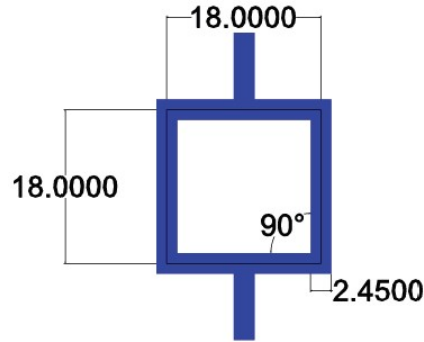


Figure 5.9: Centerline for design C_{mod} .

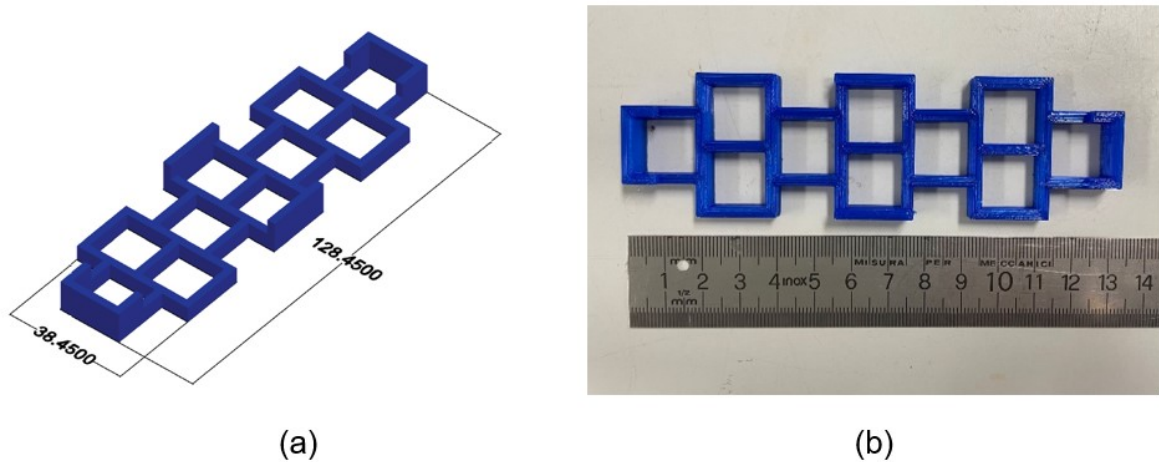


Figure 5.10: Designs of the 3D printed polymeric reinforcement with their measurements for phase 3. (a) Design C_{mod} : 90° ; (b) Printed reinforcement of design C_{mod} .

5.2. Material properties cementitious matrix material

The samples were composed of self-consolidating ECC, which included ordinary Portland Type I cement and fine sand as aggregates. The mixture also consisted of various chemical admixtures, including a viscosity modifying agent (VMA) and a superplasticizer (SP). PE fibers, measuring 6 mm in length, were used as reinforcing fibers. A detailed list of the mixture design is provided in Table 5.5.

CEM I 42.5N	Sand [0.125 - 0.250 mm]	VMA	Water	Superplasticizer (Glenium 51)	PE fibers (volume fraction)
1200	600	0.2	420	14.4	1%

Table 5.5: Self-compacting ECC mix proportion [g/l], adapted from [9].

5.3. Casting and curing

In order to create the necessary form, fresh concrete was prepared and cast into a Styrofoam mold measuring 140 by 40 by 40 mm. First the bottom of the 3D printed models was properly washed with soap and water to remove the glue layer. The models were then glued onto the molds to ensure that they remain midway and do not move during the vibration process. A soft 2-component silicone casting rubber was used to create the glue. The prepared molds

(Fig. 5.11) were set aside to dry while fresh concrete was being prepared. Ultimately, the concrete mixture was poured into the prepared molds. A representation of the mold containing the reinforcement and cementitious matrix is illustrated in Fig. 5.12.

The samples were created using the concrete mix design listed in Table 5.5. The dry ingredients were first carefully measured and manually stirred in a mixing bowl with a spoon. Afterwards wet materials (water and superplasticizer) were added to the bowl. The ingredients were mixed with a Hobart laboratory mixer for one minute. The dry materials that were stuck to the bottom of the bowl were removed using a spoon and then mixed again for another two minutes. Finally the PE fibers were added to the bowl after which mixing continued for three more minutes. The mixture was then poured into the prepared molds and vibrated for a minute. The fresh samples were covered with plastic sheets for two days, after which they were demolded and placed in a curing chamber ($20 \pm 2^\circ\text{C}$, $96 \pm 2\%\text{RH}$) for 26 days. The concrete samples need to be kept at an acceptable temperature and moisture level for an extended period of time so that hydration may produce the appropriate concrete qualities.

A day prior to testing, the samples were cut to their proper size. The length of the different reinforcements varied per design and were displayed in the numerical study. The width and height of the casted samples were kept constant at 40 mm and 10 mm, respectively. The desired sample lengths are listed in Table A.1, while the actual sample dimensions can be found in Tables A.2 and A.3 of Appendix A.

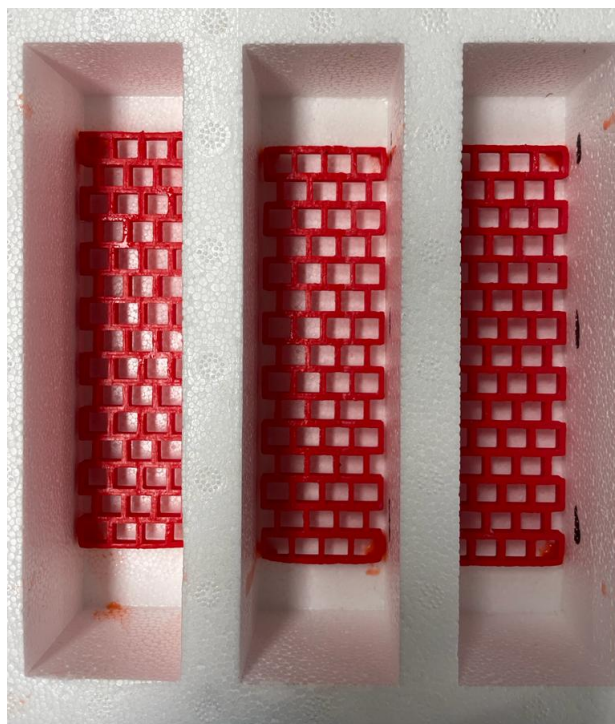


Figure 5.11: Prepared molds.

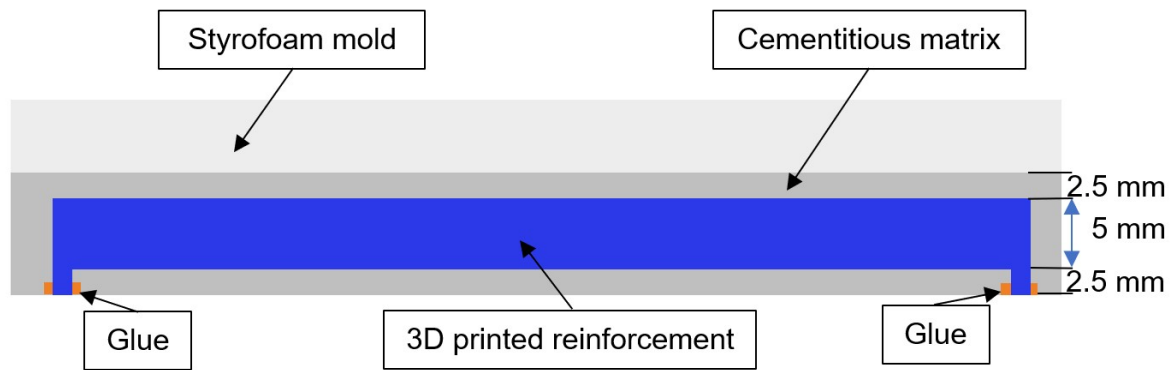


Figure 5.12: Visualization of the mold with the reinforcement and cementitious matrix.

5.4. Sample preparation

It is necessary to prepare the surface of the samples before testing to measure the in-plane deformation. The samples were removed from the curing chamber an hour prior to the tensile tests. To prepare the surface, it was dabbed dry with a paper towel and primed with several coats of white paint. Subsequently, black dots were sprayed onto the white surface, as shown in Fig. 5.13, for the purpose of performing DIC analysis.



Figure 5.13: Prepared samples for testing.

5.5. Uniaxial tensile test

Uniaxial tensile tests were performed on the 28-day-old samples using an INSTRON 8872 servo-hydraulic press. The press functions by applying a precisely controlled force or displacement to the test specimen and recording the material response. A displacement control with a constant speed of 0.005 mm/s was used in this study. Prior to testing, the samples were clamped between two non-rotating rectangular plates to prevent any potential slippage during testing. This was achieved by gluing them to the plates using a mixture of Pedikit 860 A and a liquid hardener. During testing, the bottom plate remained stationary while the top plate moved upwards. A load cell was used to measure the load and two linear variable displacement transducers (LVDTs) were positioned on either side of the prepared sample to measure the displacements. A visualization of the tensile tests on the samples is presented in Fig. 5.14. The tests yielded data on force and displacement, which were used to calculate the stresses

and strains. Tensile strength and strain capacity for each sample were obtained as indicated in Fig. 5.15.

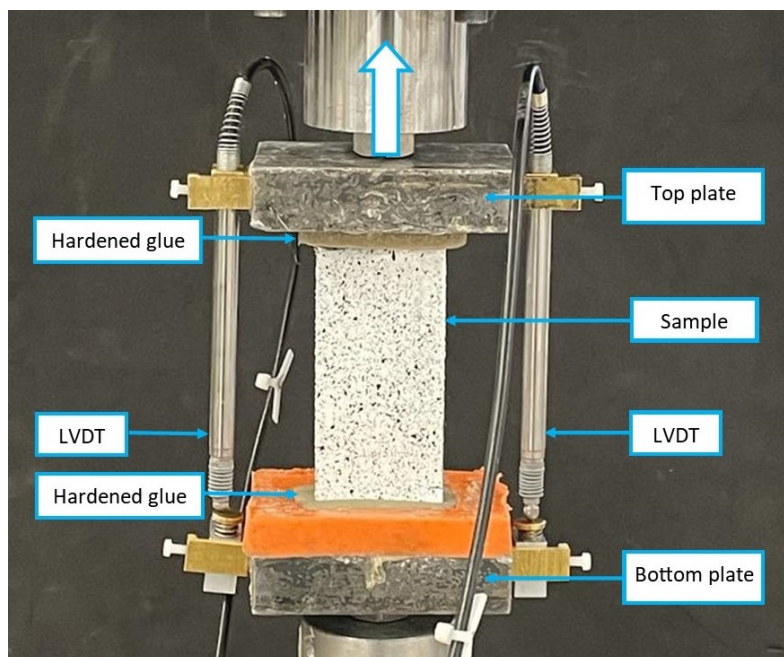


Figure 5.14: Visualization of the uniaxial tensile test.

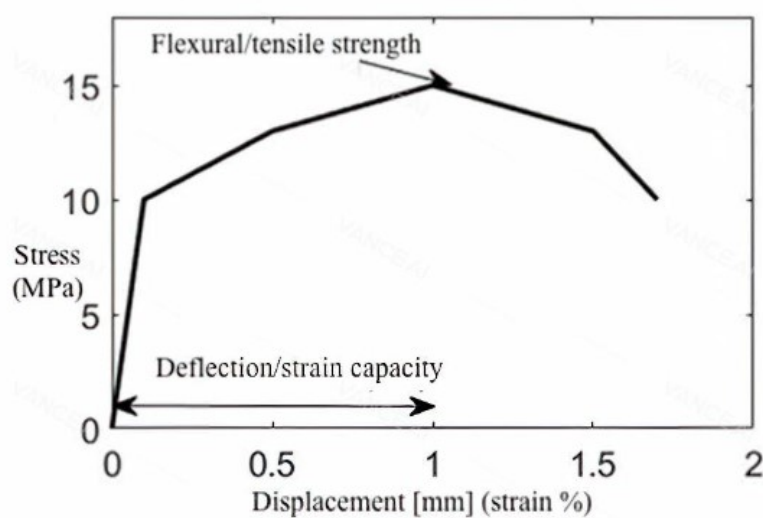


Figure 5.15: Uniaxial tensile test definitions of tensile strength and strain capacity, adapted from [1].

A camera was positioned in front of the sample during the tests to photograph the cracking process. The camera was placed in a manner that allowed it to capture the entire area of interest while maintaining perpendicularity to the surface of the sample, thus avoiding any pseudo strain resulting from out-of-plane motion. The images were taken immediately after the test started and were captured at six-second intervals. Fig. 5.16 displays the camera and sample setup.

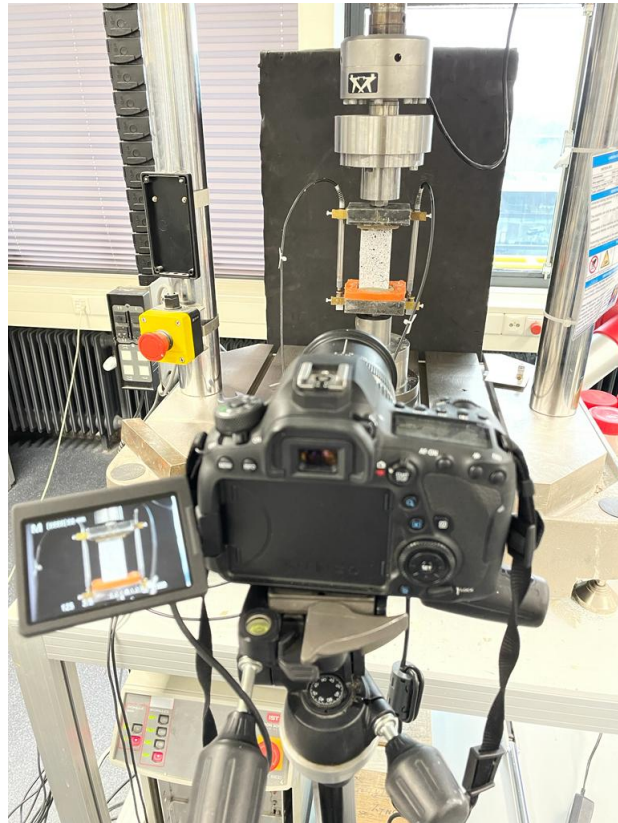


Figure 5.16: Camera placement.

Uniaxial tensile tests were conducted on three identical 3D printed TPU bars to obtain input parameters for the TPU reinforcement required for the numerical study. A small testing machine subjected the bars to displacement control with a constant rate of 0.01 mm/s. The TPU bars had a width of 1 mm and a length of 28 mm. The untested and tested bars can be seen in Fig. 5.17. Additionally, Figures 5.18 and 5.19 provide a top and side view, respectively, of the small tensile testing machine utilized for testing the TPU bars. These figures depict the load cell, clamps, and positioning of the 3D printed bar.

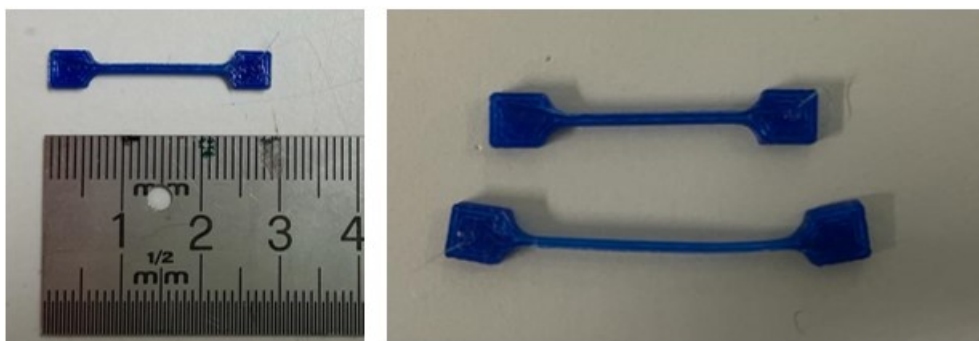


Figure 5.17: Left: Printed TPU bar; Right: untested bar compared to tested bar.

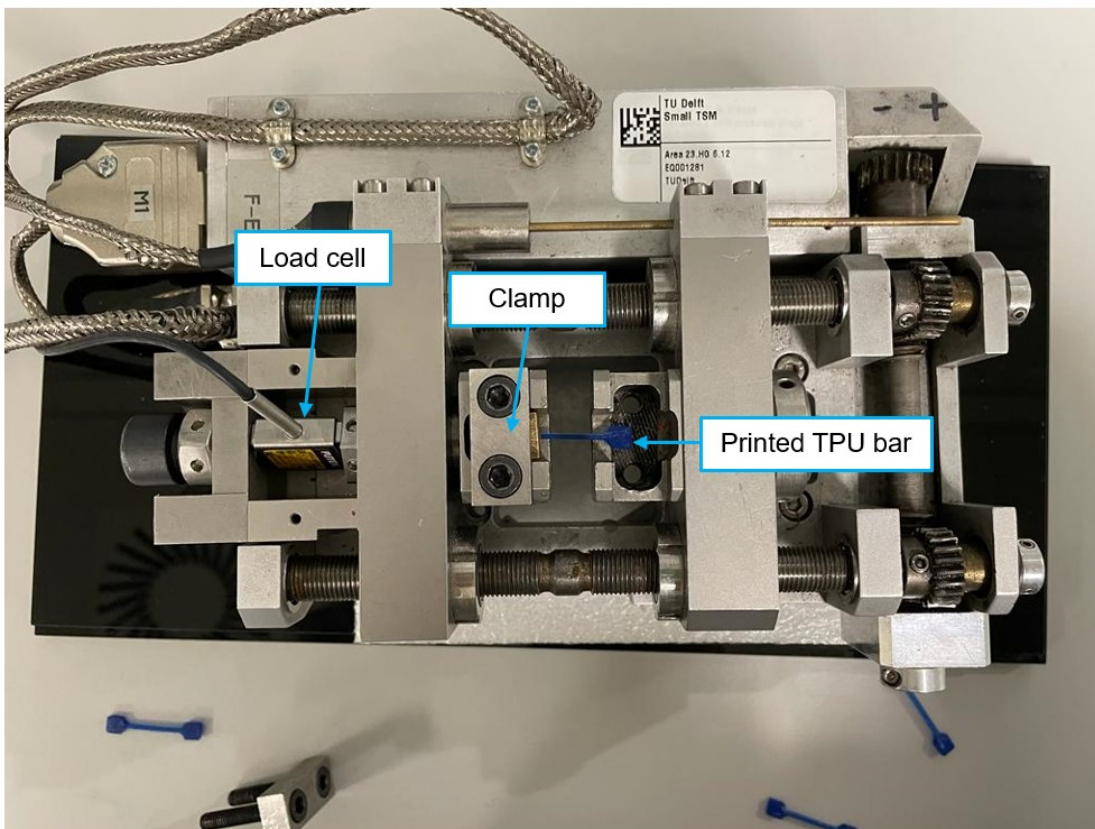


Figure 5.18: Small TSTM top view.

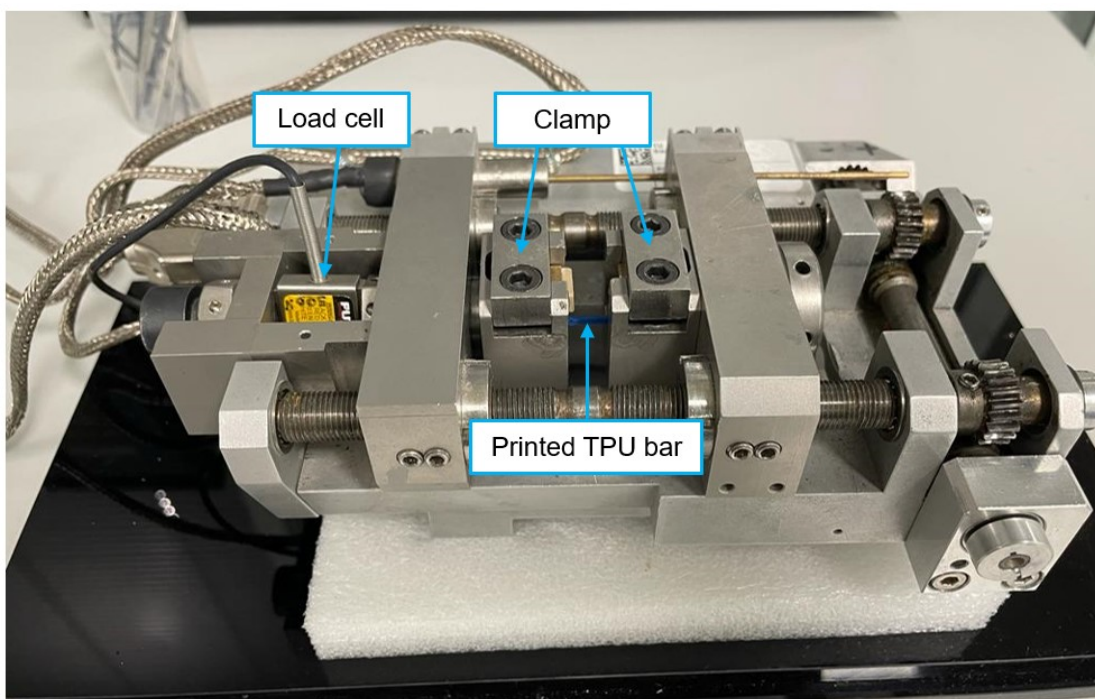


Figure 5.19: Small TSTM side view.

5.6. ABS and TPU bars results

The results of the tests carried out on ABS bars were obtained from Dr. Y. Xu within the context of this investigation. The load-displacement curves for both materials are depicted in Figures 5.20a and 5.20b. Evidently, the ABS bar undergoes fracture, whereas the TPU bar exhibits ductile behavior, a phenomenon that was anticipated based on the findings of the literature review. The load-displacement curves for the bars were averaged and subsequently transformed into stress-strain curves. This graph was then used to derive the parameters characterizing the plastic behavior.

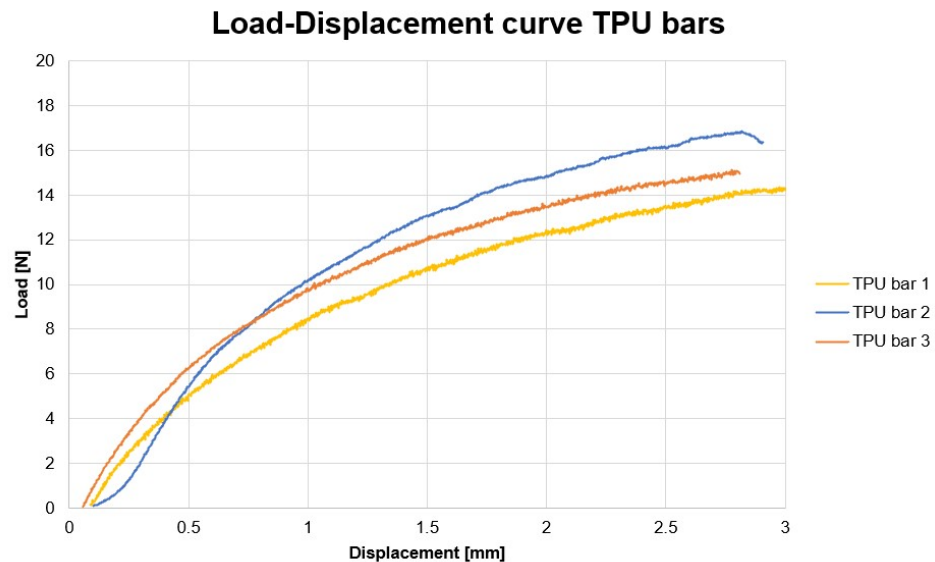
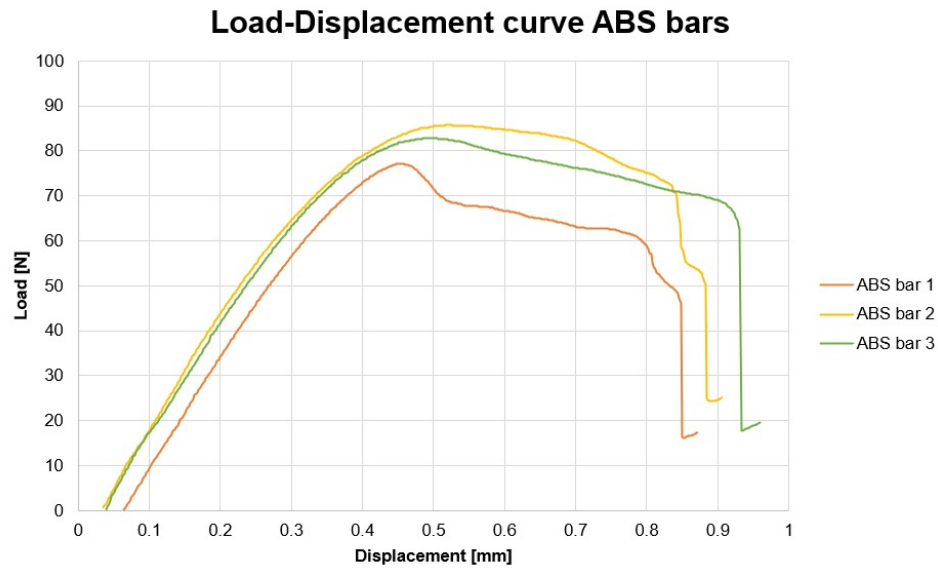


Figure 5.20: Load-displacement curves for the tested ABS and TPU bars (axes are not similar).

5.7. Summary samples

Table 5.6 presents a comprehensive overview of the samples casted and tested in the study. A total of 13 distinct design types were manufactured, with each design type represented by four individual samples. The reinforcing materials utilized in this study were ABS and TPU, with all samples containing PE fibers. Furthermore, the table below provides detailed information on the different design types, including their corresponding reinforcing material and phases. The desired sample lengths are specified in Table A.1, while the actual dimensions of the cut samples can be found in Tables A.2 and A.3 of Appendix A. The results of the experimental study are presented in the next chapter.

Design type	Angle [°]	Material reinforcement	Phase
R	-	-	-
A	63	ABS	1
A	63	TPU	1
C	90	ABS	1
C	90	TPU	1
D	117	ABS	1
D	117	TPU	1
C _{adj}	90	ABS	2
C _{adj}	90	TPU	2
D _{adj}	117	ABS	2
D _{adj}	117	TPU	2
C _{mod}	90	ABS	3
C _{mod}	90	TPU	3

Table 5.6: Summary of the tested samples.

6

Experimental Study: Results and Discussion

The numerical study focused mainly on the reinforcement, whereas the experimental study aimed to assess the performance of the composites. This chapter specifically delved into the behavior of the tested samples under uniaxial tensile tests. The findings obtained from these tests have been thoroughly documented and analyzed within this chapter.

6.1. Overview Experimental study

The objective of the experimental study was to compare the reference samples (without 3D printed reinforcement) with the reinforced samples, as well as to compare the performance of different printing materials (ABS and TPU) and various designs in relation to each other. This comparison was achieved through an analysis of the stress-strain response, focusing on extracting parameters such as strength, strain capacity, and total work of the samples. By quantitatively evaluating these parameters, a comprehensive understanding of the relative performance and characteristics of the different samples, materials, and designs was obtained.

During the uniaxial tensile tests, force-displacement curves were recorded for each tested sample. These curves were subsequently converted into stress-strain curves and analyzed. The resulting stress-strain curves were displayed for all samples, providing a comprehensive overview of their mechanical behavior. Key parameters such as the first cracking strength, tensile strength, strain capacity, and total work were determined for each specimen and compiled in a tabulated format. The total work was calculated at a strain of 0.02, allowing for comparative analysis across the different samples.

For each design type, one representative sample was selected for further analysis using DIC. A stress-strain curve was created for this chosen design, which was then compared with the stress-strain curves of the reference samples, indicated by different shades of gray. Additionally, the crack formation pattern of the chosen sample was visualized, and the corresponding stress-strain curve was plotted with specific data points corresponding to the crack formation stages. A table was included, listing the time, stress, and strain values at each data point. Furthermore, the crack widths of the samples were quantified using DIC, providing additional insights into the damage and deformation behavior of the specimens. A summary of the results are presented in Chapter 6.12.

6.2. Results Reference

The reference specimen, reinforced only with PE fibers and lacking the 3D printed polymeric materials, demonstrated a distinct multiple cracking behavior, as illustrated in Fig. 6.1. This response aligns with the well-established characteristics of ECC. The occurrence of multiple cracks is consistent with the expected behavior of ECC materials, indicating their ability to redistribute stresses and enhance energy absorption through crack formation and propagation. However, it is important to note that some samples exhibited strain softening behavior, indicating that they could not withstand additional stresses beyond the initial crack formation.

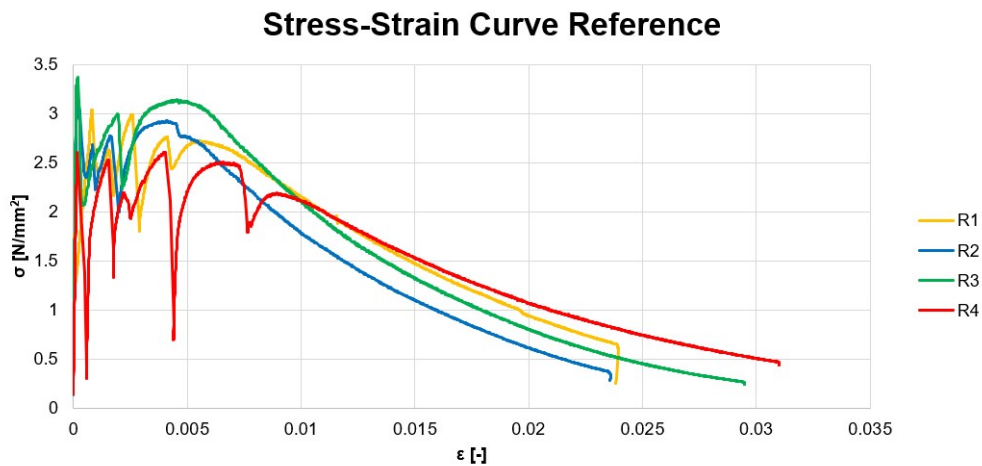


Figure 6.1: Stress-strain curves reference samples.

Table 6.1 presents the initial cracking strength, maximum strength, strain capacity, and total work values for each reference sample that underwent testing. For sample R_1 , the stress-strain curve is shown in Fig. 6.2, with the crack formation pattern indicated alongside. The various stages observed in the stress-strain curve (Fig. 6.2a) are detailed in Table 6.2, which provides information on the time, stress, and strain at each stage. These results offer valuable insights into the behavior and performance of the reference samples during the testing process. The crack formation pattern displayed only a few cracks in relation to the stress-strain curve. Fig. 6.3 displays the location of the cracks alongside the crack width curve. This Figure depicts the crack initiation sequence, showing that crack 1 appeared first, followed by the formation of crack 2. Notably, the crack width of crack 1 reached a stable value of 0.14 mm. As the test progressed, crack 2 continued to grow until the end of the test.

	R_1	R_2	R_3	R_4
First cracking strength [N/mm ²]	1.747	3.164	3.363	2.608
Max tensile strength [N/mm ²]	3.033	3.164	3.363	2.608
Strain capacity [%]	0.081	0.0181	0.0183	0.0166
Total work [J]	1.664	1.329	1.630	2.356

Table 6.1: Test results reference samples

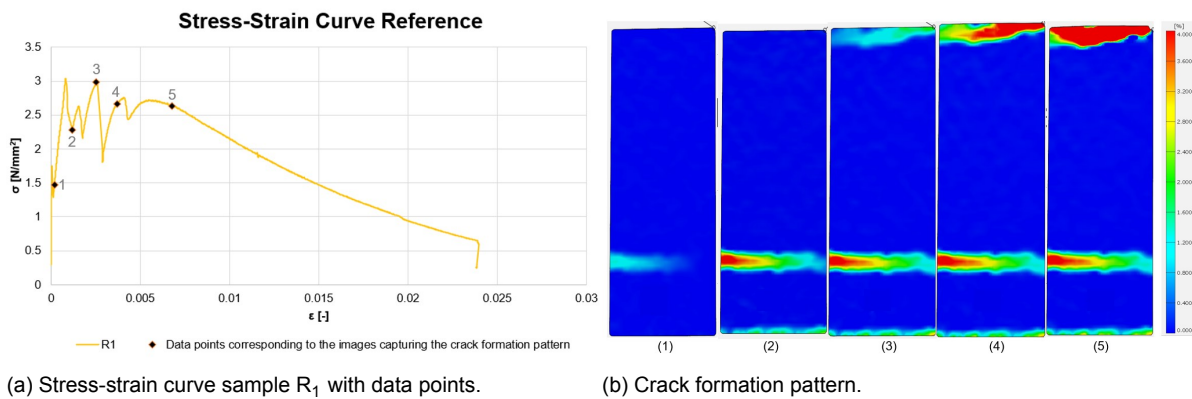


Figure 6.2: Stress-strain curve and crack formation pattern for sample R_1 .

Stage	Time [s]	Stress [N/mm ²]	Strain [-]
1	24	1.47	0.000182
2	60	2.28	0.00119
3	84	2.98	0.00254
4	102	2.67	0.00371
5	150	2.64	0.00676

Table 6.2: Stress and strain corresponding to the different stages.

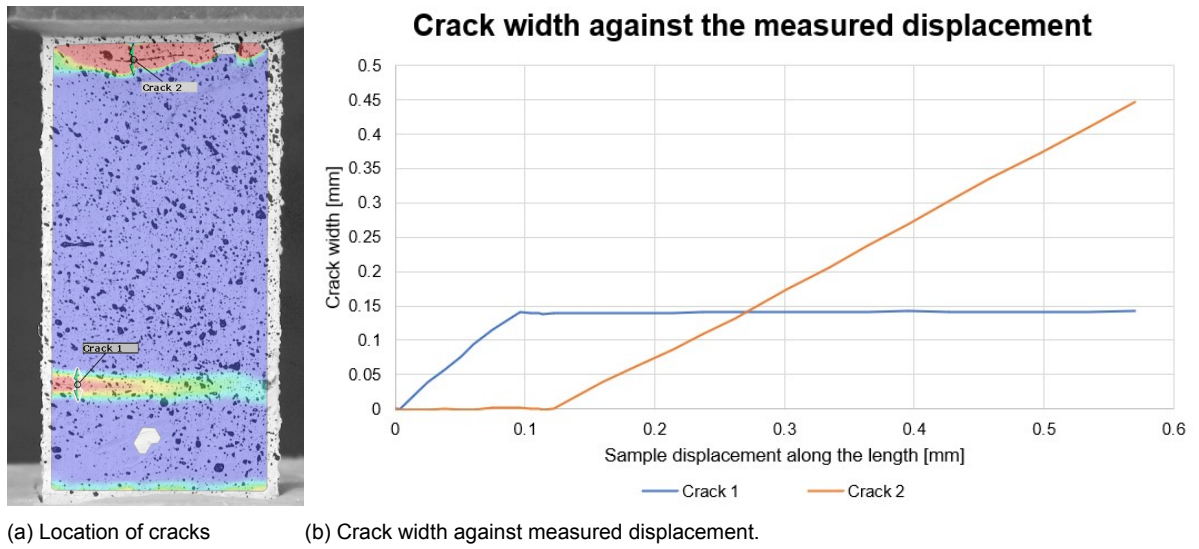


Figure 6.3: Crack location alongside the crack width curve for sample R₁.

6.3. Results Phase 1 ABS

This section presents the results obtained during the first phase of the study focusing on the material ABS. Figures 6.4, 6.8, and 6.12 depict the stress-strain behavior of samples A, C, and D, respectively. Similar to the reference samples, these samples showed strain softening characteristics. However, the reinforced samples showed a characteristic multiple cracking behavior. An important observation from the results was that the strength of the reinforced samples was lower compared to that of the reference samples.

6.3.1. Design A

Fig. 6.4 illustrates the stress-strain behavior of the samples reinforced with design A, the bowtie configuration. The experimental outcomes, encompassing the initial cracking strength, maximum tensile strength, strain capacity, and total work for each tested specimen, are presented in Table 6.3. For a more detailed investigation, sample A₁ was selected. Fig. 6.5 illustrates the stress-strain curve of sample A₁ in comparison to the reference samples. The graph reveals that the strength of the reinforced sample was lower than the reference sample. Furthermore, Fig. 6.6 demonstrates the stress-strain curve for sample A₁, alongside an indication of the pattern of crack formation. The stages identified in the stress-strain curve (Fig.6.6a) are elaborated upon in Table 6.4, offering specific insights into the timing, stress levels, and strains at each stage. Fig. 6.7 presents the cracks observed in the sample, accompanied by a graph that plots the crack width against the measured displacement.

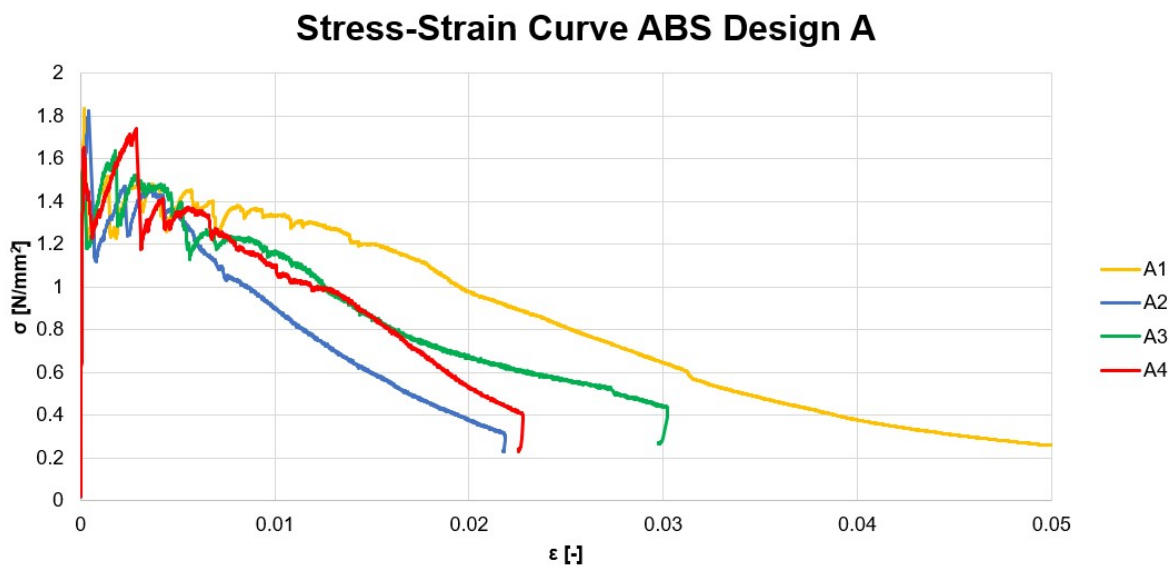


Figure 6.4: Stress-strain curves design A.

	Sample A ₁	Sample A ₂	Sample A ₃	Sample A ₄
First cracking strength [N/mm ²]	1.833	1.825	1.565	1.650
Max tensile strength [N/mm ²]	1.833	1.825	1.636	1.740
Strain capacity [%]	0.0187	0.0433	0.179	0.286
Total work [J]	0.978	0.747	0.800	0.895

Table 6.3: Test results for samples with design A.

Stress-Strain Curve ABS Design A against Reference

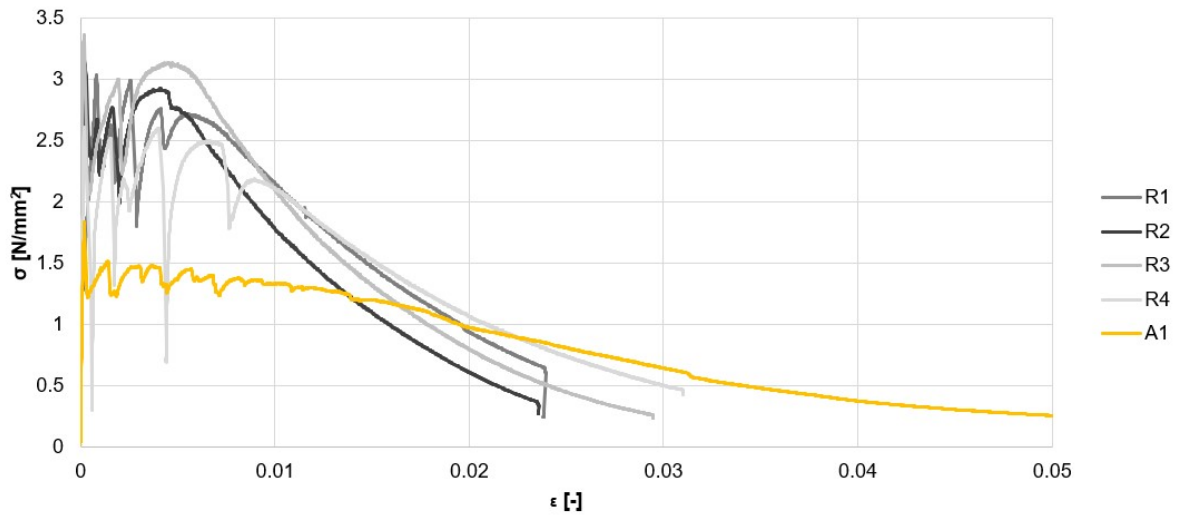
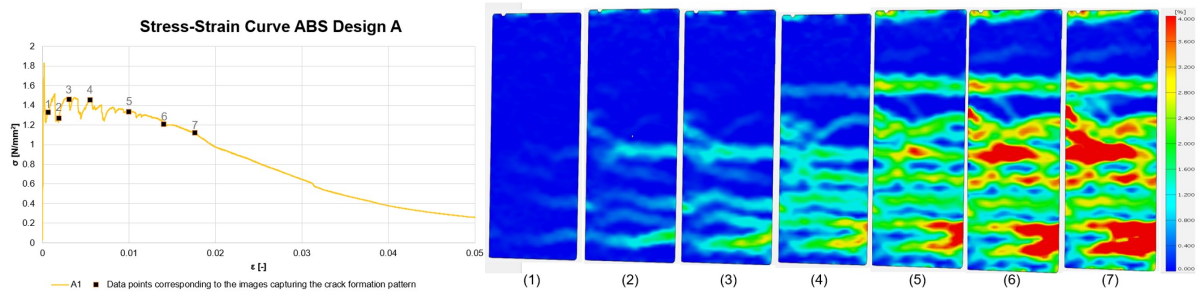


Figure 6.5: Stress-strain curves sample A_1 against reference samples.

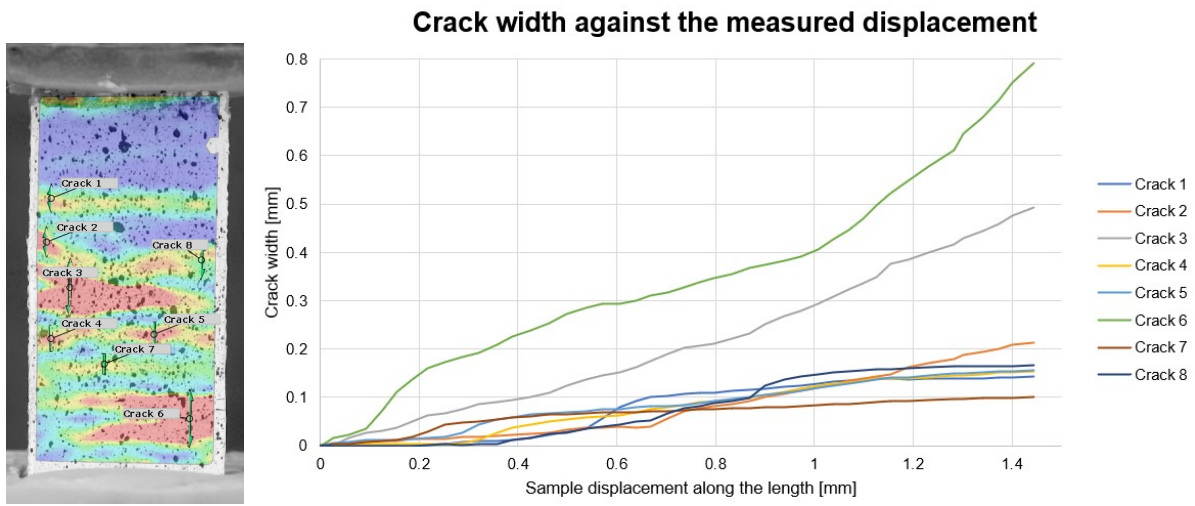


(a) Stress-strain curve sample A_1 with data points. (b) Crack formation pattern.

Figure 6.6: Stress-strain curve and crack formation pattern for sample A_1 .

Stage	Time [s]	Stress [N/mm ²]	Strain [-]
1	60	1.33	0.000689
2	78	1.26	0.00190
3	96	1.46	0.00309
4	132	1.45	0.00553
5	198	1.33	0.0100
6	258	1.21	0.0141
7	312	1.12	0.0177

Table 6.4: Stress and strain corresponding to the different stages.

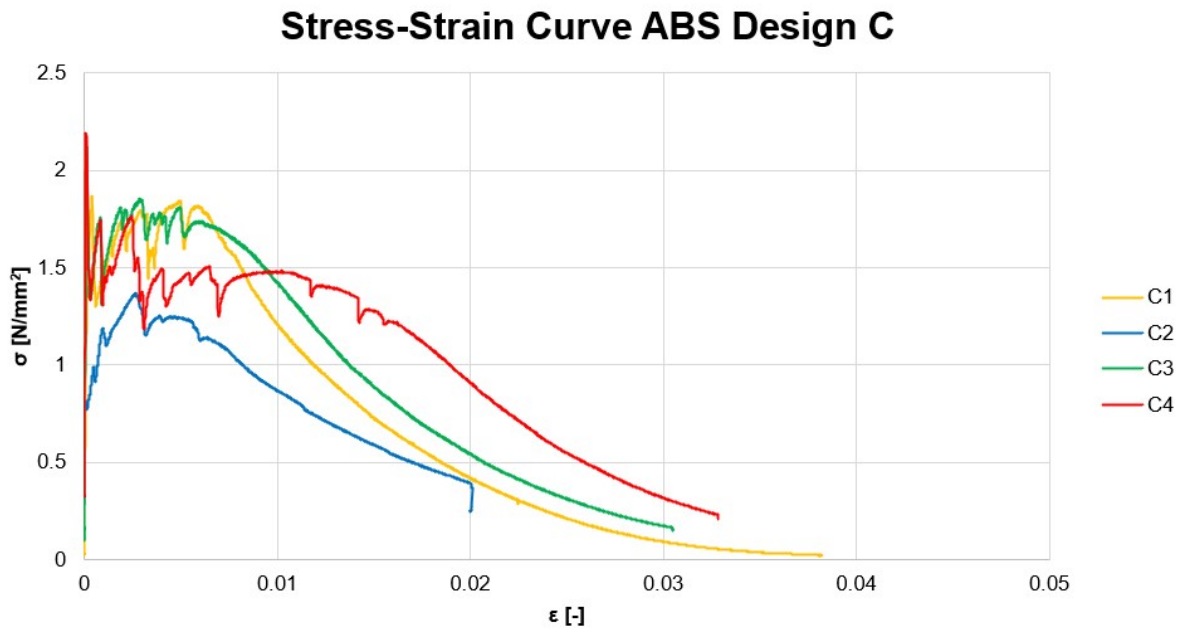


(a) Location of cracks. (b) Crack width against measured displacement.

Figure 6.7: Crack location alongside the crack width curve for sample A_1 .

6.3.2. Design C

Fig. 6.8 presents the stress-strain characteristics of the samples. Table 6.5 summarizes the testing results for each sample reinforced with the rectangular design, including values for initial cracking strength, maximum strength, strain capacity, and total work. Sample C₄ was chosen for further analysis. Fig. 6.9 displays the stress-strain curve for sample C₄ in comparison to the reference samples. It can be observed from the Figure that the strength of the reinforced sample is lower than that of the reference sample. Additionally, Fig. 6.10 exhibits the stress-strain curve with the corresponding crack formation pattern indicated. The distinct stages observed in the stress-strain curve (Fig. 6.10a) are further detailed in Table 6.6, providing specific information on the time, stress, and strain at each stage. The cracks of the sample are shown in Fig. 6.11 which also includes a graph that represents the crack width against the measured displacement.



	Sample C ₁	Sample C ₂	Sample C ₃	Sample C ₄
First cracking strength [N/mm ²]	1.867	0.812	2.119	2.19
Max tensile strength [N/mm ²]	1.867	1.367	2.119	2.19
Strain capacity [%]	0.0420	0.266	0.0115	0.00951
Total work [J]	0.939	0.718	1.193	0.906

Table 6.5: Test results for samples with design C.

Stress-Strain Curve ABS Design C against Reference

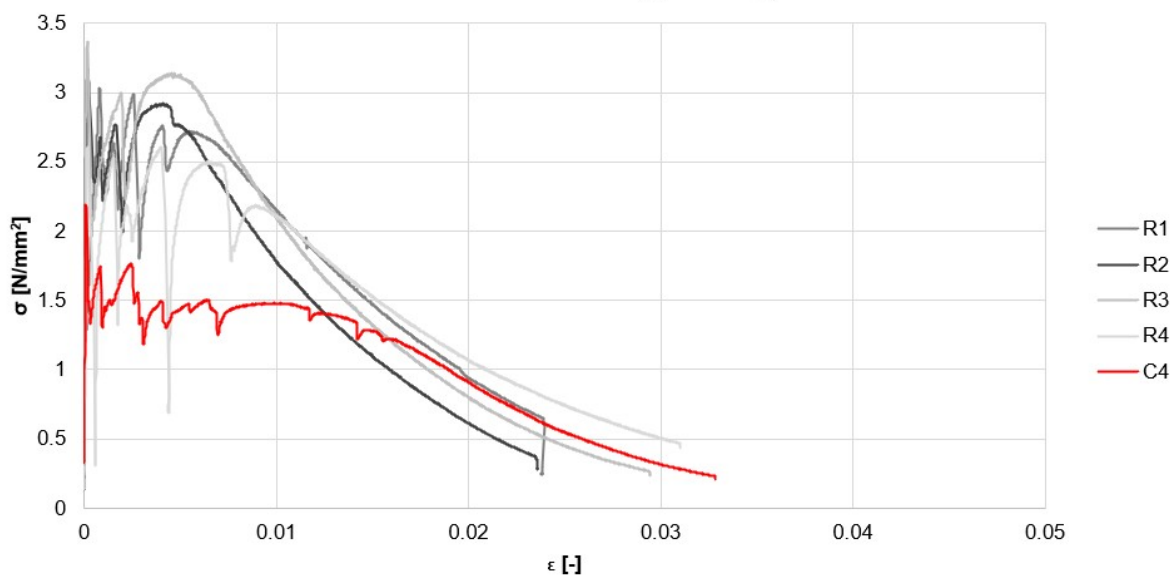
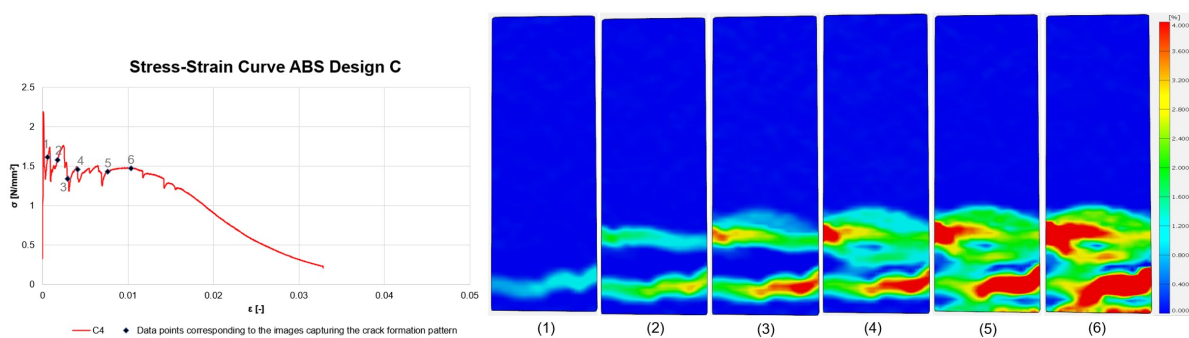


Figure 6.9: Stress-strain curves sample C_4 against reference samples.

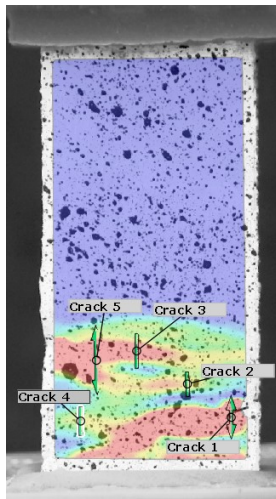


(a) Stress-strain curve sample C_4 with data points. (b) Crack formation pattern.

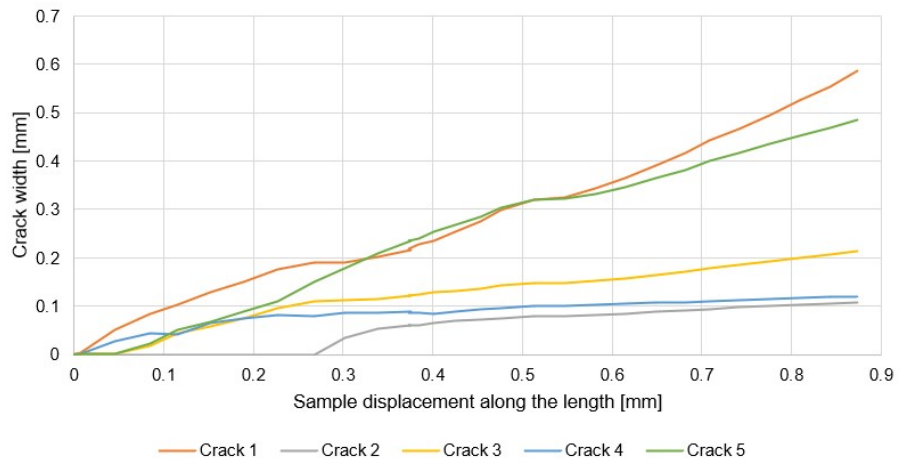
Figure 6.10: Stress-strain curve and crack formation pattern for sample C_4 .

Stage	Time [s]	Stress [N/mm ²]	Strain [-]
1	18	1.61	0.000607
2	36	1.58	0.00176
3	54	1.34	0.00293
4	72	1.46	0.00409
5	126	1.43	0.00765
6	168	1.48	0.0104

Table 6.6: Stress and strain corresponding to the different stages.



Crack width against the measured displacement



(a) Location of cracks. (b) Crack width against measured displacement.

Figure 6.11: Crack location alongside the crack width curve for sample C₄.

6.3.3. Design D

Fig. 6.12 displays the stress-strain behavior of the samples reinforced with design D, the honeycomb configuration. The experimental results for each tested specimen, are presented in Table 6.7. For a more comprehensive investigation, the focus was placed on sample D₃. Fig. 6.5 illustrates the stress-strain curve of sample D₃ in comparison to the reference samples. The plot effectively highlights that the strength of the reference sample surpassed that of the reinforced sample. Furthermore, Fig. 6.13 presents the stress-strain curve for sample D₃, accompanied by the crack formation pattern. The distinct stages showcased in Fig. 6.14a) are elaborated upon in Table 6.8, offering detailed information on the timing, stress levels, and strains at each stage. Additionally, Fig. 6.18 exhibits the detected cracks within the specimen, accompanied by a graphical representation plotting the crack width against the measured displacement. As can be seen in Fig. 6.17, cracks 1 and 2 initially showed a negative crack width.

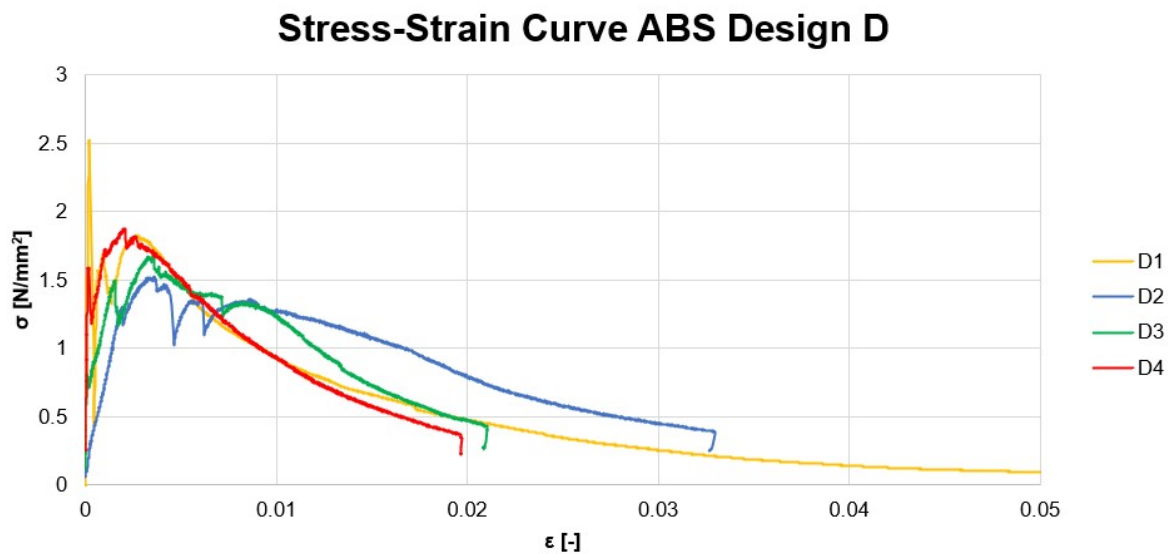


Figure 6.12: Stress-strain curves design D.

	Sample D ₁	Sample D ₂	Sample D ₃	Sample D ₄
First cracking strength [N/mm ²]	2.526	1.303	0.813	1.590
Max tensile strength [N/mm ²]	2.526	1.526	1.675	1.877
Strain capacity [%]	0.0221	0.363	0.359	0.200
Total work [J]	0.985	0.978	0.813	0.896

Table 6.7: Test results for samples with design D.

Stress-Strain Curve ABS Design D against Reference

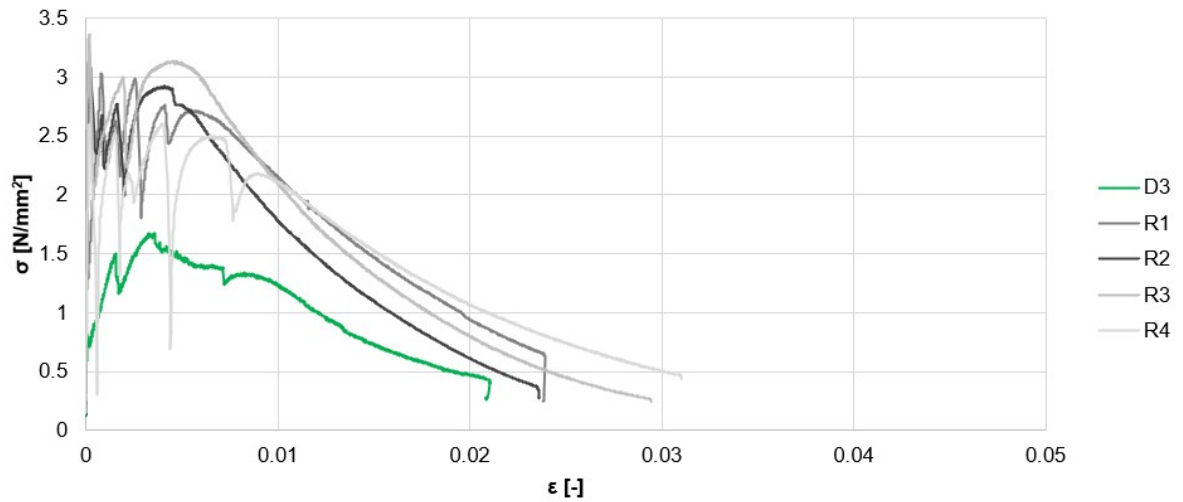
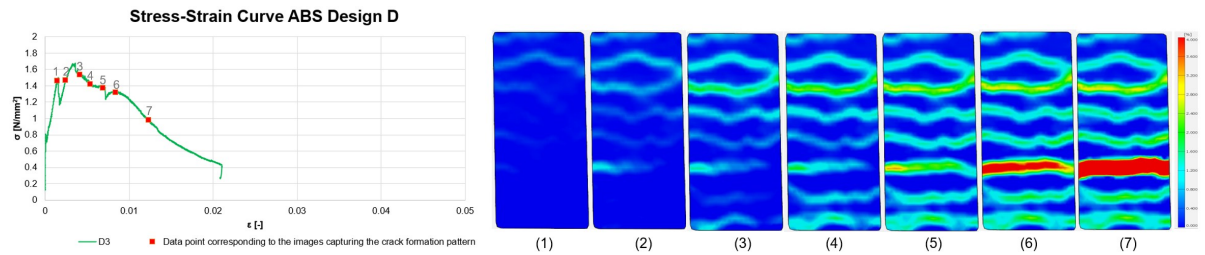


Figure 6.13: Stress-strain curves sample D_3 against reference samples.



(a) Stress-strain curve sample D_3 with data points. (b) Crack formation pattern.

Figure 6.14: Stress-strain curve and crack formation pattern for sample D_3 .

Stage	Time [s]	Stress [N/mm ²]	Strain [-]
1	60	1.462	0.00145
2	78	1.468	0.00245
3	108	1.535	0.00413
4	126	1.419	0.00536
5	150	1.375	0.00690
6	174	1.316	0.00841
7	234	0.982	0.0123

Table 6.8: Stress and strain corresponding to the different stages.

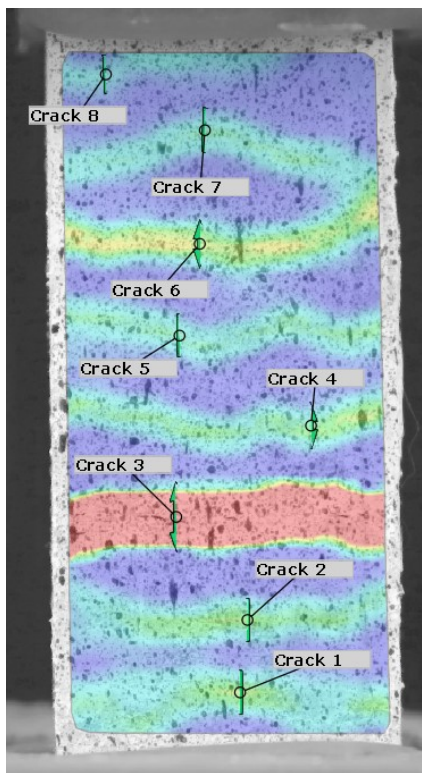


Figure 6.15: Location of cracks.

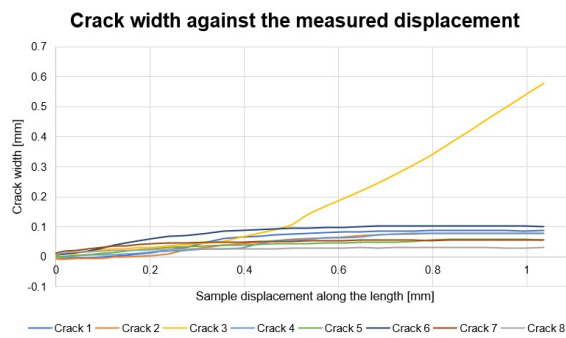


Figure 6.16: Crack width against measured displacement.

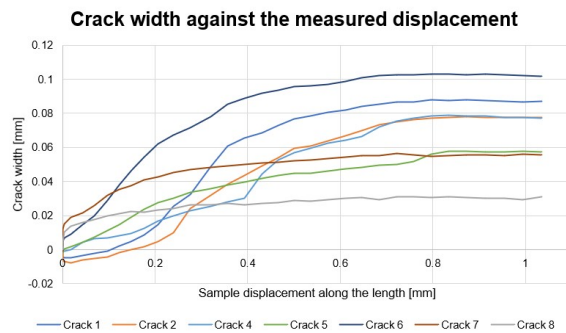


Figure 6.17: Crack width against measured displacement without crack 3.

Figure 6.18: Crack location alongside the crack width curve for sample D₃.

6.4. Results Phase 1 TPU

In this section, the results from the first phase of the study, specifically focusing on the material TPU, are presented. Figures 6.19, 6.23, and 6.27 illustrate the stress-strain behavior of samples A, C, and D, respectively, all of which clearly also exhibit strain softening characteristics. Yet, the reinforced samples demonstrated a characteristic multiple cracking behavior. Similar to the ABS reinforced samples, the strength of the reinforced samples was lower than the reference samples for the TPU reinforced samples.

6.4.1. Design A

Fig. 6.19 illustrates the stress-strain behavior of the samples reinforced with design A, the bowtie configuration. The experimental results are presented in Table 6.9, which include the initial cracking strength, maximum tensile strength, strain capacity, and total work for each tested specimen. For a more detailed investigation, sample A₂ was selected. Fig. 6.20 illustrates the stress-strain curve of sample A₂ in comparison to the reference samples. The graph reveals that the strength of the reinforced sample was lower than the reference sample. Furthermore, Fig. 6.21 demonstrates the stress-strain curve for sample A₂, alongside an indication of the pattern of crack formation. The stages identified in the stress-strain curve (Fig.6.21a) are elaborated upon in Table 6.10, offering specific insights into the timing, stress levels, and strains at each stage. Fig. 6.22 presents the cracks observed in the sample, accompanied by a graph that plots the crack width against the measured displacement.

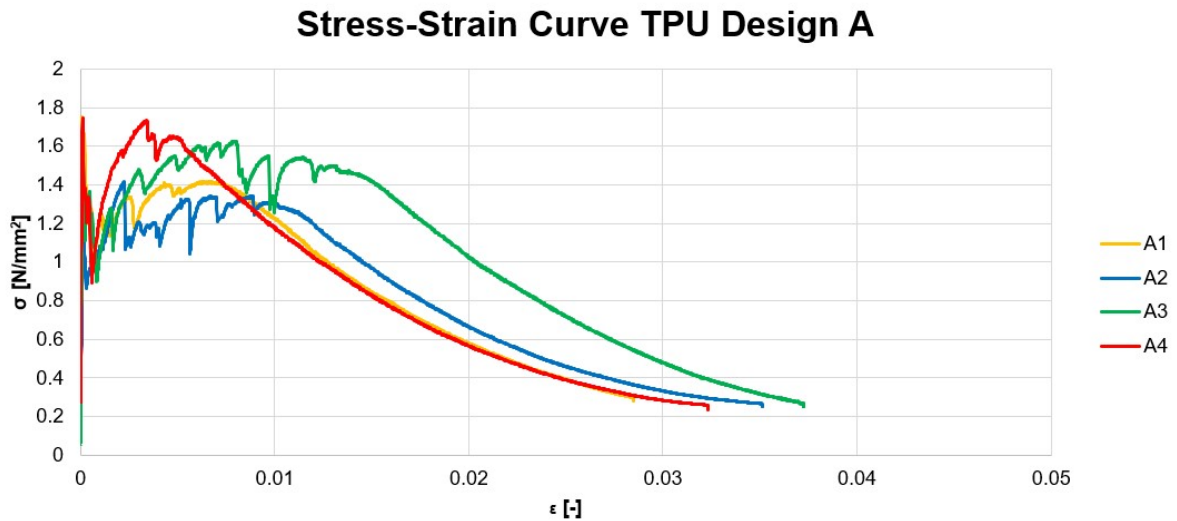


Figure 6.19: Stress-strain curves design A.

	Sample A ₁	Sample A ₂	Sample A ₃	Sample A ₄
First cracking strength [N/mm ²]	1.755	1.118	1.528	1.749
Max tensile strength [N/mm ²]	1.755	1.418	1.627	1.749
Strain capacity [%]	0.00942	0.224	0.793	0.0100
Total work [J]	1.073	0.819	1.343	0.937

Table 6.9: Test results for samples with design A.

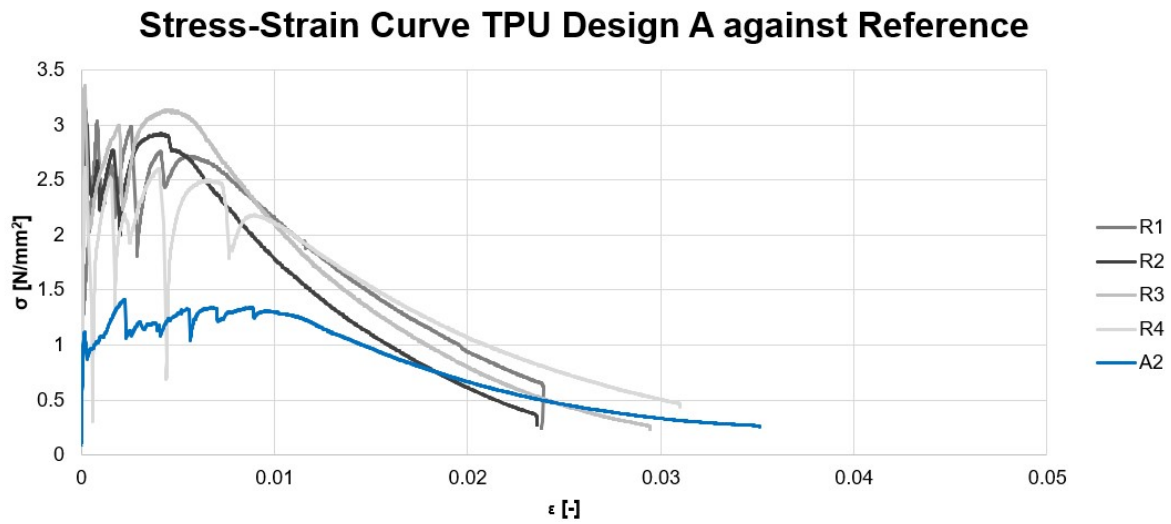
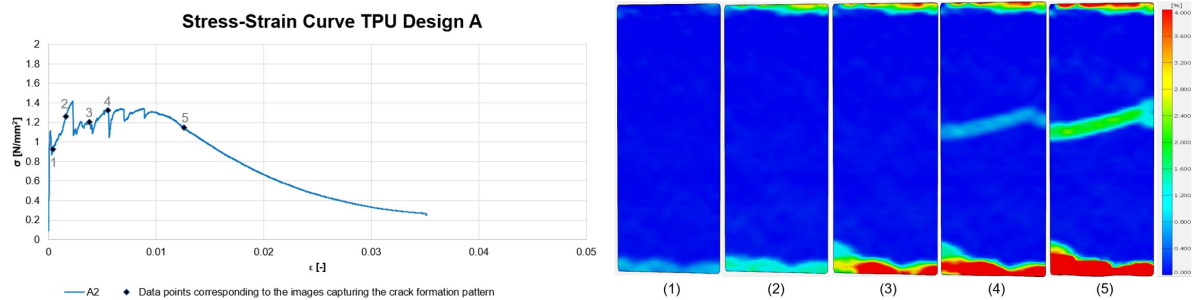


Figure 6.20: Stress-strain curves sample A₂ against reference samples.



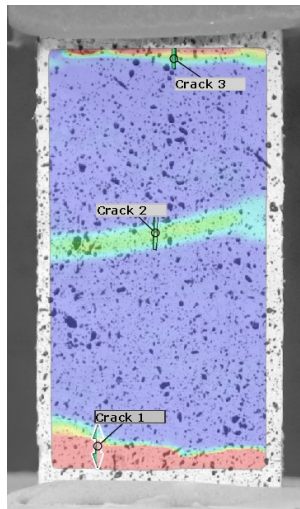
(a) Stress-strain curve sample A₂ with data points.

(b) Crack formation pattern.

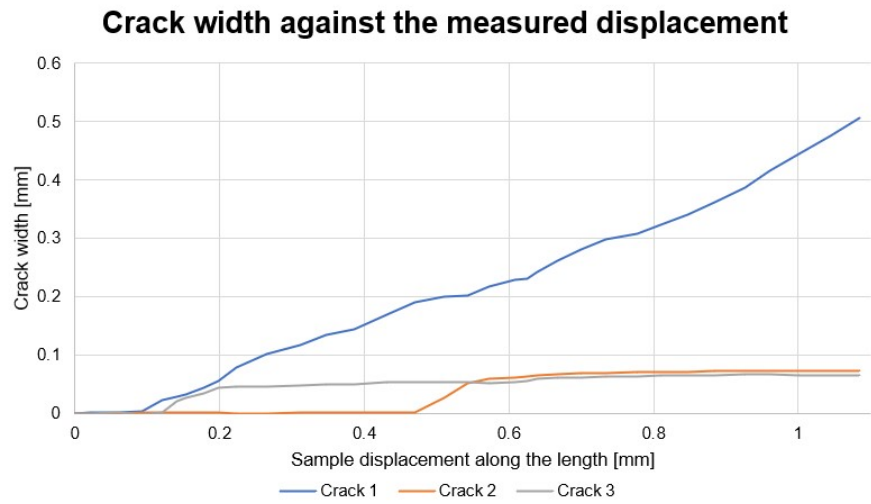
Figure 6.21: Stress-strain curve and crack formation pattern for sample A₂.

Stage	Time [s]	Stress [N/mm ²]	Strain [-]
1	24	0.92	0.000385
2	42	1.26	0.00161
3	72	1.20	0.00377
4	96	1.33	0.00550
5	198	1.14	0.0126

Table 6.10: Stress and strain corresponding to the different stages.



(a) Location of cracks.



(b) Crack width against measured displacement.

Figure 6.22: Crack location alongside the crack width curve for sample A_2 .

6.4.2. Design C

Fig. 6.23 presents the stress-strain characteristics of the samples. Table 6.11 summarizes the testing results for each sample reinforced with the rectangular design, including values for initial cracking strength, maximum strength, strain capacity, and total work. Sample C₁ was chosen for further analysis. Fig. 6.24 displays the stress-strain curve for sample C₁ in comparison to the reference samples. It can be observed from the Figure that the strength of the reinforced sample is lower than that of the reference sample. Additionally, Fig. 6.25 exhibits the stress-strain curve with the corresponding crack formation pattern indicated. The distinct stages observed in the stress-strain curve (Fig. 6.25a) are further detailed in Table 6.12, providing specific information on the time, stress, and strain at each stage. The cracks of the sample are shown in Fig. 6.26 which also includes a graph that represents the crack width against the measured displacement.

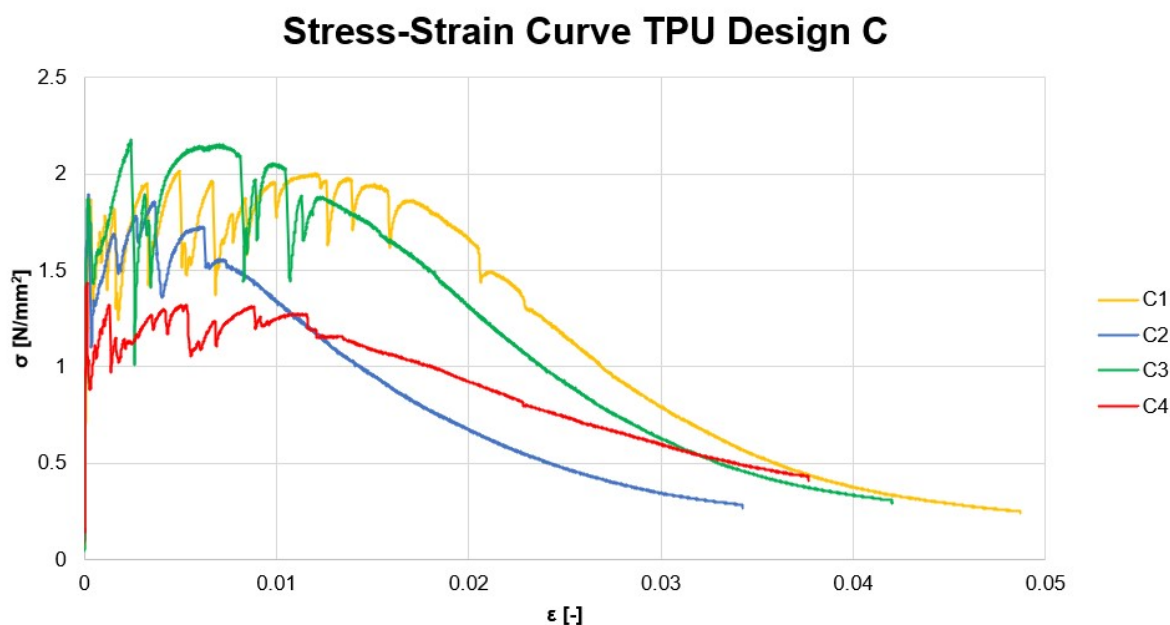


Figure 6.23: Stress-strain curves design C.

	Sample C ₁	Sample C ₂	Sample C ₃	Sample C ₄
First cracking strength [N/mm ²]	1.869	1.897	1.871	1.437
Max tensile strength [N/mm ²]	2.016	1.897	2.180	1.437
Strain capacity [%]	0.493	0.0207	0.245	0.0128
Total work [J]	2.110	1.566	2.293	1.088

Table 6.11: Test results for samples with design C

Stress-Strain Curve TPU Design C against Reference

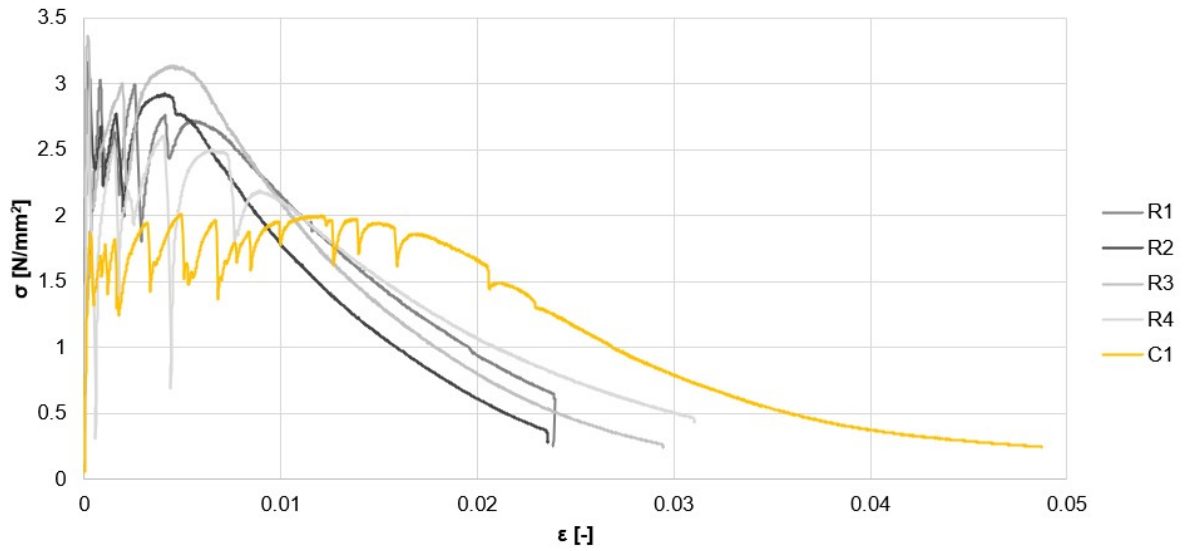
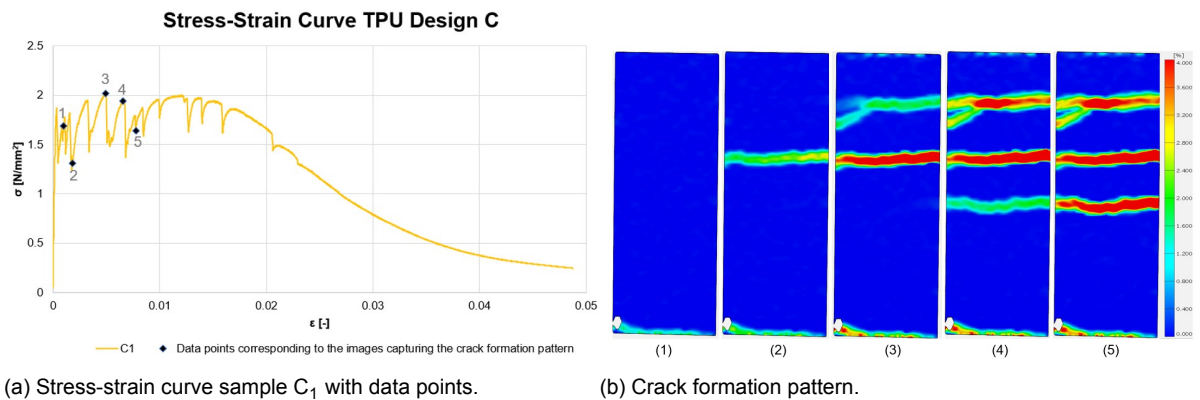


Figure 6.24: Stress-strain curves sample C_1 against reference samples.



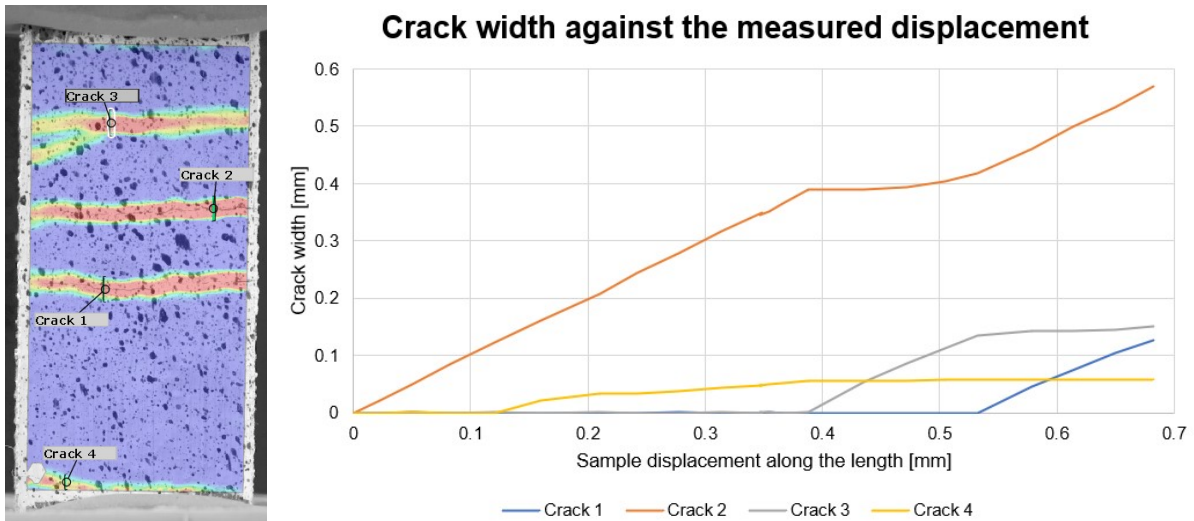
(a) Stress-strain curve sample C_1 with data points.

(b) Crack formation pattern.

Figure 6.25: Stress-strain curve and crack formation pattern for sample C_1 .

Stage	Time [s]	Stress [N/mm ²]	Strain [-]
1	30	1.69	0.000994
2	42	1.31	0.001823
3	90	2.02	0.00493
4	114	1.94	0.00653
5	132	1.64	0.00775

Table 6.12: Stress and strain corresponding to the different stages.



(a) Location of cracks. (b) Crack width against measured displacement.

Figure 6.26: Crack location alongside the crack width curve for sample C₁.

6.4.3. Design D

Fig. 6.27 displays the stress-strain behavior of the samples reinforced with design D, the honeycomb configuration. The experimental results for each tested specimen, are presented in Table 6.13. For a more comprehensive investigation, the focus was placed on sample D₄. Fig. 6.28 illustrates the stress-strain curve of sample D₄ in comparison to the reference samples. The plot effectively highlights that the strength of the reference sample surpassed that of the reinforced sample. Furthermore, Fig. 6.29 presents the stress-strain curve for sample D₄, accompanied by the crack formation pattern. The distinct stages showcased in Fig. 6.29a) are elaborated upon in Table 6.14, offering detailed information on the timing, stress levels, and strains at each stage. Additionally, Fig. 6.30 exhibits the detected cracks within the specimen, accompanied by a graphical representation plotting the crack width against the measured displacement. As can be seen in Fig. 6.30b, cracks 2 initiated first, followed by crack 3 and finally crack 1. In contrast to the ABS reinforcement, no negative crack widths were present.

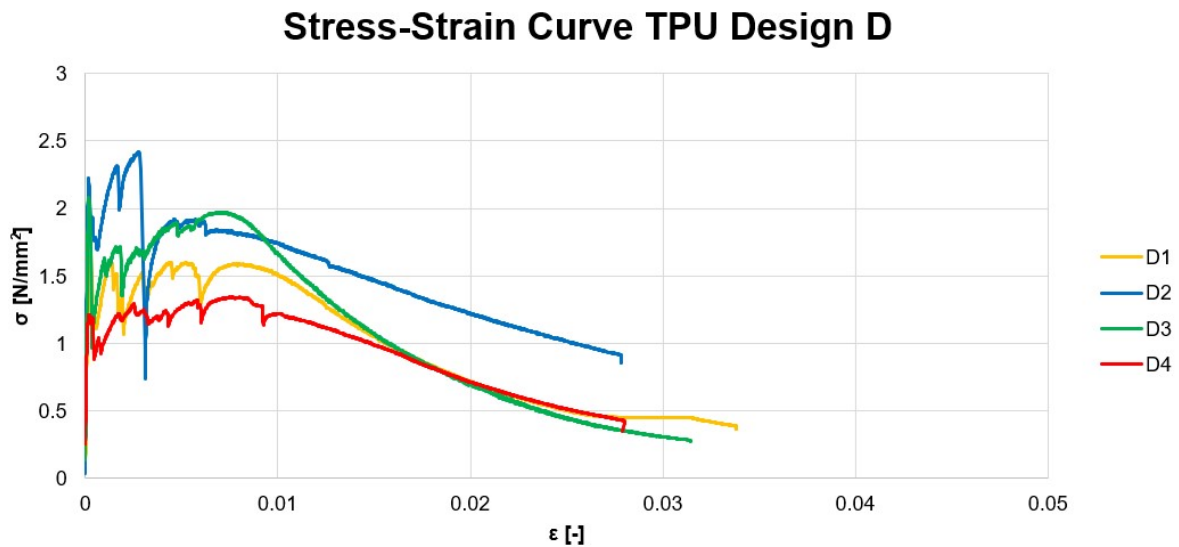


Figure 6.27: Stress-strain curves design D.

	Sample D ₁	Sample D ₂	Sample D ₃	Sample D ₄
First cracking strength [N/mm ²]	1.661	2.227	2.081	1.208
Max tensile strength [N/mm ²]	1.661	2.416	2.081	1.345
Strain capacity [%]	0.0252	0.274	0.0183	0.797
Total work [J]	1.235	1.580	1.507	0.994

Table 6.13: Test results for samples with design D.

Stress-Strain Curve TPU Design D against Reference

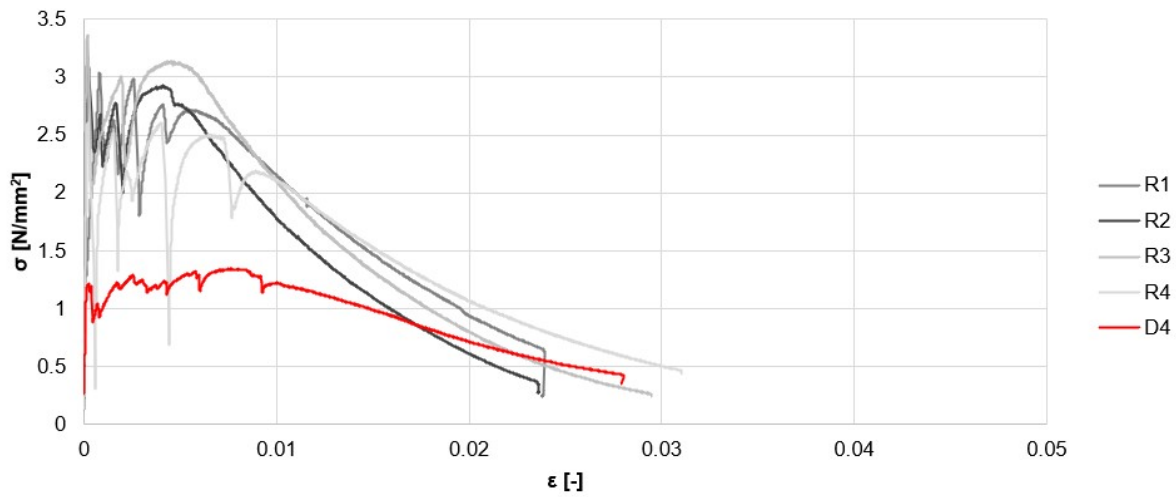
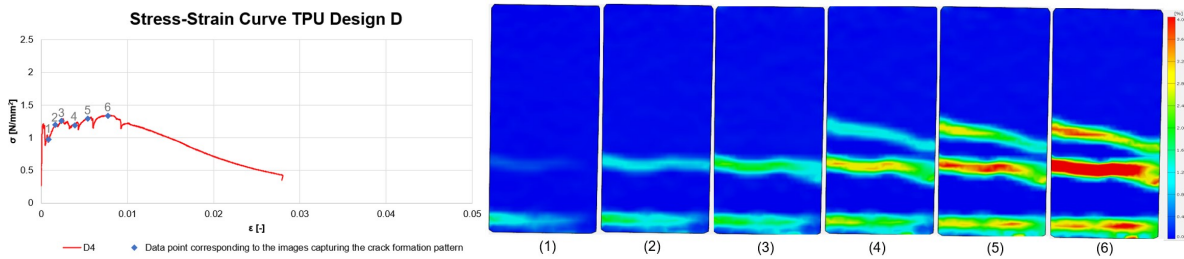


Figure 6.28: Stress-strain curves sample D₄ against reference samples.



(a) Stress-strain curve sample D₄ with data points. (b) Crack formation pattern.

Figure 6.29: Stress-strain curve and crack formation pattern for sample D₄.

Stage	Time [s]	Stress [N/mm ²]	Strain [-]
1	30	0.975	0.000867
2	42	1.203	0.00160
3	54	1.258	0.00236
4	78	1.189	0.00391
5	102	1.293	0.00543
6	138	1.336	0.00773

Table 6.14: Stress and strain corresponding to the different stages.

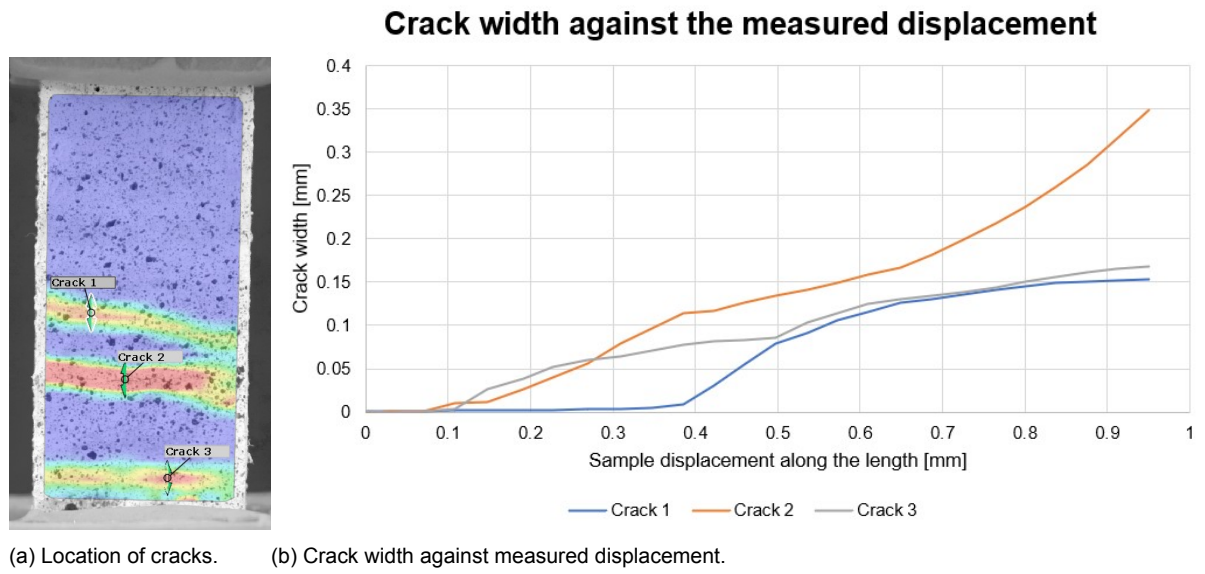


Figure 6.30: Crack location alongside the crack width curve for sample D₄.

6.5. Analysis and discussing phase 1

Table 6.15 presents the averaged values of the parameters strength, strain capacity, and work for the four samples tested per design, along with their respective standard deviations. Fig. 6.31a displays the strength of the samples with the standard deviation indicated, allowing for a clear comparison between different designs. Similarly, Fig. 6.31b illustrates the strain capacity of the reinforced samples in comparison to the reference samples, providing valuable insights into the behavior of the material. Finally, Fig. 6.31c shows the total work required for each design, illustrating the capacities of the samples for dissipating energy. These comprehensive visualizations allow for a thorough understanding and assessment of the performance of the modified designs throughout the study.

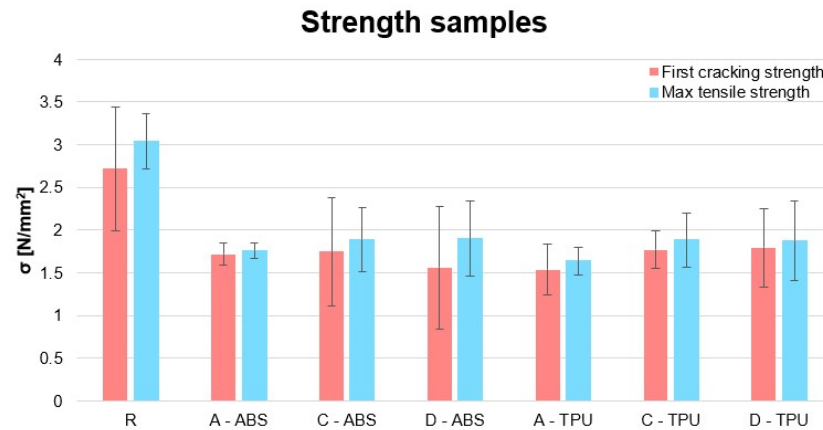
Design (Reinforcing material)	First cracking strength (Standard deviation) [N/mm ²]	Max tensile strength (Standard deviation) [N/mm ²]	Strain capacity (Standard deviation) [%]	Total work (Standard deviation) [J]
R (-)	2.721 (0.723)	3.042 (0.320)	0.0335 (0.032)	1.745 (0.434)
A (ABS)	1.718 (0.133)	1.759 (0.092)	0.132 (0.125)	0.855 (0.102)
C (ABS)	1.747 (0.639)	1.886 (0.373)	0.082 (0.123)	0.939 (0.196)
D (ABS)	1.558 (0.721)	1.901 (0.441)	0.236 (0.162)	0.918 (0.081)
A (TPU)	1.538 (0.299)	1.637 (0.158)	0.259 (0.370)	1.043 (0.225)
C (TPU)	1.769 (0.221)	1.882 (0.319)	0.193 (0.227)	1.764 (0.546)
D (TPU)	1.794 (0.459)	1.876 (0.470)	0.279 (0.365)	1.329 (0.268)

Table 6.15: Test results phase 1.

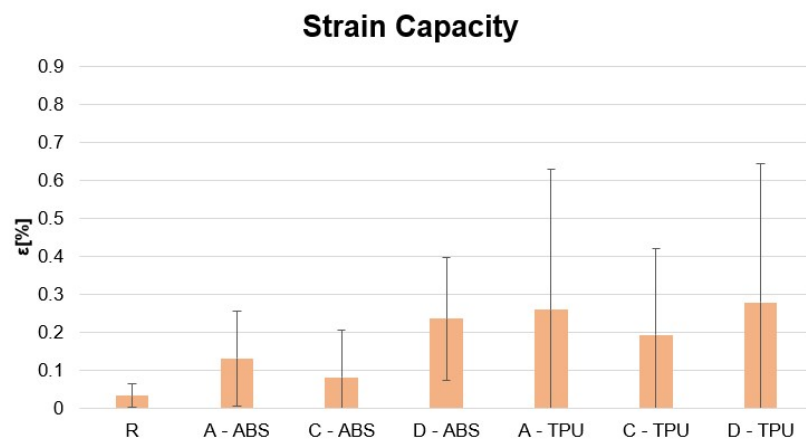
As shown in Fig. 6.31a, the strength of the reference samples was observed to be higher than that of the reinforced specimens. This disparity in strength could be attributed to complications that arose during the casting process, such as bleeding and segregation. These factors might have influenced the overall structural integrity and homogeneity of the reinforced specimens, leading to a reduction in their strength compared to the reference samples. Further investigations and optimization of the casting process are necessary to address these challenges and improve the strength of the reinforced specimens.

Upon analyzing the averaged cracking strength and tensile strength, as depicted in Fig. 6.31a, a noteworthy observation is that the maximum tensile strength surpassed the initial cracking strength, indicative of strain hardening behavior. This behavior implies that the samples exhibited an increase in strength even after the occurrence of initial cracking. Furthermore, when comparing the maximum strength of the different designs, it becomes evident that the non-auxetic designs displayed a higher maximum strength than the auxetic ones for both materials. This distinction in maximum strength highlights the influence of design geometry on the overall mechanical performance of the specimens. The non-auxetic designs demonstrated greater strength under tensile loading, which could be attributed to their inherent structural rigidity compared to the auxetic designs. However, it is worth mentioning that the auxetic design had the largest volume compared to the non-auxetic ones.

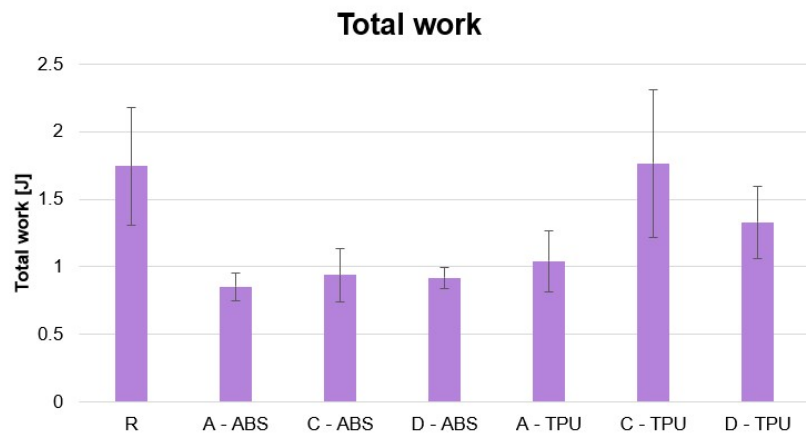
In the comparison of design A for both materials, it was evident that the ABS reinforced material exhibited a slightly higher maximum strength than TPU. However, this difference was not significant, suggesting that design A was less influenced by the material properties for this phase. Similarly, when examining design C and design D for both materials, both exhibited similar maximum strength values. This indicates that the mechanical behavior of these designs was less sensitive to the material used as well.



(a) Strength samples.



(b) Strain capacity.



(c) Total work.

Figure 6.31: Results phase 1.

Analyzing the strain capacity, as illustrated in Fig. 6.31b, both materials demonstrated a significantly higher strain capacity in comparison to the reference sample. A clear distinction can be observed when comparing the strain capacity of TPU and ABS within these samples, with TPU outperforming ABS in terms of strain capacity. This observation aligns with findings in the literature, where TPU is known for its enhanced ductile behavior compared to ABS. Additionally, when comparing the different shapes, it becomes evident that the honeycomb design

exhibits the highest strain capacity, followed by the re-entrant design, and finally the rectangular design. However, it is important to note that a large standard deviation was observed, suggesting some variability in the results. Consequently, further investigation and in-depth analysis are warranted to gain a comprehensive understanding of the factors contributing to this variability and to ensure the reliability of the findings.

In the Figures displaying the location of the cracks, a notable observation is the increased formation of cracks compared to the reference sample. The presence of a greater number of cracks in the material is indicative of its improved fracture behavior. This enhanced cracking behavior is a desirable characteristic in certain engineering applications, as it enhances the ability of the material to withstand and absorb external loads. In the case of the honeycomb design for the ABS reinforced material, an interesting phenomenon was observed where certain crack widths exhibited negative values (Fig. 6.17), indicating crack closure during the tensile testing process. This behavior was not observed in the TPU material for the honeycomb design.

In Fig. 6.31c, it is evident that the reference sample exhibited the highest total work conducted. Among the TPU material samples, design C showed comparable work, followed by design D. Conversely, all other samples displayed approximately half of the total work compared to the reference sample. In terms of energy absorption, the results indicate that the reference sample, which was the unreinforced specimen, had the highest capacity to absorb energy among all the tested samples. This implies that the addition of reinforcement materials, such as TPU or ABS, led to a reduction in the overall energy absorption capability of the specimens. However, the reason for this phenomenon lies in the substantially greater strength of the reference specimen compared to the reinforced samples. Consequently, a larger area under the force-displacement curve was enclosed by the reference sample, leading to a correspondingly higher total work.

6.6. Results Phase 2 ABS

This section presents the results obtained during the second phase of the study focusing on the material ABS. Figures 6.32, and 6.36 depict the stress-strain behavior of samples C and D, respectively. Similar to phase 1, the strength of the reference samples were higher than the reinforced samples with the 3D printed meshes.

6.6.1. Design C_{adj}

Fig. 6.32 illustrates the stress-strain characteristics of the samples. Table 6.16 summarizes the testing results for each sample reinforced with the rectangular design, including values for initial cracking strength, maximum strength, strain capacity, and total work. Sample $C_{3,adj}$ was chosen for further analysis. Fig. 6.33 displays the stress-strain curve for sample $C_{3,adj}$ in comparison to the reference samples. It can be observed from the Figure that the strength of the reinforced sample is lower than that of the reference sample. Additionally, Fig. 6.34 exhibits the stress-strain curve with the corresponding crack formation pattern indicated. The distinct stages observed in the stress-strain curve (Fig. 6.34a) are further detailed in Table 6.17, providing specific information on the time, stress, and strain at each stage. The cracks of the sample are shown in Fig. 6.35 which also includes a graph that represents the crack width against the measured displacement.

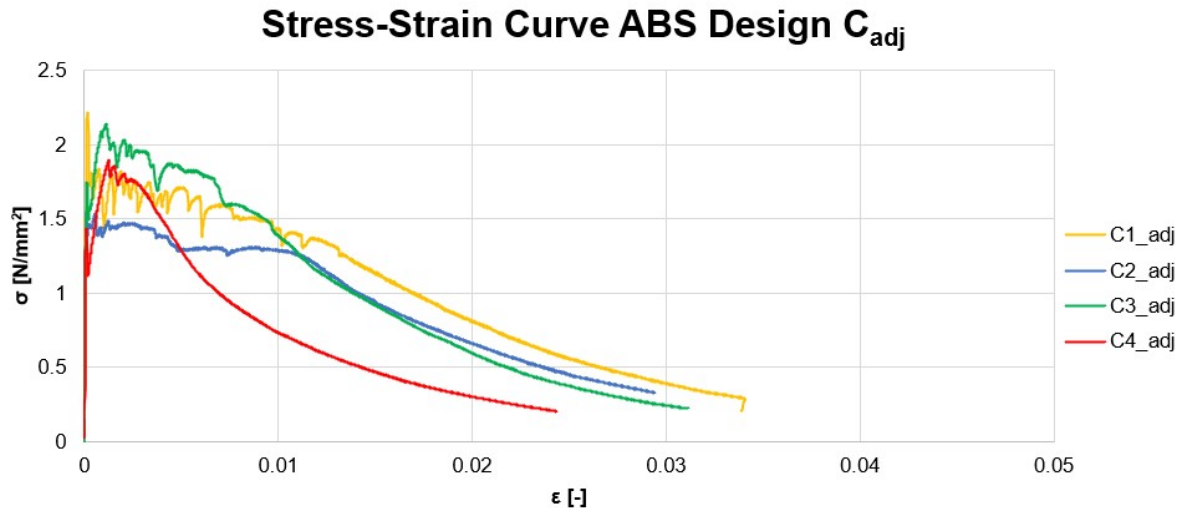


Figure 6.32: Stress-strain curves design C_{adj} .

	Sample $C_{1,adj}$	Sample $C_{2,adj}$	Sample $C_{3,adj}$	Sample $C_{4,adj}$
First cracking strength [N/mm ²]	2.219	1.542	1.750	1.438
Max tensile strength [N/mm ²]	2.219	1.542	2.141	1.895
Strain capacity [%]	0.0149	0.110	0.112	0.126
Total work [J]	1.328	0.817	1.200	0.820

Table 6.16: Test results for samples with design C_{adj} .

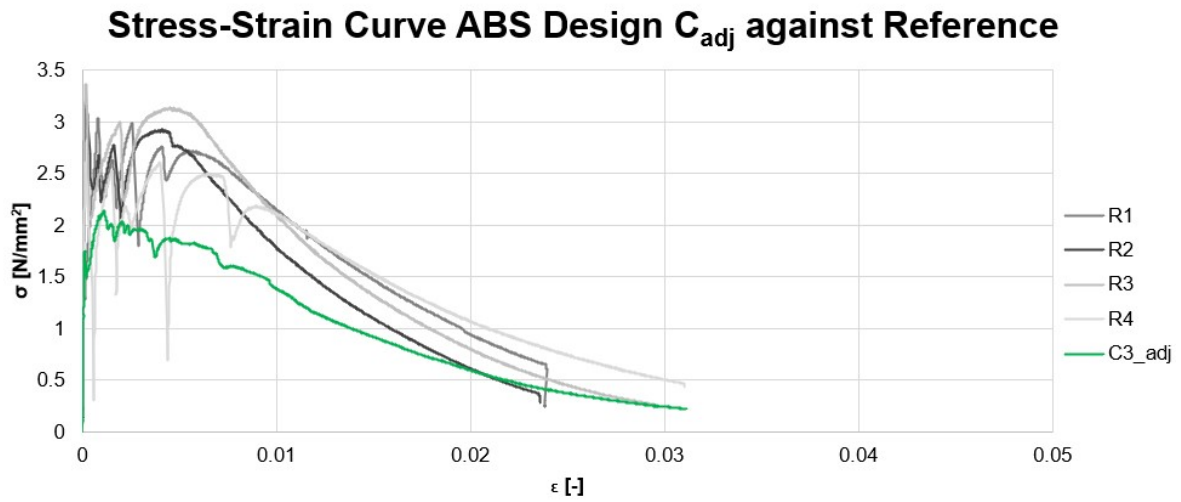
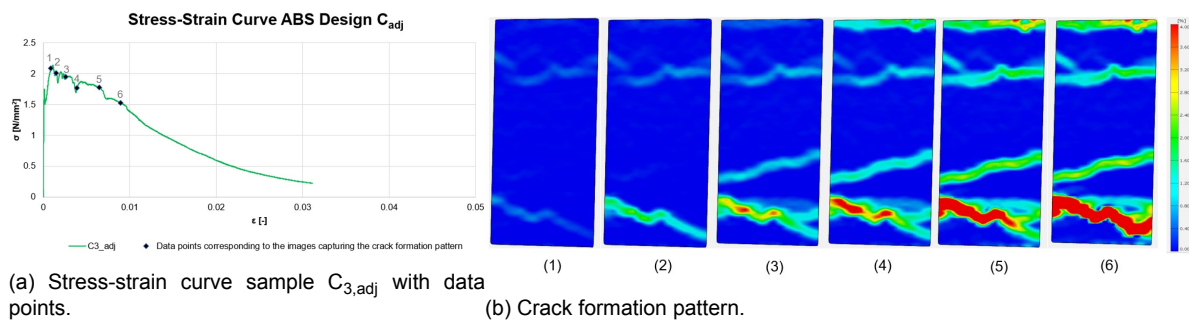


Figure 6.33: Stress-strain curves sample $C_{3,adj}$ against reference samples.



(a) Stress-strain curve sample $C_{3,adj}$ with data points.

(b) Crack formation pattern.

Figure 6.34: Stress-strain curve and crack formation pattern for sample $C_{3,adj}$.

Stage	Time [s]	Stress [N/mm ²]	Strain [-]
1	48	2.092	0.000866
2	60	2.012	0.00149
3	78	1.947	0.00260
4	96	1.769	0.00389
5	138	1.776	0.00645
6	174	1.525	0.00896

Table 6.17: Stress and strain corresponding to the different stages.

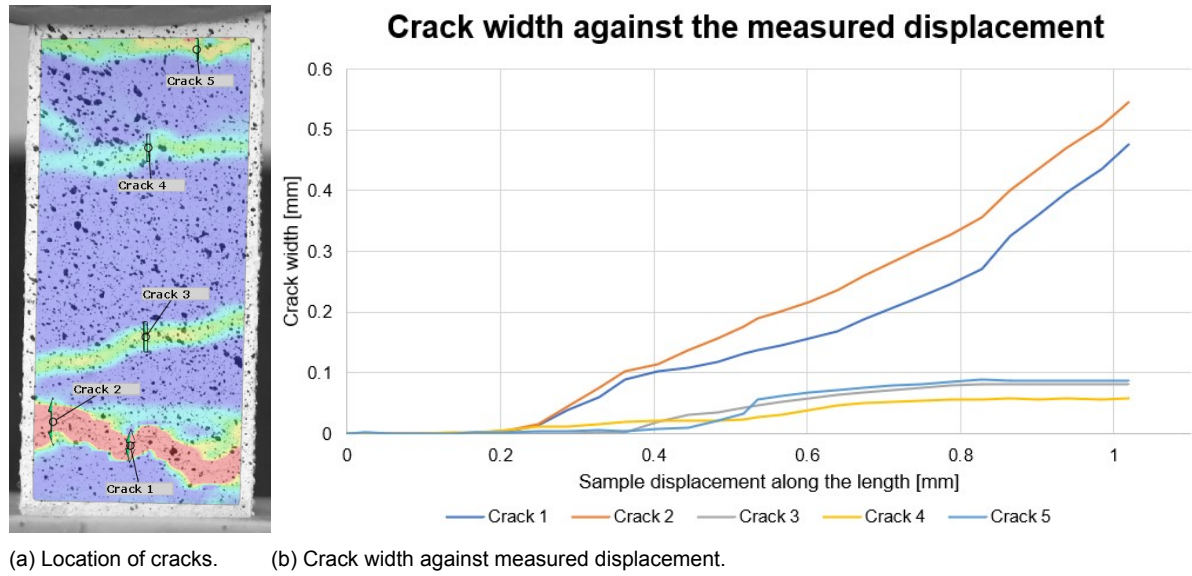


Figure 6.35: Crack location alongside the crack width curve for sample $C_{3,adj}$.

6.6.2. Design D_{adj}

Fig. 6.36 displays the stress-strain behavior of the samples reinforced with design D, the honeycomb configuration. The experimental results for each tested specimen, are presented in Table 6.18. For a more comprehensive investigation, the focus was placed on sample $D_{4,adj}$. Fig. 6.37 illustrates the stress-strain curve of sample $D_{4,adj}$ in comparison to the reference samples. The plot effectively highlights that the strength of the reference sample surpassed that of the reinforced sample. Furthermore, Fig. 6.38 presents the stress-strain curve for sample $D_{4,adj}$, accompanied by the crack formation pattern. The distinct stages showcased in Fig. 6.38a) are elaborated upon in Table 6.19, offering detailed information on the timing, stress levels, and strains at each stage. Additionally, Fig. 6.39 exhibits the detected cracks within the specimen, accompanied by a graphical representation plotting the crack width against the measured displacement. As illustrated in Fig. 6.39b, negative crack widths were observed in some cracks, similar to the phase 1 behavior observed in the ABS reinforced sample with the honeycomb configuration.

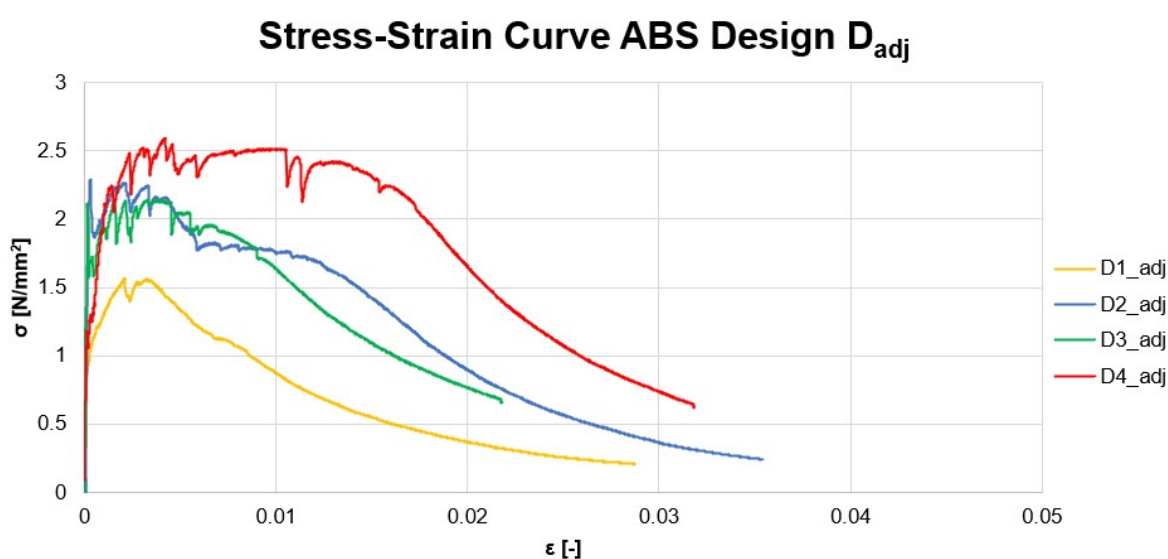


Figure 6.36: Stress-strain curves Design D_{adj} .

	Sample $D_{1,adj}$	Sample $D_{2,adj}$	Sample $D_{3,adj}$	Sample $D_{4,adj}$
First cracking strength [N/mm^2]	0.946	2.289	1.199	1.185
Max tensile strength [N/mm^2]	1.567	2.289	2.145	2.597
Strain capacity [%]	0.209	0.0302	0.158	0.421
Total work [J]	0.870	1.378	1.505	2.127

Table 6.18: Test results for samples with design D_{adj} .

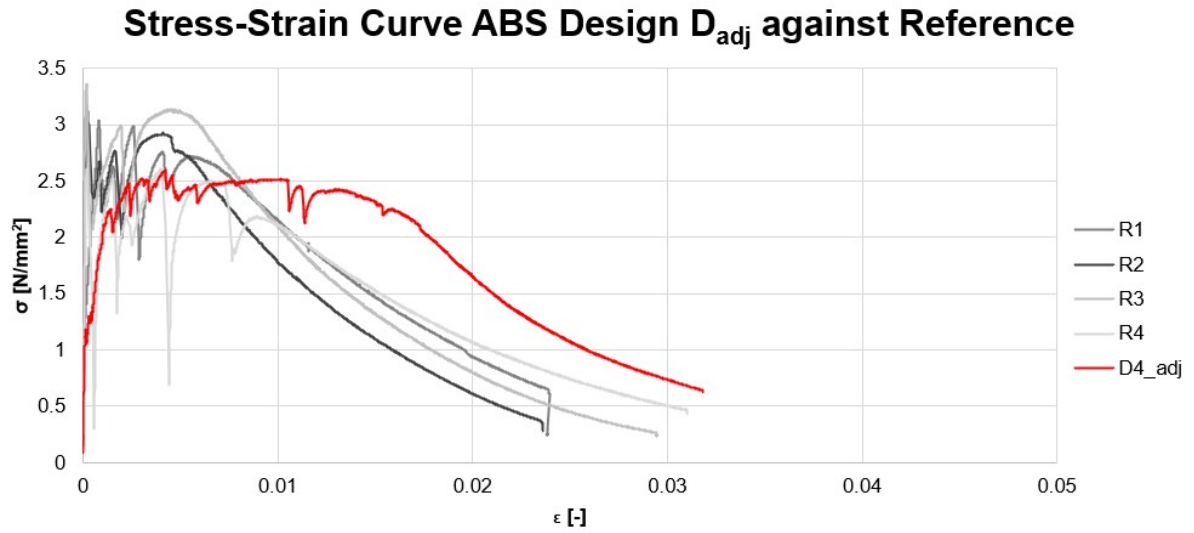


Figure 6.37: Stress-strain curves sample $D_{4,adj}$ against reference samples.

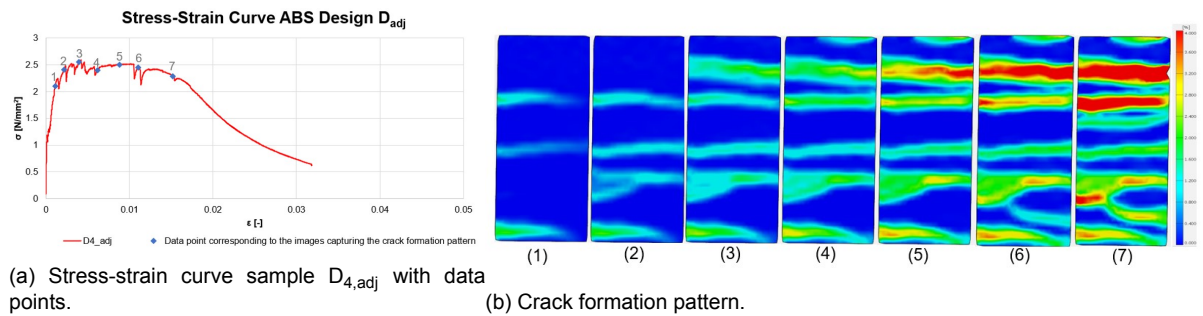
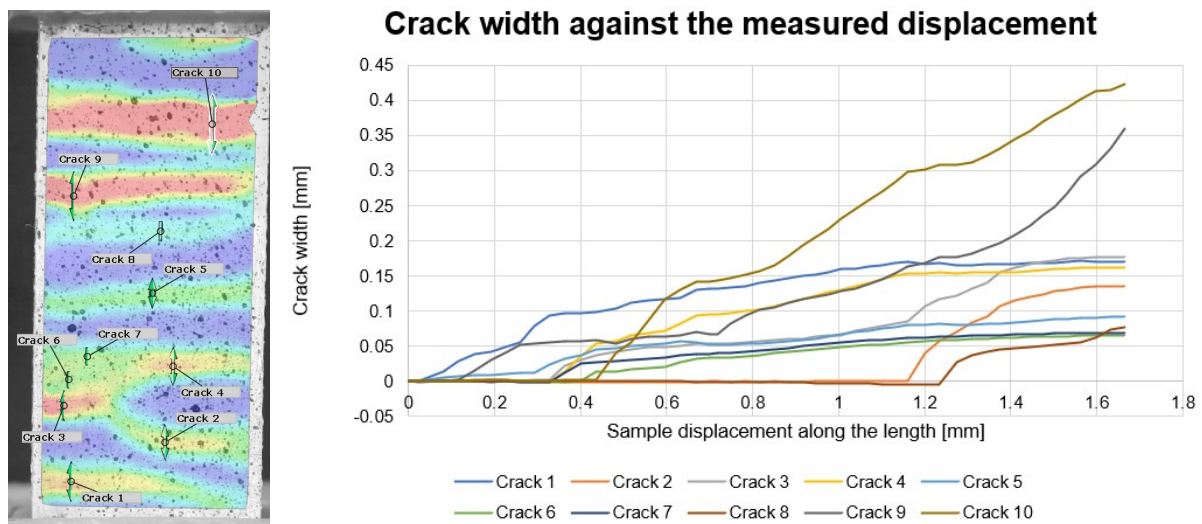


Figure 6.38: Stress-strain curve and crack formation pattern for sample $D_{4,adj}$.

Stage	Time [s]	Stress [N/mm ²]	Strain [-]
1	54	2.104	0.00111
2	72	2.406	0.00215
3	102	2.549	0.00396
4	138	2.398	0.00618
5	180	2.503	0.00878
6	216	2.451	0.0110
7	282	2.289	0.0152

Table 6.19: Stress and strain corresponding to the different stages.



(a) Location of cracks. (b) Crack width against measured displacement.

Figure 6.39: Crack location alongside the crack width curve for sample $D_{4,adj}$.

6.7. Results Phase 2 TPU

In this section, the results from the first phase of the study, specifically focusing on the material TPU, are presented. Figures 6.40, and 6.44 illustrate the stress-strain behavior of samples C and D, respectively, all of which clearly also exhibit strain softening characteristics.

6.7.1. Design C_{adj}

Presented in Fig. 6.40 are the stress-strain curves of the samples. Table 6.20 summarizes the testing results for each sample reinforced with the rectangular design, including values for initial cracking strength, maximum strength, strain capacity, and total work. Sample $C_{3,adj}$ was chosen for further analysis. Fig. 6.41 displays the stress-strain curve for sample $C_{3,adj}$ in comparison to the reference samples. It can be observed from the Figure that the strength of the reinforced sample is lower than that of the reference sample. Additionally, Fig. 6.42 exhibits the stress-strain curve with the corresponding crack formation pattern indicated. The distinct stages observed in the stress-strain curve (Fig. 6.42a) are further detailed in Table 6.21, providing specific information on the time, stress, and strain at each stage. The cracks of the sample are shown in Fig. 6.43 which also includes a graph that represents the crack width against the measured displacement.

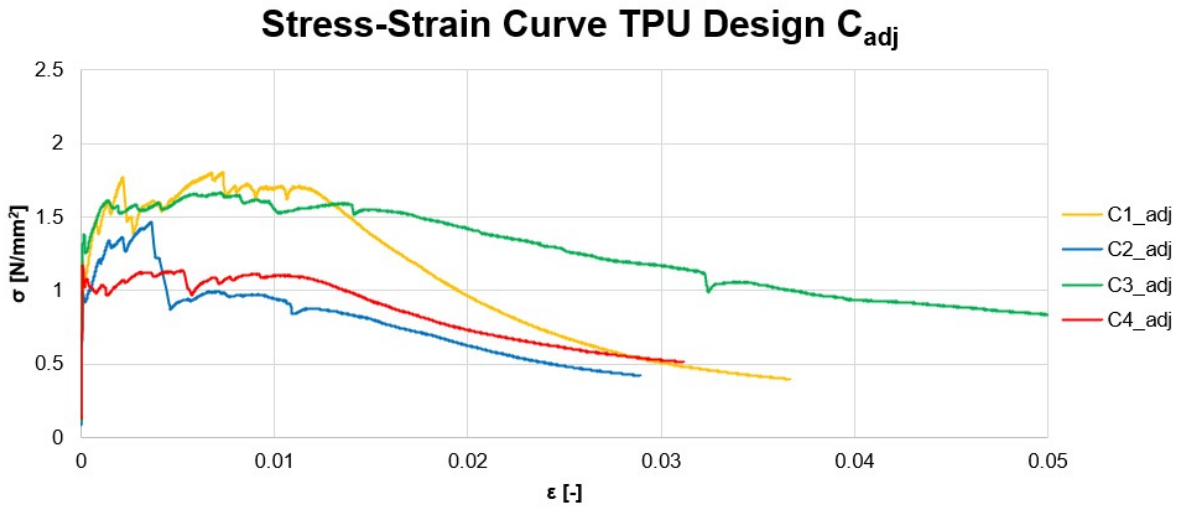


Figure 6.40: Stress-strain curves Design C_{adj} .

	Sample $C_{1,adj}$	Sample $C_{2,adj}$	Sample $C_{3,adj}$	Sample $C_{4,adj}$
First cracking strength [N/mm ²]	1.199	0.994	1.385	1.169
Max tensile strength [N/mm ²]	1.802	1.462	1.666	1.169
Strain capacity [%]	0.733	0.359	0.722	0.00861
Total work [J]	1.238	0.861	1.167	0.855

Table 6.20: Test results for samples with design C_{adj} .

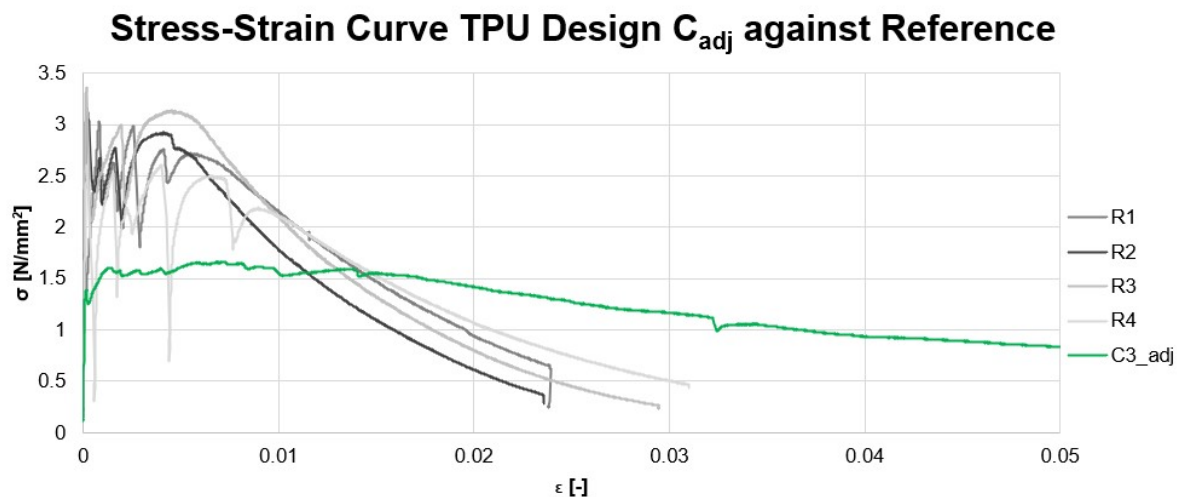
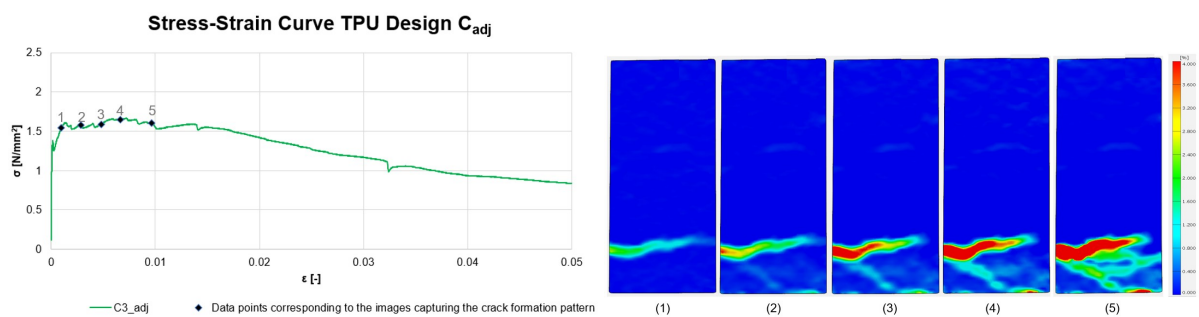


Figure 6.41: Stress-strain curves sample $C_{3,adj}$ against reference samples.



(a) Stress-strain curve sample $C_{3,adj}$ with data points.

(b) Crack formation pattern.

Figure 6.42: Stress-strain curve and crack formation pattern for sample $C_{3,adj}$.

Stage	Time [s]	Stress [N/mm ²]	Strain [-]
1	36	1.543	0.00095
2	66	1.581	0.00282
3	96	1.590	0.0048
4	126	1.648	0.00662
5	174	1.604	0.00966

Table 6.21: Stress and strain corresponding to the different stages.

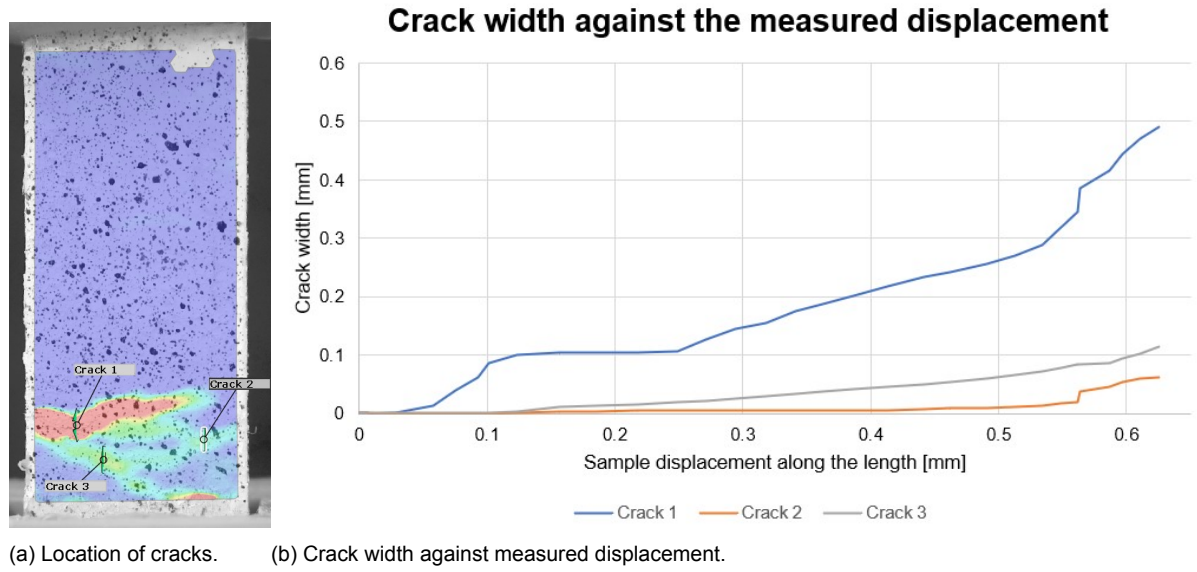


Figure 6.43: Crack location alongside the crack width curve for sample $C_{3,adj}$.

6.7.2. Design D_{adj}

Illustrated in Fig. 6.44 is the stress-strain behavior of specimens reinforced with design D, utilizing the honeycomb configuration. The experimental results for each tested specimen, are presented in Table 6.22. For a more comprehensive investigation, the focus was placed on sample $D_{3,adj}$. Fig. 6.45 illustrates the stress-strain curve of sample $D_{3,adj}$ in comparison to the reference samples. The plot effectively highlights that the strength of the reference sample surpassed that of the reinforced sample. Furthermore, Fig. 6.46 presents the stress-strain curve for sample $D_{3,adj}$, accompanied by the crack formation pattern. The distinct stages showcased in Fig. 6.46a) are elaborated upon in Table 6.23, offering detailed information on the timing, stress levels, and strains at each stage. Additionally, Fig. 6.47 exhibits the detected cracks within the specimen, accompanied by a graphical representation plotting the crack width against the measured displacement.

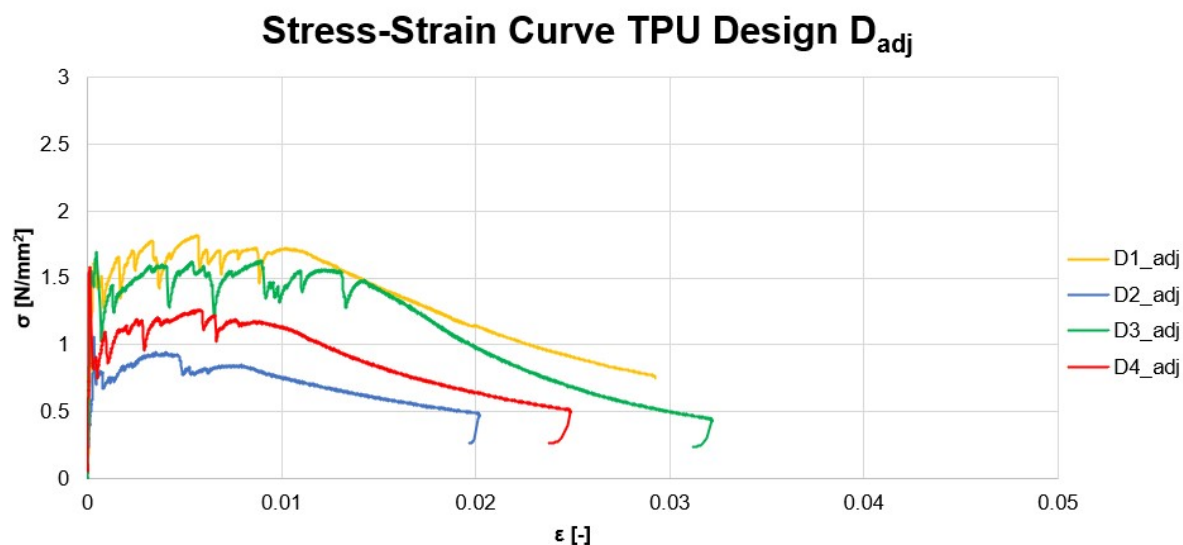


Figure 6.44: Stress-strain curves Design D_{adj} .

	Sample $D_{1,adj}$	Sample $D_{2,adj}$	Sample $D_{3,adj}$	Sample $D_{4,adj}$
First cracking strength [N/mm ²]	1.611	1.064	1.550	1.578
Max tensile strength [N/mm ²]	1.819	1.064	1.691	1.578
Strain capacity [%]	0.567	0.0353	0.0454	0.0103
Total work [J]	1.486	0.564	1.249	0.807

Table 6.22: Test results for samples with design D_{adj} .

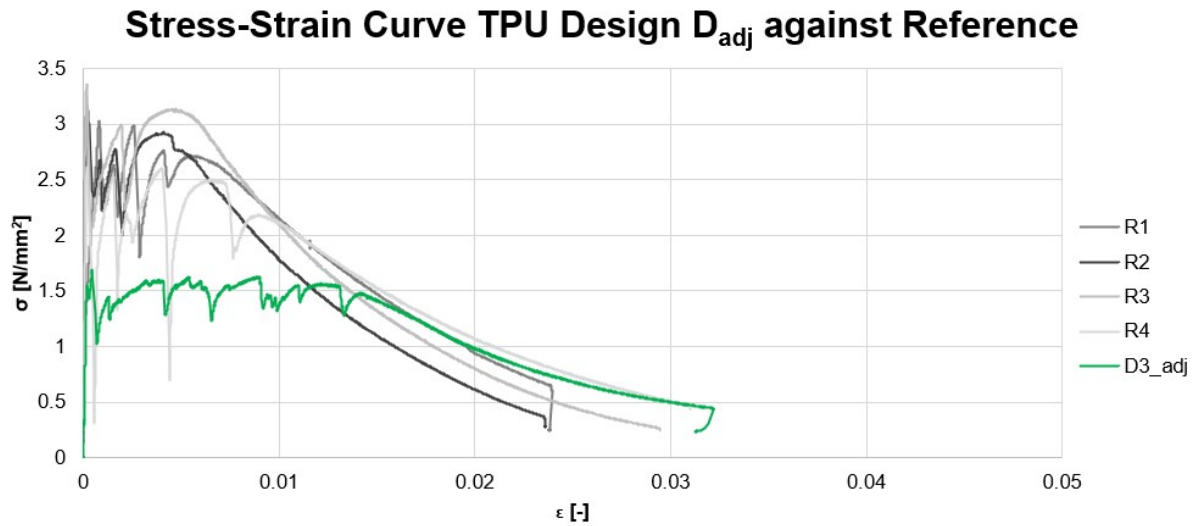
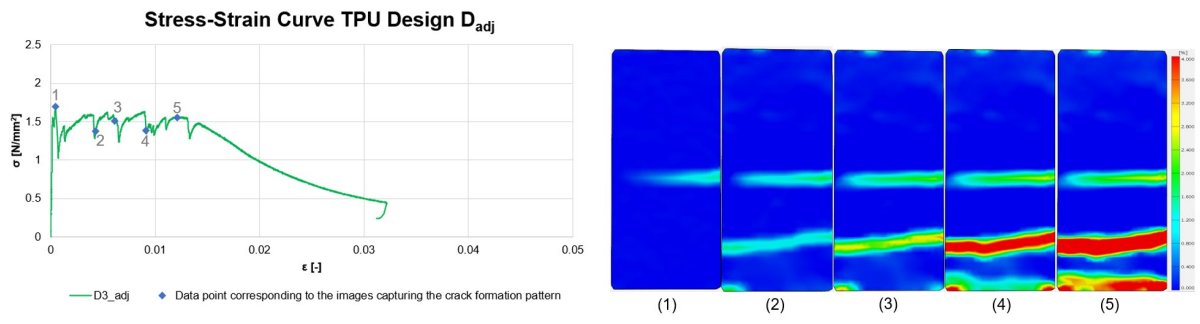


Figure 6.45: Stress-strain curves sample D against reference samples.



(a) Stress-strain curve sample $D_{3,adj}$ with data points.

(b) Crack formation pattern.

Figure 6.46: Stress-strain curve and crack formation pattern for sample $D_{3,adj}$.

Stage	Time [s]	Stress [N/mm ²]	Strain [-]
1	54	1.691	0.000454
2	114	1.371	0.00432
3	144	1.511	0.00610
4	192	1.384	0.00913
5	240	1.550	0.0121

Table 6.23: Stress and strain corresponding to the different stages.

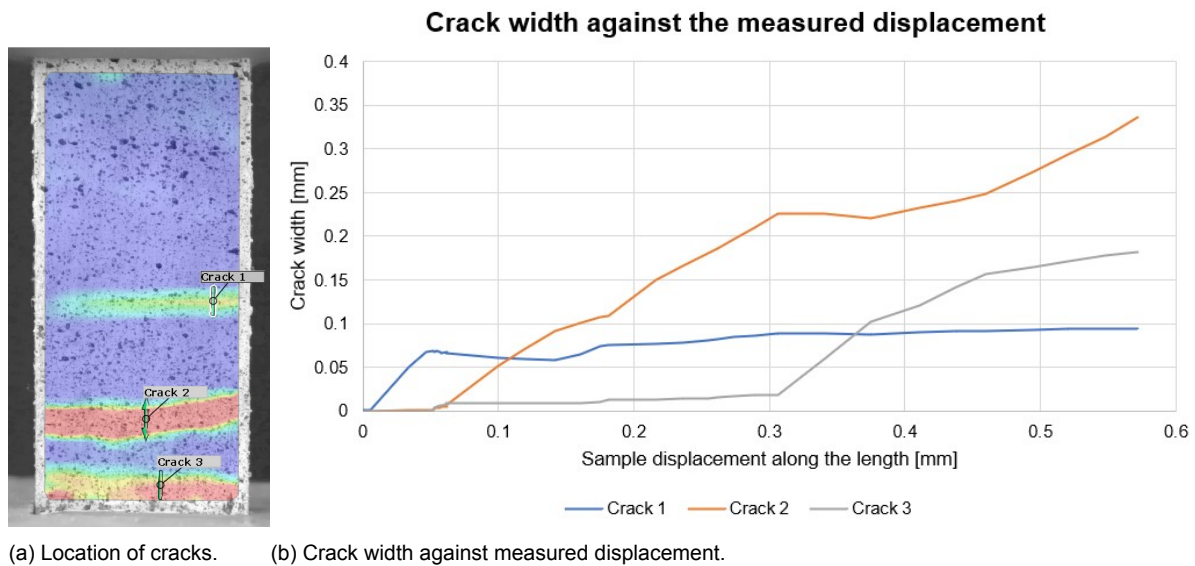


Figure 6.47: Crack location alongside the crack width curve for sample $D_{3,adj}$.

6.8. Analysis and discussing phase 2

Table 6.24 provides a comprehensive overview of the average values and standard deviations of strength, strain capacity, and work for the four samples tested per design in phase 2. Fig 6.48a presents the strength data for the samples along with their respective standard deviations. This allows for a clear assessment of the variations between different designs and phases. Additionally, Fig 6.48b visually illustrates the strain capacity of the reinforced samples in comparison to the reference samples. Finally, Fig 6.48c showcases the total work required for each design, providing valuable insights into the energy absorption capabilities of the materials.

Design (Reinforcing material)	First cracking strength (Standard deviation) [N/mm ²]	Max tensile strength (Standard deviation) [N/mm ²]	Strain capacity (Standard deviation) [%]	Total work (Standard deviation) [J]
R (-)	2.721 (0.723)	3.042 (0.320)	0.0335 (0.032)	1.745 (0.434)
C _{adj} (ABS)	1.733 (0.35)	1.945(0.313)	0.091(0.051)	1.041 (0.262)
D _{adj} (ABS)	1.405 (0.601)	2.15(0.432)	0.205(0.163)	1.47 (0.517)
C _{adj} (TPU)	1.187 (0.16)	1.525(0.275)	0.456(0.345)	1.031 (0.202)
D _{adj} (TPU)	1.451 (0.259)	1.538(0.331)	0.165(0.269)	1.027 (0.417)

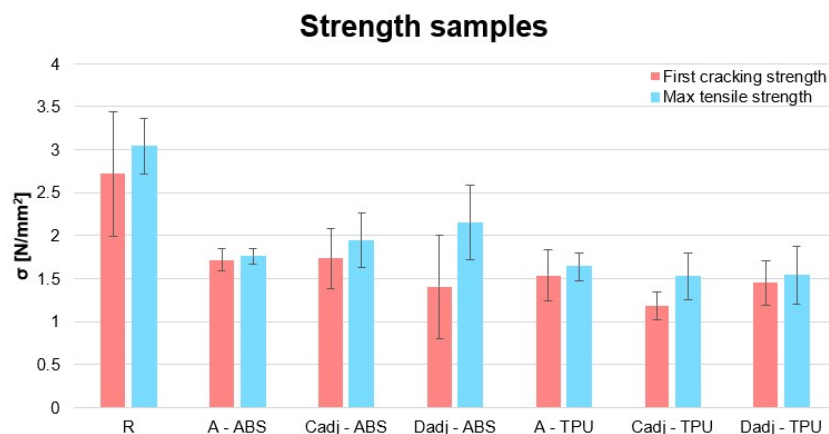
Table 6.24: Test results phase 2.

During this phase, a notable trend was observed where the reference samples displayed higher strength values in comparison to the reinforced ones. It was also observed that for all the reinforced samples, the maximum tensile strength exceeded the initial cracking strength, indicating strain hardening behavior. A comparison between the two materials revealed that ABS exhibited a higher maximum strength than the TPU reinforced samples, aligning with findings from the literature study, which also highlighted the higher load-bearing capacity of ABS over TPU. This difference in strength can be attributed to the inherent mechanical properties and material composition of ABS, which enables it to withstand higher forces and stresses compared to TPU. The results highlight the significance of material selection and design optimization to achieve desired mechanical performance in specific applications.

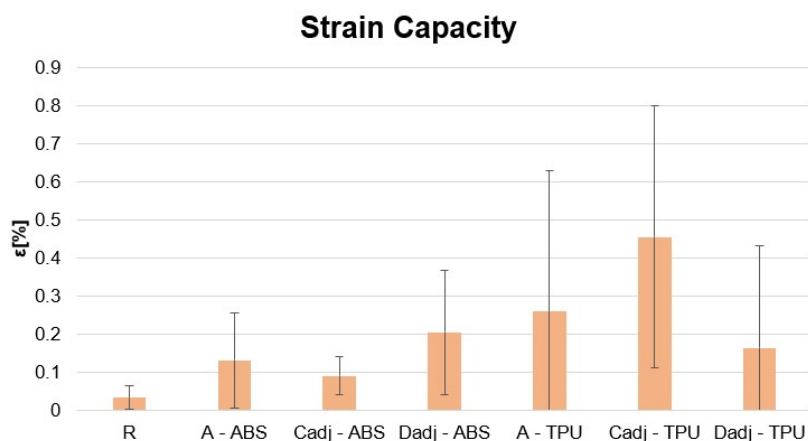
Upon analyzing the strain capacity, as depicted in Fig. 6.48b, both TPU and ABS materials exhibited significantly higher strain capacity compared to the reference sample. Notably, when comparing the strain capacity of TPU and ABS within these samples, TPU demonstrated superior performance in terms of strain capacity for Design C. However, for Design D, the strain capacity of the ABS reinforced material was slightly higher, although the difference was not substantial. It is worth mentioning that the standard deviation for this phase was quite large, indicating some variability in the results. These observations align well with findings from the literature, where TPU is known for its superior ductile behavior when compared to ABS.

During this phase, the honeycomb design for the ABS reinforced material displayed a similar phenomenon to the first phase. As illustrated in Fig. 6.39b, certain crack widths exhibited negative values, indicating crack closure during the tensile testing process. However, this behavior was not observed in the TPU material for the honeycomb design.

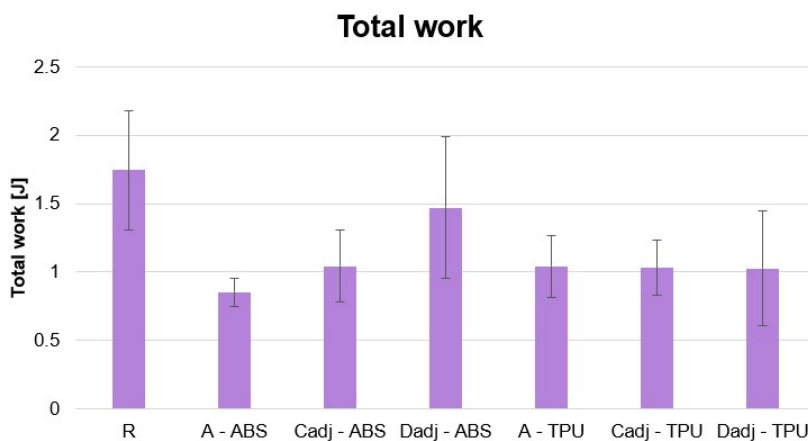
In Fig. 6.48c, the data clearly demonstrates that the reference sample displayed the highest total work conducted. Among the ABS material samples, Design D exhibited the highest work, followed by Design C. Conversely, for the TPU material, both designs showed comparable work. Regarding energy absorption, the findings suggest that the reference sample



(a) Strength samples.



(b) Strain capacity.



(c) Total work.

Figure 6.48: Results phase 2.

exhibited the highest capacity to absorb energy among all the tested samples. This indicates that the addition of reinforcing elements, such as 3D printed polymeric materials, did not improve the energy absorption capability for this phase either. However, reflecting back on the trend observed in the previous phase, the strength once again proved considerably higher for the reference sample in comparison to the reinforced samples, thus resulting in the highest total work.

6.8.1. Comparison phase 1 and 2

When evaluating the strength of the ABS material for Design A, C_{adj} , and D_{adj} (Fig. 6.49), the honeycomb design demonstrated the highest maximum strength, followed by the rectangular one, and finally the re-entrant design. In contrast, for the TPU material, the trend was reversed, with Design A exhibiting the largest strength, and the non-auxetic designs displaying lower strength, albeit not significantly lower.

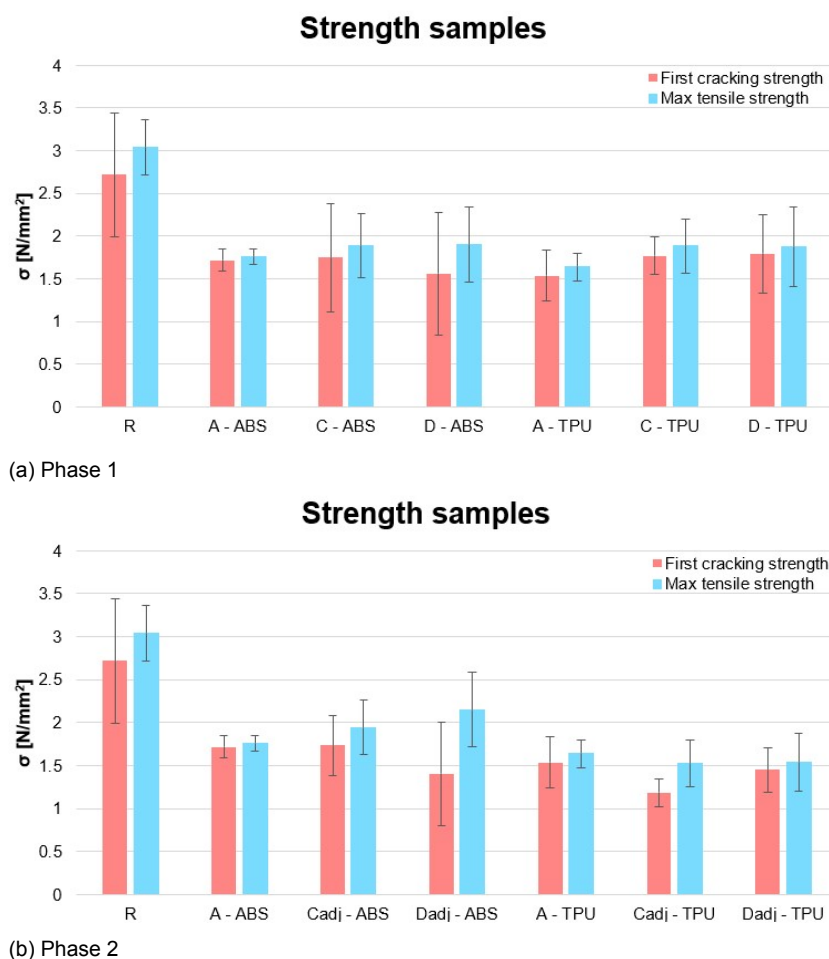


Figure 6.49: Strength comparison phase 1 and 2

For the rectangular designs, Design C and C_{adj} of the ABS material, an increase in volume did not lead to an increase in maximum strength. Conversely, for the TPU material, an increase in volume resulted in a decrease of the maximum strength. When evaluating the strength of Design D for the ABS reinforced sample, Design D_{adj} exhibited a larger strength; however, for TPU, the situation was reversed, with Design D showing higher strength compared to D_{adj} .

When comparing the strain capacity of Design A, C_{adj} , and D_{adj} for the ABS material (Fig. 6.50), the honeycomb design exhibited the largest strain, followed by the re-entrant design, and finally the rectangular one. In contrast, for the TPU material, Design C_{adj} displayed the largest strain capacity, followed by the re-entrant design, and finally the honeycomb. Notably, these designs had the same volume in comparison to each other.

Considering the rectangular designs for the ABS reinforced samples, Design C and C_{adj} , no significant change in the value of the strain capacity was observed (Figures 6.50). However, for the TPU material, an increase in volume resulted in an increase in strain capacity. Similarly, when comparing Design D and D_{adj} for the ABS material, Design D exhibited a slightly larger

strain capacity, although the difference was not substantial. On the other hand, for the TPU material, Design D with the smaller volume displayed a larger strain capacity.

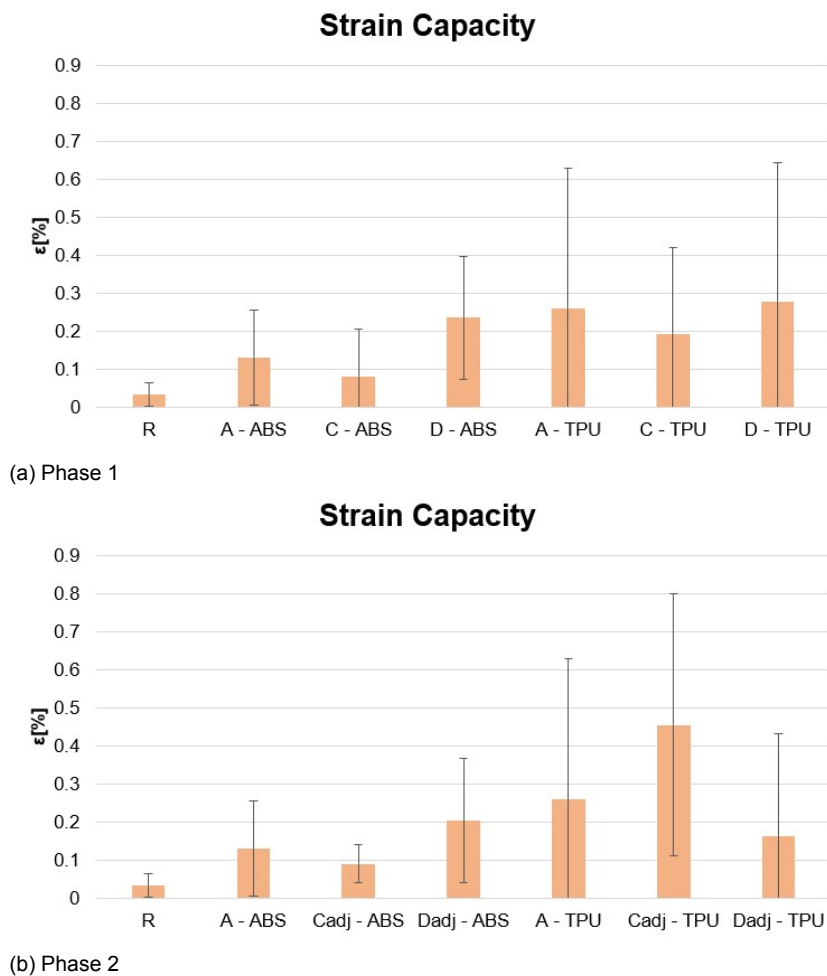


Figure 6.50: Strain capacity comparison phase 1 and 2

6.9. Results Phase 3 ABS

The results obtained during the third phase of this study focusing on the material ABS are presented in this section. The reinforcement was made larger to make it easier for the fibers to pass through. Fig. 6.51 displays the stress-strain behavior of tested samples, all of which clearly also exhibit strain softening characteristics. Despite the enlargement of the reinforcement, the strength of the reference samples continued to surpass that of the reinforced samples.

6.9.1. Design C_{mod}

The stress-strain curves of the tested samples are illustrated in Fig. 6.51. Table 6.25 summarizes the testing results for each sample reinforced with the enlarged rectangular design, including values for initial cracking strength, maximum strength, strain capacity, and total work. Sample $C_{2,mod}$ was chosen for further analysis. Fig. 6.52 displays the stress-strain curve for sample $C_{2,mod}$ in comparison to the reference samples. It can be observed from the Figure that the strength of the reinforced sample is lower than that of the reference sample. Additionally, Fig. 6.53 exhibits the stress-strain curve with the corresponding crack formation pattern indicated. The distinct stages observed in the stress-strain curve (Fig. 6.53a) are further detailed in Table 6.26, providing specific information on the time, stress, and strain at each stage. The cracks of the sample are shown in Fig. 6.54 which also includes a graph that represents the crack width against the measured displacement.

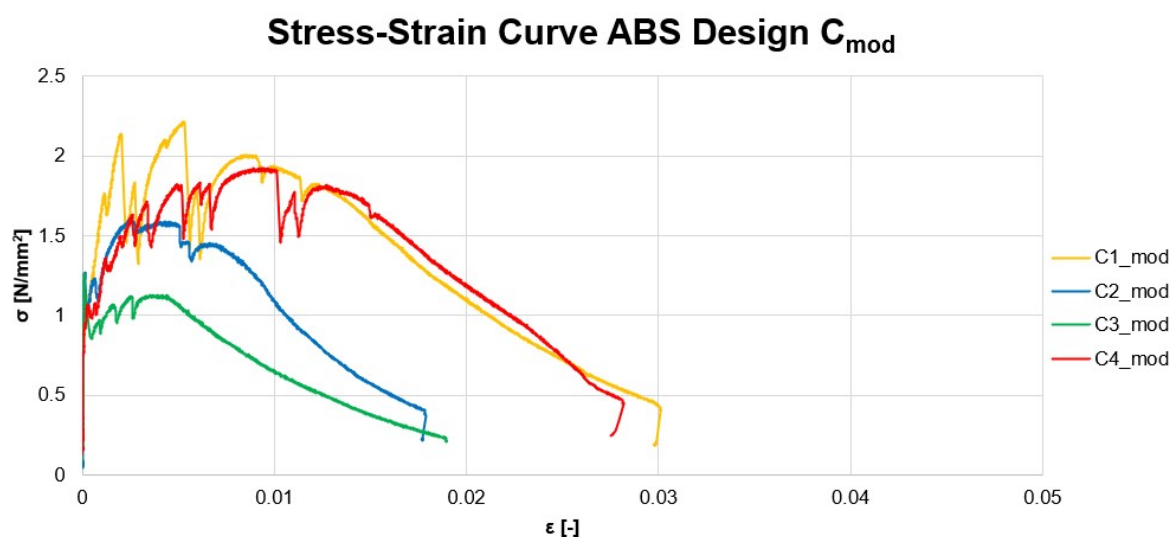


Figure 6.51: Stress-strain curves Design C_{mod} .

	Sample $C_{1,mod}$	Sample $C_{2,mod}$	Sample $C_{3,mod}$	Sample $C_{4,mod}$
First cracking strength [N/mm ²]	0.703	1.271	1.264	1.067
Max tensile strength [N/mm ²]	2.216	1.602	1.264	1.924
Strain capacity [%]	0.533	0.254	0.00814	0.948
Total work [J]	1.965	1.014	0.636	1.461

Table 6.25: Test results for samples with design C_{mod} .

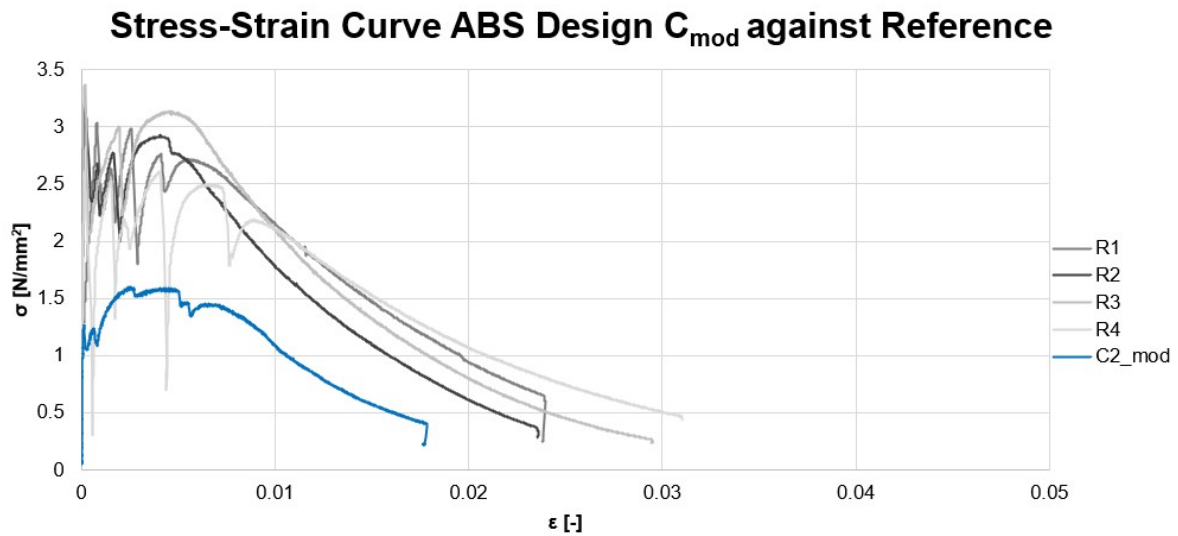


Figure 6.52: Stress-strain curves sample $C_{2,mod}$ against reference.

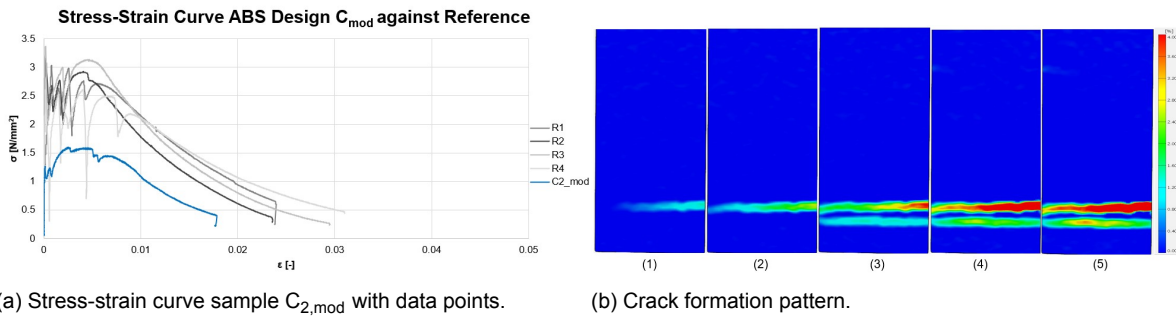
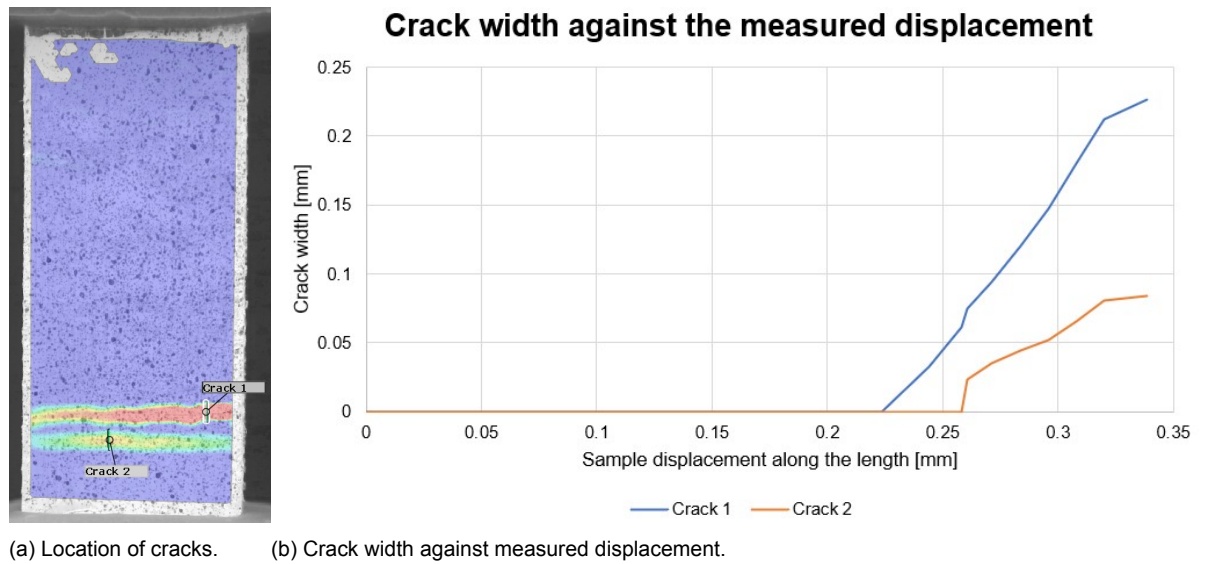


Figure 6.53: Stress-strain curve and crack formation pattern for sample $C_{2,mod}$.

Stage	Time [s]	Stress [N/mm ²]	Strain [-]
1	54	1.691	0.000454
2	114	1.371	0.00432
3	144	1.511	0.00610
4	192	1.384	0.00913
5	240	1.550	0.0121

Table 6.26: Stress and strain corresponding to the different stages.



(a) Location of cracks. (b) Crack width against measured displacement.

Figure 6.54: Crack location alongside the crack width curve for sample $C_{2,mod}$.

6.10. Results Phase 3 TPU

This section elaborates on the findings of the third phase, which focused on the TPU material. Fig. 6.55 showcases the stress-strain behavior of the tested samples, all of which also demonstrate strain-softening characteristics. Much like the ABS-reinforced specimens, the strength of the reference samples continued to exceed that of the reinforced samples.

6.10.1. Design C_{mod}

Fig. 6.55 illustrates the stress-strain behavior of the samples reinforced with enlarged rectangular configuration for the material TPU. The experimental results are presented in Table 6.27, which include the initial cracking strength, maximum tensile strength, strain capacity, and total work for each tested specimen. For a more detailed investigation, sample $C_{3,mod}$ was selected. Fig. 6.56 illustrates the stress-strain curve of sample $C_{3,mod}$ in comparison to the reference samples. The graph reveals that the strength of the reinforced sample was lower than the reference sample. Furthermore, Fig. 6.57 demonstrates the stress-strain curve for sample $C_{3,mod}$, alongside an indication of the pattern of crack formation. The stages identified in the stress-strain curve (Fig. 6.57a) are elaborated upon in Table 6.28, offering specific insights into the timing, stress levels, and strains at each stage. Fig. 6.58 presents the cracks observed in the sample, accompanied by a graph that plots the crack width against the measured displacement.

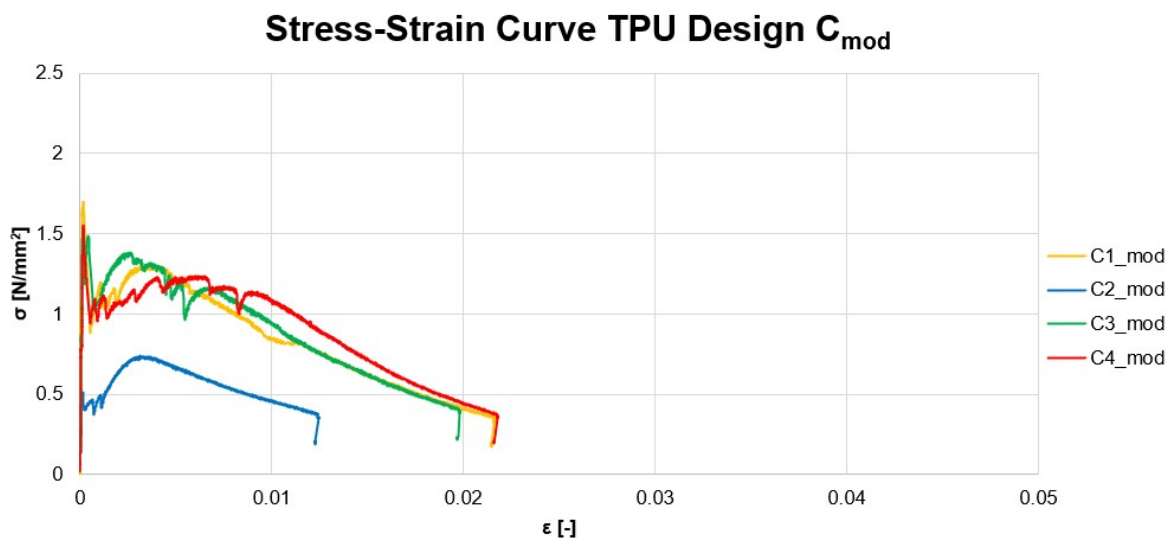


Figure 6.55: Stress-strain curves Design C_{mod} .

	Sample $C_{1,mod}$	Sample $C_{2,mod}$	Sample $C_{3,mod}$	Sample $C_{4,mod}$
First cracking strength [N/mm ²]	1.704	0.515	1.539	1.551
Max tensile strength [N/mm ²]	1.704	0.739	1.539	1.551
Strain capacity [%]	0.014	0.313	0.0144	0.0180
Total work [J]	0.996	0.378	0.899	1.058

Table 6.27: Test results for samples with design C_{mod} .

Stress-Strain Curve TPU Design C_{mod} against Reference

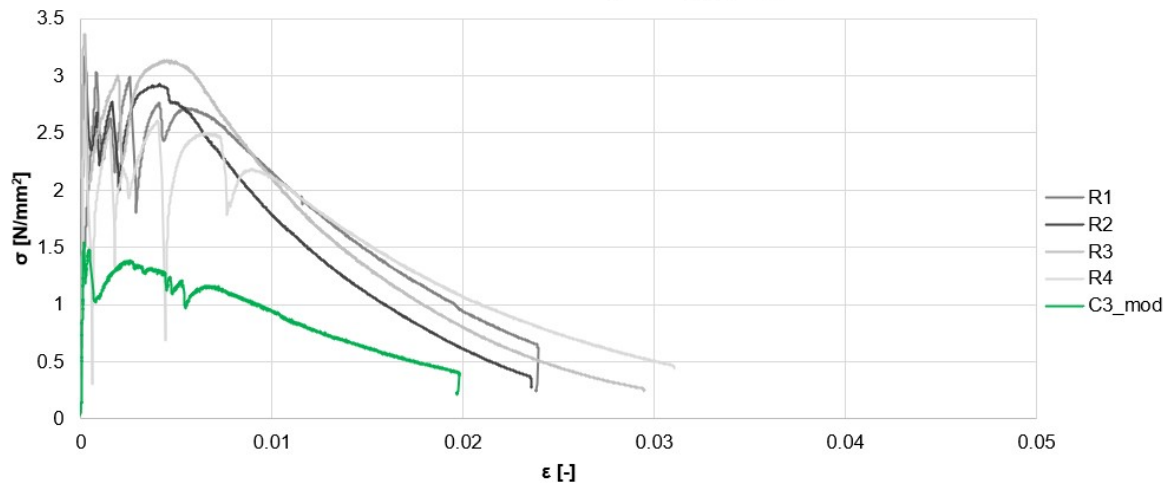
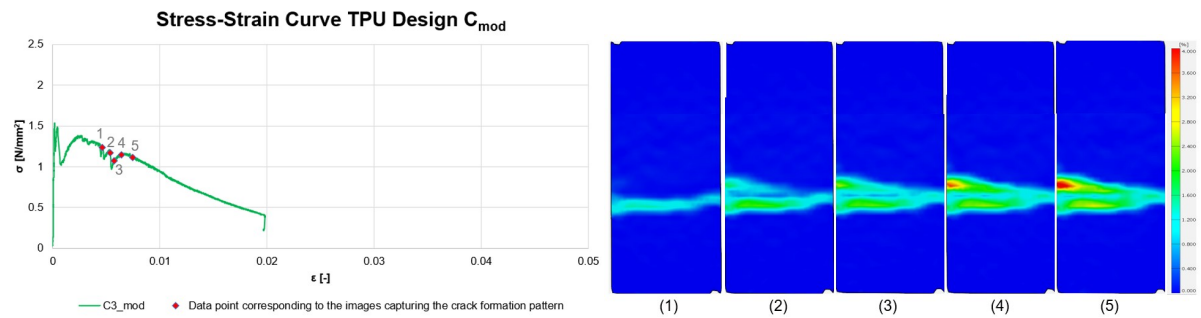


Figure 6.56: Stress-strain curves sample $C_{3,mod}$ against reference.



(a) Stress-strain curve sample $C_{3,mod}$ with data points.

(b) Crack formation pattern.

Figure 6.57: Stress-strain curve and crack formation pattern for sample $C_{3,mod}$.

Stage	Time [s]	Stress [N/mm ²]	Strain [-]
1	120	1.234	0.00461
2	132	1.168	0.00532
3	138	1.075	0.00573
4	150	1.145	0.00641
5	168	1.109	0.00746

Table 6.28: Stress and strain corresponding to the different stages.

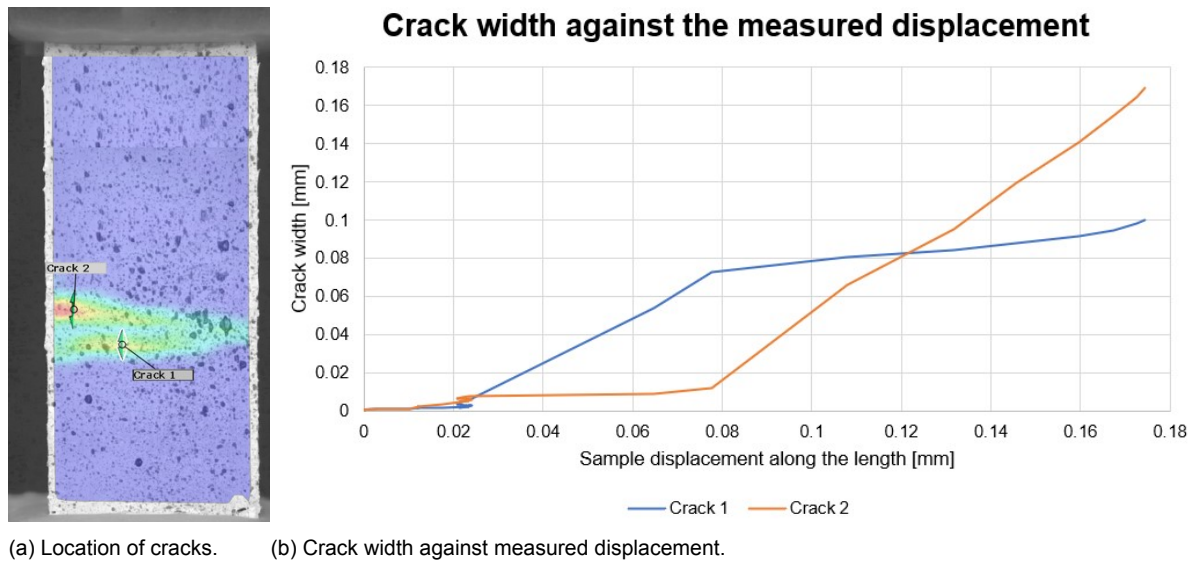


Figure 6.58: Crack location alongside the crack width curve for sample $C_{3,mod}$.

6.11. Analysis and discussing phase 3

Table 6.29 presents the averaged values of the parameters strength, strain capacity, and work for the four samples tested per design, along with their respective standard deviations for phase 3. Fig 6.59a displays the strength of the samples with the standard deviation indicated, allowing for a clear comparison between different designs and phases. Similarly, Fig 6.59b illustrates the strain capacity of the reinforced samples in comparison to the reference samples. Finally, Fig 6.59c shows the total work required for each design.

Design (Reinforcing material)	First cracking strength (Standard deviation) [N/mm ²]	Max tensile strength (Standard deviation) [N/mm ²]	Strain capacity (Standard deviation) [%]	Total work (Standard deviation) [J]
R (-)	2.721 (0.723)	3.042 (0.320)	0.0335 (0.032)	1.745 (0.434)
C _{mod} (ABS)	1.076 (0.266)	1.752 (0.41)	0.436 (0.403)	1.269 (0.573)
C _{mod} (TPU)	1.327 (0.547)	1.383 (0.436)	0.09 (0.149)	0.833 (0.31)

Table 6.29: Test results phase 3.

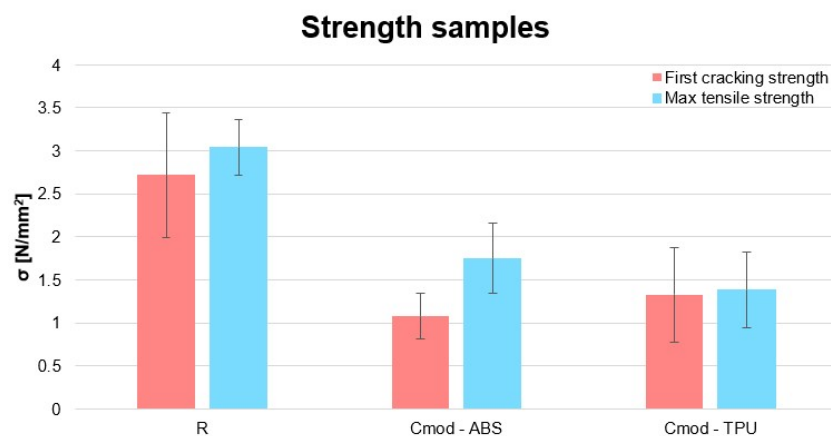
In phase 3, only a design with an angle of 90 degrees was tested for the modified samples. Regarding the tension tests conducted on the modified specimens, both the ABS reinforced and TPU reinforced samples exhibited strain softening behavior as illustrated in Figures 6.51 and 6.55. After the initial cracking of the ABS reinforced samples, they demonstrated the ability to sustain increasing levels of stress, except when reaching failure. This strain hardening behavior was observed across all modified samples reinforced with ABS, except for sample C_{3,mod}. Notably, the maximum tensile strength was typically observed after reaching the first cracking strength. In contrast, the TPU reinforced samples showed a different response. While some samples, such as sample C_{2,mod}, were able to achieve higher stress levels than the initial cracking stress, the overall trend indicated that the TPU reinforced samples were unable to sustain increasing levels of stress beyond the initial crack. However, it is worth mentioning that the TPU reinforced samples exhibited a higher initial cracking strength compared to the ABS reinforced samples (Fig. 6.59a).

These observations clearly indicate different behaviors between the two reinforcing materials. The ABS reinforced samples demonstrated a more favorable response with sustained stress increase after initial cracking, while the TPU reinforced samples showed limited ability to sustain stress beyond the initial crack. This distinction highlights the significant influence of the chosen reinforcing material on the mechanical behavior and performance of the specimens. However, it should be noted that the strength of the reference samples remained higher than that of the reinforced specimens as seen in Fig. 6.59a. This difference may be credited to factors previously mentioned, such as bleeding and segregation.

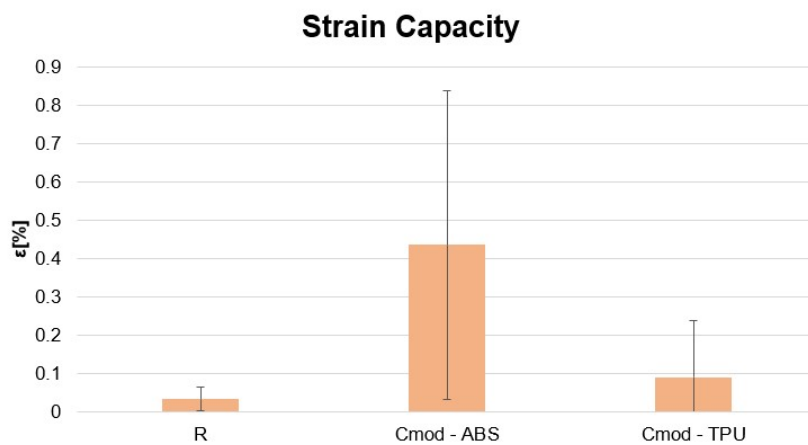
Analyzing the strain capacity, as depicted in Fig. 6.59b, both materials exhibited a higher strain capacity compared to the reference sample. Specifically, the ABS material demonstrated a strain capacity approximately 13 times higher than the reference sample, while the TPU material exhibited around 3 times higher strain capacity. When comparing the strain capacity of the two materials within the modified samples, it is evident that the ABS material outperforms TPU in terms of strain capacity.

Finally, when evaluating the total work conducted (Fig. 6.59c), it is evident that the reference sample exhibited the highest value, with the ABS material showing 0.75 times the work of the reference sample and the TPU material showing 0.5 times the work. These findings suggest that the addition of reinforcing elements, such as 3D printed polymeric materials, did

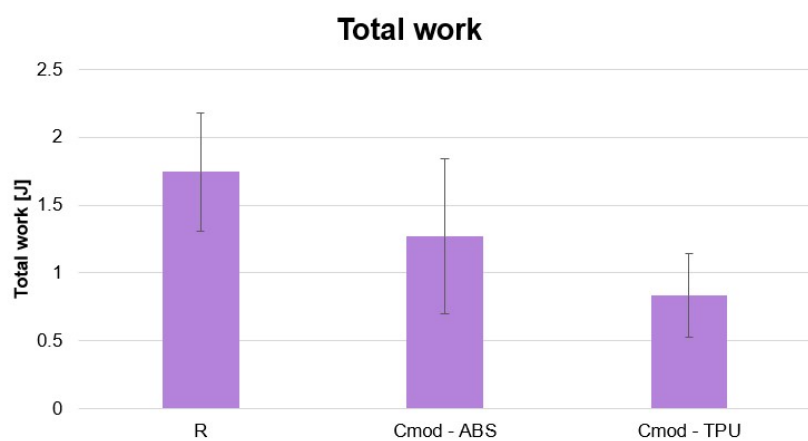
not improve the energy absorption capability for this phase either. However, the standard deviation was quite large.



(a) Strength samples.



(b) Strain capacity.



(c) Total work.

Figure 6.59: Results phase 3.

6.11.1. Comparison phase 2 and 3

The results obtained from phase 2 of the experiment are discussed and compared with those from phase 3. The volume of the modified samples remained constant with the adjusted ones. Fig. 6.60 presents a comparison of the load-displacement curves between the adjusted designs and the modified ones for the materials ABS, while Fig. 6.61 shows the corresponding comparison for the material TPU. Fig. 6.62 presents a comparison between the two phases concerning strength, strain capacity, and total work. The key distinction between the two phases was the cell size of the reinforcement.

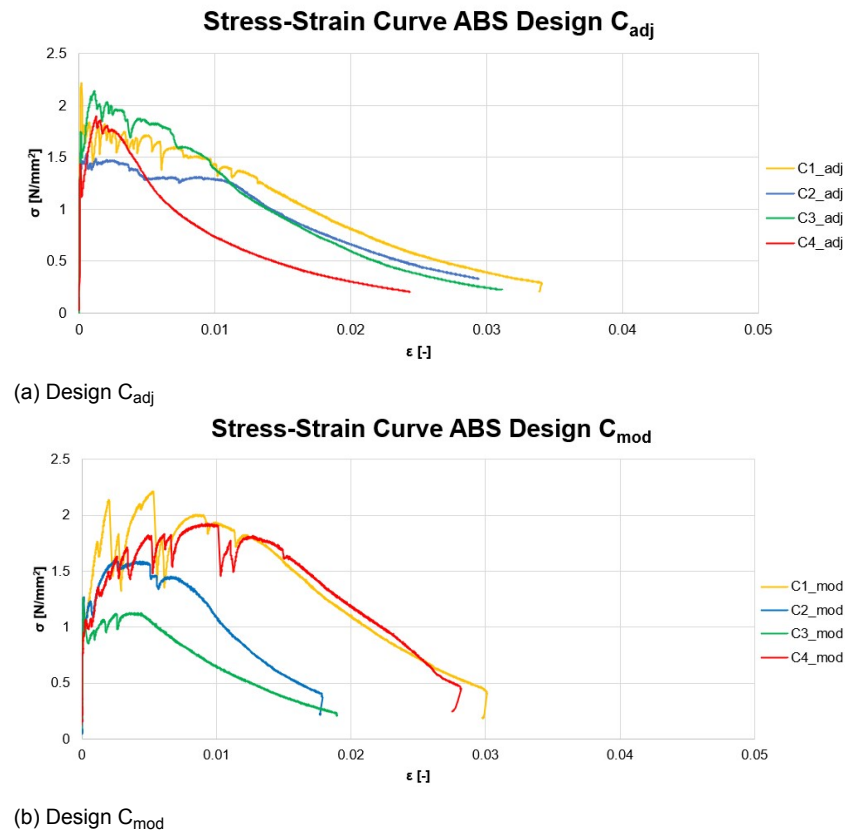


Figure 6.60: Stress-strain curves comparison phase 2 and 3 for material ABS.

When evaluating the tensile strength of the adjusted samples in comparison to the modified samples for both ABS and TPU materials (see Fig. 6.62a), it is evident that the maximum tensile strength for the adjusted samples was slightly higher, though the difference is not significant. Turning to the strain capacity comparison (see Fig. 6.62b), it can be observed that the modified sample exhibited a notably higher value than the adjusted sample for the ABS material. However, for the TPU material, the trend was reversed, with the adjusted sample displaying a higher strain capacity. It is worth noting that the standard deviation for the samples C_{mod} -TPU and C_{mod} -ABS was relatively high, indicating some variability in the results. Further investigation and analysis are required to understand the factors contributing to this variability. Finally, the comparison of the total work revealed that there was no significant change in energy absorption due to a change in the cell size. The reference sample continued to exhibit the largest energy absorption capacity, indicating that altering the cell size did not substantially impact the overall energy absorption capability.

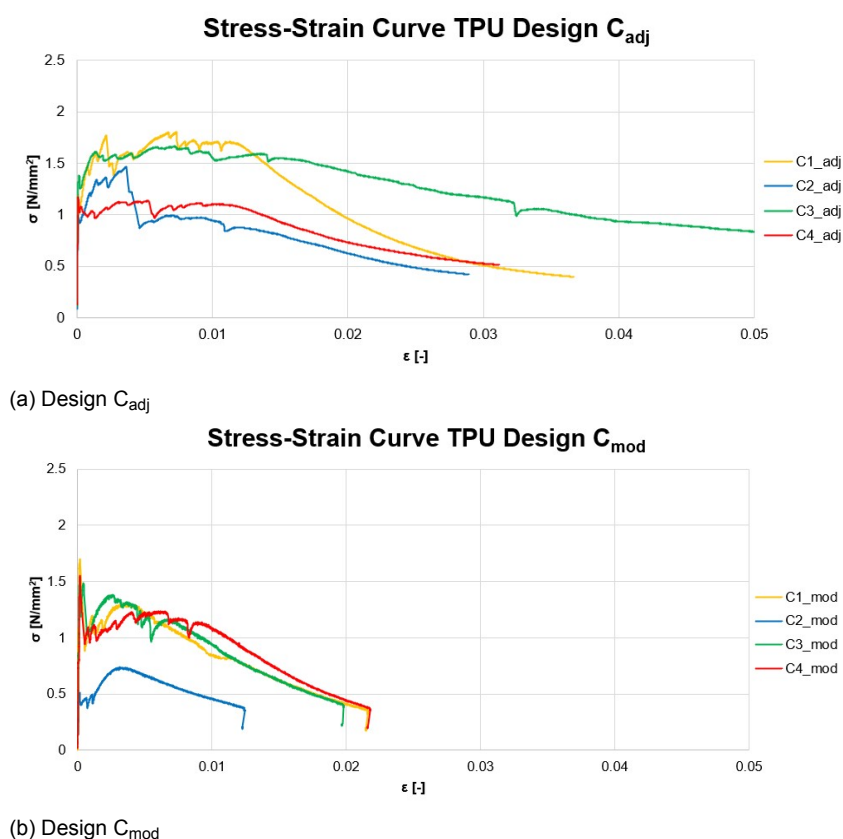


Figure 6.61: Stress-strain curves comparison phase 2 and 3 for material TPU.

6.12. Summary results and discussion samples

This section provides a summary of the results obtained from the different phases of the study. The results clearly demonstrate that it is indeed possible to enhance the deformation capacity of ECC by employing 3D printed auxetic and non-auxetic reinforcements. The 3D printed reinforcement improved the ductility of conventional ECC.

An important finding from the results was that the reference samples exhibited a higher strength compared to the samples with 3D reinforcement casted into them. This difference in strength can be attributed to the occurrence of bleeding and segregation during the casting process of the samples reinforced with the 3D printed meshes. In some cases, excessive air voids were also present in the samples. Additionally, in the samples from phases 1 and 2, the fibers did not uniformly pass through the reinforcement, leading to a non-uniform distribution of fibers. Furthermore, the crack formation pattern exhibited fewer cracks than what was illustrated in the stress-strain curves. This observation could be attributed to the limitations in the resolution of the DIC software and the images captured.

The comparison between the two materials revealed that ABS demonstrated a higher maximum strength than the TPU reinforced samples, emphasizing the superior load-bearing capacity of ABS over TPU. This difference in strength can be attributed to the inherent mechanical properties and material composition of ABS, enabling it to withstand higher forces and stresses in comparison to TPU. These results underscore the significance of material selection and design optimization to achieve desired mechanical performance for specific applications.

Additionally, a distinct difference was observed when comparing the strain capacity of TPU and ABS within these samples, with TPU exhibiting better strain capacity. Such insights emphasize the importance of considering material properties and their influence on performance

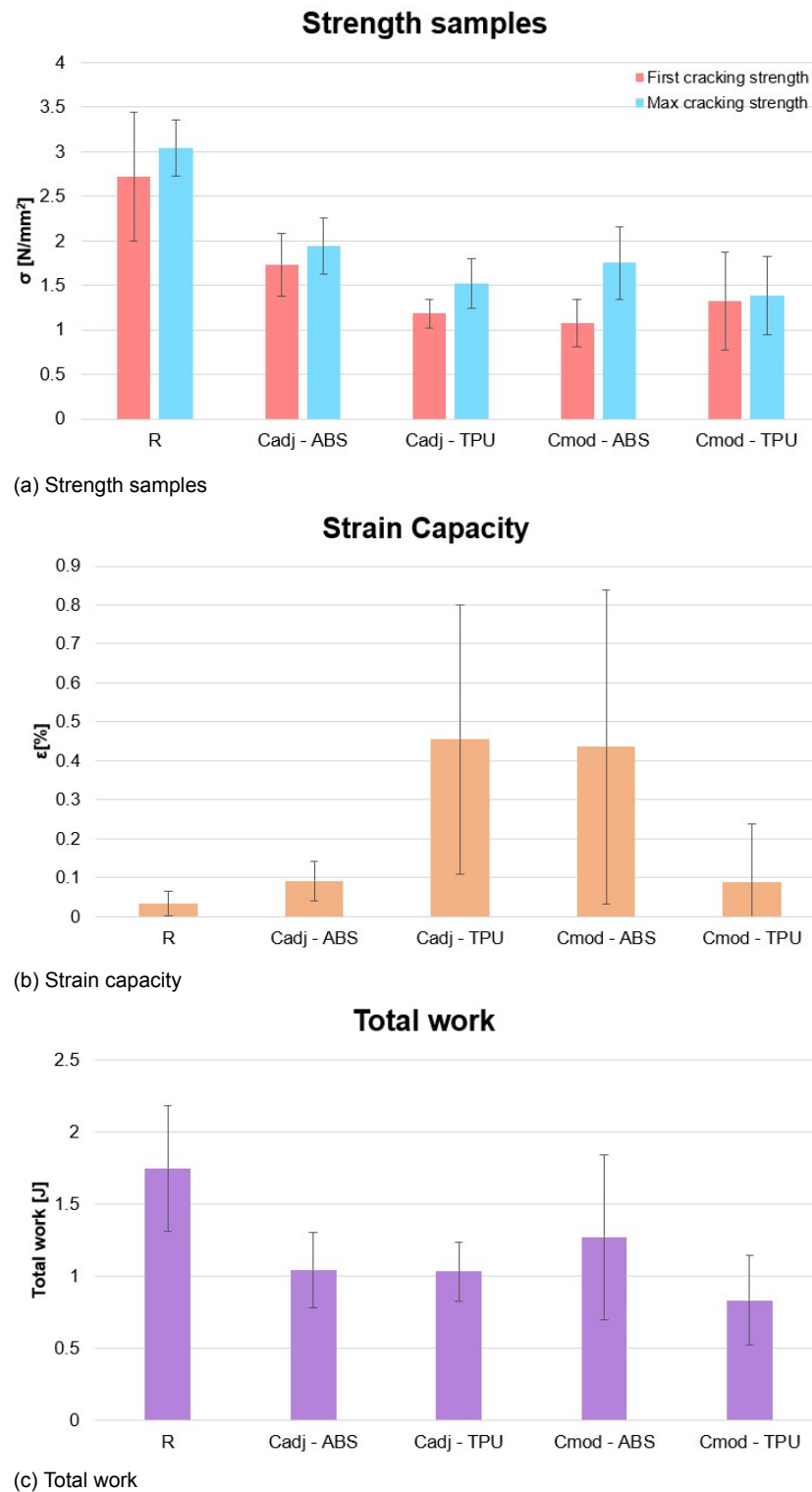


Figure 6.62: Comparison of phase 2 and 3 samples

characteristics when designing structures or components.

The modified samples demonstrate potential for further research, as the strain capacity of the modified samples was observed to be higher when compared to the reference samples without reinforcement. An interesting observation was made regarding the casting quality

of the modified samples, which proved to be superior to that of the first two phases. The incorporation of fibers in the reinforcement allowed for easier embedding, and as a result, less vibration was required during the casting process. While the modified samples only required 10 seconds of vibration, the first two phases necessitated a full minute. This improvement in casting quality has led to reduced imperfections in the modified samples, making them more reliable for subsequent testing and evaluation. Further investigation and exploration of the modified samples are required to fully understand their potential applications and the influence of the modified parameters on their performance. The data obtained from this study serves as a valuable foundation for future research projects aimed at optimizing and advancing the use of these materials in practical engineering applications.

While this study primarily focused on the 3D printed reinforcement and mesh designs, it is important to acknowledge that the performance of the composite is not only determined by the reinforcement design, but also by the properties of the matrix. In this research, OPC was used as the matrix material. However, it is noteworthy that the selection of cement type can significantly influence the overall performance of the composite. Therefore, it is advised to explore the use of different cement types to comprehensively evaluate their impact on the mechanical properties, and overall performance of the composite material.

7

Conclusions and Recommendations

In this chapter we will answer the main research question and two sub-questions that were introduced in chapter 1. In addition to providing answers, this chapter also presents recommendations for future work.

7.1. Conclusions

In this research, the deformation capacity of ECC was studied by incorporating 3D printed auxetic and non-auxetic reinforcements at four different angles for the ABS and TPU materials. Furthermore, numerical models were developed to analyze the behavior of the various reinforcing designs. Additionally, experimental tests, including uniaxial tensile tests, were conducted to assess the mechanical properties of the composite materials.

The main research question of this study was: "Is it possible to increase the deformation capacity of ECC when reinforced with 3D printed auxetic and non-auxetic reinforcements?" The findings from this research clearly demonstrate that the deformation capacity of ECC enhanced by employing 3D printed auxetic and non-auxetic reinforcements. This successful outcome validates the first hypothesis, which stated that "The incorporation of 3D printed reinforcement in ECC will lead to an increase in deformation capacity compared to conventional ECC."

The reference specimen, without such reinforcements, exhibited typical strain hardening behavior observed in ECC, characterized by a relatively low strain capacity, quantified at approximately 0.0335%. Conversely, all specimens reinforced with 3D printed polymeric meshes showcased a remarkable capability to undergo larger strains, exceeding twice the magnitude of strain displayed by the reference sample. This phenomenon is evidenced by the data presented in Figures 6.31b, 6.48b, and 6.59b. Moreover, regardless of their design, all tested reinforced specimens displayed strain hardening during the tension tests. However, distinct responses were observed among reinforced specimens with different reinforcement patterns.

The incorporation of 3D printed auxetic reinforcements into ECC has significant implications for the performance and resilience of the material. This is particularly important in applications where high ductility and deformation capacity are essential. The enhanced deformation capacity observed in ECC, due to these innovative reinforcements, makes the material more suitable for use in scenarios requiring superior strain capacity and improved structural performance.

The first sub-question aimed to explore the influence of different 3D printing materials (ABS and TPU) on the strength and strain capacity of the reinforced ECC. Numerical simulations revealed distinct mechanical differences between the two materials. ABS exhibited significantly higher load-bearing capacity, owing to its high stiffness and ability to withstand larger applied loads before failure. On the other hand, the elastic and flexible nature of TPU provide it with a higher deformation capacity, allowing it to sustain substantial deformations without experiencing failure. Remarkably, the TPU material did not reach the point of fracture even under high applied stress, demonstrating its exceptional strength.

The experimental study further confirmed the higher strength of the ABS reinforced samples compared to the TPU reinforced samples. ABS has a better load-bearing capacity than TPU and can tolerate more forces and strains. Moreover, the strain capacity comparison within the samples revealed that TPU outperformed ABS, highlighting the enhanced ductile behavior of TPU. This underscores the importance of considering material properties in designing structures or components.

In summary, the choice of 3D printing material (ABS or TPU) significantly impacts the strength and strain capacity of the reinforcement. ABS is more suitable for applications requiring structural integrity and resistance to deformation, while TPU is preferred for applications needing high flexibility and deformation capacity without fracture. The specific mechanical requirements of each application should dictate the appropriate choice of printing material for the reinforcement. It is noteworthy that, despite the reference sample exhibiting the highest strength due to the casting process and mixture design, the reinforced samples displayed im-

proved strain capacity compared to the reference sample. This supports the validity of the second hypothesis, stating that "The use of ABS as the 3D printing material for reinforcement in ECC will result in enhanced load-bearing capacity compared to TPU as the 3D printing material."

Finally, the second sub-question revolved around the influence of altering parameters such as angle, volume, and size on the mechanical properties of the reinforcement. The study revealed that these factors indeed have a notable impact on the mechanical properties.

Firstly, the angle of the reinforcing structure played a crucial role in determining its auxetic or non-auxetic behavior. Designs with negative angles, such as bowtie structures, exhibited auxetic behavior characterized by lateral expansion under tensile loading. Conversely, designs with positive angles, like rectangular and honeycomb structures, displayed non-auxetic behavior with lateral contraction under tensile loading. The auxetic designs demonstrated lower stiffness and higher strain capacity, making them suitable for applications where flexibility and deformation capacity are essential. On the other hand, non-auxetic designs, particularly honeycomb structures, exhibited higher stiffness and load-bearing capacity, making them suitable for applications requiring structural rigidity and resistance to deformation.

Secondly, adjusting the volume resulted in changes to parameters such as length, thickness, and width. These alterations influenced the overall strength and stiffness of the reinforcement. Thicker and wider elements generally provided higher load-bearing capacity and stiffness. Moreover, modifying the width and thickness affected the stress distribution within the reinforcement, impacting its overall performance and failure mechanisms. Consequently, an increase of the volume of the reinforcement led to higher overall stiffness and load-bearing capacity, as a larger volume of reinforcing material contributed to a stronger and more rigid structure.

It is crucial to keep in mind that changing these values may result in compromises in a number of mechanical qualities. For example, increasing stiffness and load-bearing capacity may come at the expense of reduced strain capacity and flexibility. Similarly, designs with higher strain capacity and deformation capability may sacrifice some load-bearing capacity and stiffness.

The experimental study confirmed that changes in volume altered the strength and strain capacity of the samples for both materials. Likewise, modifications in cell size also affected the mechanical properties. In summary, the study results validated the hypothesis that altering the angle and size of 3D printed reinforcement designs significantly influenced the mechanical properties of ECC. Different configurations led to increased strain capacity and improved performance, demonstrating the importance of thoughtful parameter selection in enhancing the material's mechanical characteristics.

In conclusion, certain aspects of the reinforced samples demonstrated enhancement, particularly in terms of strain capacity, while other aspects, such as strength, exhibited a decrease. The difference in strength can be attributed to the occurrence of bleeding and segregation during the casting process. The utilization of the modified samples in the casting process may help in reducing imperfections and enhance the overall strength of the reinforced materials.

7.2. Recommendations

There are numerous areas that still require further investigation to improve our understanding. In this study, OPC was utilized as the matrix material. Nonetheless, it should be emphasized that the choice of cement type can have a substantial impact on the overall performance of the composite. As a result, it is highly recommended to explore the application of various cement types to conduct a comprehensive evaluation of their influence on the mechanical properties, and overall performance of the composite material. Such further investigations would contribute significantly to a deeper understanding of the interaction between the matrix and reinforcement components.

Future studies should also consider examining different water-to-binder ratios. While a specific ratio was employed in this research, exploring the effects of varying ratios is essential. The water-to-binder ratio plays a vital role in the hydration process and resulting microstructure, significantly affecting mechanical strength, and other crucial properties [67]. A systematic exploration of a range of water-to-binder ratios will enable a comprehensive understanding of their impact on material performance and characteristics. This investigation will provide valuable insights for optimizing the water-to-binder ratio, thereby enhancing overall material quality and suitability for specific applications.

In addition to fabricating fiber-reinforced samples, it is recommended to prepare reference samples without fibers for the modified samples. This will provide a baseline for comparison and enable a comprehensive analysis of the mechanical properties and performance of the fiber-reinforced samples. By including reference samples, the effects of fiber incorporation can be accurately assessed, allowing for a more thorough understanding of the material behavior and the specific contributions of the fibers.

Moreover, in the context of the modified designs, it is recommended to investigate angles beyond the 90 degree angle examined in this study. Exploring angles such as 52, 63, and 117 degrees will contribute to a more comprehensive understanding of their influence on the behavior and performance of the modified designs. A systematic investigation of various angles will provide insights into factors such as structural integrity, mechanical properties, and overall performance, aiding in optimizing design parameters and expanding the applicability of the modified designs across different scientific and engineering fields.

Additionally, apart from utilizing PE fibers with a length of 6 mm, it is advised to incorporate other fiber types such as PVA fibers and explore different fiber sizes. Such investigations will provide valuable insights into the influence of fiber characteristics, and sizes on the overall performance and behavior of the composite material.

To comprehensively understand the behavior of auxetic materials, it is essential to explore various auxetic shapes and sizes. Investigating different geometric configurations, including aspect ratios, dimensions, and patterns, will deepen our understanding of auxetic properties. This exploration will provide valuable insights into how specific shapes and sizes impact mechanical response, deformation characteristics, and potential applications. Consequently, it will expand the design possibilities and optimization strategies for auxetic materials in various scientific and engineering fields.

Lastly, considering the printing parameters of 3D printing is crucial to the properties of the printed reinforcement. While this research maintained constant printing parameters, it is recommended to conduct further investigations on the influence of these parameters on the characteristics and performance of the printed reinforcement. By systematically varying and optimizing printing parameters, a deeper understanding can be obtained regarding their effects on structural integrity, mechanical properties, and surface quality of the printed reinforcement. This knowledge will contribute to advancing fabrication techniques and optimizing the 3D printing process for reinforced materials, thereby enhancing their overall performance

and applicability.

Summary Recommendations:

- Exploring the influence of cement types
- Examine various water-to-binder ratios
- Explore the modified designs
- Different fiber types and sizes
- Different auxetic shapes and sizes
- Printing parameters

In the world of construction materials, where innovation and resilience are paramount, the exploration of ECC reinforced with 3D printed auxetic and non-auxetic reinforcements has unveiled a realm of endless possibilities. As this chapter comes to a close, structural engineering and material science are about to enter a revolutionary period. A whole new set of attributes will be made possible by this method.

Bibliography

- [1] Yading Xu and Branko Šavija. “Development of strain hardening cementitious composite (SHCC) reinforced with 3D printed polymeric reinforcement: Mechanical properties”. In: *Composites Part B: Engineering* 174 (2019), p. 107011.
- [2] Chu-Kia Wang and Charles G Salmon. “Reinforced concrete design”. In: (1979).
- [3] Ashfaque Jhatial et al. “Effect of steel fibres on the compressive and flexural strength of concrete”. In: *International Journal of ADVANCED AND APPLIED SCIENCES* 5 (Aug. 2018), pp. 16–21. DOI: [10.21833/ijaas.2018.10.003](https://doi.org/10.21833/ijaas.2018.10.003).
- [4] Asfandiar K Dhalla and George Winter. “Steel ductility measurements”. In: *Journal of the Structural Division* 100.2 (1974), pp. 427–444.
- [5] Perumalsamy N Balaguru and Surendra P Shah. “Fiber-reinforced cement composites”. In: (1992).
- [6] Qiang Fu et al. “Effect and action mechanism of fibers on mechanical behavior of hybrid basalt-polypropylene fiber-reinforced concrete”. In: *Structures* 34 (2021), pp. 3596–3610. ISSN: 2352-0124. DOI: <https://doi.org/10.1016/j.istruc.2021.09.097>. URL: <https://www.sciencedirect.com/science/article/pii/S2352012421009449>.
- [7] Kosmas Sideris and P. Manita. “Residual mechanical characteristics and spalling resistance of fiber reinforced self-compacting concretes exposed to elevated temperatures”. In: *Construction and Building Materials* 41 (Apr. 2013), pp. 296–302. DOI: [10.1016/j.conbuildmat.2012.11.093](https://doi.org/10.1016/j.conbuildmat.2012.11.093).
- [8] Victor Li. “Advances in ECC research”. In: *ACI Special Publication on Concrete: Material Science to Applications* (June 2011).
- [9] Victor Li, H. Kong, and Yin-Wen Chan. “Development of Self-Compacting Engineered Cementitious Composites”. In: (1998).
- [10] Jinying Liu and Victor C Li. “Strain hardening behavior of engineered cementitious composites”. In: *Journal of materials in civil engineering* 17.4 (2005), pp. 441–448.
- [11] Victor C. Li et al. “On the emergence of 3D printable Engineered, Strain Hardening Cementitious Composites (ECC/SHCC)”. In: *Cement and Concrete Research* 132 (2020), p. 106038. ISSN: 0008-8846. DOI: <https://doi.org/10.1016/j.cemconres.2020.106038>. URL: <https://www.sciencedirect.com/science/article/pii/S0008884620300557>.
- [12] Victor Li, SX Wang, and C. Wu. “Tensile strain-hardening behavior of polyvinyl alcohol engineered cementitious composite (PVA-ECC)”. In: *ACI Materials Journal* 98 (Nov. 2001), pp. 483–492.
- [13] Kamal H Khayat. “Self-consolidating concrete: applying what we know”. In: *Concrete international* 24.7 (2002), pp. 49–54.
- [14] Kamal H Khayat. “Innovative cementitious composites for the next century”. In: *Materials and Structures* 36.262 (2003), pp. 624–632.

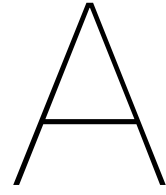
- [15] Edwin John Hearn. "Mechanics of Materials 2: The mechanics of elastic and plastic deformation of solids and structural materials". In: (1997).
- [16] Guijun Yang and Soo-Jin Park. "Deformation of Single Crystals, Polycrystalline Materials, and Thin Films: A Review". In: *Materials* 12.12 (2019). ISSN: 1996-1944. DOI: [10.3390/ma12122003](https://doi.org/10.3390/ma12122003). URL: <https://www.mdpi.com/1996-1944/12/12/2003>.
- [17] David R.H. Jones and Michael F. Ashby. "Chapter 3 - Elastic Moduli". In: (2019). Ed. by David R.H. Jones and Michael F. Ashby, pp. 31–47. DOI: <https://doi.org/10.1016/B978-0-08-102051-7.00003-8>. URL: <https://www.sciencedirect.com/science/article/pii/B9780081020517000038>.
- [18] Jan GM Van Mier. "Concrete fracture: a multiscale approach". In: (2012).
- [19] Roderic Lakes. "Advances in negative Poisson's ratio materials". In: *Advanced Materials* 5.4 (1993), pp. 293–296. DOI: <https://doi.org/10.1002/adma.19930050416>. eprint: <https://onlinelibrary.wiley.com/doi/pdf/10.1002/adma.19930050416>. URL: <https://onlinelibrary.wiley.com/doi/abs/10.1002/adma.19930050416>.
- [20] George Neville Greaves et al. "Poisson's ratio and modern materials". In: *Nature materials* 10.11 (2011), pp. 823–837.
- [21] Andrew Horwood and Nachiappan Chockalingam. "Chapter 2 - Principles of materials science". In: (2023). Ed. by Andrew Horwood and Nachiappan Chockalingam, pp. 91–174. DOI: <https://doi.org/10.1016/B978-0-323-85212-8.00002-x>. URL: <https://www.sciencedirect.com/science/article/pii/B978032385212800002x>.
- [22] Harry Marsh and Francisco Rodríguez-Reinoso. "CHAPTER 2 - Activated Carbon (Origins)". In: (2006). Ed. by Harry Marsh and Francisco Rodríguez-Reinoso, pp. 13–86. DOI: <https://doi.org/10.1016/B978-008044463-5/50016-9>. URL: <https://www.sciencedirect.com/science/article/pii/B9780080444635500169>.
- [23] Ken E Evans. "Auxetic polymers: a new range of materials". In: *Endeavour* 15.4 (1991), pp. 170–174. ISSN: 0160-9327. DOI: [https://doi.org/10.1016/0160-9327\(91\)90123-s](https://doi.org/10.1016/0160-9327(91)90123-s). URL: <https://www.sciencedirect.com/science/article/pii/016093279190123S>.
- [24] Chuanwei Huang and Lang Chen. "Negative Poisson's Ratio in Modern Functional Materials". In: *Advanced Materials* 28.37 (2016), pp. 8079–8096. DOI: <https://doi.org/10.1002/adma.201601363>. eprint: <https://onlinelibrary.wiley.com/doi/pdf/10.1002/adma.201601363>. URL: <https://onlinelibrary.wiley.com/doi/abs/10.1002/adma.201601363>.
- [25] Andrew Alderson and K. Alderson. "Auxetic materials". In: *Proceedings of The Institution of Mechanical Engineers Part G-journal of Aerospace Engineering - PROC INST MECH ENG G-J A E* 221 (Apr. 2007), pp. 565–575. DOI: [10.1243/09544100JAERO185](https://doi.org/10.1243/09544100JAERO185).
- [26] Fatih Usta, Halit S. Türkmen, and Fabrizio Scarpa. "Low-velocity impact resistance of composite sandwich panels with various types of auxetic and non-auxetic core structures". In: *Thin-Walled Structures* 163 (2021), p. 107738. ISSN: 0263-8231. DOI: <https://doi.org/10.1016/j.tws.2021.107738>. URL: <https://www.sciencedirect.com/science/article/pii/S0263823121002019>.
- [27] Hang Yang and Li Ma. "Design and characterization of axisymmetric auxetic metamaterials". In: *Composite Structures* 249 (2020), p. 112560. ISSN: 0263-8223. DOI: <https://doi.org/10.1016/j.compstruct.2020.112560>. URL: <https://www.sciencedirect.com/science/article/pii/S0263822320313131>.

- [28] Jianjun Zhang et al. "Tensile behavior of an auxetic structure: Analytical modeling and finite element analysis". In: *International Journal of Mechanical Sciences* 136 (2018), pp. 143–154. ISSN: 0020-7403. DOI: <https://doi.org/10.1016/j.ijmecsci.2017.12.029>. URL: <https://www.sciencedirect.com/science/article/pii/S0020740317322476>.
- [29] X. Lu, V.B.C. Tan, and T.E. Tay. "Auxeticity of monoclinic tetrachiral honeycombs". In: *Composite Structures* 241 (2020), p. 112067. ISSN: 0263-8223. DOI: <https://doi.org/10.1016/j.compstruct.2020.112067>. URL: <https://www.sciencedirect.com/science/article/pii/S0263822319342837>.
- [30] Zhonggang Wang. "Recent advances in novel metallic honeycomb structure". In: *Composites Part B: Engineering* 166 (2019), pp. 731–741. ISSN: 1359-8368. DOI: <https://doi.org/10.1016/j.compositesb.2019.02.011>. URL: <https://www.sciencedirect.com/science/article/pii/S1359836818328178>.
- [31] Xin Ren et al. "Auxetic metamaterials and structures: a review". In: *Smart materials and structures* 27.2 (2018), p. 023001.
- [32] Lulu Wei et al. "A novel star auxetic honeycomb with enhanced in-plane crushing strength". In: *Thin-Walled Structures* 149 (2020), p. 106623. ISSN: 0263-8231. DOI: <https://doi.org/10.1016/j.tws.2020.106623>. URL: <https://www.sciencedirect.com/science/article/pii/S0263823119315423>.
- [33] Jianjun Zhang, Guoxing Lu, and Zhong You. "Large deformation and energy absorption of additively manufactured auxetic materials and structures: A review". In: *Composites Part B: Engineering* 201 (2020), p. 108340. ISSN: 1359-8368. DOI: <https://doi.org/10.1016/j.compositesb.2020.108340>. URL: <https://www.sciencedirect.com/science/article/pii/S1359836820333898>.
- [34] Roderic Lakes. "Foam Structures with a Negative Poisson's Ratio". In: *Science* 235.4792 (1987), pp. 1038–1040. DOI: [10.1126/science.235.4792.1038](https://doi.org/10.1126/science.235.4792.1038). eprint: <https://www.science.org/doi/pdf/10.1126/science.235.4792.1038>. URL: <https://www.science.org/doi/abs/10.1126/science.235.4792.1038>.
- [35] Dixon Correa, Carolyn Seepersad, and Michael Haberman. "Mechanical design of negative stiffness honeycomb materials". In: *Integrating Materials and Manufacturing Innovation* 4 (Dec. 2015). DOI: [10.1186/s40192-015-0037-9](https://doi.org/10.1186/s40192-015-0037-9).
- [36] Graeme W. Milton. "Composite materials with poisson's ratios close to -1 ". In: *Journal of the Mechanics and Physics of Solids* 40.5 (1992), pp. 1105–1137. ISSN: 0022-5096. DOI: [https://doi.org/10.1016/0022-5096\(92\)90063-8](https://doi.org/10.1016/0022-5096(92)90063-8). URL: <https://www.sciencedirect.com/science/article/pii/0022509692900638>.
- [37] K.L Alderson and K.E Evans. "The fabrication of microporous polyethylene having a negative Poisson's ratio". In: *Polymer* 33.20 (1992), pp. 4435–4438. ISSN: 0032-3861. DOI: [https://doi.org/10.1016/0032-3861\(92\)90294-7](https://doi.org/10.1016/0032-3861(92)90294-7). URL: <https://www.sciencedirect.com/science/article/pii/0032386192902947>.
- [38] Jianjun Zhang and Guoxing Lu. "Dynamic tensile behaviour of re-entrant honeycombs". In: *International Journal of Impact Engineering* 139 (2020), p. 103497. ISSN: 0734-743X. DOI: <https://doi.org/10.1016/j.ijimpeng.2019.103497>. URL: <https://www.sciencedirect.com/science/article/pii/S0734743X19303197>.

- [39] Tiantian Li et al. "Exploiting negative Poisson's ratio to design 3D-printed composites with enhanced mechanical properties". In: *Materials Design* 142 (2018), pp. 247–258. ISSN: 0264-1275. DOI: <https://doi.org/10.1016/j.matdes.2018.01.034>. URL: <https://www.sciencedirect.com/science/article/pii/S026412751830042X>.
- [40] Christa P. de Jonge, Helena M. A. Kolken, and Amir A. Zadpoor. "Non-Auxetic Mechanical Metamaterials". In: *Materials* 12.4 (2019). ISSN: 1996-1944. DOI: [10.3390/ma12040635](https://doi.org/10.3390/ma12040635). URL: <https://www.mdpi.com/1996-1944/12/4/635>.
- [41] G Domínguez-Rodríguez, JJ Ku-Herrera, and A Hernández-Pérez. "An assessment of the effect of printing orientation, density, and filler pattern on the compressive performance of 3D printed ABS structures by fuse deposition". In: *The International Journal of Advanced Manufacturing Technology* 95 (2018), pp. 1685–1695.
- [42] Amelia Carolina Sparavigna. "Paper-based Metamaterials: Honeycomb and Auxetic Structures". In: *International Journal of Sciences* (Jan. 2014), pp. 22–25. DOI: [10.18483/ijSci.597](https://doi.org/10.18483/ijSci.597).
- [43] Kaufui Wong. "K.V. Wong, A.Hernandez, "A Review of Additive Manufacturing," ISRN Mechanical Engineering, Vol 2012 (2012), Article ID 208760, 10 pages." In: *ISRN Mechanical Engineering* 2012 (Aug. 2012). DOI: [10.5402/2012/208760](https://doi.org/10.5402/2012/208760).
- [44] I. Gibson et al. *Additive Manufacturing Technologies*. 3rd. Springer, 2015. DOI: [10.1007/978-1-4939-2113-3](https://doi.org/10.1007/978-1-4939-2113-3). URL: <https://doi.org/10.1007/978-1-4939-2113-3>.
- [45] N. Hopkinson, Richard Hague, and Philip Dickens. "Rapid Manufacturing: An Industrial Revolution for the Digital Age". In: (May 2006), pp. 1–285. DOI: [10.1002/0470033991](https://doi.org/10.1002/0470033991).
- [46] Tuan D. Ngo et al. "Additive manufacturing (3D printing): A review of materials, methods, applications and challenges". In: *Composites Part B: Engineering* 143 (2018), pp. 172–196. ISSN: 1359-8368. DOI: <https://doi.org/10.1016/j.compositesb.2018.02.012>. URL: <https://www.sciencedirect.com/science/article/pii/S1359836817342944>.
- [47] Jahar Bhowmik. "Optimization of Fused Deposition Modeling Process Parameters: A Review of Current Research and Future Prospects". In: (May 2019). DOI: <https://doi.org/10.1007/s40436-014-0097-7>.
- [48] Anoop Kumar Sood, R.K. Ohdar, and S.S. Mahapatra. "Parametric appraisal of mechanical property of fused deposition modelling processed parts". In: *Materials Design* 31.1 (2010), pp. 287–295. ISSN: 0261-3069. DOI: <https://doi.org/10.1016/j.matdes.2009.06.016>. URL: <https://www.sciencedirect.com/science/article/pii/S0261306909002945>.
- [49] Seyed Hamid Reza Sanei and Diana Popescu. "3D-Printed Carbon Fiber Reinforced Polymer Composites: A Systematic Review". In: *Journal of Composites Science* 4.3 (2020). ISSN: 2504-477X. DOI: [10.3390/jcs4030098](https://doi.org/10.3390/jcs4030098). URL: <https://www.mdpi.com/2504-477X/4/3/98>.
- [50] R. Srinivasan et al. "Prediction of tensile strength in FDM printed ABS parts using response surface methodology (RSM)". In: *Materials Today: Proceedings* 27 (2020). First International conference on Advanced Lightweight Materials and Structures, pp. 1827–1832. ISSN: 2214-7853. DOI: <https://doi.org/10.1016/j.matpr.2020.03.788>. URL: <https://www.sciencedirect.com/science/article/pii/S2214785320325700>.

- [51] Xin Wang et al. "3D printing of polymer matrix composites: A review and prospective". In: *Composites Part B: Engineering* 110 (2017), pp. 442–458. ISSN: 1359-8368. DOI: <https://doi.org/10.1016/j.compositesb.2016.11.034>. URL: <https://www.sciencedirect.com/science/article/pii/S1359836816321230>.
- [52] Tao Xu et al. "Mechanical Properties of Additively Manufactured Thermoplastic Polyurethane (TPU) Material Affected by Various Processing Parameters". In: *Polymers* 12 (Dec. 2020), p. 3010. DOI: [10.3390/polym12123010](https://doi.org/10.3390/polym12123010).
- [53] J.D Moore. "Acrylonitrile-butadiene-styrene (ABS) - a review". In: *Composites* 4.3 (1973), pp. 118–130. ISSN: 0010-4361. DOI: [https://doi.org/10.1016/0010-4361\(73\)90585-5](https://doi.org/10.1016/0010-4361(73)90585-5). URL: <https://www.sciencedirect.com/science/article/pii/S0010436173905855>.
- [54] CS Schollenberger, H Scptt, and GR Moore. "Polyurethan VC, a virtually crosslinked elastomer". In: *Rubber Chemistry and Technology* 35.3 (1962), pp. 742–752.
- [55] H.J. Qi and M.C. Boyce. "Stress–strain behavior of thermoplastic polyurethanes". In: *Mechanics of Materials* 37.8 (2005), pp. 817–839. ISSN: 0167-6636. DOI: <https://doi.org/10.1016/j.mechmat.2004.08.001>. URL: <https://www.sciencedirect.com/science/article/pii/S0167663604001140>.
- [56] Jianhua Xiao and Yanfeng Gao. "The manufacture of 3D printing of medical grade TPU". In: *Progress in Additive Manufacturing* 2 (2017), pp. 117–123.
- [57] F.M. Sánchez-Arévalo and G. Pulos. "Use of digital image correlation to determine the mechanical behavior of materials". In: *Materials Characterization* 59.11 (2008), pp. 1572–1579. ISSN: 1044-5803. DOI: <https://doi.org/10.1016/j.matchar.2008.02.002>. URL: <https://www.sciencedirect.com/science/article/pii/S1044580308000636>.
- [58] Zabala Jorge, Peñafiel Ronny, and Oscar Sotomayor. "On the Digital Image Correlation Technique". In: *Materials Today: Proceedings* 49 (2022). Advances in Mechanical Engineering Trends, pp. 79–84. ISSN: 2214-7853. DOI: <https://doi.org/10.1016/j.matpr.2021.07.476>. URL: <https://www.sciencedirect.com/science/article/pii/S2214785321053475>.
- [59] Bing Pan et al. "Two-dimensional digital image correlation for in-plane displacement and strain measurement: a review". In: *Measurement science and technology* 20.6 (2009), p. 062001.
- [60] Nick McCormick and Jerry Lord. "Digital Image Correlation". In: *Materials Today* 13.12 (2010), pp. 52–54. ISSN: 1369-7021. DOI: [https://doi.org/10.1016/S1369-7021\(10\)70235-2](https://doi.org/10.1016/S1369-7021(10)70235-2). URL: <https://www.sciencedirect.com/science/article/pii/S1369702110702352>.
- [61] B. Mobasher. "5 - Textile fiber composites: Testing and mechanical behavior". In: (2016). Ed. by Thanasis Triantafillou, pp. 101–150. DOI: <https://doi.org/10.1016/B978-1-78242-446-8.00006-9>. URL: <https://www.sciencedirect.com/science/article/pii/B9781782424468000069>.
- [62] "Abaqus Analysis User's Guide: Overview of the Abaqus finite element system". In: *Abaqus 6.13, SIMULIA* (2013). URL: <http://130.149.89.49:2080/v2016/books/usb/default.htm>.
- [63] "Abaqus Analysis User's Guide: Part types". In: *Abaqus 6.13, SIMULIA* (2013). URL: <http://130.149.89.49:2080/v2016/books/usb/default.htm>.

- [64] “Abaqus Analysis User’s Guide: Understanding the role of the Step module”. In: *Abaqus 6.13, SIMULIA* (2013). URL: <http://130.149.89.49:2080/v2016/books/usb/default.htm>.
- [65] “Abaqus Analysis User’s Guide: Understanding constraints”. In: *Abaqus 6.13, SIMULIA* (2013). URL: <http://130.149.89.49:2080/v2016/books/usb/default.htm>.
- [66] Christopher Joseph Zmuda. “Design of Structural Composites with Auxetic Behavior”. In: (Apr. 2017).
- [67] P.-C Aitcin. “The importance of the water–cement and water–binder ratios”. In: (Dec. 2016), pp. 3–13. DOI: [10.1016/B978-0-08-100693-1.00001-1](https://doi.org/10.1016/B978-0-08-100693-1.00001-1).



Tables

Design	Length [mm]	Width [mm]	Height [mm]
R	100	40	10
A	94.5	40	10
C	100	40	10
D	101.7	40	10
C _{adj}	100	40	10
D _{adj}	101.7	40	10
C _{mod}	108	40	10

Table A.1: Desired dimensions of the samples

Sample	Reinforcing Material	L [mm]	W [mm]	H1 [mm]	H2 [mm]	H3 [mm]	Avg H [mm]
R1		98	40	10.5	11	10.5	10.667
R2		99	40	9	9	10	9.333
R3		100	40	10	10	10	10
R4		99	40	16	16	16	16
A1	ABS	94	40	10	10.5	10	10.167
A2	ABS	91	40	11	11	11.5	11.167
A3	ABS	94	40	10	9	10	9.667
A4	ABS	94	40	10	11	12	11
C1	ABS	98	40	11	13	12	12
C2	ABS	98	40	11	11	10	10.667
C3	ABS	99	40	12	12	11	11.667
C4	ABS	98	40	10	11	10	10.333
D1	ABS	98	40	12	12.5	12	12.167
D2	ABS	101	40	10	11	11	10.667
D3	ABS	99	40	10	10	9	9.667
D4	ABS	99	40	11	11	12	11.333
A1	TPU	92	40	13	13	14	13.333
A2	TPU	93	40	10	10	10	10
A3	TPU	93	40	13	13	13	13
A4	TPU	93	40	11	11	11	11
C1	TPU	98	40	14	15	16	15
C2	TPU	99	40	16	16	15	15.667
C3	TPU	100	40	16	16	16	16
C4	TPU	99	40	12	12	12	12
D1	TPU	101	40	12	12	12	12
D2	TPU	101	40	10	12	13	11.667
D3	TPU	101	40	13	13	13	13
D4	TPU	99.5	40	12	10	12	11.333
C _{1,adj}	ABS	98	40	12	13	12	12.333
C _{2,adj}	ABS	98	40	8	9	10	9
C _{3,adj}	ABS	101	40	11	11	11	11
C _{4,adj}	ABS	97	40	12	12	12	12
D _{1,adj}	ABS	101	40	10	9	9	9.333
D _{2,adj}	ABS	100	40	10	11	11	11
D _{3,adj}	ABS	103	40	12	12	12	12
D _{4,adj}	ABS	102	40	12	11.5	11	11.5
C _{1,adj}	TPU	100	40	12	12	12	12
C _{2,adj}	TPU	100	40	10	10	11	10.333
C _{3,adj}	TPU	100	40	11	10	10	10.33
C _{4,adj}	TPU	101.5	40	12	11	11	11.333
D _{1,adj}	TPU	101	40	12	12	12	12
D _{2,adj}	TPU	99	40	9	10	11	10
D _{3,adj}	TPU	101	40	10	12	11	11
D _{4,adj}	TPU	101.5	40	10	10	10	10

Table A.2: Actual dimensions of the cut samples

Sample	Reinforcing Material	L [mm]	W [mm]	H1 [mm]	H2 [mm]	H3 [mm]	Avg H [mm]
C _{1,mod}	ABS	107	40	14	13	14	13.667
C _{2,mod}	ABS	108	40	12	12	12.5	12.167
C _{3,mod}	ABS	107	40	11	11	12	11.333
C _{4,mod}	ABS	107	40	11	11	10	10.667
C _{1,mod}	TPU	107	40	13	13	14	13.333
C _{2,mod}	TPU	109	40	11	13	14	12.667
C _{3,mod}	TPU	108	40	10	12	13	11.667
C _{4,mod}	TPU	109	40	12	14	13	13

Table A.3: Actual dimensions of the cut samples

B

Numerical Study

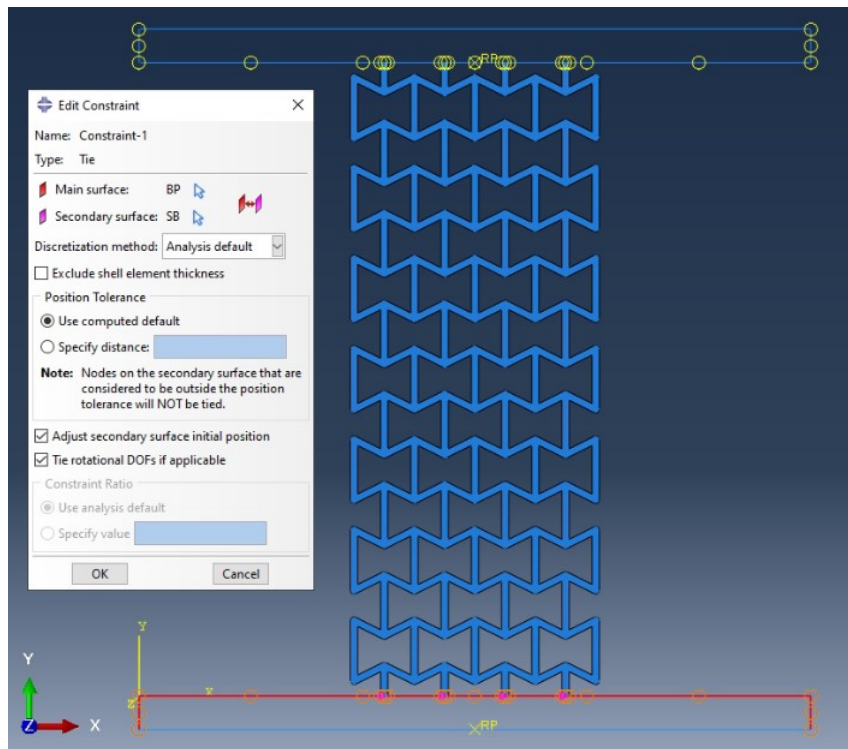


Figure B.1: Tie constraint bottom

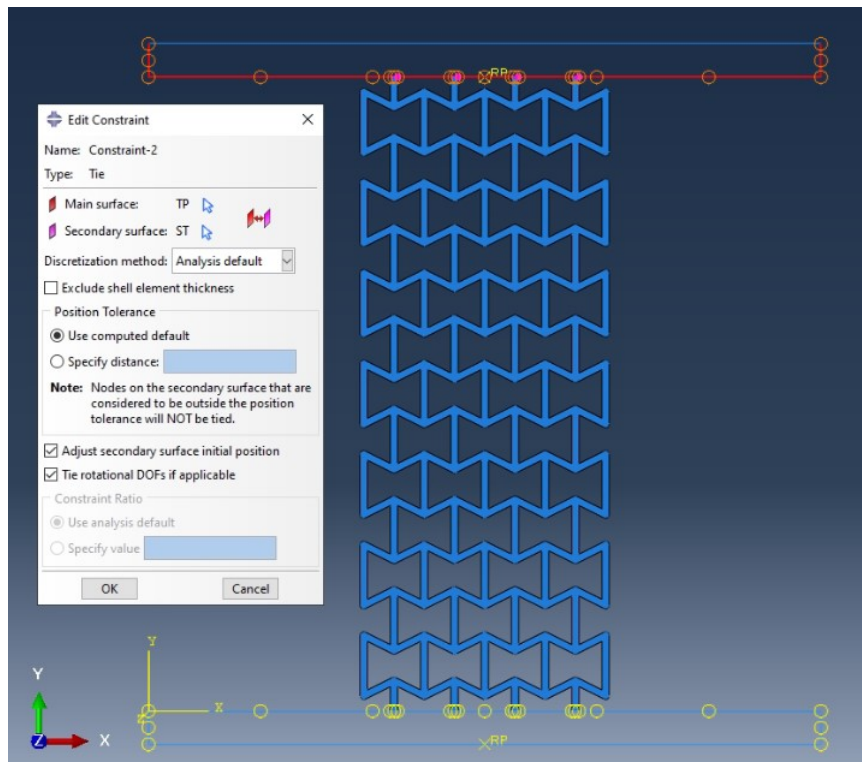


Figure B.2: Tie constraint top

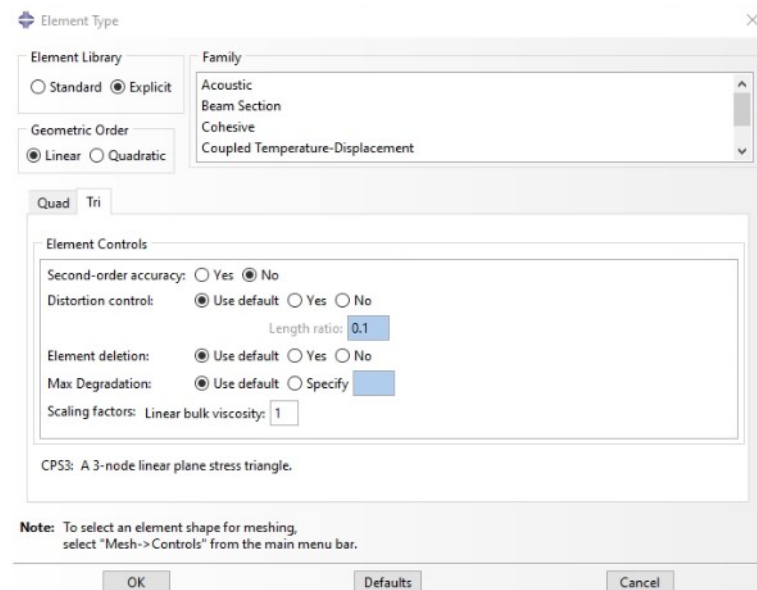


Figure B.3: Element type

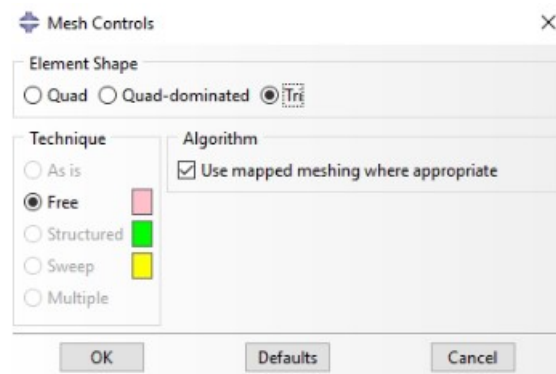


Figure B.4: Mesh controls

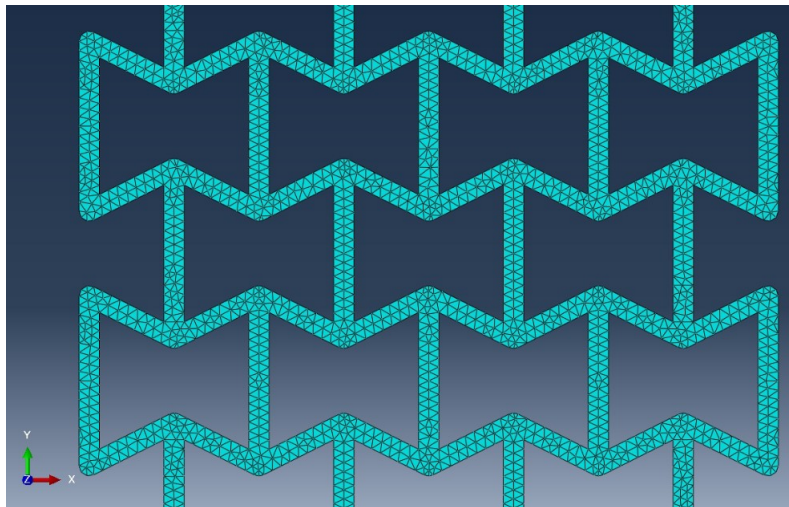


Figure B.5: Triangular shaped mesh

C

Experimental Study



Figure C.1: Sample R₁ backside showing multiple cracks



Figure C.2: Sample C₁-TPU backside showing multiple cracks



Figure C.3: Air void in Sample B-ABS



Figure C.4: Sample B casting complications



Figure C.5: Segregation

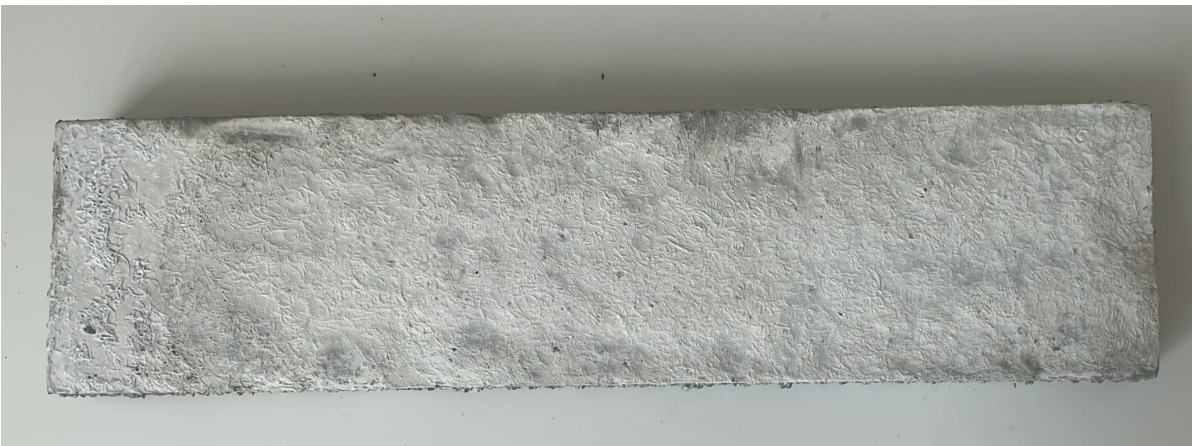


Figure C.6: Sample surface as a result from bleeding and segregation